Development and characterization of magnetic particle reinforced polymers for additive manufacturing processes

by

Balakrishnan Nagarajan

A thesis submitted in partial fulfillment of the requirements for the degree of

Doctor of Philosophy

Department of Mechanical Engineering
University of Alberta

ABSTRACT

Additive manufacturing enables the production of complex parts with less tooling and minimum material wastage. Polymer composites with magnetic functionality are promising for many applications like sensors, non-contact actuators and permanent magnets for electromechanical devices. The primary goal of this research work is to develop magnetic particle reinforced polymers and engineer additive manufacturing processes for manufacturing magnetic field responsive composites and permanent magnets involving hard ferrites and critical rare earth materials. Two different additive manufacturing techniques namely, stereolithography and material jetting were utilized to manufacture both isotropic and anisotropic magnetic composites. Irrespective of the additive manufacturing technique, developing magnetic polymer formulations that offer synergistic properties are a prerequisite for developing composites with engineered properties. The research study is broadly classified into four sections. The first section deals with the manufacture of isotropic magnetic field responsive composites using a stereolithography process. A commercial 3D printer with the capability of printing UV curable resins was utilized. Adopting a structured experimental framework, the curing behavior of magnetic particle reinforced formulations and dimensional variability in printed magnetic composites were evaluated. It was observed that characteristics of 3D printed magnetic structures depend on the formulation materials, 3D printing equipment and the process parameters. The second section of the study deals with the manufacture of field structured magnetic composites using material jetting additive manufacturing process. The finite element method in magnetics was used to develop permanent magnet-based particle alignment

fixtures to orient ferromagnetic particles during the printing process. Directionality analysis using microscopic images was conducted to evaluate the orientation angle and count of oriented structures at specific orientation angles. Fundamental work carried out in this section enabled the development of a 3D printer with magnetic particle alignment capability. Ferromagnetic particle reinforced formulations were engineered to exhibit enhancement in low shear viscosity and time dependent viscosity recovery that enabled control of particle aggregation, particle chaining and control of microstructure distortions in the UV curable polymers. X-Ray diffraction technique was used to identify the orientation of the easy axis of magnetization in anisotropic specimens. Magnetic characterization conducted on field-structured composites exhibited enhanced magnetic characteristics along the direction of field structuring. The third section of the study entailed the manufacture of permanent magnets using magnetic particles and additive reinforced epoxy resin formulations. Modifications in rheological behavior of polymer formulations was achieved adopting multimodal magnetic particle mixtures and additive materials. Control of particle settling, modifications in rheological behavior and geometric stability were accomplished using an additive that enabled controlling the formulation behavior at different process conditions. The characterization of magnetic polymers and composites using rheometry, scanning electron microscopy, X-ray diffraction and magnetometry analyses enabled correlating of the behavior observed in different stages of the manufacturing processes. In the fourth section of the study, an acrylate based UV curable photopolymer was engineered for additional thermal cure, and permanent magnets with a filler loading of up to 80 wt% were printed using the engineered

formulation. Overall, this research work broadens the capabilities for manufacturing magnetic composites with properties tailored for a multitude of engineering applications and provides a framework to understand to role of engineering material formulations to suit a wide range of processing conditions and requirements.

PREFACE

Certain sections of this thesis document have been published previously by the author or will be published in peer reviewed journal papers. Following is a list describing the publication status of this research work.

- Chapter 2 has been published in Manufacturing Letters (journal - Elsevier)
- Chapter 3 has been prepared for submission as a journal and conference paper
- Chapter 4 has been published in Additive Manufacturing (journal - Elsevier)
- Chapter 5 has been prepared for submission as a journal paper
- Chapter 6 has been published in Journal for Manufacturing and Materials Processing
- Results included in Chapter 7 will be published in at a suitable conference and as peer reviewed journal papers after additional experimental validation

ACKNOWLEDGEMENT

First and foremost, I would like to sincerely thank my advisors Dr. Pierre Mertiny and Dr. Ahmed Jawad Qureshi for their valuable guidance, continuous support and supervision throughout my doctoral program. Their mentoring and encouragement during different phases of this journey has helped me to become more independent in research and develop professionally. I would like to extend my thanks to Dr. Uttandaraman Sundararaj and Dr. Simon Trudel for providing access to their lab facilities and assistance with rheological and magnetic characterization. I would like to thank Milad Kamkar and Martin Schon for their assistance with the rheological and magnetic characterization. I would like to express my appreciation to the employees of NanoFAB and the Department of Earth Sciences at the University of Alberta for providing training and assistance with the characterization techniques like scanning electron microscopy and X-ray diffraction. I would like to thank the technicians from the Machine Shop in Mechanical Engineering for their technical support with different equipment. I express my gratitude to the University of Alberta Future Energy Systems research initiative and associated funding from the Canada First Research Excellence Fund, which has made this research possible. I would like to thank my fellow colleagues for their continuous support throughout my research. Finally, none of this would have been possible without the support of my father Nagarajan Harisubramanian, my mother Akilandam Nagarajan, my brother Venkatakrishnan Nagarajan and my wife Sowmya Rajan for their continuous love, support and inspiration.

TABLE OF CONTENTS

LIST OF TABLES

LIST OF FIGURES

CHAPTER 1: INTRODUCTION

1. Overview of Chapter 1

Chapter 1 provides an introduction to different fundamental scientific and manufacturing subject matter related to this PhD research work. Concepts and technical literature related to magnetism, magnetic materials, manufacturing methods for permanent magnets, structure property relationships, applications of magnetic materials in flywheel energy storage systems, microscale components, additive manufacturing (AM) methods and material behavior requirements for AM processes are discussed. Chapter 1 concludes with stating the hypothesis, motivation, objectives and the significance of this thesis research work.

1.1 Magnetism – An introduction

Magnetism deals with the science of a material's ability to attract or repel ferrous objects without any physical contact. Magnetism in materials originates from the spin of a nucleus, orbital motion of the electrons and spin of the electrons. Magnetism is associated with the angular momentum of elementary particles, and hence, the orbital moments can be understood in terms of Bohr's atom model where the electrons revolve around the nucleus in circular orbits. The magnetic dipole moment, which is a fundamental magnetic quantity, is expressed in terms of angular momentum as follows:

$$m = -\frac{e}{2m_e} l \tag{1.1}$$

In Eq. 1.1, e is the charge of an electron, l is the angular momentum and m_e is the mass of an electron. These electron spins lead to the inherent magnetization in materials. In

many naturally occurring materials the resultant magnetic moment is zero, whereas in magnetic materials, there exists a resultant moment of certain magnitude depending on the orientation of the electron spins resulting in a net magnetization [1]. Magnetism is primarily classified into five types namely, diamagnetism, paramagnetism, ferromagnetism, ferrimagnetism and antiferromagnetism. These classifications are based on the net contribution of the magnetic moments in materials to their overall magnetization. Materials exhibit diamagnetism when their magnetic response opposes the applied external magnetic field. Examples of diamagnetic materials include copper, silver, gold and bismuth. Paramagnetism is a type where the magnetization is weak but aligns parallel to the direction of applied external magnetic field. Material examples include aluminum, platinum and manganese. Diamagnetic and paramagnetic materials require an externally applied magnetic field to exhibit magnetic behavior. In ferromagnetic materials, the magnetic moments orient themselves along the direction of the applied magnetic field and retain the magnetization direction even when the external field is removed. Iron, cobalt, nickel and some rare earth materials belong to the category of ferromagnetic materials. Ferrimagnetism is a scenario where the magnetic moments in materials have opposite directions with different magnitude of magnetization. This difference in magnitude results in a net magnetization. Iron oxide (Fe_3O_4), yttrium- iron garnet and γ-Fe_2O_3 are the most familiar ferrimagnetic materials. Anti-ferromagnetism arises when the neighboring electrons align themselves in the opposite direction with equal magnetic moments. Hence, the net magnetization is zero and such materials are unable to retain the magnetization in the absence of an external magnetic field [2].

1.2 Fundamental terminologies in magnetism

Magnetization of a material, M, is defined as the magnetic moment, m, generated per unit volume of material, V. Mathematically, magnetization is expressed as

$$M = \frac{m}{V} \tag{1.2}$$

Magnetic fields are produced when an electrical charge is in motion. This can be due to the orbital motion and spin of electrons or due to electric current flowing through a conductor. When a magnetic field is present in a free space there is always a magnetic flux associated with it. The magnetic flux is denoted by φ and it is measured in units of Weber. In the case of a permanent magnet the magnetic moment (m) is given by

$$m = pl\,;\ \left\{ p\ = \frac{\varphi}{\mu_0} \right\} \tag{1.3}$$

where p is the pole strength and l is the dipole length. The magnetization (M) is thus expressed as

$$M = \frac{\varphi}{\mu_0 A} = \frac{B}{\mu_0} \tag{1.4}$$

The magnetization (M) is an inherent contribution of the magnetic material and there is no external electric current present to generate the magnetic field. However, in the presence of an applied field (H), the magnetic flux density (B) or magnetic induction in free space is expressed as

$$B = \mu_0 H \tag{1.5}$$

where μ_0 is the permeability of free space. However, in other media, μ_0 is replaced with μ which represents the permeability of the medium. In Eq.1.5, it should be noted that B is not a linear function of H. For ferromagnetic materials μ varies rapidly with the

magnetic field (H). Magnetic flux density primarily consists of two contributions, i.e., one from the magnetic field (H), and the other from magnetization (M). The magnetic induction in free space is $\mu_0 H$ and induction from the magnetization of the material is $\mu_0 M$. The resultant magnetic induction is a vector sum of the two quantities

$$B = \mu_0(H + M) \tag{1.6}$$

Magnetic materials are primarily classified based on susceptibility or permeability. The permeability is defined as

$$\mu = \frac{B}{H} \tag{1.7}$$

Magnetic susceptibility is defined as

$$\chi = \frac{M}{H} \tag{1.8}$$

The susceptibility of ferromagnetic materials is positive and typically ranges between 50 and 10,000 [2]. Susceptibility of a material depends on the direction in which it is measured.

1.3 Ferromagnetism and magnetic domain theory

Among many types of magnetism discussed before, ferromagnetism is of great interest as it is the underlying principle behind the behavior of permanent magnet materials. It is necessary to understand ferromagnetic materials on a microscopic scale (at the level of magnetic domains) to establish the evolution of magnetic properties. In a microscopic scale, magnetization varies within the ferromagnetic material. A ferromagnetic material contains physical regions of uniform magnetization called magnetic domains. Magnetic domains are a natural consequence of different energy contributions like anisotropy energy, exchange energy, magnetoelastic energy and

magnetostatic energy [3]. According to magnetic domain theory, the atomic magnetic moments in a ferromagnetic material are ordered even in the demagnetized state. However, due to the net configuration of individual domains, there exists a difference between the magnetized and demagnetized states. The direction of alignment varies from one domain to another since magnetic moments tend to align along certain crystallographic axis (axis of easy magnetization) in the absence of an external field. The natural direction of magnetization within a ferromagnetic domain usually lies along one or more easy axes. This tendency in magnetic materials is called magneto crystalline anisotropy and the energy associated is called anisotropy energy [1]. Exchange energy describes the interaction between neighboring magnetic moments. This exchange interaction enables adjacent moments to couple, enabling ferromagnetism in materials. Magnetoelastic energy arises from the interaction between magnetization and mechanical strain of the crystallographic lattice. When stresses are present in a magnetic material, they tend to have a preferred magnetization direction. The contribution from the magnetization of the material is called the magnetostatic energy. The process of rearranging the magnetic domains accomplished by applying an external magnetic field is called “magnetization”. At low applied magnetic fields, the growth of magnetic domains occurs for domains aligned parallel to the direction of applied magnetic field, and magnetic domains pointing opposite to the magnetic field experience domain size reduction. At moderate field strength, the atomic magnetic moments in the direction opposing the applied field overcomes the anisotropy energy and rotate from their original direction of magnetization to the crystallographic easy axis nearest to the applied field direction. In simple terms, the

domains undergo a rotation in the applied magnetic field. At higher magnetic field strength, all the magnetic moments are aligned along the preferred crystallographic easy axis lying close to the field direction. This results in a material with domains pointing towards a single direction [2]. The dynamics of such magnetic domains under the influence of an external magnetic field gives rise to ferromagnetic behavior.

1.4 Ferromagnetic material behavior and properties

The fundamental characteristic of a ferromagnetic material is its irreversible nonlinear response of its magnetization to an externally applied magnetic field. The bulk magnetic properties of a ferromagnetic material is a plot of magnetic induction for different applied magnetic field strengths. This plot is called a hysteresis loop and it primarily determines the suitability of ferromagnetic materials for different applications. For example, magnetic materials for electromagnets should exhibit low remanence and coercivity so that the magnetization is reduced to zero. Conversely, magnetic materials for permanent magnets need high remanence and coercivity to retain maximum magnetization. Many parameters useful in characterizing magnetic materials are obtained from the hysteresis loops. Three important parameters include saturation magnetization (Ms), remanent magnetization (Mr) and coercivity (Hc). Figure 1.1 shows the magnetization (M) versus applied field (H) curve normally referred to as the hysteresis curve. Once the external field is applied the domains begin to align in the direction of the field and magnetization occurs. The curve plateaus at a point (Point A) and it is referred to as saturation magnetization. No matter how much additional field is applied, the ferromagnet will not gain magnetization above this point. At the point where the applied field is zero (Point B) the ferromagnet retains some

magnetization. This is known as remanence or retentivity. It is the measure of remaining magnetization when the applied field is zero.

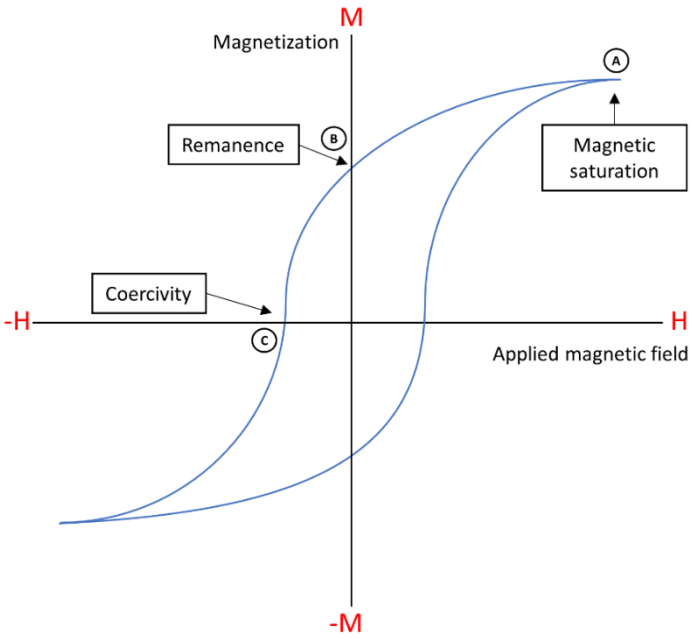

Figure 1.1: Hysteresis loop of a ferromagnetic material (Ms – Saturation magnetization, MR – Remanence, Hc – Coercivity).

H_c is referred to as the coercivity of the ferromagnetic material. It is the reverse field required to drive the magnetization to zero after being saturated (Point C). One of the fundamental characteristics of a permanent magnet is its ability to generate a strong magnetic field in the absence of an external magnetic field. The critical property that determines the ability to generate a magnetic field is remanent magnetization. Magnetic domains within the ferromagnetic materials play a significant role in determining the overall remanent magnetization of the material. Magnetic domain theory suggests the alignment of magnetic domains along the magnetic easy axis. The extent to which the domains remain aligned once the external magnetic field is removed determines the remanent magnetization. The ability of a material to resist demagnetization is determined by coercivity. Many applications involve magnetic materials to withstand

demagnetizing fields. Coercivity is primarily determined by the ability of domain walls to move within the material. If the domain walls are difficult to move or nucleate, larger magnetic fields will be required to demagnetize the material, and hence, the material has a high coercivity. Temperature is one of the primary factors affecting magnetic properties as ferromagnetic materials experience a transition to paramagnetic behavior. an important parameter is the Curie temperature at which a material experiences sudden drop in remanent magnetization and coercivity. With increasing temperature, the atoms gain enough thermal energy to disrupt the magnetic ordering (i.e. thermal energy overcomes the exchange energy) resulting in the magnetic behavior transition [2].

Properties of magnetic materials are classified into intrinsic and extrinsic properties. Magnetic characteristics of a material that are dependent on the crystal structure and chemical composition are referred to as intrinsic properties. Such properties include spontaneous magnetization, magneto crystalline anisotropy and Curie temperature [4] [5] [6]. Magnetic properties derived from the hysteresis loops are referred to as extrinsic properties. Extrinsic magnetic properties include remanence and coercivity that reflect the actual magnet morphology. Remanence and coercivity obtained from hysteresis loops of ferromagnetic materials are dependent on the morphology, metallurgical microstructure and defects present within the material [6]. Based on properties like remanence and coercivity, magnetic materials are classified for applications like permanent magnets, electric motors, inductors, magnetic recording and power generation. Magnetic materials are further classified into hard and soft magnetic materials depending on their coercivity values. Materials with coercivity values less than 1000 A/m are considered magnetically soft, and materials with

coercivity greater than 10000 A/m are considered magnetically hard. Soft magnetic materials are utilized in applications that require amplifying the magnetic flux generated by electric currents. Hard magnetic materials are used in applications that involve generating a high magnetic flux like electric motors, generators, moving coil meters and control devices for electron beams [2].

1.5 Manufacturing methods for permanent magnets and associated properties

Critical factors that govern the successful manufacturing of permanent magnets are the material composition, microstructure and the processing route. Common manufacturing process routes include sintering, polymer bonding and hot deformation. Methods commonly used to make polymer-bonded permanent magnets include compression molding, injection molding and calendaring. Irrespective of the adopted manufacturing technique, one common step in magnet manufacturing processes is the application of an external magnetic field to align the crystallographic easy axis to obtain anisotropic magnetic characteristics [7]. Even though commercially available magnetic materials are polycrystalline in nature, understanding the significance of texturing magnets can be understood from the Stoner-Wohlfarth model for hysteresis for single domain particle systems [2]. Figure 1.2 exhibits the hysteresis loops for anisotropic and isotropic magnetic particle distribution. With the particles aligned applying an external magnetic field, the hysteresis loop would be broader with remanence values nearly equivalent to the saturation magnetization whereas for an isotropic particle distribution, the remanence is half its saturation.

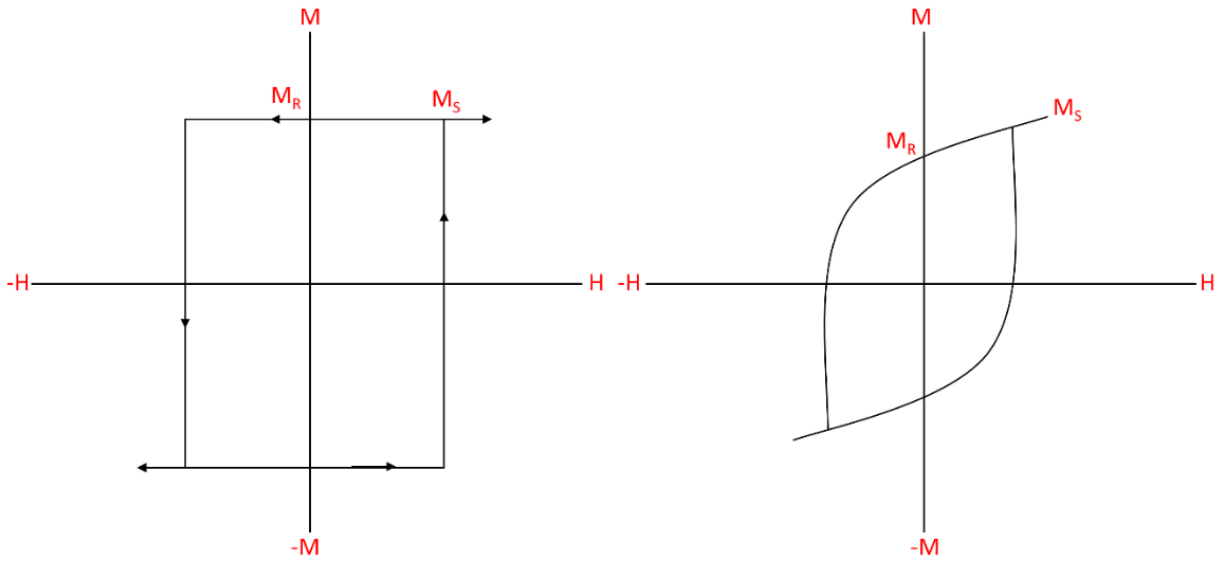

Figure 1.2: Schematic of a hysteresis loop for single domain particle with applied field parallel (left) and perpendicular (right) to the direction of magnetization.

Examples from technical literature include neodymium iron boron (NdFeB) magnets fabricated by Xiao-Lei and co-workers using injection molding technique [8]. In this work, anisotropic NdFeB powder mixed with a polymeric binder was warm pressed in the presence of an electromagnetic field of 2.5 Tesla in magnitude. Field structured magnetic composites were fabricated using uniaxial and biaxial magnetic fields producing chain like and sheet like particle structures. Such composites exhibited large anisotropies in magnetic remanence due to the local field effects combined with the large crystalline anisotropy of the material [9]. Enhancements in magnetic susceptibility was observed for Fe based nanoparticles along the direction of particle structuring [10]. Bonded hybrid magnets using NdFeB blended with ferrite and carbonyl iron powder were fabricated using a compression molding technique. It was found that the addition of ferrite enhanced the coercivity of the polymer bonded magnets [11]. It was observed that the resultant magnetic properties were dependent on the type of magnetic powder, polymer, loading factor and molding technology [12].

Compaction pressure applied during the compression molding process was observed to enhance remanence and decrease coercivity as reported in the technical literature [13]. Similarly, ferrite based magnets have also been manufactured using powder injection molding technique and later sintered to achieve the best magnetic properties [14]. Remanence magnetization of strontium ferrite permanent magnets textured in a magnetic field were enhanced by a factor of 1.4 compared to their isotropic counterparts [15]. Apart from the above mentioned examples, permanent magnet materials find significant applications in energy storage devices and composites developed in microscale for many micro-electromechanical-systems (MEMS) applications.

1.6 Applications in flywheel energy storage systems

A flywheel energy storage device can be considered a mechanical battery that converts rotational kinetic energy to electrical energy and vice versa. Flywheel systems employing composite material rotors have been considered primarily for applications where high power capacity is required [16]. Recently, flywheel systems were developed as true energy storage devices, which are also known as electromechanical batteries. One remarkable example of a flywheel energy storage system is the "Gyrobus", which was developed by Maschinenfabrik Oerlikon in Switzerland in the 1950's. Disk shaped flywheels were initially made out of steel and had a maximum speed of 3000 rotations per minute (rpm). In recent times, high strength materials like fiber reinforced polymer composites are used to manufacture flywheel rotors. A flywheel energy storage system (FESS) experiences negligible performance degradation during charge-discharge cycles and can be designed to have large power

and energy capacity by selecting the appropriate electrical machine and flywheel rotor. In a FESS, a single electrical machine functions as both the motor and generator. Other important components of a FESS are low-friction bearings (magnetic), a vacuum enclosure, and a power electronics unit. Modern-day flywheels operate at high speeds, typically ranging from 30,000 to 50,000 rpm. High-strength and light-weight materials like carbon fiber and glass fibers are mainly used to manufacture flywheel rotors. A FESS employs an electrical machine (motor/generator unit) to spin the flywheel to high speeds and convert rotational kinetic energy back to electrical energy. High speed electrical machines are generally equipped with permanent magnet materials that have high saturation magnetization and large coercive force. Ha et al. optimized the design of a hybrid composite flywheel rotor with integrated permanent magnets attached to the inner rims of a flywheel rotor [17]. An emerging design approach is to integrate the electrical machine functionality into the flywheel rotor by incorporating magnetic particles into composite polymer matrix. Suitable rare earth materials like NdFeB and samarium-cobalt have been tested for flywheel applications. Rare earth magnetic particles in a size range of 100 to 150 μm were found to be appropriate for the application, and composite flywheel rims were manufactured by the process of filament winding [18]. Fiber reinforced composite materials combined with high energy permanent magnet materials enabled the development of magnetically loaded composite rotors with mechanical and magentic properties for utilization as an external rotor for a brushless permanent magnet electrical machine [19]. Mason et al. identified the potential of a magentically loaded fiber reinforced rotor with an Halbach magnetized configuration appropriate for FESS applications. By loading the fiber

reinforced rotor with hard magentic particles, a permanent magnet rim(s) can be integrated with the flywheel rotor. Additionally, composites with soft magnetic particles were observed to be suitable for magnetic bearings used for flywheels [20]. Apart flywheel rotor systems, magentic composites were also developed with charactertics suitable for flywheel lift magnet applications using bi-disperse iron particles [21]. Edwards et al. developed magnetic composites for electromechanical applications by incorporating iron particles in epoxy resin [22]. Reductions in mechanical properties were observed, and the focus was on enhancing the magnetic characteristics. Integrating magnetic particles with fiber reinforced composites enabled developing processes to tailor the needs for various electromechanical applications in terms of both mechanical and magnetic properties.

1.7 Applications in microscale systems

Functional magnetic composites, magnetic shape memory alloys, magnetic micro electromechanical systems (MEMS) and magnetic elastomers use a variety of magnetic materials [23]. Magnetic forces offer an attractive option for actuation in MEMS devices due to contact free actuation capabilities. Microscale magnetic actuation capabilities have led to the implementation in a variety of microfluids and MEMS devices. In the field of micro-robotics, magnetic forces are used to provide wireless control and power to perform complex three-dimensional motions. Integration of different magnetic fillers with the polymer resin remains a significant challenge in the fabrication process [24]. Fabrication of micromagnets using traditional ultraviolet (UV) lithography and micro-molding techniques have already been reported in the technical literature. However, technical challenges like controlling suspension

viscosity for spin coating processes, particle settling, and precise control of particle alignment still exist in the fabrication of magnetically loaded polymer composites for microscale applications [25]. A micropump with diffuser elements and an integrated composite magnet was developed using NdFeB magnet powder dispersed in polydimethylsiloxane (PDMS) resin [26]. High performance NdFeB micromagnets using magnetron sputtering and high power plasma etching techniques have been reported in the technical literature [27]. Using low modulus membrane materials, elastic hard magnetic films with the ability to produce bi-directional deflections in an external magnetic field were fabricated using microfabrication approaches [28]. Mechanically compliant, magnetically responsive micro structures using a ferromagnetic photoresist containing nickel nanospheres dispersed in photosensitive epoxy resin (SU8) were fabricated using UV lithography based approaches [29]. Screen printing was used as a technique to fabricate strontium ferrite thick films with an easy axis orientation perpendicular to the films surface [30]. Hard magnetic films were fabricated by embedding anisotropic NdFeB particles in a polymethylmethacrylate polymer matrix for MEMS applications. Fabricated thick films exhibited out of plane macroscopic magnetic anisotropy [31]. The immense capabilities of magnetic field responsive materials in terms of magnetic actuation, deformation capabilities like stretching, bending, rotation upon exposure to magnetic fields and abilities for controllable drug release and shape memory devices have made polymer based magnetic materials a topic of intensive research [32]. Even though many robust manufacturing approaches exist, new innovations in materials and manufacturing processes can significantly enhance the performance of many functional devices. One

such fast emerging technology is Additive Manufacturing (AM), which will be detailed din the next section.

1.8 Additive manufacturing – Current state for the art

Additive manufacturing, also known 3D printing, is a rapid prototyping technique where a component is built by adding the material in a layer-wise fashion. AM is a freeform fabrication approach that enables manufacturing parts with complex geometrical shapes with very minimal material wastage. The basic AM process involves steps starting with model design using a computer aided design (CAD) software, manipulation of printing data known as STL files ('STL' was originally associated with the term of Stereolithography), machine setup, automated part building and post processing [33]. Components from a wide variety of materials such as metals, polymers, composites and ceramics have been made using AM methodologies. Among these materials, polymers and composites are materials of interest for a variety of applications in a wide range of industries. AM techniques for polymer based materials include fused deposition modelling (FDM), stereolithography (SLA), material jetting, inkjet printing, binder jetting and powder bed fusion. Compared to many traditional manufacturing approaches, AM methods offer the advantage of product development and manufacture at shorter lead times with minimum tooling and material wastage. The primary focus of the present research is on stereolithography and material jetting based manufacturing approaches utilizing UV curable and thermally curable polymer formulations.

Stereolithography or vat-photopolymerization is an AM technology that involves curing of a liquid photosensitive polymer using UV irradiation that supplies

the energy necessary to induce a chemical reaction [34]. Upon UV irradiation, a crosslinking reaction is initiated in the multifunctional prepolymer by reactive species called free radicals. The prepolymer contains "photo-initiators" as one of its constituents, which upon UV irradiations generates free radicals to initiate the polymerization reaction through photophysical and photochemical processes. The highly exothermic curing process creates highly crosslinked polymer network. The reaction kinetics are strongly influenced by light intensity, resin composition and temperature. Figure 1.3 shows a basic schematic of the stereolithography process.

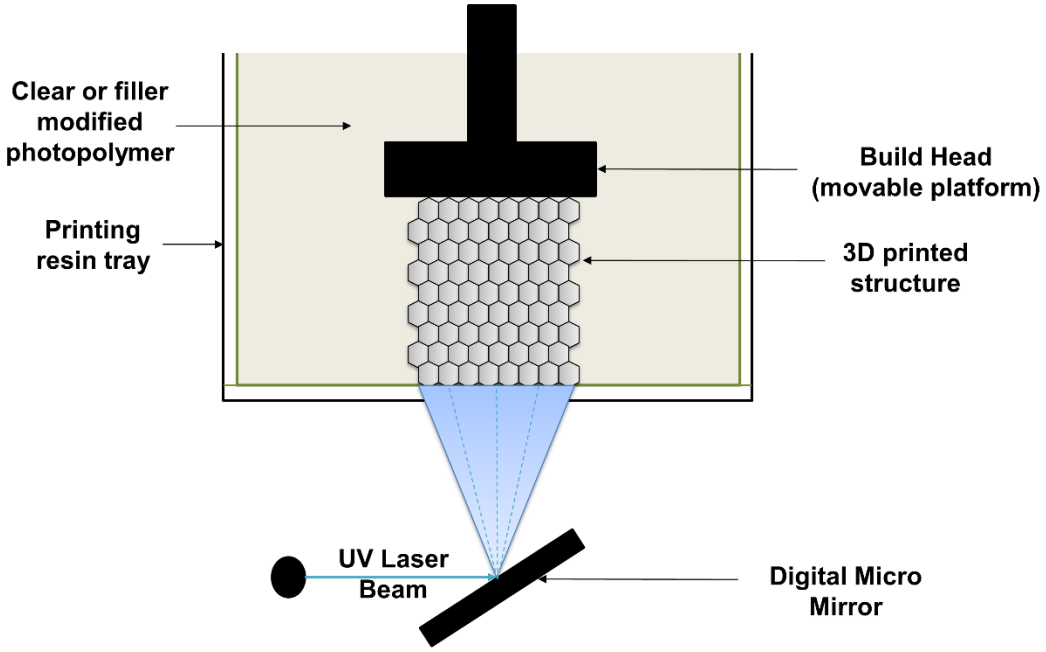

Figure 1.3: Schematic of a stereolithography process.

There are three different configurations widely adopted for the photopolymerization process. They are vector scan, mask projection and two photon polymerization configurations. In this research a commercial stereolithography printer based on mask projection is utilized. Layer-wise curing in stereolithography process where the entire layer is irradiated using UV is called mask projection

stereolithography. In the mask projection approach, a large radiation beam is patterned by a device called a Digital Micromirror Device (DMD) [33]. Materials used in stereolithography processes comprise of polymerizable oligomers, photo initiators, reactive diluents and other additives. Photo initiators are the fundamental and most important component as they serve as materials for initiating the polymerization reaction and directly govern the rate of cure. Photo initiators are classified into free radical initiators and cationic initiators. The majority of stereolithography resin systems based on acrylate monomers utilize free radical photo initiators. The molecular structure of the acrylate monomer is shown in Figure 1.4, where symbols C, O and H represent the carbon, oxygen and hydrogen atoms and R denotes vinyl groups. A vinyl group is a molecular structure with a carbon-carbon double bond. It should be noted that it is these vinyl groups that enable crosslinking of the photopolymer.

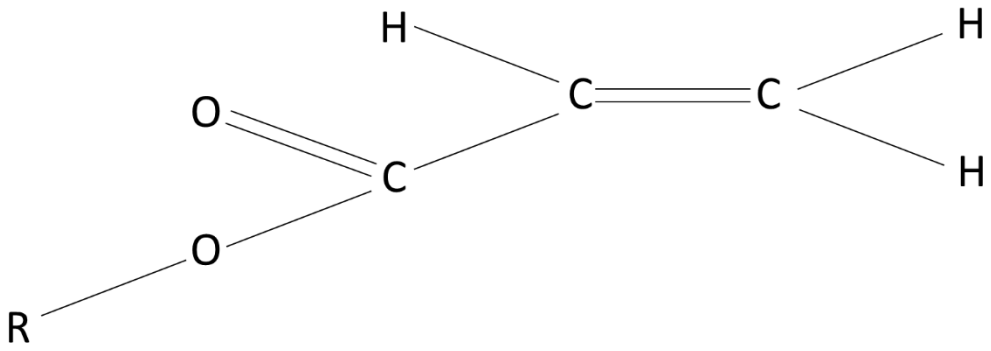

Figure 1.4: Molecular structure of acrylate monomer.

Photosensitive polymers reinforced with metal and ceramic fillers have been a rapidly evolving research field in AM. Development and characterization of ceramic structures have been widely reported in the technical literature [35]–[39]. Several

factors like the type of formulation materials, UV laser characteristics and machine tunable process parameters were observed to influence the successful fabrication of ceramic structures. It was observed that the rheological properties of the formulation materials governed different aspects of the manufacturing process, ranging from dispersion stability to resolution of the printed components [40]–[42]. Considering the development of ceramic structures, the process involves de-binding and sintering where the polymeric material is removed to allow the ceramic materials to fuse together.

Similar to stereolithography, researchers have also developed techniques like inkjet printing, material jetting and direct writing to develop polymer based solid structures and polymers reinforced with ceramics and metal fillers. A fundamental schematic of the material jetting process is depicted in Figure 1.5.

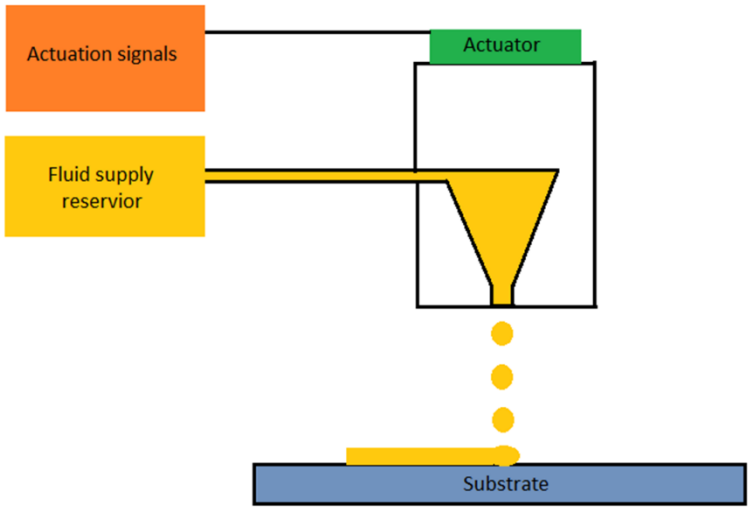

Figure 1.5: Schematic of a material jetting process.

Depending on the type of the deposition system, the material dispensing is either in the form of droplets or a continuous jet. Material jetting as a manufacturing technique has primarily been adopted for applications like electronic packaging, optics and applications that require two-dimensional printed structures. Printing machines capable of three-dimensional printing with acrylate photopolymers and waxy polymers have been developed by industries. Material deposition was controlled varying both material and process parameters. Prominent material variables include viscosity and surface tension, and strategies were adopted to modify the fluid properties. Machine parameters included the frequency of droplet deposition, velocity and distance between the nozzle tip and substrate. Micro stereolithography of ceramic structures using alumina particles dispersed in a photosensitive polymer stabilized using a surfactant has been reported in the technical literature [43]. For continuous material jetting process for ceramic materials, Tay et al. determined the surface free energies of several substrates, spreading of dispensed droplets and identified the role of fluid properties like surface free energy and surface tension [44]. Printing of solder pastes using droplet based printing technology gained rapid momentum as there was a continuous drive towards developing complex integrated circuits at lower costs and smaller device geometry [45]. There has been growing interests in developing additively manufactured structures for functional electronics. Espalin et al. showed that with the base dielectric structure fabricated using stereolithography, material jetting technique was utilized to dispense conductive inks in channels to provide electrical interconnects [46]. Using a metal jet, 3D structures were fabricated dispensing molten metal drops; the technique enabled development of metal structures using the jetting process [47].

Utilizing fundamental methods to control colloidal suspension rheology, enhanced control over composition and printed architectures were achieved [48]. Lithium ion micro battery architectures with possible applications in microelectronics and biomedical devices were printed using the material jetting technique. Using inks that exhibited viscoelastic properties, thin walled anode and cathode structures were printed, and resultant structures exhibited high areal energy density [49]. A review of AM techniques utilized for bioprinting presented by Tasnim et al. elucidates the importance of material jetting used as a tool for printing tissues from stem cells using bio inks [50].

As observed from the above examples involving material jetting as a tool to develop 3D printed structures, there are many technical challenges to establish a successful process. Primary challenges include the development of formulation materials, droplet generation strategies, control of material deposition, material behavior control on the substrate, curing of the deposited material, and control of deposition on previously deposited layers. Additional challenges include operational considerations like path planning of the deposition head, generation of negative pressure to pull the material back into the nozzle once the deposition is complete, nozzle clogging and cleaning of nozzles.

1.9 Understanding materials for AM processes

Materials developed for AM processes need to meet certain multidisciplinary requirements in order to facilitate a successful manufacturing process and satisfy product performance specification. In freeform fabrication, material selection governs many aspects of the manufacturing process, including determining process parameters,

component geometry, material microstructure and final mechanical and functional properties of the manufactured component. The prime focus of this research being the utilization of stereolithography and material jetting to produce magnetic composites, understanding how the developed materials behave during processing and usage is vital. One of the areas of primary concern is the behaviour of particles in the polymer system, their influences on rheological properties, and suitability of polymer formulations for the AM processes.

Filler modified polymer dispersions contain the base polymer reinforced with fillers that enable achieving the intended property enhancements in fabricated components. When these fillers are dispersed in the polymer matrix, they are acted upon by a multitude of forces. The hydrodynamic force acting on the particle is expressed as

$$F^h = 6\pi\eta a V \tag{1.9}$$

where a is the particle radius, V is the velocity of the particle and η is the viscosity of the suspending medium. Particles are additionally subjected to gravity, and consequently, the gravity force acting is given by Archimede's principle as follows:

$$F^g = \left(\rho_p - \rho_m\right)\left(\frac{4}{3}\right)\pi a^3 g \tag{1.10}$$

where ρ_{p} and ρ_{m} are the densities of the particle and the suspending medium and g is the acceleration due to gravity. Apart from these forces, other effects include Vanderwall's, electrostatic, magnetostatic and induced forces in external electrical and magnetic fields. In many real case scenarios, interactions between particles can be controlled only if the right measures are taken as part of the formulation and dispersion

method. The quality of the degree of dispersion is observed to be one of the prime factors governing many fundamental aspects of filler modified polymer behaviour [51].

Stereolithography and material jetting AM processes demand stringent rheological requirements to control a broad set of material and process behaviour requirements like settling control and aggregation control. It is only by controlling the behaviour of the dispersed particles that the manufacturing process is enabled. The base resins used for stereolithography primarily exhibit Newtonian behaviour [52]. Rheological characteristics of suspensions are influenced by particle size, particle size distribution, particle interactions, surface properties of the particles and particle shape. With increasing volume fraction of the solid filler, suspensions exhibit non-Newtonian fluid behaviour where viscosity is dependent on shear rate [53]. Similarly, for a material jetting process the materials should exhibit shear-dependent viscosity reduction to enable dispensing and sufficient viscosity recovery properties to maintain the geometry of the deposited material [54]. Similar approaches have been adopted for extrusion type additive manufacturing of thermoplastic materials [55], [56]. Ceramic material formulations have been well studied in the technical literature, and formulations employing surfactant materials have been ascertained as efficient means for achieving formulation stability and viscosity reduction [41]. Nevertheless, stabilizing magnetic materials has been rather difficult using surfactant materials for micron sized particles due to the presence if dipole-dipole interactions [57]. In the case of magneto-rheological fluids, where magnetic nano or microparticles are dispersed in a polar or non-polar carrier, ionic or non-ionic surfactants were observed to enhance the stability through electrostatic and steric stabilization mechanisms [58], [59].

Polymeric resins with incorporated fillers, modified using additives, exhibit shear thinning or shear thickening material behaviour. The obtained material behaviour is highly dependent on shear rate. Several viscosity models exist to characterize the properties of such formulations. The power law viscosity model is expressed as follows [60]:

$$\eta = k\dot{\gamma}^{n-1} \tag{1.11}$$

where η is the viscosity, $\dot{\gamma}$ is the shear rate, k is the consistency index (or) viscosity and n is the flow index. A flow index $n < 1$ indicates shear thinning behaviour; $n > 1$ signifies shear thickening behaviour; and $n = 1$ indicates Newtonian behaviour. Another model utilized to describe non-Newtonian viscosity is the Cross model, which is utilized when viscosity at intermediate shear rates exhibits power law type behaviour. This model is mathematically expressed as [51]

$$\eta - \eta_\infty = \frac{\eta_0 - \eta_\infty}{1 + (k\dot{\gamma})^m} \tag{1.12}$$

where η_0 is zero shear viscosity, $\eta_\infty$is infinite shear viscosity, k is the cross constant and m is the Cross exponent. To determine yield stress of a formulation, the Bingham model and Herschel Bulkley model are widely used. The Bingham model is expressed as follows:

$$\tau = \tau_0 + \eta\dot{\gamma} \tag{1.13}$$

where τ is the shear stress, τ_0 is the yield stress, η is the viscosity and $\dot{\gamma}$ is the shear rate. The difference Herschel-Bulkley model compared to the Bingham model is the inclusion of a power law material behavior term

$$\tau = \tau_0 + C\dot{\gamma}^n \tag{1.14}$$

where n is the Herschel Bulkley index and C is the consistency index [60]. Utilizing the mathematical models, it is possible to quantify the rheological properties of different formulations. Selecting the right model also enables determining properties without significant overestimation.

The rheological characteristics of the developed formulations govern many aspects of the material and process behaviour ranging from particle aggregation to finalizing the process parameters for the deposition process. Dispersions exhibit a yield point primarily due to intermolecular forces due to dipole-dipole interactions. Bonds through intermolecular hydrogen bonds build up three-dimensional network forces and exhibit a solid-like structure resulting in elastic material behaviour in the low deformation ranges. Materials with the ability to build a network structure undergo structural decomposition under the influence of external forces and time-dependent structural regeneration once the force is removed.

Analyzing the complex rheological properties of the materials enables a deeper understanding of the material behaviour. Materials developed for AM processes like extrusion, material jetting and direct writing are expected to satisfy many fundamental conditions, one among which is deposit shape control, which is primarily governed by the nature of the deposited material. Basic characteristics of materials used for material jetting processes are often time-dependent, and hence, understanding the material response enables constructing a robust manufacturing framework. Materials with a viscoelastic character possess combined properties of elastic solids and viscous fluids. Combined behavior according to Newton's laws and Hooke's laws can be observed in

such viscoelastic materials. An ideal viscous behaviour represented by Newton's law in expressed as follows:

$$\tau = \eta \,.\dot{\gamma} \tag{1.15}$$

The shear viscosity is independent of the degree and duration of the applied shear load, and an ideal viscous behaviour can be represented using a dashpot model. Once the load is removed, the fluid remains in the deformed state. The ideal elastic deformation behavior according to Hooke's law is expressed by:

$$\sigma = E \,.\epsilon \text{ (or) } \tau = G \,.\gamma \tag{1.16}$$

where σ represents tensile stress, ϵ is tensile strain, E is the elastic modulus, τ represents shear stress, γ is shear strain and G is the shear modulus. A spring model is used to represent an ideally elastic solid. Once the applied load is removed the spring recoils elastically returning to the initial state.

One basic model to capture the behaviour of viscoelastic materials is the Maxwell model, which is expressed by a series combination of a spring and dashpot element. In this combination, the spring exhibits instantaneous deformation proportional to the applied load. Under constant load, the dashpot starts to move and continues to move while the force is applied. Upon load removal, the spring recoils back while the dashpot position remains unchanged. The Maxwell model is expressed as follows:

$$\dot{\gamma} = \left(\frac{\tau}{\eta}\right) + \left(\frac{\dot{\tau}}{G}\right) \tag{1.17}$$

Another basic model describing viscoelastic materials is the Kelvin-Voigt model, which is mathematically represented as follows:

$$\tau = G\gamma + \eta\dot{\gamma} \tag{1.18}$$

The behaviour of a viscoelastic material according to the Kelvin-Voigt model involves a spring and dashpot element in parallel. Under the influence of an external load, both components deform simultaneously. The motion of the spring is slowed by the presence of the dashpot. Upon load removal, the presence of the dashpot leads to a time-dependent recovery of the system. Classifying material viscoelastic response is critical for identifying the material behaviour and associated manufacturing process conditions [56], [60]. Oscillatory rheology tests are often utilized to examine viscoelastic materials like polymer solutions and dispersions. Oscillatory tests are also referred to as dynamic mechanical analysis (DMA). Such tests enable determining the material parameters storage modulus, loss modulus, and damping factor. The storage modulus is a measure of the deformation energy stored in the sample, while the loss modulus signifies the energy dissipated during the deformation process. The damping factor is expressed as the ratio between the viscous and the elastic portion. The literature referenced above provides guidance on physical phenomena that govern both material and process conditions.

1.10 Research hypothesis, motivation and thesis objectives

The present section elucidates (i) the motivation for conducting this research, (ii) the hypothesis that was formed based on equipment and material considerations along with scientific fundamentals, and (iii) the objectives constructed based on initial scientific knowledge relating to materials, equipment and processes. This research was inspired by technical literature related to the development of magnetic composites for flywheel energy storage systems, which enabled establishing a fundamental research

direction toward developing magnetically loaded polymer composites. It was hypothesized, that using contemporary AM methods, magnetic composites with permanent magnet properties can be fabricated with filler loadings that enable their use in high performance electrical machines such as flywheel energy storage systems. Upon identifying promising AM equipment and scientific methodologies for constructing novel AM devices, the following research objectives were derived from the hypothesis with the goal of adapting and designing equipment and material systems that possess the required capabilities. With this fundamental hypothesis as a baseline, the following objectives were established:

- Investigate the capabilities of commercially available stereolithography technology to construct magnetic composites and ascertain if the material formulations can be printed with filler loadings desired for a permanent magnet.
- Develop and test devices to construct field structured magnetic composites by aligning magnetic particles within the polymer matrix for selected AM processes with the motive of amplifying magnetic properties and create magnetic composites with anisotropic properties.
- Develop AM capabilities based on material jetting technology for fabricating polymer bonded permanent magnets with the focus of understanding the capabilities and uncertainties of the developed equipment, materials and processes within the established research framework.

Based on the initial hypothesis, the overarching motivation became exploring materials and processes to construct magnetic particle reinforced composites using stereolithography and material jetting approaches. Magnetic structures with isotropic

and anisotropic magnetic properties were sought using UV, thermal and dual cure resin formulations developed as a part of this research.

Chapters 2 and 3 of this document detail the development of magnetic composites using stereolithography processes. Approaches towards the formulation of novel ferromagnetic particle reinforced polymers, the evaluation of their curing behaviour, investigations of dimensional stability and attempts printing composites with high filler loadings were undertaken.

Chapters 3 and 4 focus on the development of anisotropic magnetic composites using the material jetting approach. An experimental system realized through finite element simulations to drive the material jetting equipment development is presented. The behavior of magnetic particles in polymer and the influence of rheological modifiers were studied. Experimental observations were correlated to the rheological characteristics of the developed formulations. Magnetic characterization was conducted to understand the anisotropic characteristics of the 3D printed magnetic composite.

Chapters 5 and 6 describes the study of permanent magnets that were obtained from material jetting additive manufacturing processes. Chapter 5 describes the printing of a highly viscous magnetic particle reinforced epoxy resin using an in-house developed material jetting printer. The ability of the equipment to deposit magnetic pastes and the behaviour of the developed material formulation was assessed. Magnetic characterization was conducted to evaluate the effect of hybrid material formulations on the magnetic properties. The subject of Chapter 6 is the fabrication of milled fiber

reinforcement and platetype magnetic particles based permanent magnetic composites. A dual cure acrylate resin (UV / heat cure) was developed and permanent magnets were fabricated using the developed formulation. Furthermore, the influence of an external magnetic field on developing textured permanent magnets was studied.

1.11 Significance of the research work

This research project has been designed to address fundamental material and manufacturing process related issues to construct the knowledge and understanding related to manufacturing magnetic particle reinforced polymer composites using additive manufacturing techniques.

1. Stereolithography is a well established process for clear photopolymers and ceramics. Printing composites with magnetic functionality is challenging and a currently evolving process. To the author's knowledge, there is no custom available magnetic particle reinforced formulation for AM processes. Furthermore, a 3D printer capable of printing standard clear and colour resins is utilized to print magnetic composites. Overall, the research entailed developing the material formulations, understanding the 3D printing equipment and the capabilities to print magnetic polymer composites using stereolithography.
2. Developing field structured magnetic composites using material jetting was undertaken in the second phase of the project. Printing anisotropic magnetic structures involved understanding the fundamental physics of magnetic particles along with the material jetting process up to the development of novel material jetting equipment with particle alignment capability. The foundations

towards developing material jetting equipment with capability to alignment magnetic particles was realized through finite element simulations. An initial experimental setup was developed to evaluate the particle alignment behaviour in polymers. The proposed formulations, alignment setups and process scenarios were engineered to print composites with isotropic and anisotropic magnetic particle distribution using the material jetting process.

3. Permanent magnets find applications in many electrical and electronic applications. The third phase of the research work places emphasis on the development of permanent magnets using material jetting processes. Hybrid magnetic particle and additive modified material formulations developed as a part of this research enabled printing permanent magnets and additionally controlling material behaviour at various manufacturing process stages. Rheological characterization was conducted to correlate the material behaviour observed at different stages of the manufacturing process. Furthermore, a UV curable prepolymer was modified for a combined UV and thermal cure to manufacture permanent magnets. Overall, the developed material formulations and utilized equipment enabled understanding process capabilities and other uncertainties at a fundamental level required to construct robust manufacturing equipment, materials and processes.

Overall, the research developed through this work shall be employed to develop robust materials and manufacturing processes to construct magnetic composite structures using AM processes.

1.12 References

[1] J. M. D. Coey, *Magnetism and Magnetic Materials*. Cambridge: Cambridge University Press, 2001.

[2] D. Jiles, *Introduction to magnetism and magnetic materials*. CRC press, 2015.

[3] C. Kittel, "Physical theory of ferromagnetic domains," *Rev. Mod. Phys.*, vol. 21, no. 4, p. 541, 1949.

[4] J. P. Gavigan and D. Givord, "Intrinsic and extrinsic properties of rare earth-transition metal compounds and permanent magnets," *J. Magn. Magn. Mater.*, vol. 84, no. 3, pp. 288–298, 1990.

[5] J. M. D. Coey, "Perspective and prospects for rare earth permanent magnets," *Engineering*, 2019.

[6] R. Skomski and D. J. Sellmyer, "Intrinsic and Extrinsic Properties of Advanced Magnetic Materials," in *Handbook of Advanced Magnetic Materials*, Y. Liu, D. J. Sellmyer, and D. Shindo, Eds. Boston, MA: Springer US, 2006, pp. 1–57.

[7] D. Brown, B.-M. Ma, and Z. Chen, "Developments in the processing and properties of NdFeb-type permanent magnets," *J. Magn. Magn. Mater.*, vol. 248, no. 3, pp. 432–440, Aug. 2002.

[8] T. Ye *et al.*, "Application of magnetic field in fabrication process of anisotropic bonded nd-fe-b magnet," *J. Iron Steel Res. Int.*, vol. 13, pp. 279–281, 2006.

[9] J. Martin, E. Venturini, J. Odinek, and R. Anderson, "Anisotropic magnetism in field-structured composites," *Phys. Rev. E*, vol. 61, no. 3, pp. 2818–2830, Mar. 2000.

[10] J. E. Martin, E. L. Venturini, and D. L. Huber, "Giant magnetic susceptibility enhancement in field-structured nanocomposites," *J. Magn. Magn. Mater.*, vol. 320, no. 18, pp. 2221–2227, Sep. 2008.

[11] J. Schneider and R. Knehans-Schmidt, "Bonded hybrid magnets," *J. Magn. Magn. Mater.*, vol. 157–158, pp. 27–28, May 1996.

[12] B. . Ma, J. . Herchenroeder, B. Smith, M. Suda, D. . Brown, and Z. Chen, "Recent development in bonded NdFeB magnets," *J. Magn. Magn. Mater.*,

vol. 239, no. 1–3, pp. 418–423, Feb. 2002.

[13] X. H. Zhang, W. H. Xiong, Y. F. Li, and N. Song, “Effect of process on the magnetic and mechanical properties of Nd-Fe-B bonded magnets,” *Mater. Des.*, vol. 30, no. 4, pp. 1386–1390, 2009.

[14] D. Drummer and S. Messingschlager, “Material Characterization of Strontium Ferrite Powders for Producing Sintered Magnets by Ceramic Injection Molding (MagnetPIM),” *Adv. Mater. Sci. Eng.*, vol. 2014, pp. 1–8, 2014.

[15] S. V. Ketov, Y. D. Yagodkin, and V. P. Menushenkov, “Structure and magnetic properties of strontium ferrite anisotropic powder with nanocrystalline structure,” *J. Alloys Compd.*, vol. 509, no. 3, pp. 1065–1068, Jan. 2011.

[16] M. Krack, M. Secanell, and P. Mertiny, “Cost optimization of hybrid composite flywheel rotors for energy storage,” *Struct. Multidiscip. Optim.*, vol. 41, no. 5, pp. 779–795, 2010.

[17] S. K. Ha, H.-I. Yang, and D.-J. Kim, “Optimal design of a hybrid composite flywheel with a permanent magnet rotor,” *J. Compos. Mater.*, vol. 33, no. 16, pp. 1544–1575, 1999.

[18] D. Fullwood, C. Haehl, and B. Lively, “Magnetically loaded filament wound composites,” in *SAMPE Conference Proceedings: Material and Process Innovations: Changing Our World. Long Beach, CA, May 18-22, 2008. Society for the Advancement of Material and Process Engineering. CD-ROM-5pp.*

[19] J. M. Buckley, K. Atallah, C. M. Bingham, and D. Howe, “Magnetically loaded composite for roller drives,” 1998.

[20] P. E. Mason, K. Atallah, and D. Howe, “Hard and soft magnetic composites in high-speed flywheels,” *Proc. Int. Comm. Compos. Mater. Seattle, WA, USA*, vol. 12, 1999.

[21] J. E. Martin, L. E. S. Rohwer, and J. Stupak, “Elastic magnetic composites for energy storage flywheels,” *Compos. Part B Eng.*, vol. 97, pp. 141–149, Jul. 2016.

[22] L. E. Edwards, J. M. Yon, I. P. Bond, and P. H. Mellor, “STRUCTURAL MAGNETIC COMPOSITES FOR USE IN ELECTRO-MECHANICAL

APPLICATIONS," in *20th International Conference on Composite Materials, Copenhagen*, 2015, no. July, pp. 19–24.

[23] O. Gutfleisch, M. A. Willard, E. Brück, C. H. Chen, S. G. Sankar, and J. P. Liu, "Magnetic Materials and Devices for the 21st Century: Stronger, Lighter, and More Energy Efficient," *Adv. Mater.*, vol. 23, no. 7, pp. 821–842, Feb. 2011.

[24] H. Li, T. J. Flynn, J. C. Nation, J. Kershaw, L. Scott Stephens, and C. A. Trinkle, "Photopatternable NdFeB polymer micromagnets for microfluidics and microrobotics applications," *J. Micromechanics Microengineering*, vol. 23, no. 6, p. 065002, Jun. 2013.

[25] A. Khosla and S. Kassegne, "Fabrication of NdFeB-based permanent rare-earth micromagnets by novel hybrid micromolding process," *Microsyst. Technol.*, vol. 21, no. 11, pp. 2315–2320, Nov. 2015.

[26] C. Yamahata, C. Lotto, E. Al-Assaf, and M. A. M. Gijs, "A PMMA valveless micropump using electromagnetic actuation," *Microfluid. Nanofluidics*, vol. 1, no. 3, pp. 197–207, Jul. 2005.

[27] Y. Jiang, S. Masaoka, M. Uehara, T. Fujita, K. Higuchi, and K. Maenaka, "Micro-structuring of thick NdFeB films using high-power plasma etching for magnetic MEMS application," *J. Micromechanics Microengineering*, vol. 21, no. 4, p. 045011, Apr. 2011.

[28] W. Wang, Z. Yao, J. C. Chen, and J. Fang, "Composite elastic magnet films with hard magnetic feature," *J. Micromechanics Microengineering*, vol. 14, no. 10, pp. 1321–1327, Oct. 2004.

[29] N. Damean, B. A. Parviz, J. N. Lee, T. Odom, and G. M. Whitesides, "Composite ferromagnetic photoresist for the fabrication of microelectromechanical systems," *J. Micromechanics Microengineering*, vol. 15, no. 1, pp. 29–34, Jan. 2005.

[30] Z. C. Yuan, A. J. Williams, T. C. Shields, S. Blackburn, and C. B. Ponton, "The production of Sr hexaferrite thick films by screen printing," *J. Magn. Magn. Mater.*, vol. 247, pp. 257–269, 2002.

[31] J. J. Romero *et al.*, "Anisotropic polymer bonded hard-magnetic films for

microelectromechanical system applications," *J. Appl. Phys.*, vol. 99, no. 8, p. 08N303, Apr. 2006.

[32] J. Thévenot, H. Oliveira, O. Sandre, and S. Lecommandoux, "Magnetic responsive polymer composite materials," *Chem. Soc. Rev.*, vol. 42, no. 17, p. 7099, 2013.

[33] I. Gibson, D. Rosen, and B. Stucker, *Additive Manufacturing Technologies*. New York, NY: Springer New York, 2015.

[34] P. J. Bartolo, *Stereolithography: Materials, Processes and applications*. Springer,London, 2011.

[35] X. Zhang, X. . Jiang, and C. Sun, "Micro-stereolithography of polymeric and ceramic microstructures," *Sensors Actuators A Phys.*, vol. 77, no. 2, pp. 149–156, Oct. 1999.

[36] S. Baba, T. Harada, H. Shimizu, Y. Doshida, and S. Tanaka, "Colloidal processing using UV curable resin under high magnetic field for textured ceramics," *J. Eur. Ceram. Soc.*, vol. 36, no. 11, pp. 2739–2743, 2016.

[37] N. Reis, C. Ainsley, and B. Derby, "Digital microfabrication of ceramic components," *Am. Ceram. Soc. Bull.*, vol. 82, no. 9, 2003.

[38] J. W. Halloran *et al.*, "Photopolymerization of powder suspensions for shaping ceramics," *J. Eur. Ceram. Soc.*, vol. 31, no. 14, pp. 2613–2619, 2011.

[39] C. Sun and X. Zhang, "The influences of the material properties on ceramic micro-stereolithography," *Sensors Actuators, A Phys.*, vol. 101, no. 3, pp. 364–370, 2002.

[40] T. Chartier, A. Badev, Y. Abouliatim, P. Lebaudy, and L. Lecamp, "Stereolithography process: Influence of the rheology of silica suspensions and of the medium on polymerization kinetics – Cured depth and width," *J. Eur. Ceram. Soc.*, vol. 32, no. 8, pp. 1625–1634, Jul. 2012.

[41] C. Hinczewski, S. Corbel, and T. Chartier, "Ceramic suspensions suitable for stereolithography," *J. Eur. Ceram. Soc.*, vol. 18, no. 6, pp. 583–590, Jan. 1998.

[42] S. P. Gentry and J. W. Halloran, "Depth and width of cured lines in photopolymerizable ceramic suspensions," *J. Eur. Ceram. Soc.*, vol. 33, no. 10, pp. 1981–1988, 2013.

[43] A. Goswami, K. Ankit, N. Balashanmugam, A. M. Umarji, and G. Madras, "Optimization of rheological properties of photopolymerizable alumina suspensions for ceramic microstereolithography," *Ceram. Int.*, vol. 40, no. 2, pp. 3655–3665, 2014.

[44] B. Y. Tay and M. J. Edirisinghe, "Investigation of some phenomena occurring during continuous ink-jet printing of ceramics," *J. Mater. Res.*, vol. 16, no. 2, pp. 373–384, 2001.

[45] Q. Liu and M. Orme, "High precision solder droplet printing technology and the state-of-the-art," *J. Mater. Process. Technol.*, vol. 115, no. 3, pp. 271–283, 2001.

[46] D. Espalin, D. W. Muse, E. MacDonald, and R. B. Wicker, "3D Printing multifunctionality: structures with electronics," *Int. J. Adv. Manuf. Technol.*, vol. 72, no. 5–8, pp. 963–978, 2014.

[47] K. Yamaguchi, "Generation of 3-dimensional microstructure by metal jet," *Microsyst. Technol.*, vol. 9, no. 3, pp. 215–219, 2003.

[48] J. C. Conrad, S. R. Ferreira, J. Yoshikawa, R. F. Shepherd, B. Y. Ahn, and J. A. Lewis, "Designing colloidal suspensions for directed materials assembly," *Curr. Opin. Colloid Interface Sci.*, vol. 16, no. 1, pp. 71–79, 2011.

[49] K. Sun, T. Wei, B. Y. Ahn, J. Y. Seo, S. J. Dillon, and J. A. Lewis, "3D printing of interdigitated Li-Ion microbattery architectures," *Adv. Mater.*, vol. 25, no. 33, pp. 4539–4543, 2013.

[50] N. Tasnim *et al.*, "3D bioprinting stem cell derived tissues," *Cell. Mol. Bioeng.*, vol. 11, no. 4, pp. 219–240, 2018.

[51] J. Mewis and N. J. Wagner, *Colloidal suspension rheology*. Cambridge University Press, 2012.

[52] V. S. D. Voet *et al.*, "Biobased Acrylate Photocurable Resin Formulation for Stereolithography 3D Printing," *ACS Omega*, vol. 3, no. 2, pp. 1403–1408, Feb. 2018.

[53] B. A. Horri, P. Ranganathan, C. Selomulya, and H. Wang, "A new empirical viscosity model for ceramic suspensions," *Chem. Eng. Sci.*, vol. 66, no. 12, pp. 2798–2806, Jun. 2011.

[54] A. K. Bastola, M. Paudel, and L. Li, “Development of hybrid magnetorheological elastomers by 3D printing,” *Polymer (Guildf).*, vol. 149, pp. 213–228, Aug. 2018.

[55] C. Duty *et al.*, “What makes a material printable? A viscoelastic model for extrusion-based 3D printing of polymers,” *J. Manuf. Process.*, vol. 35, pp. 526–537, 2018.

[56] C. E. Duty *et al.*, “A Viscoelastic Model for Evaluating Extrusion-Based Print Conditions,” Oak Ridge National Lab.(ORNL), Oak Ridge, TN, USA, 2017.

[57] R. Ganguly and I. K. Puri, “Field-assisted self-assembly of superparamagnetic nanoparticles for biomedical, MEMS and BioMEMS applications,” *Adv. Appl. Mech.*, vol. 41, pp. 293–335, 2007.

[58] I. Jönkkäri, M. Isakov, and S. Syrjälä, “Sedimentation stability and rheological properties of ionic liquid–based bidisperse magnetorheological fluids,” *J. Intell. Mater. Syst. Struct.*, vol. 26, no. 16, pp. 2256–2265, Nov. 2015.

[59] M. T. López-López, P. Kuzhir, G. Bossis, and P. Mingalyov, “Preparation of well-dispersed magnetorheological fluids and effect of dispersion on their magnetorheological properties,” *Rheol. Acta*, vol. 47, no. 7, pp. 787–796, Sep. 2008.

[60] T. G. Mezger, “The Rheology Handbook,” *Pigment Resin Technol.*, vol. 38, no. 5, p. prt.2009.12938eac.006, Sep. 2009.

CHAPTER 2: ADDITIVE MANUFACTURING FERROMAGNETIC POLYMERS USING STEREOLITHOGRAPHY – MATERIALS AND PROCESS DEVELOPMENT

2. Overview of Chapter 2

Chapter 2 details a study on fabricating magnetic field responsive composites using stereolithography based AM process. A commercial opensource 3D printer (Autodesk Ember) with an inbuilt capability to print components with three different photopolymer resins (standard clear, investment casting and CMYK resins) was utilized. Technical contributions in this chapter include

- Magnetic particle reinforced UV curable formulation development with ability to resist gravitational settling
- Rheological characterization to determine suspension properties and understand role of additives
- Dimensional characterization to estimate differences between designed and manufactured composites
- FT-IR spectroscopy study to understand the influence of machine tunable parameters

2.1 Introduction

Stereolithography is an AM technology where a pre-polymer is transformed to a cured solid by light exposure [1]. Materials with the capability to react physically and/or dimensionally in response to external stimulus like heat, light, electric and magnetic fields, find extensive applications in sensors, actuators, and other electro-mechanical applications [2, 3]. In this context, magnetic composites are of importance

for many sensor types and non-contact actuation applications. Cantilever type structures using ferromagnetic polymers have previously been printed using stereolithography [4]. Leigh et al. fabricated flow sensing devices by introducing magnetite particles in polymers using micro-stereolithography [5]. A variety of novel methodologies towards manufacturing composites with anisotropic magnetic properties have been reported in the technical literature [6]. Domingo-Roca and co-workers fabricated magnetic soft magnetic composites with randomly oriented magnetic domains via AM [7]. Norbert Löwa utilized a vat photopolymerization technique to 3D print structures reinforced with magnetic nanoparticles and identified the need to control process related issues like settling, homogeneity and processability [8]. In order to develop successful manufacturing techniques, advancements in materials research, process development and material characterization play a vital role [9].

In the present research, we report a custom developed ferromagnetic polymer with controllable particle settling and modifiable rheological properties. The behavior of the ferromagnetic pre-polymer was studied using rheological measurements. Printed composites were (i) characterized using scanning electron microscopy (SEM) to observe particle distribution and dispersion, (ii) tested for dimensional accuracy using a coordinate measuring machine (CMM), and (iii) studied for absorbance characteristics using Fourier transform infrared spectroscopy (FTIR). The present study aims at contributing to the development of stereolithography processes for producing three-dimensional polymer-based magnetic field responsive composites.

2.2 Experimental procedures

2.2.1 Materials and suspension preparation

To formulate the magnetic suspension, strontium ferrite ($SrFe_{12}O_{19}$) micro particles (MP) with an average particle diameter of 1.41µm (DOWA Electronics Materials Co. Ltd., Tokyo, Japan) were added in desired quantities to an ultraviolet light (UV) curable pre-polymer (PR48 by Autodesk Inc., San Rafael, California, USA). The suspension was mechanically agitated for 10 minutes using an impeller agitator, followed by sonication using a 15-second pulsed on/off mode for 15 minutes using a Q500 tip sonicator (Qsonica, Newtown, Connecticut, USA). Afterwards, the rheological additive BYK-7410ET (BYK-Chemie GmbH, Wesel, Germany) was added, and the suspension was mechanically blended for 15 minutes. The suspension was degassed in a vacuum chamber to remove entrapped air and volatiles for 15 to 30 minutes. Suspensions prepared with 5 wt% of magnetic filler and 0.2, 0.4 and 0.6 wt% of rheological additive were used for the experiments.

2.2.2 Assessment of particle settling

Magnetic particles dispersed in the UV curable pre-polymer tend to settle due to gravity. This sedimentation effect in turn affects the printability by hindering light penetration required for the curing process. Prepared ferromagnetic suspensions were filled in graduated tubes, and the settling of particles was captured using a digital camera at different intervals of time. The minimum rheological additive quantity effective in controlling particle settling was assessed using the obtained photographs.

2.2.3 Suspension rheological analysis

The rheological behavior of magnetically loaded pre-polymer suspensions was assessed using a rotational rheometer (RheolabQC, Anton Paar GmbH, Graz, Austria).

Viscosity curves derived from the measurements were used to interpret the behavior of the magnetic suspensions. The shear thinning index (STI) was calculated as the ratio between the viscosities at a low and high shear rates [10]. The Herschel-Bulkley equation (Eq. 1) was used to fit the flow curves and derive yield strengths of the magnetic suspensions.

$$\tau = \tau_0 + C\dot{\gamma}^n \tag{2.1}$$

where τ_0 is the yield point, C is the flow coefficient, τ is shear stress, and $\dot{\gamma}$ and n are the shear rate and Herschel-Bulkley index, respectively [11].

2.2.4 Additive manufacturing magnetic polymer composites and characterization

Composites with magnetic fillers were manufactured using an Ember Digital Light Processing (DLP) SLA 3D printer (Autodesk). The printer utilizes a 5 W power LED and Digital Micromirror Device (DMD) with over one million 50 μm size mirrors spaced at 7.6 μm. The printer is capable of producing parts with a resolution of 50 μm in the X and Y axis and between 10 – 100 μm in the Z axis. Build volume of the Ember is 64 mm x 40 mm x 134 mm in the X, Y and Z axis respectively. The printer uses digital images that have a resolution of 1280x800 pixels to define every layer of the print. Basic components of the Autodesk Ember DLP 3D printer and component printed for characterization is shown in Figure 2.1.

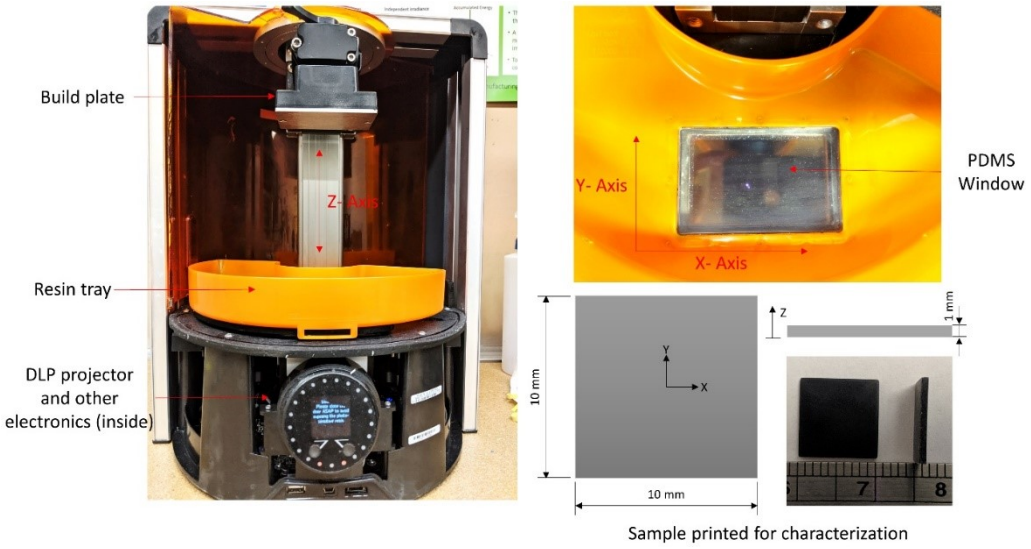

Figure 2.1: Autodesk Ember DLP 3D printer and sample printed for characterization.

Samples were prepared employing the suspension engineered with 5 wt% magnetic filler and 0.4 wt% rheological additive loading. Variations in printed sample thickness (Z-axis) as a function of layer thickness setting (10 and 50µm) and part position on the print head were evaluated. For this purpose, square plates (10 mm x 10 mm) with thicknesses of 0.25, 0.5, 0.75, 1.0 mm were printed with a constant exposure time of 3 seconds. Samples were tested for dimensional accuracy in thickness direction using a CMM (Crysta-Plus M443, Mitutoyo, Takatsu-ku, Kawasaki, Japan) with a resolution of 0.0001 mm. SEM was carried out using an EVO M10 microscope (Carl Zeiss AG, Oberkochen, Germany) operated at an accelaration voltage of 20 kV. Specimens for SEM were coated with carbon prior to imaging. FTIR was conducted with UV curable polymer pre-cure and post-cure. FTIR profiles were observed for peak reduction and flattening that is a direct indication of monomer conversion. An Alpha FTIR spectrometer (Bruker, Billerica, Massachusetts, USA) equipped with a single bounce

attenuated total reflectance diamond crystal was employed to collect a spectrum at a resolution of 4 cm^{-1} over a range from 410 cm^{-1} to 4000 cm^{-1}.

2.3 Results and discussion

In this section, results observed in this fundamental work that enabled identification of the newly developed ferromagnetic polymer, machine and process characteristics that contribute to the development of stereolithography process for printing magnetic composites are presented.

2.3.1 Particle settling control

As illustrated in Figure 2.2, the sample with 0.2 wt% rheological additive exhibited significant particle settling, leaving a clear supernatant on the top of the settled magnetic particles (Though not shown in Figure 2.2, a similar behavior was observed for 0.3 wt%).

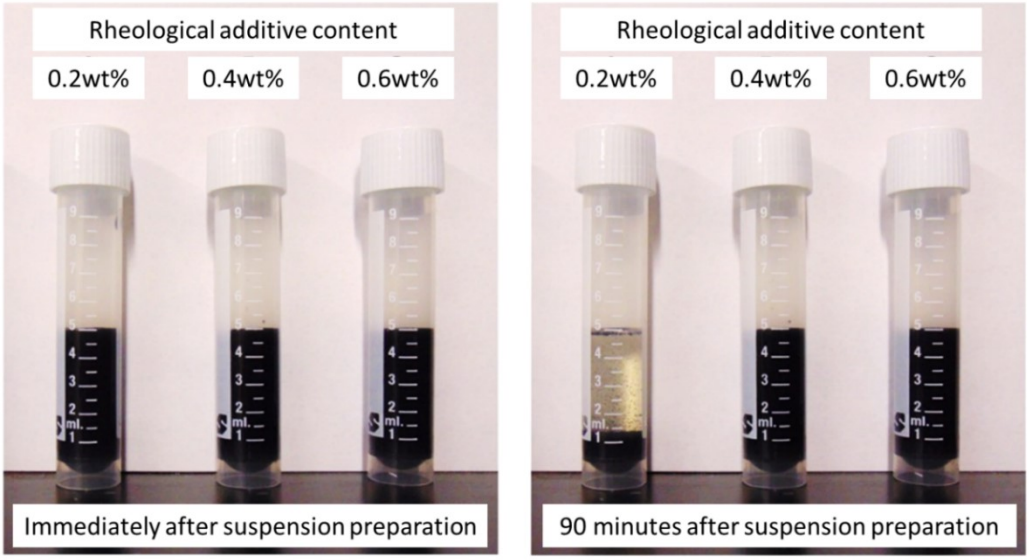

Figure 2.2: Photographs illustrating magnetic filler settling in UV curable pre-polymer.

On the other hand, particle settling was mitigated in samples that contained 0.4 wt% and 0.6 wt% rheological additives. From the settling analysis, 0.4 wt% rheological additive loading was selected as it effectively controlled particle settling observed from photographs taken at two different time intervals. Notably, this quantity is 0.1 wt% lower compared to a previous study by the present authors where a proof of concept for controlling particle settling was discussed [12].

2.3.2 Suspension rheological properties

Viscosity curves and calculated rheological properties of magnetic suspensions are shown in the graph and insert in Figure 2.3, respectively. An STI greater than unity and a Herschel-Bulkley index (HBI) less than unity signify shear thinning behavior of the magnetic suspensions, i.e., a reduction in viscosity is observed with increasing shear rates indicating Non-Newtonian behavior [13]. The viscosity at low shear rates and the yield strength (YS) of the suspensions were observed to increase with increasing rheological additive content. It is therefore inferred that a gelling effect caused by the rheological additives raises shear viscosity and YS of the suspensions [14]. The prepolymer exhibits shear thinning behaviour as the three-dimensional network structure gets distorted with increasing shear rates and aligns with material flow.

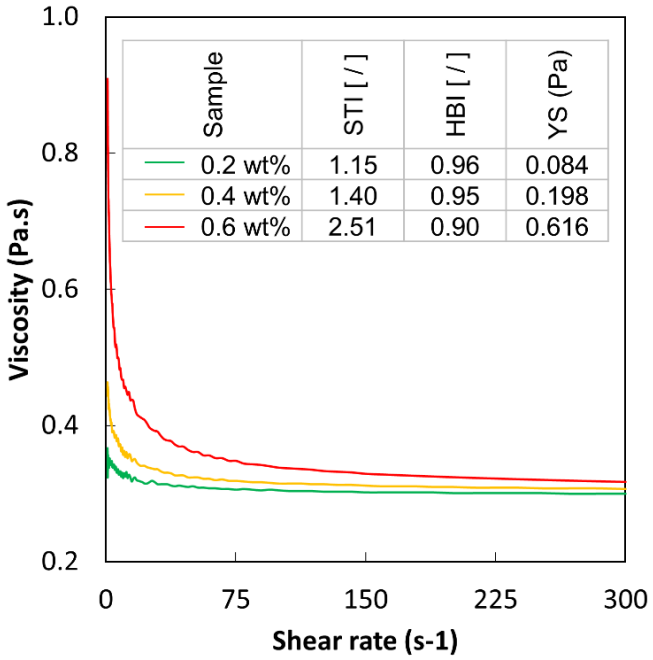

Figure 2.3: Viscosity versus shear rate for magnetic suspensions with calculated rheological properties.

2.3.3 Characteristics of magnetic field responsive composites

SEM images of the composites shown in Figure 2.4 reveal that magnetic particles are distributed in the composite but aggregated within the printed layers. The formation of particle clusters through aggregation is believed to be the result of magnetic interactions between the dispersed particles, which is a function of particle size, particle magnetization, and permeability of the dispersed medium [15]. It was expected that the rheological additives enable control of particle aggregation by enhancing the medium's shear viscosity and yield strength and imparting a gel structure as observed in the technical literature for magneto-rheological fluids [16]. From the present observations it is inferred that even though 0.4 wt% of rheological additive mitigates particle settling, this additive quantity is still insufficient to control particle aggregation. The features observed from the side view in SEM images of 3D printed samples, like stacked layers, broken sections and uneven surfaces, are considered to be

the result of parameters that were adopted for the initial printing process. These parameters require further investigation and refinement.

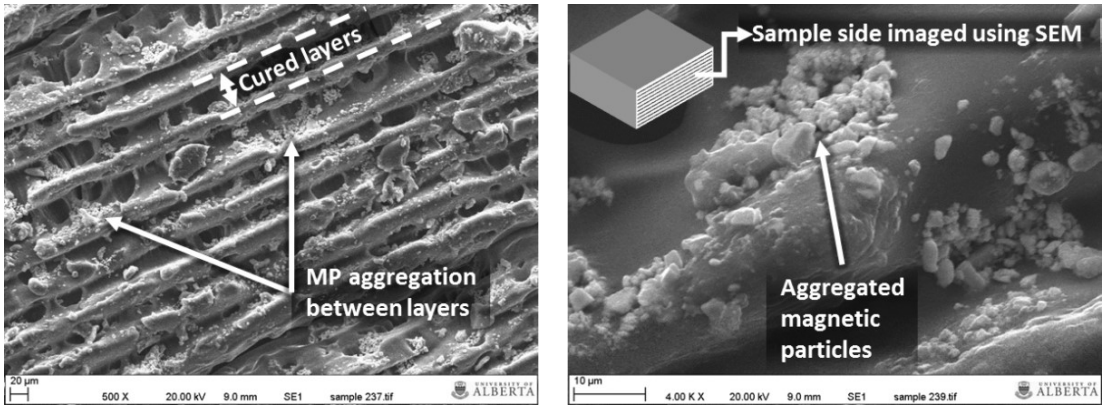

Figure 2.4: SEM image showing layers of a stereolithography fabricated structure with particle aggregations (left); magnification of aggregated magnetic particles in composite (right).

Figure 2.5 shows thickness data obtained from samples using the CMM. Samples were printed in regions as indicated by the insert in the graph on the right-hand side of Figure 2.5.

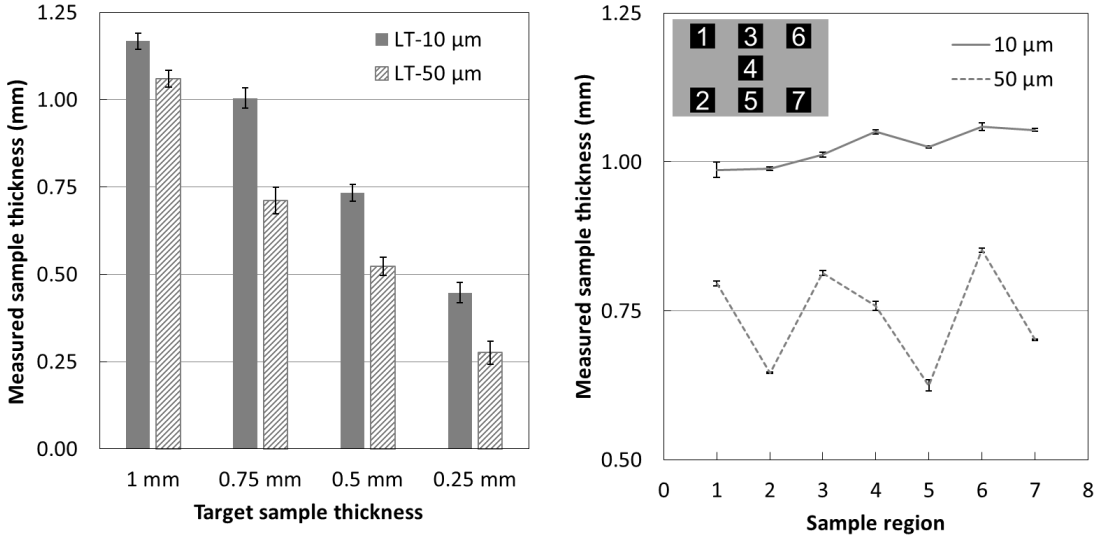

Figure 2.5: Sample dimensions as a function of target sample thickness for different layer thickness (LT) settings (left); variation of fabricated sample thickness for different print regions for the case of 0.75 mm target sample thickness (right).

Composites fabricated using the developed magnetic pre-polymer exhibited significant variations in thickness depending on the print region and layer thickness settings. It was observed that a layer thickness setting of 10 μm yielded sample thickness values that were on average 44% greater that the target thickness, whereas the average deviation for the 50 μm layer thickness setting was only 6.6% for the fabricated specimens. In terms of dimensional variations increasing or decreasing from print region to print region, similar trends for both layer thickness settings were observed for regions 2-3, 4-5, 5-6 and 6-7, whereas trends were different for regions 1-2 and 3-4. Some dimensional variations were expected due to variations in light intensity across the print bed as reported in the technical literature [17]. Other parameters like a certain opaqueness of the resin tray window, cure depth as a function exposure time, particle aggregation and other machine tunable parameters are expected to have further influenced the dimensional characteristics.

FTIR spectra of the liquid pre-polymer and cured specimens printed using layer thicknesses of 10 μm and 50 μm are depicted in Figure 2.6. Signals corresponding to C=C bonds in the acrylate regions (1600 cm^{-1} to 1660 cm^{-1}, 1400 cm^{-1} to 1430 cm^{-1} and 800 cm^{-1} to 830 cm^{-1}) decreased in cured samples as observed in the technical literature [18], indicating monomer conversion dependent on layer thickness settings. Furthermore, results observed in this research have enabled identification of liquid prepolymer, printed sample and process characteristics that serve as individual entities and fundamental building blocks to construct stereolithography process for manufacturing magnetic composites.

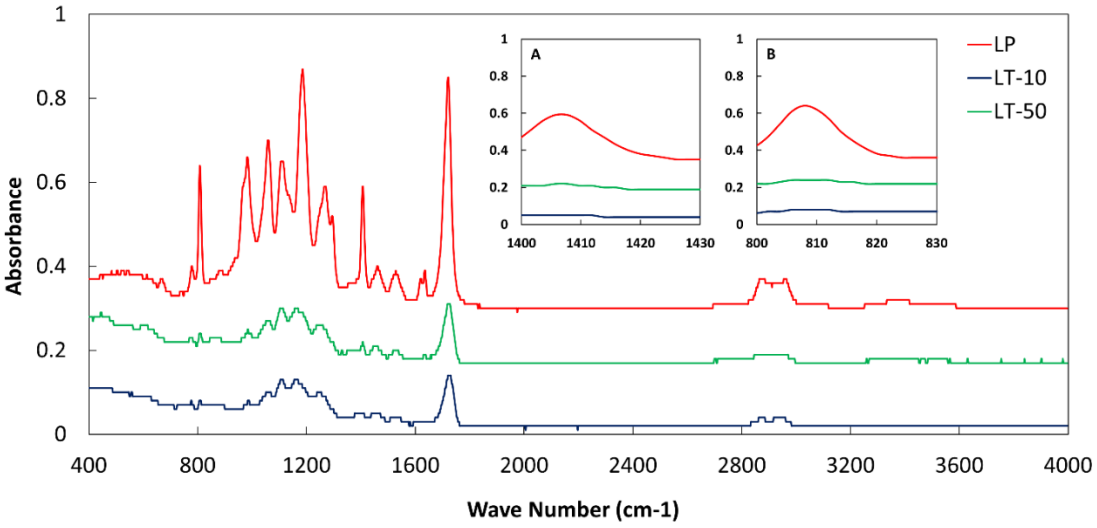

Figure 2.6: FTIR spectra of liquid polymer (LP) and specimens printed using layer thickness settings of 10 µm (LT-10) and 50 µm (LT-50). (Inside the graph) A, B – Spectral regions 1400-1430 and 800-830 showing peak flattening indicating monomer conversion.

2.4 Conclusions

In the present study, a novel material formulation for stereolithography AM with controlled particle settling and modifiable rheological properties has been demonstrated. The effective rheological additive quantity to mitigate settling was determined as 0.4 wt%. Rheological behaviour analysis provided insight into suspensions where at low shear rates, viscosity and yield point of the magnetic suspension increased significantly with increasing rheological additive content. SEM images revealed particle aggregation between stacked layers which is attributed to the magnetic attraction between particles. For the employed AM equipment, the layer thickness setting and print region were observed to significantly influence deviations form target thicknesses of the printed components. From FTIR spectroscopy, flattening of peaks, which directly correspond to the degree of monomer conversion, was observed in comparison to the liquid pre-polymer suspension. The results obtained

from this study underline the importance of considering the suspension composition in conjunction with manufacturing parameters for the design of composite components fabricated by sstereolithography AM. Future work will focus on utilizing the developed ferromagnetic polymer and optimizing manufacturing parameters for stereolithography processes to allow for the printing of composites with higher filler loadings, high dimensional accuracy and uniform particle dispersion and distribution.

2.5 References:

[1] P. J. Bartolo, *Stereolithography: Materials, Processes and applications*. Springer,London, 2011.

[2] M. Zarek, M. Layani, I. Cooperstein, E. Sachyani, D. Cohn, and S. Magdassi, "3D Printing: 3D Printing of Shape Memory Polymers for Flexible Electronic Devices (Adv. Mater. 22/2016)," *Adv. Mater.*, vol. 28, no. 22, pp. 4166–4166, Jun. 2016.

[3] I. T. Garces and C. Ayranci, "A view into additive manufactured electro-active reinforced smart composite structures," *Manuf. Lett.*, vol. 16, pp. 1–5, Apr. 2018.

[4] C. Credi, A. Fiorese, M. Tironi, R. Bernasconi, L. Magagnin, M. Levi, and S. Turri, "3D Printing of Cantilever-Type Microstructures by Stereolithography of Ferromagnetic Photopolymers," *ACS Appl. Mater. Interfaces*, vol. 8, no. 39, pp. 26332–26342, Oct. 2016.

[5] S. J. Leigh, C. P. Purssell, J. Bowen, D. A. Hutchins, J. A. Covington, and D. R. Billson, "A miniature flow sensor fabricated by micro-stereolithography employing a magnetite/acrylic nanocomposite resin," *Sensors Actuators A Phys.*, vol. 168, no. 1, pp. 66–71, Jul. 2011.

[6] B. Nagarajan, A. F. E. Aguilera, M. Wiechmann, A. J. Qureshi, and P. Mertiny, "Characterization of magnetic particle alignment in photosensitive polymer resin: A preliminary study for additive manufacturing processes," *Addit. Manuf.*, 2018.

[7] R. Domingo-Roca, J. C. Jackson, and J. F. C. Windmill, "3D-printing polymer-

based permanent magnets," *Mater. Des.*, vol. 153, pp. 120–128, Sep. 2018.

[8] N. Löwa, J. Fabert, D. Gutkelch, H. Paysen, O. Kosch, and F. Wiekhorst, "Journal of Magnetism and Magnetic Materials 3D-printing of novel magnetic composites based on magnetic nanoparticles and photopolymers," *J. Magn. Magn. Mater.*, vol. 469, no. September 2018, pp. 456–460, 2019.

[9] A. Kumar, "Methods and Materials for Smart Manufacturing: Additive Manufacturing, Internet of Things, Flexible Sensors and Soft Robotics," *Manuf. Lett.*, vol. 15, pp. 122–125, Jan. 2018.

[10] "Standard Test Method for Shear Thinning Index of Non-Newtonian Liquids Using a Rotational Viscometer BT - Standard Test Method for Shear Thinning Index of Non-Newtonian Liquids Using a Rotational Viscometer." 18AD.

[11] J. Mewis and N. J. Wagner, *Colloidal Suspension Rheology*. Cambridge: Cambridge University Press, 2011.

[12] B. Nagarajan, A. F. E. Aguilera, A. Qureshi, and P. Mertiny, "Additive Manufacturing of Magnetically Loaded Polymer Composites: An Experimental Study for Process Development," in *ASME 2017 International Mechanical Engineering Congress and Exposition*, 2017, p. V002T02A032-V002T02A032.

[13] T. G. Mezger, "The Rheology Handbook," *Pigment Resin Technol.*, vol. 38, no. 5, p. prt.2009.12938eac.006, Sep. 2009.

[14] R. Berndlmaier, "Rheology additives for coatings," in *Handbook of coating additives*, D. J. M. John J. Florio, Ed. Marcel Dekker Inc, pp. 363–403.

[15] M. T. López-López, P. Kuzhir, G. Bossis, and P. Mingalyov, "Preparation of well-dispersed magnetorheological fluids and effect of dispersion on their magnetorheological properties," *Rheol. Acta*, vol. 47, no. 7, pp. 787–796, Sep. 2008.

[16] J. de Vicente, M. T. López-López, F. González-Caballero, and J. D. G. Durán, "Rheological study of the stabilization of magnetizable colloidal suspensions by addition of silica nanoparticles," *J. Rheol. (N. Y. N. Y).*, vol. 47, no. 5, pp. 1093–1109, Sep. 2003.

[17] K. Mostafa, A. J. Qureshi, and C. Montemagno, “Tolerance Control Using Subvoxel Gray-Scale DLP 3D Printing,” in *Volume 2: Advanced Manufacturing*, 2017.

[18] V. S. D. Voet, T. Strating, G. H. M. Schnelting, P. Dijkstra, M. Tietema, J. Xu, A. J. J. Woortman, K. Loos, J. Jager, and R. Folkersma, “Biobased Acrylate Photocurable Resin Formulation for Stereolithography 3D Printing,” *ACS Omega*, vol. 3, no. 2, pp. 1403–1408, Feb. 2018.

CHAPTER 3: MAGNETICALLY LOADED POLYMER COMPOSITES USING STEREOLITHOGRAPHY – MATERIAL PROCESSING AND CHARACTERIZATION

3. Overview of Chapter 3

In Chapter 3, an intensive experimental approach is described to understand the printing capabilities of the employed 3D printer, curing behavior of the developed material formulations and push the limits of the 3D printer to print magnetic composites with increased filler loading. Technical contributions in this chapter include:

- Dimensional variation assessment in thickness as a function of process and material parameters
- Development and utilization of an experiment methodology to identify the role of formulation materials on curing behavior of ferromagnetic polymers
- Printing composites using formulations engineered with increased magnetic filler loading
- Characterization of tensile properties and least printable dimensions using the developed formulation and the adopted process parameters
- The last section contains additional and supportive results obtained as a part of this research.
    - Dimensional variations in length and width of magnetic composite
    - Analysis of variations in CMM measurements for determining curing characteristics
    - Influence of process and material parameters on cured thickness
    - Results in last section will be published in conference proceedings

3.1 Introduction

AM enables producing complex 3D parts using a layer-based fabrication approach [1]. AM technology with the ability to provide design flexibility and material savings has created a significant impact in many industries such as the aerospace, automotive, medical and energy sectors. One such AM technology is stereolithography (SLA), where a photosensitive polymer is transformed into a cured solid using light exposure [2] (typically ultraviolet (UV) light). Among many AM techniques available for polymers, SLA enables printing complex structures with the best accuracy [3]. Materials with the ability to respond to external stimuli such as light, heat, electric and magnetic fields, find applications in sensors, actuators, and many other applications [4]. Developing stimuli-responsive structures is known as '4D printing', where functional properties may be achieved by introducing fillers to the base polymer. As such, filler modified photopolymers enable developing smart materials and structures that transform their shape and dimensions in a predetermined way [5]. In this context, high-performance magnetic composites play an important role in a variety of sensor and actuator applications. Magnetic forces are desirable for non-contact actuation mechanisms in many electromechanical systems. Driven by external energy sources without the need for physical contact, such magnetic systems can be controlled remotely in closed spaces and also in liquid media [6]. Significant contributions have been made by researchers toward developing materials and printing processes for fabricating magnetic particle reinforced polymers. Cantilever type microstructures were printed employing SLA for polymer-based micro-electromechanical system devices utilizing a magnetic iron oxide based photosensitive resin formulation [7]. Flow sensing devices were fabricated by Leigh et al. adopting a micro-

stereolithography technique utilizing a magnetite nanoparticle reinforced polymer formulation [8]. Löwa et al. printed magnetic composites using a commercial SLA printer and identified that sonication enabled controlling magnetic nanoparticle settling and dispersion homogeneity. Additionally, a geometry demonstrator was utilized to analyze the printable features considering printing orientations of magnetic structures [9]. Domingo-Roca et al. utilized a SLA and screen printing approach to fabricate polymer-based permanent magnets and identified a methodology to manipulate the orientation of magnetic domains using a poling process using permanent magnets [10]. Magnetic field responsive polymer composites with tunable mechanical and magnetic properties were made adopting a formulation containing 6 wt% iron oxide particles [11]. AM processes have additionally enabled the fabrication composites with user-defined microstructural orientations in polymers. Martin et al. demonstrated the ability of printing composites using SLA with controlled filler orientation applying external magnetic fields [12]. Nagarajan et al. developed strategies to accomplish particle alignment in photosensitive polymers and studied the influence of magnetic field strength and magnetization time for a material jetting based AM process [13]. Some fundamental issues reported by researchers working with magnetic particle reinforced polymers are particle settling, dispersion stability, homogeneity and aggregation control. The current researchers addressed the issue of particle settling by modifying the photosensitive resin using additives [14]. The integration of additives enabled long-term material stability suitable for SLA processes. Additionally, magnetic field responsive polymer composites were fabricated using a commercial 3D printer [15].

Additive manufacturing of filler modified polymers requires substantial knowledge of the formulated material, i.e., its viscosity, photocuring properties, and capabilities of the 3D printer. Understanding the mechanism of radiation curing using ultraviolet photons (UV) is imperative in order to engineer formulations for photopolymerization. Acrylate based resin materials are predominantly used in stereolithography based AM process. Such materials undergo polymerization initiated by free radicals that are released upon UV excitation. The mechanism for the photopolymerization reaction involves three major steps, i.e., initiation, propagation and termination. The reaction mechanism is graphically indicated in Figure 3.1

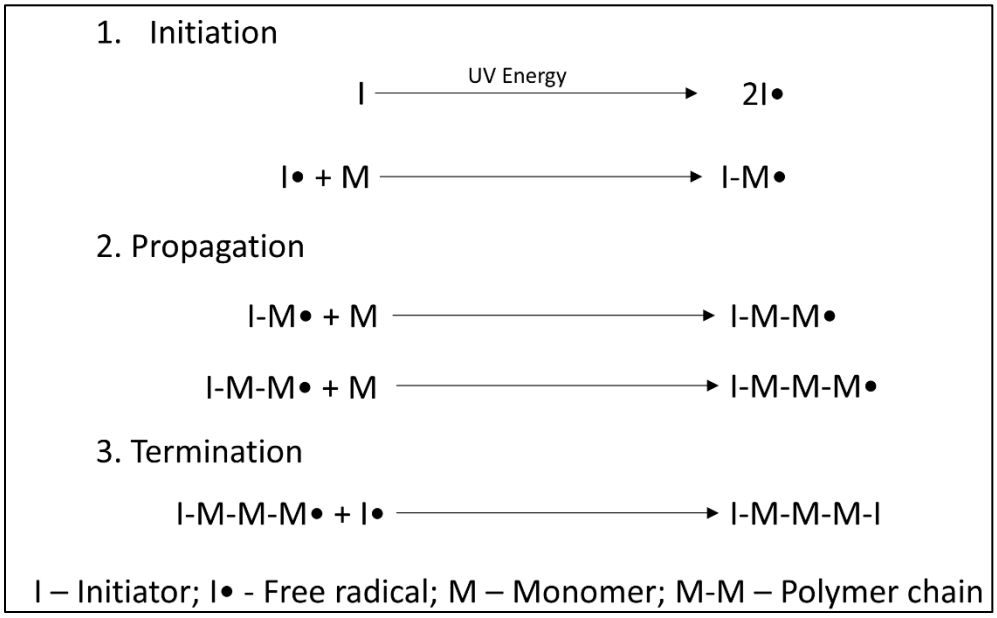

Figure 3.1: Photopolymerization reaction mechanism

Absorption of the UV energy by the photo initiator present in the resin formulation generates free radicals that further react with the monomers resulting in a chain reaction. Two radicals combine at the end to stop this chain reaction. Evaluating the optical properties of photopolymer resin formulations is essential to ensure their

printability. In 3D printing processes employing photopolymerization, penetration of light follows the Beer-Lambert law as expressed in Eq.3.1.

$$P_Z = P_0 e^{-\frac{z}{D_p}} \tag{3.1}$$

where P_z is the power of the light emitting diode, P_0 is the powder at the surface, D_p is the depth at which the intensity falls to 1/e to the surface light intensity. The working curve model developed for a stereolithography process derived from the Beer-Lambert law of absorption reveals two important characteristic parameters for the printed material, i.e., depth of penetration (D_p) and critical energy (E_c) [16]. The working curve model has been used extensively for studying the curing behavior of polymers, which is usually called Jacob's working curve equation, defined by Eq.3.2.

$$C_d = D_p * ln\left(\frac{E_O}{E_c}\right) \tag{3.2}$$

where C_d is the cured depth of resin, D_p is the penetration depth of UV light until 1/e (approximately 37%) of attenuation of light intensity is reached compared to its original intensity at the surface of the resin [17]. E_c is the critical energy, which represents the minimum energy required to initiate the photopolymerization reaction, and E_0 is the average energy of UV light supplied by the UV projector at the surface of the resin. The current working curve model has gained broad acceptance in its description for resin curing behavior and fitting to experimental data for specific resin compositions and experiment conditions [18]. Another model extensively adopted to characterize resins with ceramic fillers while considering the scattering effect of filler particles is defined by Eqs.3.3 and 3.4.

$$C_d \approx \left(\frac{d}{\varphi Q}\right) * ln\left(\frac{E_O}{E_c}\right) \tag{3.3}$$

$$Q \approx \left(\frac{\Delta n}{n_0}\right)^2 * (\frac{d}{\boldsymbol{\lambda}})^2 \tag{3.4}$$

In Eqs.3.3 and 3.4, d is the mean particle size, φ is the volume fraction of filler, λ is the UV wavelength, Δn is the difference between the refractive index of filler particles and polymer and n_0, the refractive index of the polymer [19]. The working curve is a semi-log plot of cured depth versus incident energy represented by a straight line, where D_p (slope of the line) and E_c (abscissa intercept) are purely parameters of the resin. Hence, by utilizing the D_p and E_c of ferromagnetic polymers with different combinations of filler loading, filler type, additive loading, and additive type, an insight into exposure parameters and how the materials contribute to the curing process can be obtained. Accurate measurement of cured depth is necessary to determine the D_p and E_c and further manipulate exposure parameters for a reliable 3D printing process. Measurement of cured depth is subject to higher variability as there is no defined methodology for making such measurement. Measuring cured depth utilizing micrometers, calipers, stylus profilometer, and laser confocal microscopy has been reported in the technical literature [17], [20]. Even though experimental methods are available to determine the material parameters mentioned in equations 3 and 4, the need for specialized equipment is always challenging. Moreover, modification of filler modified polymer systems using additives to address a multitude of material and process issues adds additional complexity to determining material properties.

In the present research, the authors utilize an in-house developed ferromagnetic polymer to 3D print magnetic composites, determine its geometric characteristics, and evaluate its curing behavior. A design of experiment (DOE) framework was utilized to explore material and process parameters that influence the printed magnetic composite thickness and its variation across the build head. To accomplish printing composites with higher magnetic filler loading, the curing behavior of polymers was first studied, and parameters like cured depth and critical energy were determined. An in-house developed experimental framework was utilized to determine curing behavior and significant material parameters. Based on this fundamental understanding, composites were printed with polymers engineered with 10 wt % and 25 wt% of magnetic filler loading. The present study aims to further the understanding of how materials utilized to formulate ferromagnetic resins, 3D printing equipment, and 3D printing process parameters influence the properties of the base polymer and 3D printed magnetic composites.

3.2 Materials and methods

3.2.1 Equipment and materials

In this study, magnetically loaded polymer resin was developed to be printed using an Ember Digital Light Processing (DLP) SLA 3D printer (Autodesk Inc., San Rafael, California, USA). The printing resolution, as indicated by the manufacturer, is 50 μm in the horizontal X and Y axes and between 10 and 100 μm in the vertical Z axis. The build volume of the printer is 64 mm by 40 mm by 134 mm in the X, Y and Z-axis, respectively. Every print layer is defined by digital images with a resolution of 1280 by 800 pixels.

Magnetic materials utilized in this research include strontium ferrite ($SrFe_{12}O_{19}$, abbreviated herein as SrFeO) powder having an average particle diameter of 1.41 μm (DOWA Electronics Materials Co. Ltd., Tokyo, Japan) and neodymium iron boron ($Nd_2Fe_{14}B$, abbreviated herein as NdFeB) powder having an average particle diameter of 5 μm (MQFP powder, Magnequench Inc., Pendleton, Indiana, USA). Ferromagnetic polymers were formulated by dispersing the magnetic powders in PR-48 (UV curable urethane acrylate) resin obtained from Colorado Photopolymer Solutions (Boulder, Colorado, USA). Two different types of additives, Disparlon 6900-20X (indicated herein as Disparlon) (King Industries, Norwalk, Connecticut, USA) and BYK-7410ET (indicated herein as BYK) (BYK-Chemie GmbH, Wesel, Germany) were used to stabilize the dispersion. The efficiency of the additives in mitigating particle settling has previously been tested with the polymer system in previous work by the present authors [14]. Mechanical mixing using an impeller agitator (Calframo Ltd., Georgian Bluffs, Ontario, Canada) and sonication using a Q500 tip sonicator (Qsonica, Newtown, Connecticut, USA) were the two dispersion methodologies and corresponding equipment used to disperse the additives and magnetic particles in the UV curable polymer.

3.3 Experiment methodology

3.3.1 Analysis of dimensional variation in magnetic composite thickness

The first objective of this research is to characterize the dimensional precision in terms of thickness of 3D printed magnetic composites across the build head. Parameters like magnetic filler loading, rheological additive type, and additive loading were considered as the adopted material parameters that influence the rheological properties of the final magnetic suspension [15], [21]. Magnetic filler loading was

restricted within 5 wt% for this initial study. From the technical literature, it was observed that an increase in magnetic filler loading also increases the viscosity of the resultant suspension [22]. The working mechanism of the DLP printer involves tray rotation at a specific speed, which shears the resin in between the resin tray surface and the surface of the aluminum build head. Machine tunable parameters like layer thickness, exposure time per projection, wait before exposure and separation slide velocity (SSV) were considered in the DOE study as the parameters representing height variation of the build head from the resin tray surface, time of UV light projection, time for recoating a new resin layer and the rotation velocity of the resin tray enabling a new resin layer to move within the UV exposure zone, respectively. The adopted process parameters were observed to influence both mechanical and geometric properties of 3D printed polymeric solids as reported in the technical literature [23], [24]. Khaled et al. adopted a DOE framework to identify the machine tunable process parameters that influence the horizontal resolution of the 3D printed polymer parts [24]. The DLP printer and the developed material formulation introduces several uncontrollable variabilities during the experiments. Examples of uncontrollable factors include clouding of the resin tray's polydimethylsiloxane windows, aggregation of magnetic particles with respect to time and destruction, and regeneration of hydrogen bonds due to the rheological additives. The DLP printer tray rotation is expected to constantly change the magnetic particle dispersion and distribution in the magnetic suspension. A seven factor, two level, L8 Taguchi DOE was developed using the Minitab software (Minitab Inc., State College, Pennsylvania, USA) to identify and evaluate the influential material and process parameters, as indicated in Table 3.1.

Table 3.1: DOE developed using the Taguchi method for dimensional variation analysis in printed magnetic composite thickness.

Exp. No	ET/P (s)	MFL (wt%)	LT (µm)	AT	WBE (s)	AL (wt%)	SSV (rpm)
1	3	1	10	Disparlon	1.5	0.5	4
2	3	1	10	BYK	3	1	10
3	3	5	50	Disparlon	1.5	1	10
4	3	5	50	BYK	3	0.5	4
5	6	1	50	Disparlon	3	0.5	10
6	6	1	50	BYK	1.5	1	4
7	6	5	10	Disparlon	3	1	4
8	6	5	10	BYK	1.5	0.5	10

ET/P	**Exposure time per projection (s)**
MFL	Magnetic filler loading (wt%)
LT	Layer thickness (µm)
AT	Additive type
WBE	Wait before exposure (s)
AL	Additive loading (wt%)
SSV	Separation slide velocity (rpm)

To characterize the magnetic composite thickness, a simple cuboid with dimensions of 15 mm by 10 mm by 1 mm in terms of length, width and thickness was designed and printed using the developed formulations containing SrFeO magnetic fillers. Six samples were printed at six zones on the build head, as indicated in Figure 3.1. The thickness of the sample was measured using a Coordinate Measuring Machine (CMM) (Crysta-Plus M443, Mitutoyo, Takatsu, Kawasaki, Japan) with a resolution of 0.1 µm to evaluate deviations from target dimension.

Figure 3.2: Arrangement of samples for dimensional accuracy experiments. Numbers on samples represent printing zones 1 to 6 on the build head.

3.3.2 Investigation of ferromagnetic polymer curing behavior

The second objective of this research is to quantitatively determine the curing behavior of ferromagnetic polymers for AM processes. An experimental approach using the DLP printer was developed to determine significant material parameters, like D_p and E_c. To evaluate the influence of exposure energy on the cured layer thickness of the material, a diagnostic print file that consists of rasterized images and print settings was developed. The print file contained an image of ten rectangles, each with an area of 2.4 cm^2. The print settings were tuned so that each rectangle receives a predetermined number of UV projections influencing the exposure energy for each rectangle in the grid. Exposure time per projection is the only parameter modified through the printer settings to obtain different levels of exposure energy. Irradiance, which is also called as intensity, is the radiant power per unit area received by the resin. The average light power intensity, as indicated by the manufacturer of the printer is 18.5 mW/cm^2. The energy density, which influences the depth of cure is related to the intensity of the UV light and exposure time. In this study, the exposure energy or dose is the product of irradiance, exposure time per projection, and number of projections.

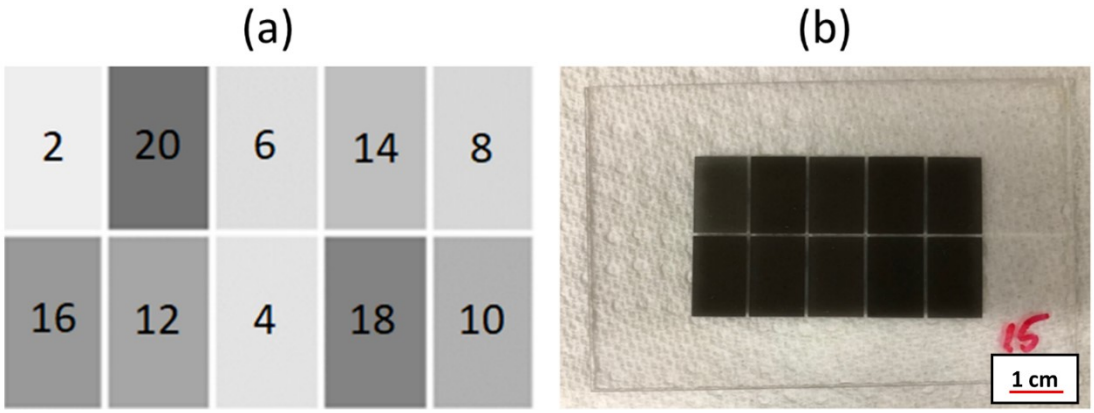

Figure 3.3: (a). *Ten rectangle image stack design where numbers indicate the instances of UV light being projected on each rectangle, i.e., from left to right and top to bottom, 2, 20, 6, 14, 8, 16, 12, 4, 18, 10; (b) Photo of printed file on an acrylic sheet for thickness characterization.*

To investigate the curing behavior of the developed ferromagnetic polymers, a five-factor, two-level factorial design was used to understand the influence of parameters like magnetic filler loading, filler type, rheological additive type, additive loading and exposure time per projection. Eight different ferromagnetic polymers were prepared based on the fractional factorial design developed using the Minitab software. Experiments were conducted in triplicate.

Prior to the experiment, the build head and resin tray of the DLP printer were removed. A measured quantity of the ferromagnetic polymer was dispensed on an acrylic substrate, and the resin was contained within a 3D printed acrylate template to maintain the desired sample geometry. After exposure to UV light inside the DLP printer using the designed print files, the acrylic template was removed and any uncured resin was drained. The cured layers adhering to the acrylic substrate were further rinsed with isopropyl alcohol to remove uncured resin. Measurements were conducted after keeping the sample overnight for drying. The thickness of the cured ferromagnetic

polymer layers was measured relative to the acrylic substrate surface using the CMM. Figure 3.4 shows the measurement setup for data acquisition. Each measurement with the CMM represented a single point, and hence, ten points at different locations over the cured layers were measured and then averaged.

Table 3.2: DOE for investigating the curing behavior of ferromagnetic polymers

S.No	**MFL (wt%)**	**MFT**	**AL (wt%)**	**AT**	**ET/P (s)**
1	10	NdFeB	0.5	BYK	12
2	30	SrFeO	0.5	BYK	3
3	10	SrFeO	1	Disparlon	3
4	30	SrFeO	1	BYK	12
5	10	SrFeO	0.5	Disparlon	12
6	30	NdFeB	1	Disparlon	12
7	10	NdFeB	1	BYK	3
8	30	NdFeB	0.5	Disparlon	3

MFL	**Magnetic filler loading (wt%)**
MFT	Magnetic filler type
AL	Additive loading (wt%)
AT	Additive type
ET/P	Exposure time per projection (s)

Figure 3.4: Thickness measurement setup for acquiring data for the working curve model: (a) Fixing a sample by securing four corners of the acrylic substrate with plasticine on the CMM granite table; (b) Measuring the thickness of a rectangle of a sample using the CMM probe.

3.3.3 Fabrication of polymer composites with increased filler loading and composite characterization

This research sought to print polymer composites using formulations engineered with 10 wt% and 25 wt% filler loading, utilizing the understanding obtained from ferromagnetic polymer curing behavior. Composites were printed using the same CAD geometry adopted to characterize thickness variations across the build head. The resulting dimensions of composites were measured using a digital Vernier caliper having a resolution of 0.01 mm. Tensile properties of 3D printed ferromagnetic composites were evaluated based on ISO 527 [25], using a '1BB' specimen geometry and an Instron 3360 series universal testing machine (Norwood, Massachusetts, USA). A crosshead speed of 0.5 mm/min was applied. From the test data, load versus displacement curve were obtained and tensile strengths were determined. Additionally, magnetic particle loaded cantilevers were printed using a resin with 10 wt% NdFeB, and print dimensions were characterized using optical microscopy.

3.4 Results and Discussion

3.4.1 Analysis of dimensional variation in composite sample thickness

The thickness variation of composite samples printed using the same target geometry across different regions on the build head was evaluated as a function of material and process parameters as per the DOE established in Table 3.1. Based on the measured thicknesses of all composite samples, the main influencing parameters and their trend of influence were determined. A Taguchi DOE analysis was conducted using the Minitab software to compute the average values for each level and parameter. Using the difference between the averaged composite thickness between the two levels, i.e., the 'Delta' value in Table 3.3, a ranking of the parameters was established to understand the order of significance of the adopted parameters. Results of the Taguchi analysis that enabled the computation of averaged mean effects are shown in Table 3.3. Based on the rankings in Table 3.3 the top three factors having substantial influence on the sample thickness are layer thickness, magnetic filler loading, and exposure time per projection. The most significant change in sample thickness was observed for a layer thickness setting varying from 1.2179 mm for 10 μm layers to 0.8724 mm for 50 μm layers. Exposure time per projection, which controls the incident energy for photopolymerization, introduced significant differences in final sample thickness as reflected by the order of ranking. The inverse behavior observed for exposure time and layer thickness indicates the need for optimizing the parameters to print dimensionally stable composites. To further illustrate the impact of the studied process parameters, the main effects plot shown in Figure 3.5 was prepared. The graph illustrates the strong effect of the layer thickness parameter on sample thickness. Increasing magnetic filler loading also raised sample thickness. On the other hand, an increased additive loading

resulted in reduced sample thickness as it was known that the additives enhance the viscosity of the magnetic suspension. The obtained results are congruent with observations in the technical literature, i.e., a high viscosity resin enables printing composites with high resolution [26]. The influence of additive type, wait before exposure, and separation slide velocity on sample thickness were observed to be minor compared to the other parameters studied.

Table 3.3: DOE response table for means of sample thickness for printed magnetic composites.

Level	ET/P (s)	MFL (wt%)	LT (µm)	AT	WBE (s)	AL (wt%)	SSV
1	0.9755	0.9587	1.2179	1.0368	1.0769	1.0749	1.0541
2	1.1148	1.1316	0.8724	1.0535	1.0134	1.0154	1.0362
Delta	0.1394	0.1729	0.3455	0.0167	0.0635	0.0595	0.0178
Rank	3	2	1	7	4	5	6

ET/P	Exposure time per projection (s)
MFL	Magnetic filler loading (wt%)
LT	Layer thickness (µm)
AT	Additive type
WBE	Wait before exposure (s)
AL	Additive loading (wt%)
SSV	Separation slide velocity (rpm)

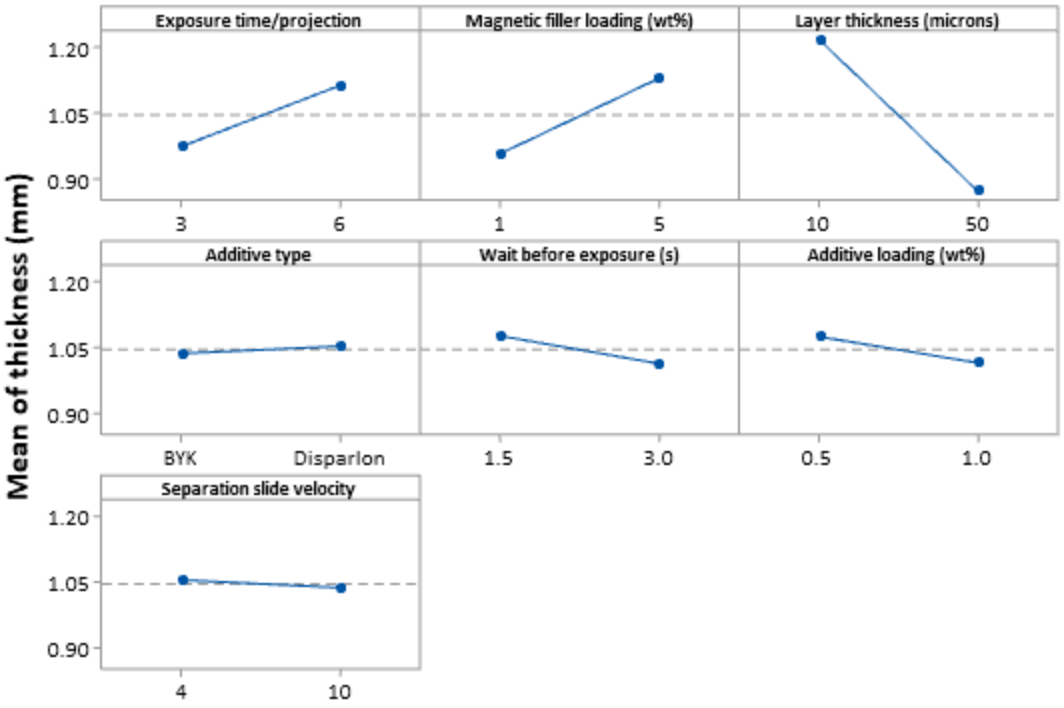

Figure 3.5: Main effects plot representing mean of measured thickness.

Replicate thickness measurements conducted on the samples enabled determining signal-to-noise (S/N) ratios through the Taguchi DOE. A wide spectrum of thickness data was obtained from all the experiments ranging from 0.69 mm to 1.49 mm, and hence a "nominal is the best" quality characteristic was adopted. The S/N ratio, a measure to identify the effect of every controllable parameter considering the mean thickness and standard deviations on the response variable, is calculated based on Eq.3.5 [27].

$$S/N = 10 * log\left(\frac{Y^2}{S^2}\right) \tag{3.5}$$

where Y is the mean of responses for the given factor level combination, and S is the standard deviation of the responses. S/N ratios calculated using Eq.5 are expressed in Table 3.4.

Table 3.4: Response table for signal-to-noise ratios for sample thickness of printed magnetic composites ('Nominal is the best' quality characteristic).

Level	ET/P (s)	MFL (wt%)	LT (µm)	AT	WBE (s)	AL (wt%)	SSV
1	21.16	18.94	23.44	21.13	22.72	22.33	22.06
2	22.57	24.78	20.28	22.60	21.01	21.40	21.66
Delta	1.41	5.84	3.16	1.47	1.71	0.93	0.40
Rank	5	1	2	4	3	6	7

It was observed that the parameter ranking based on S/N ratio is different compared to the ranking based on the means of composite sample thickness. From Table 3.4, it is understood that the parameters that cause significant variabilities are magnetic filler loading, layer thickness, and wait before exposure. An interaction matrix based on the average of all responses for mean thickness is attached as part of supplementary figures to aid in understanding the interactions between various adopted parameters in the study.

The average thicknesses of magnetic composite samples obtained from CMM measurements were observed to exhibit a unique variation pattern across the build head as seen in Figure 3.6. Legends in Figure 3.6 refer to the experiment numbers listed in Table 3.1, while the zone number shown on the ordinate represents magnetic composite samples printed in printing zones designated in Figure 3.2. The graphs in Figure 3.6 indicate that irrespective of the adopted material and process parameters, samples printed in zone 3 had the greatest thickness and samples printed in zone 4 exhibited the lowest thickness.

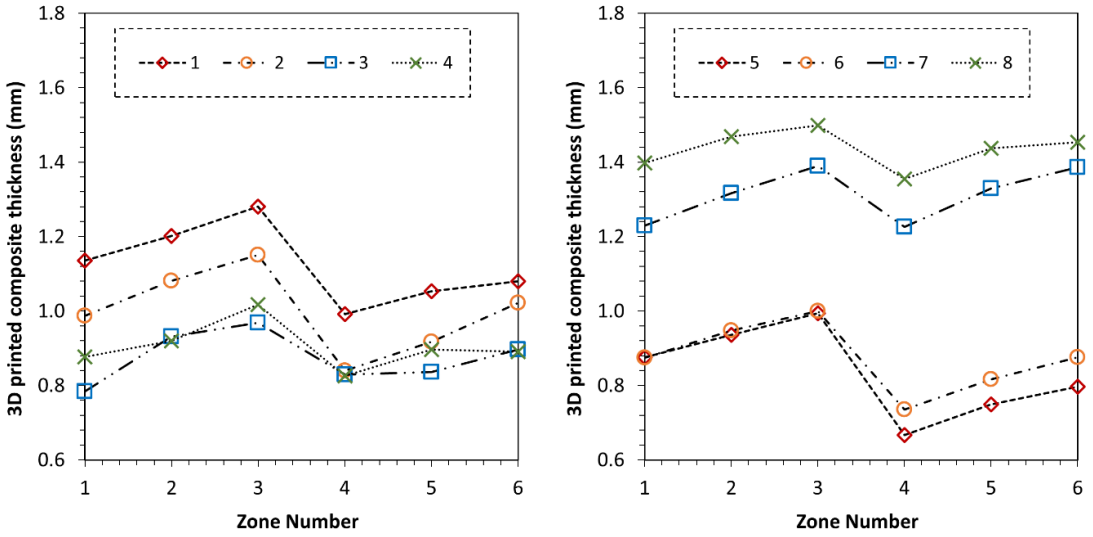

Figure 3.6: Thickness variation of 3D printed magnetic composite samples across six printing zones (as designated in Figure 3.1) on the build head; Legend indicates experiment numbers 1 to 8 as indicated in Table 3.1; (Left) Experiment 1 to 4, (Right) Experiment 5 to 8.

Obtained thickness measurements for every experiment listed in Table 3.1 was further expressed in the form of box plots to elucidate the thickness variability of composite samples. The mean value of thickness for samples printed in experiment 2 was observed to be close to the target thickness of 1 mm. Experiments 3, 4 & 8 were observed to exhibit least variation in composite sample thickness.

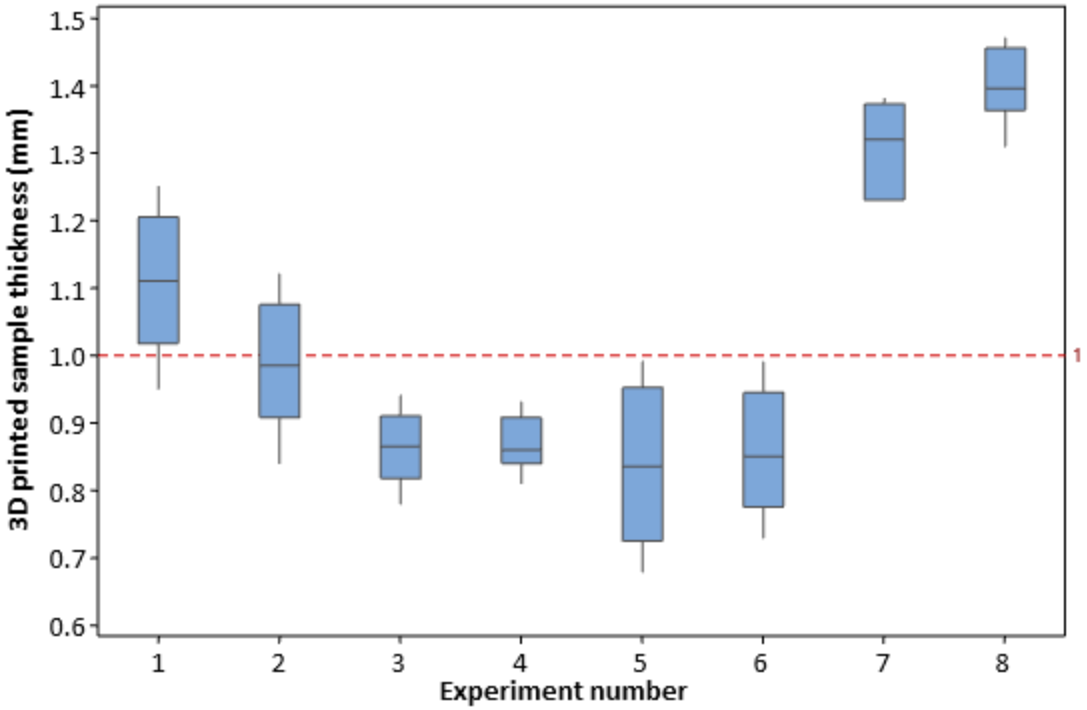

Figure 3.7: Boxplot for thickness of samples produced from each experiment listed on DOE with a targeted sample thickness of 1mm, shown as the reference line on the graph.

3.4.2 Analysis of ferromagnetic polymer composites curing behavior

In this analysis, the influence of parameters like magnetic filler loading, filler type, additive loading, additive type, and exposure time per projection on ferromagnetic polymer composites curing behavior was investigated. Curing behavior was studied with the objective of engineering the process for printing ferromagnetic polymer resins with increased filler loading. Cured depth was measured using the CMM to construct the working curves for all formulations listed in Table 3.2. From the working curves, characteristic curing parameters like light penetration depth and critical energy were derived. The working curves depicted in a semi log graph of the measured cured depth and energy dose are shown in Figure 3.8.

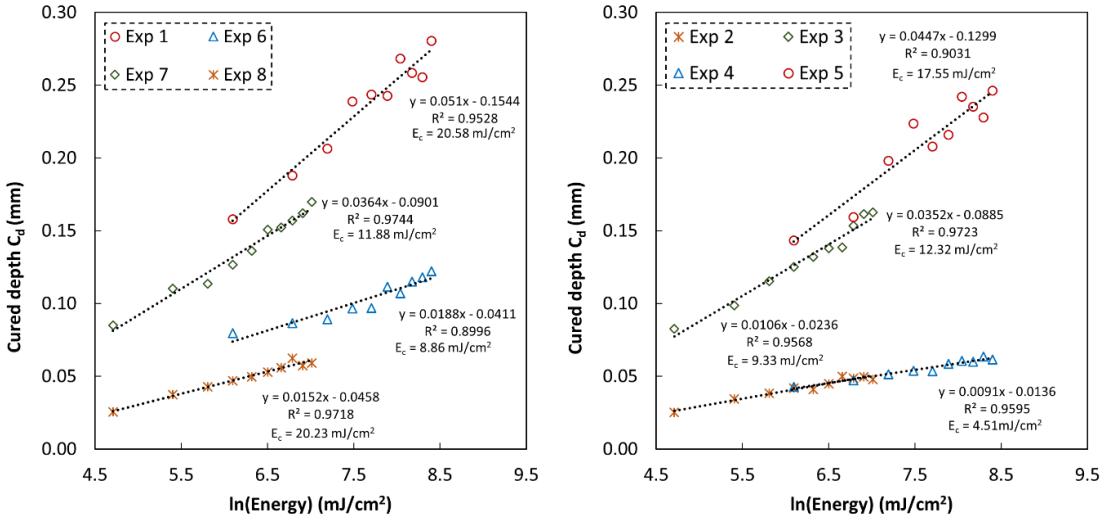

Figure 3.8: Working curves for cured depth versus curing light energy dose. Left: Samples with strontium ferrite filler; Right: Samples with NdFeB filler. For experiment numbers ("Exp") refer to Table 3.2.

From the linear fits expressed in Figure 3.8 the resin characteristic parameters 'depth of penetration' (D_p) and 'critical energy for polymerization' (E_c) were derived. Equations in Figure 3.8 represent the linear fits for curves plotted in linear scale (not semi log) where "y" represents the cured thickness measured using the CMM and "x" represents the energy incident on the resin during the light exposure process. D_p is obtained from the slope of the linear fits, and E_c is obtained using the abscissa intercept of the working curves. The DOE framework developed and listed in Table 3.2 was evaluated for the obtained depth of penetration (D_p). The main effects plot that represents the averaged effects is expressed in Figure 3.9.

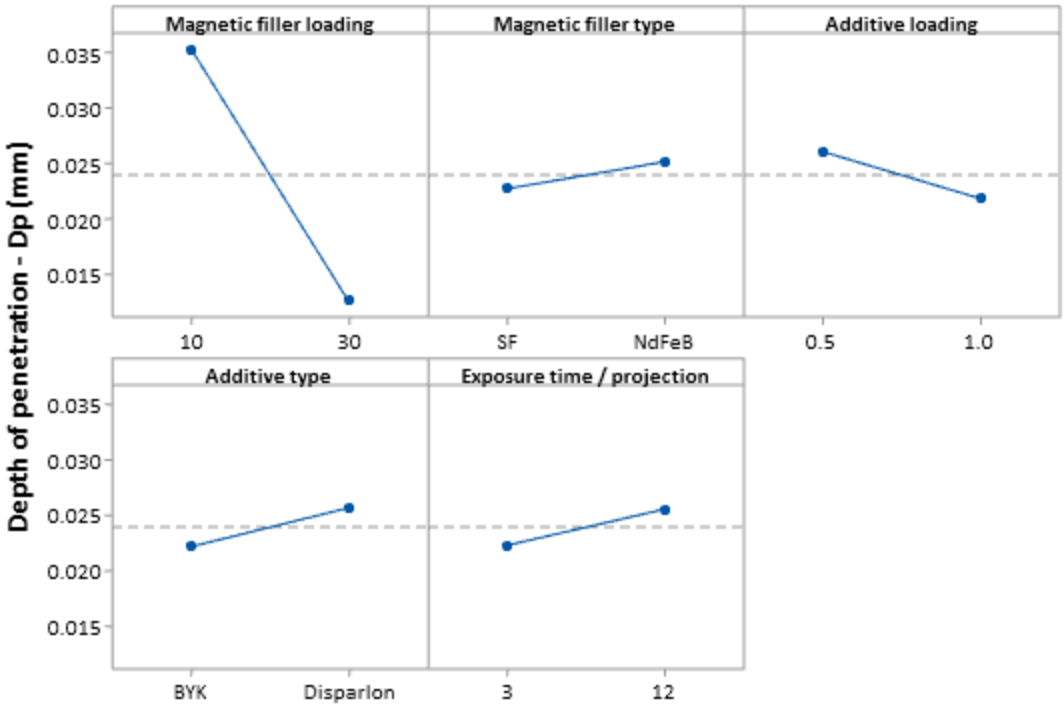

Figure 3.9: Main effects plots representing mean of depth of penetration (D_p).

From Figure 3.9, the depth of penetration was observed to decrease strongly with increasing magnetic filler loading. This behavior corresponds with Eq.3.3, i.e., the cured depth is inversely proportional to filler loading. Depth of penetration for composites containing strontium ferrite filler was observed to be lower compared to NdFeB, which is attributed to particle size, that is, the higher surface area to volume ratio of strontium ferrite as compared to NdFeB. It was further observed that an increase in rheological additive loading led to a decrease in the depth of penetration as the suspension experiences increase in its low shear viscosity [15]. The effectiveness of the additive materials in the polymer systems additionally depends on its type. It was observed that the formulation engineered with BYK 7410 additive decreased the depth of penetration compared to Disparlon 6900-20X. An increase in depth of penetration

was additionally observed with an increase in exposure time per projection as this influences the incident energy on the photosensitive ferromagnetic polymer composites.

An Analysis of Variance (ANOVA) was conducted to further understand the significance of experimental parameters on the response variable 'depth of penetration'. Table 3.5 summarizes the ANOVA results, where the headings 'DF', 'Adj SS', 'Adj MS', 'F-value' and 'P-value' refer respectively to the degree of freedom, adjusted sums of squares, adjusted mean squares, significance indicator, and probability measuring evidence against the null hypothesis.

Table 3.5: ANOVA results for depth of penetration (D_p).

Source	DF	Adj SS	Adj MS	F-Value	P-Value
Model	7	0.003420	0.000489	26.66	0.000
Blocks	2	0.000077	0.000039	2.11	0.153
Linear	5	0.003343	0.000669	36.48	0.000
MFL	1	0.003073	0.003073	167.69	0.000
MFT	1	0.000030	0.000030	1.62	0.221
AL	1	0.000116	0.000116	6.34	0.023
AT	1	0.000066	0.000066	3.58	0.077
ET/P	1	0.000058	0.000058	3.17	0.094
Error	16	0.000293	0.000018		
Total	23	0.003713			

From the ANOVA results in Table 3.5, it can be concluded that magnetic filler loading and additive loading are the factors primarily affecting the depth of penetration with a confidence level greater than 95% (P-value < 0.05). Depth of penetration is expressed as a linear statistical model to derive the main effects of the adopted

parameters. A zero P-value for the model signifies that the linear statistical model explains variations in the response and provides a strong evidence against the null hypothesis. The experiment was designed with blocks to account for uncontrollable variables and the differences that might occur during the measurement process. From the ANOVA, it was observed that the blocks that randomized experiments were insignificant.

A Pareto bar chart and normal probability plot for the effects were created to understand the significance of experimental parameters and the direction of the effects on the depth of penetration. The Pareto chart indicating the magnitude of the effects is shown in Figure 3.10. In the chart the bars representing the adopted process parameters that cross the red reference line are considered to be statistically significant.

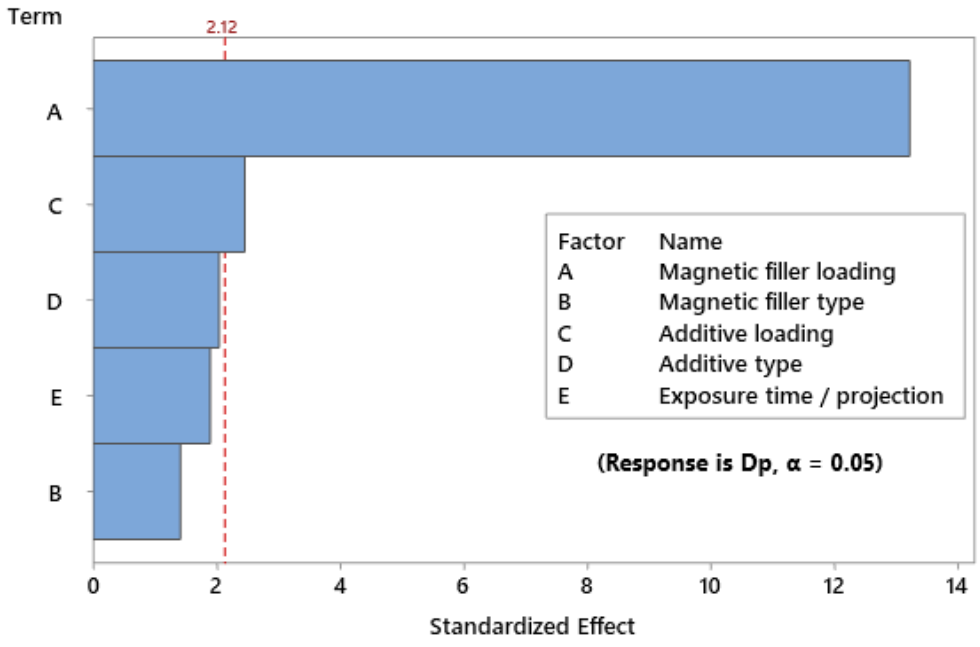

Figure 3.10: Pareto chart of factors affecting the response variable 'depth of penetration'.

The normal probability plot depicted in Figure 3.11 enables understanding the magnitude and the direction of the effects in a single graph. The plot includes a distribution fit line where all effects are zero. Factors to the left of the line reduce the response variable when changing a parameter from a low to a high level whereas factors to the right increase the response. Figure 3.10 confirms filler loading and additive loading to be the most significant factors.

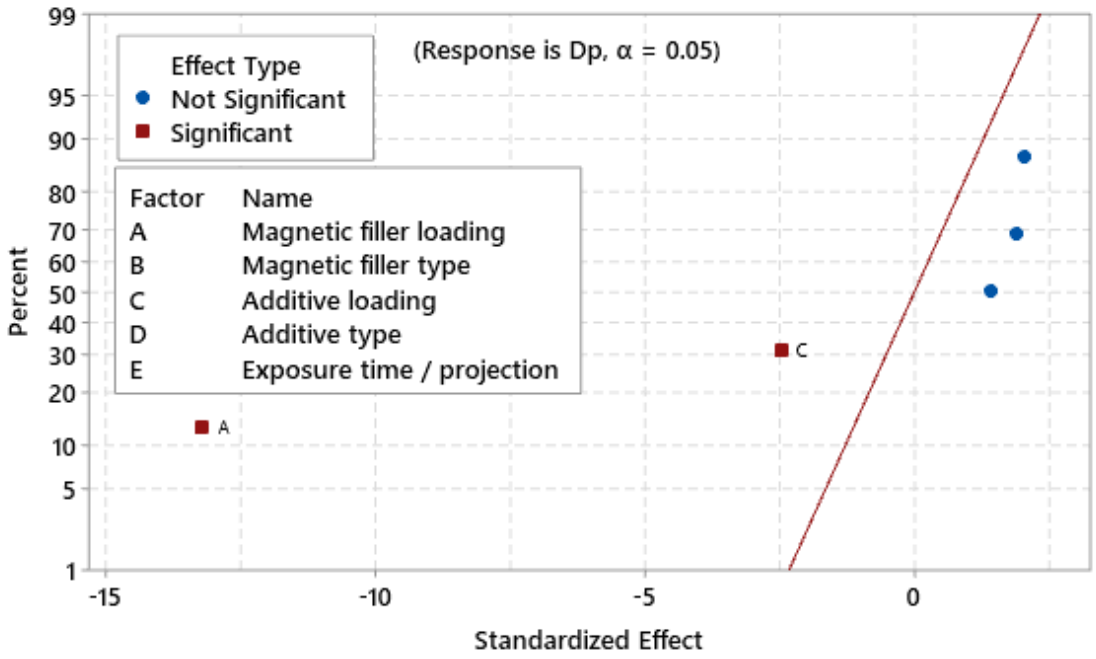

Figure 3.11: Normal probability plot of factors affecting the response variable 'depth of penetration'.

3.4.3 Printability tests, capabilities, and characteristics of 3D printed magnetic composites

Utilizing the understanding obtained from the ferromagnetic polymer composite curing behavior analysis, printability experiments of magnetic composites containing 10 wt% and 25 wt% of SrFeO and NdFeB magnetic fillers were conducted. The formulation was engineered with 0.5 wt% of BYK 7410 additive to achieve stability against particle settling during the fabrication process. Even though the curing

behavior analysis enabled establishing the critical UV irradiation energy for polymerization, the exposure parameters had to be tuned further, considering adhesion to the aluminum build head and to subsequent cured composite layers. Printing magnetic polymer composites was attempted using a layer thickness setting of 10 μm, exposure times as indicated in Table 3.6, and maintaining all other machine tunable parameters at their respective default settings used for a Autodesk CMYK (PR-57) resin printable using the DLP printer. The standard machine settings in terms of exposure time for the PR-57 resin with a layer thickness setting of 10 μm are 8 seconds (148 mJ/cm^2) for the first layer, 4 seconds (74 mJ/cm^2) for the next four print layers, and 1.2 seconds (22.2 mJ/cm^2) for all remaining print layers. Table 3.6 indicates the exposure time utilized for printing magnetic composites and corresponding energy density (values in brackets) calculated using the intensity of UV light and exposure time [20]. Simple magnetic composites cuboids with dimensions of 15 mm by 10 mm by 1 mm were fabricated

Table 3.6: Exposure parameters used to 3D print magnetic composites.

Specimen No.	**Magnetic filler type**	**Exposure time for first four print layers**	**Exposure time from fifth layer**	**Average composite thickness (mm)**
1	10wt% NdFeB	11s (203.5 mJ/cm^2)	3.5s (64.75 mJ/cm^2)	0.97
2	10wt% SrFeO	13s (240.5 mJ/cm^2)	5s (92.5 mJ/cm^2)	1.06
3	25wt% NdFeB	16s (296 mJ/cm^2)	8s (148 mJ/cm^2)	-
4	25wt% SrFeO	20s (370 mJ/cm^2)	10.5s (194.25 mJ/cm^2)	-

Composites containing 10 wt% of NdFeB and SrFeO fillers were successfully printed. With 25 wt% magnetic fillers, it was observed that the cured layers did not adhere to the build head and cured resin fragments were observed to be floating within the resin tray. To further check the capability of printing composites with 25 wt% magnetic fillers, machine settings like the separation/approach slide rotation velocity were reduced from 12 to 4 rpm, and the Z axis separation velocity was reduced from 1.5 mm/s to 1.2 mm/s. Changing these settings enabled printing the composites but defects could still be observed as seen in Figure 3.12. Some considerable processing challenges include reliable adhesion of the first cured layer to the aluminum build head and the subsequent cured magnetic composite layers. Poor adhesion sometimes resulted in cured fragments just floating in the resin tray. Such fragments posed additional challenge during the manufacturing process. At every instance of a print failure, the resin was filtered using a paint strainer to remove cured fragments.

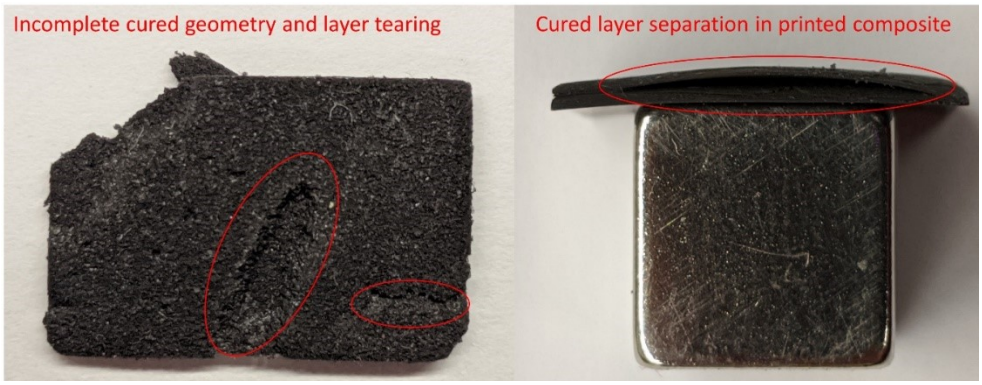

Figure 3.12: Observed defects in SrFeO composite (left) and NdFeB composite (right) printed using resins containing 25 wt% magnetic fillers.

From Figure 3.12, it was understood that even though composites were printable using a resin engineered with 25 wt% magnetic particles, further analyses on machine parameters are required to achieve printing components without defects.

Further characterization and analyses were conducted with 10 wt% of NdFeB and SrFeO filler resin. Figure 3.13 shows the image of 3D printed magnetic composites attracted to the surface of a permanent magnet (N52 grade).

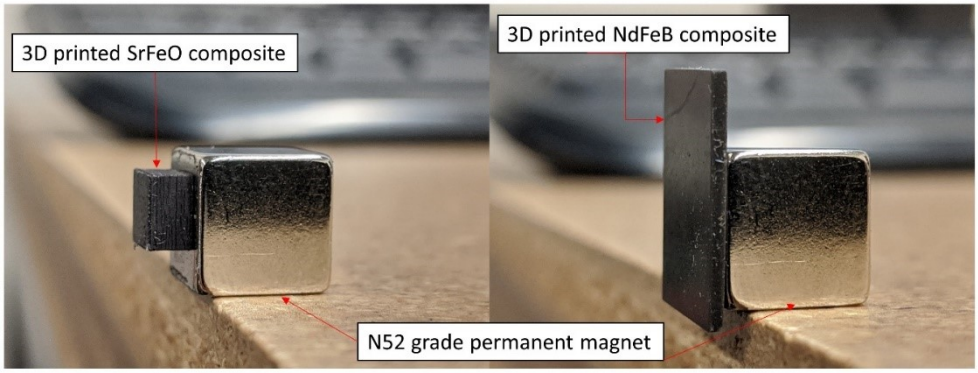

Figure 3.13: 3D printed magnetic composites attracted to the surface of N52 grade permanent magnets.

To assess the mechanical properties, dog bone type specimens were printed using the parameters indicated in Table 3.6. A total of four samples were printed and tested for each filler type. The tensile characteristics are depicted in Figure 3.14, which shows that the composite containing NdFeB fillers exhibits higher tensile properties than the composite containing the SrFeO magnetic filler. The average ultimate tensile strength of NdFeB and SrFeO magnetic composites were 28.1 MPa and 22.0 MPa, respectively. It should be noted that in spite of adopting a higher exposure time for the resin containing SrFeO fillers, its properties were lower compared to the NdFeB composite. The Young's modulus determined for the NdFeB and SrFeO composites using the chord slope method as indicated in ISO 527 are 656.5 MPa and 536.7 MPa, respectively.

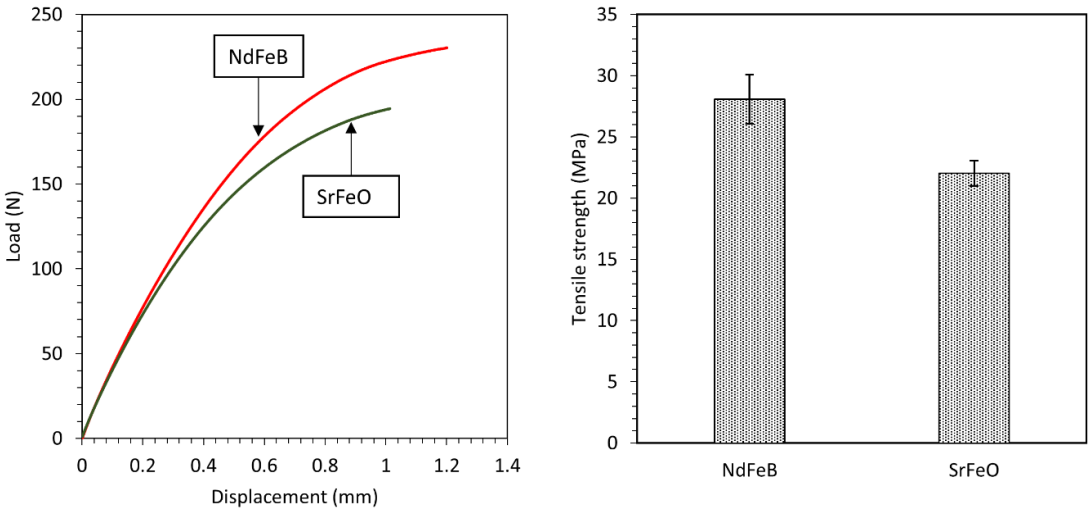

Figure 3.14: (Left) Load (vs) Displacement curves of magnetic composites (Right) Tensile strength of magnetic composites.

Apart from the process parameters, properties of polymer composites also depend on the filler dispersion and distribution within the manufactured composite. Using the 10 wt% NdFeB resin, cantilever type structures were 3D printed with the parameters listed in Table 3.6. All cantilever structures were printed in the same batch and further characterized for their width using an optical microscope. Figure 3.15 shows the target width of prepared cantilevers (value in white box) and the corresponding measured dimension. It was observed that the minimum printed dimension was 0.13 mm using the DLP printer with the in-house engineered magnetic filler modified resin formulation.

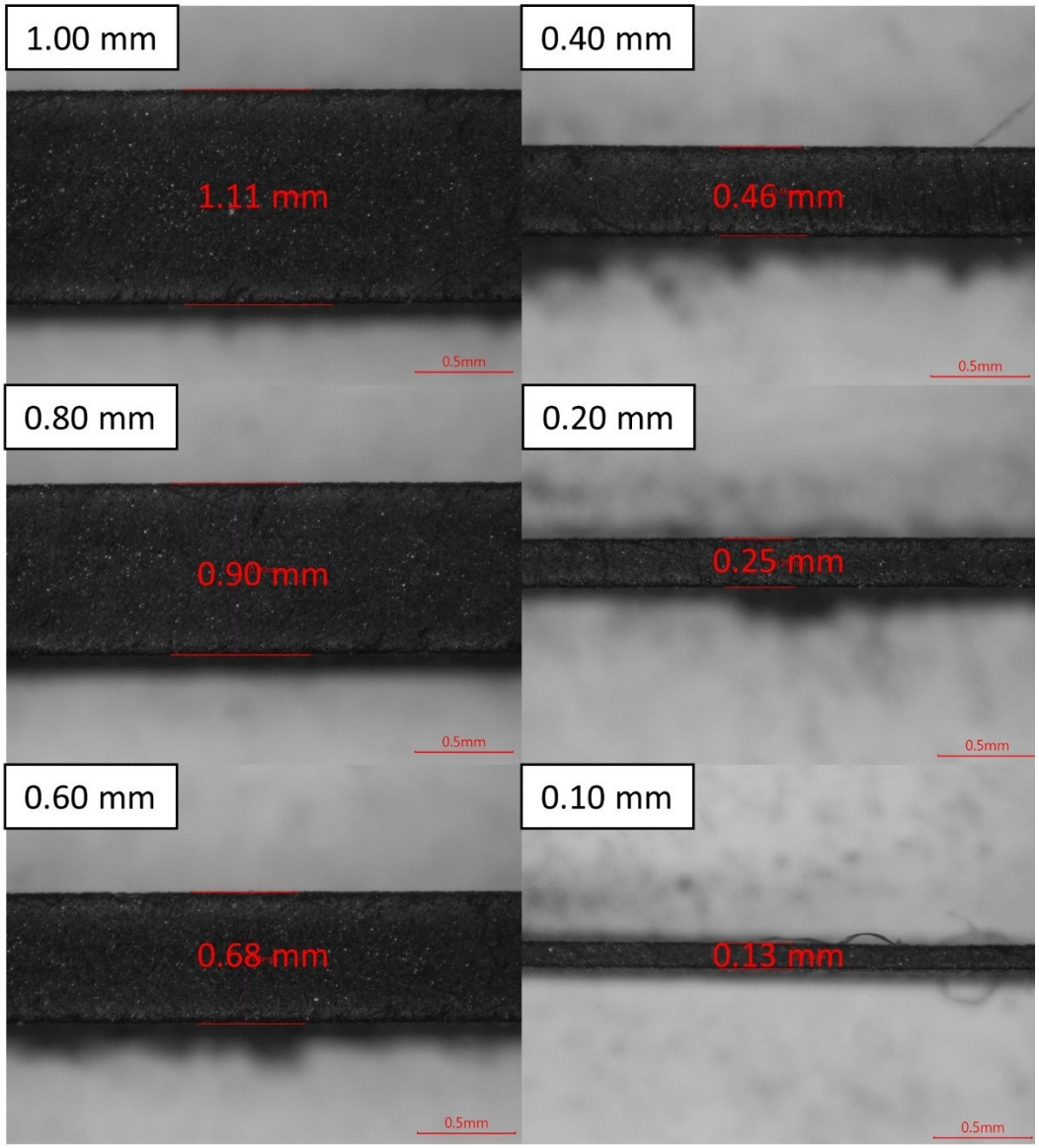

Figure 3.15: Dimensional characterization of cantilever type structures using optical microscopy (Number within white rectangle represents target dimensions).

3.5 Additional and supportive results

3.5.1 Parameters interaction matrix for mean composite thickness

In Section 3.5.1, the influence of material and process parameters on composite thickness was analyzed. Utilizing the average of all responses, an interaction matrix was derived to understand the interactions between different parameters adopted in the

study. Interaction plot was derived using Minitab software based on the average of all responses.

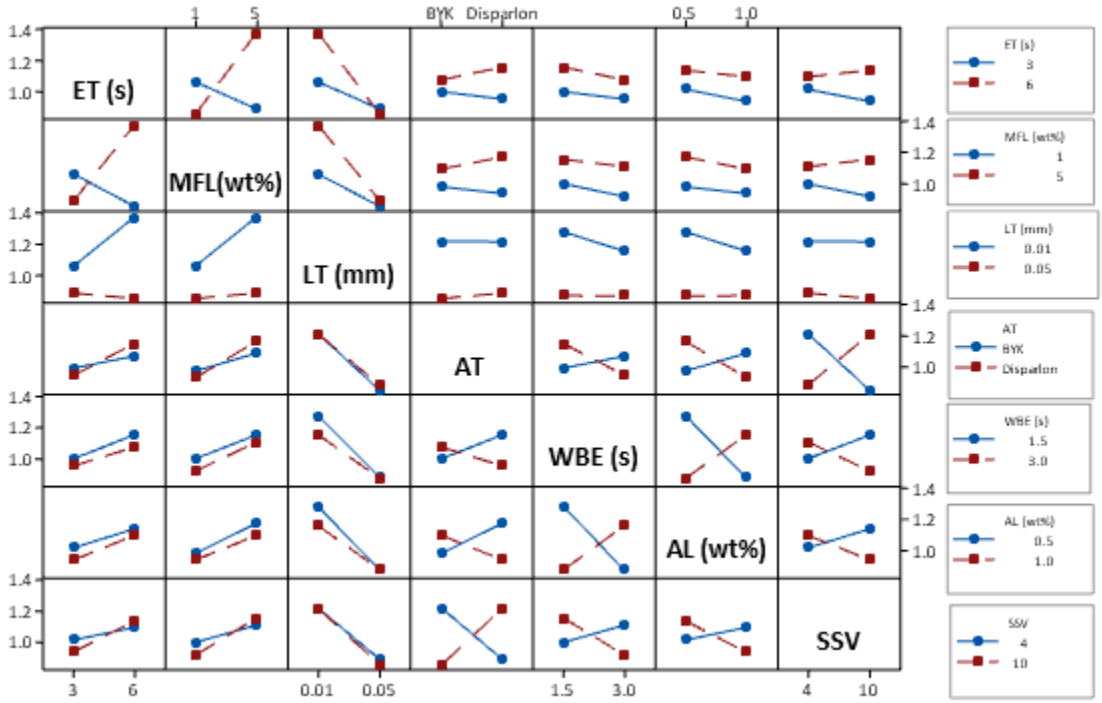

Figure 3.16. Interaction plot for parameters utilized (Abbreviations: ET – Exposure time, MFL – Magnetic filler loading, LT – Layer thickness, AT – Additive type, WBE – Wait before exposure, AL – Additive loading, SSV – Separation slide velocity).

3.5.2 Analysis of dimensional variation in composite width and length

Similar to the results observed for variations in printed magnetic composite thickness in Section 3.5.1, the width and the length of the same magnetic composites was measured to evaluate the influence of material and process parameters. Printed magnetic composite samples were measured using a digital Vernier caliper (Mitutoyo, Japan) to observe for the existence of any variational patterns and evaluate the influence of material and process parameters as indicated in Table 3.1.

Table 3.7: Response table for means – sample width.

Level	ET/P (S)	MFL (wt%)	LT (µm)	AT	WBE (s)	AL (wt%)	SSV
1	10.04	10.10	10.12	10.07	10.09	10.07	10.08
2	10.14	10.08	10.05	10.11	10.09	10.10	10.09
Delta	0.10	0.02	0.07	0.04	0.00	0.03	0.01
Rank	1	5	2	3	7	4	6

From the analysis of means, exposure time per projection, layer thickness and additive type significantly influence the composite width. Additionally, signal to noise ratio was used as a tool to identify the parameters that cause variability in the obtained results

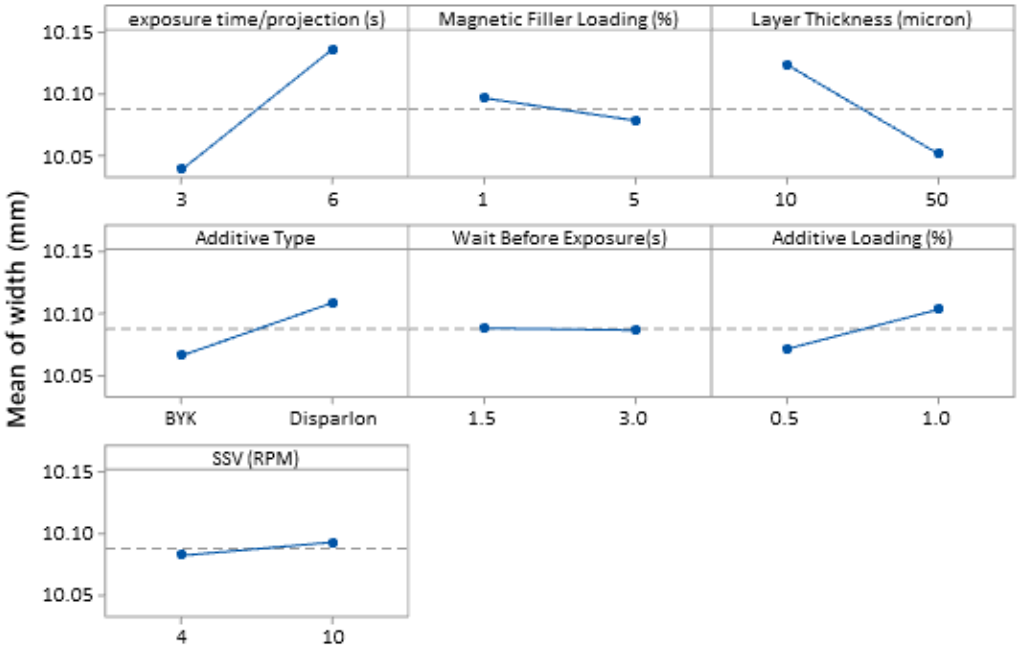

Figure 3.17: Main effects plot for sample width.

Table 3.8: Response table for signal to noise ratio (Nominal is the best quality characteristic).

Level	ET/P	MFL (wt%)	LT (µm)	AT	WBE (S)	AL (wt%)	SSV
1	44.84	46.15	44.01	45.53	44.96	44.33	44.49
2	45.34	44.03	46.16	44.65	45.22	45.85	45.69
Delta	0.50	2.12	2.15	0.88	0.26	1.52	1.20
Rank	6	2	1	5	7	3	4

From the S/N ratio analysis, it is observed that the most significant parameters influencing the composite width are layer thickness, magnetic filler loading and additive loading. The average width of the magnetic composites is plotted with respect to their printing zones to check for the existence of any variational patterns.

From Figure 3.17 it is evident that the trend in increase or decrease in composite width is also dependent on the printing zone. From the box plot it is additionally understood that the composite width in most of the print cases is above the designed dimensions of 10 mm.

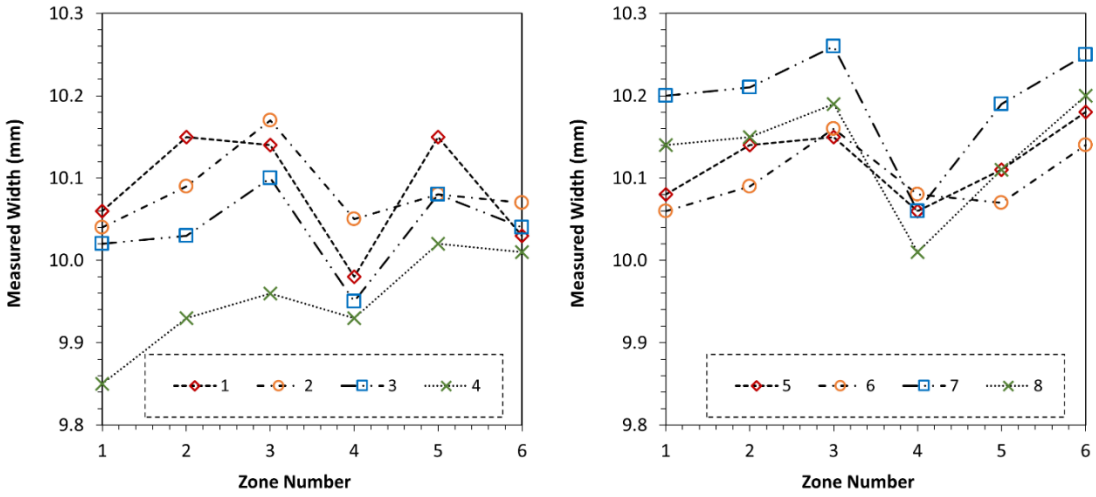

Figure 3.18: Width variation of samples across 6 printing zones on the build head (Left) Experiment 1 to 4 (Right) Experiment 5 to 8.

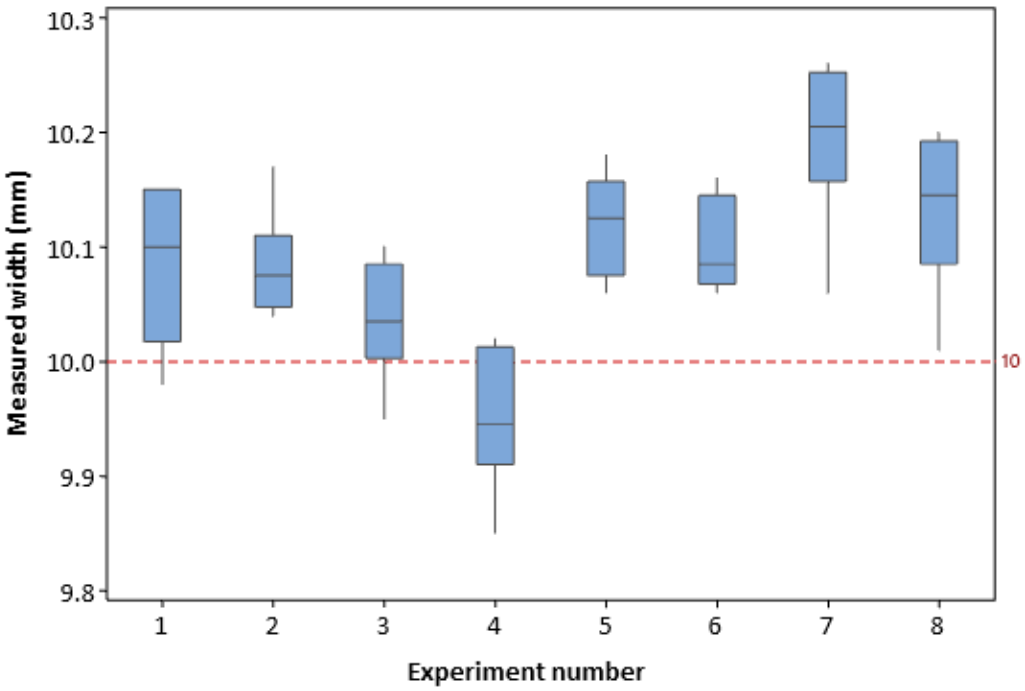

Figure 3.19: Boxplot for sample width produced from each experiment listed on DOE with a targeted sample width of 10mm, shown as the reference line on the graph

Similar measurements and analysis were also conducted for the composite length and the results are expressed as follows.

Table 3.9: Response table for mean of length.

Level	ET/P (s)	MFL (wt%)	LT (µm)	AT	WBE (s)	AL (wt%)	SSV
1	15.05	15.12	15.14	15.08	15.10	15.08	15.10
2	15.15	15.08	15.06	15.12	15.10	15.12	15.10
Delta	0.09	0.05	0.07	0.03	0.01	0.05	0.00
Rank	1	4	2	5	6	3	7

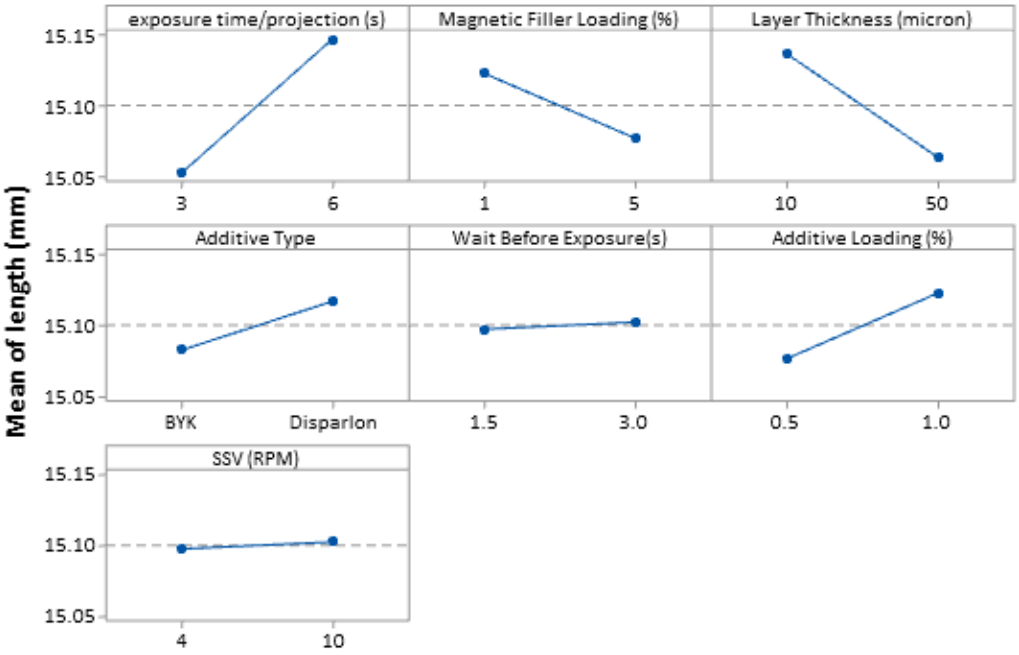

Figure 3.20: Main effects plot of sample length

Table 3.10: Response table for signal to noise ratio for sample length.

Level	ET/P (s)	MFL (wt%)	LT (µm)	AT	WBE (s)	AL (wt%)	SSV
1	48.97	46.96	46.75	48.56	48.74	46.79	47.99
2	46.95	48.96	49.18	47.37	47.19	49.14	47.94
Delta	2.02	2.00	2.43	1.19	1.55	2.35	0.05
Rank	3	4	1	6	5	2	7

From the means and signal to noise ratio analysis the parameters influencing sample length are exposure time per projection, layer thickness and additive loading. The variational pattern in sample length as observed in Figure 3.20 is identical only in a few regions and does not adhere to any specific pattern as observed for sample thickness and width. Additionally, from the box plot expressed in Figure 3.21, the length of the composite in most of the experiment cases was observed to be higher than the designed value of 15 mm.

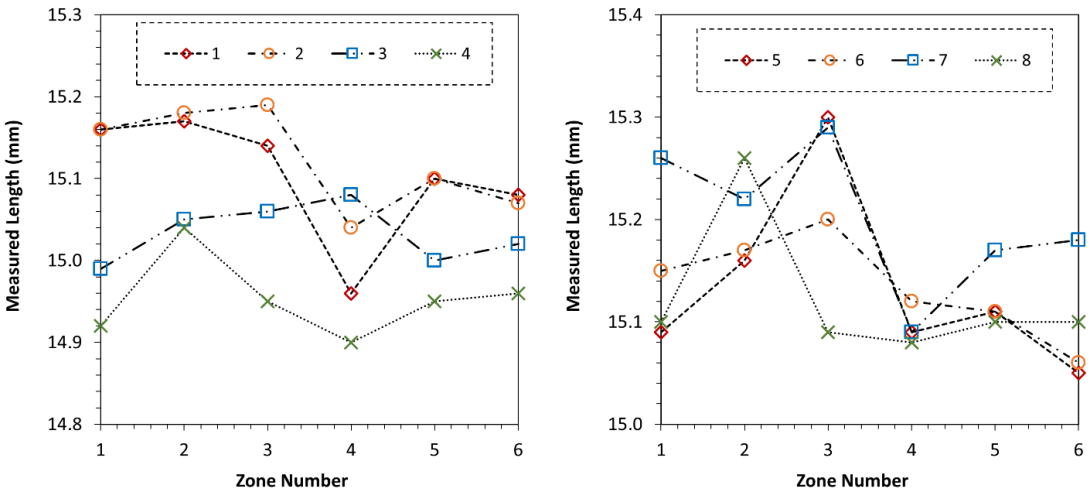

Figure 3.21: Length variation of samples across 6 printing zones on the build head (Left) Experiment 1 to 4 (Right) Experiment 5 to 8.

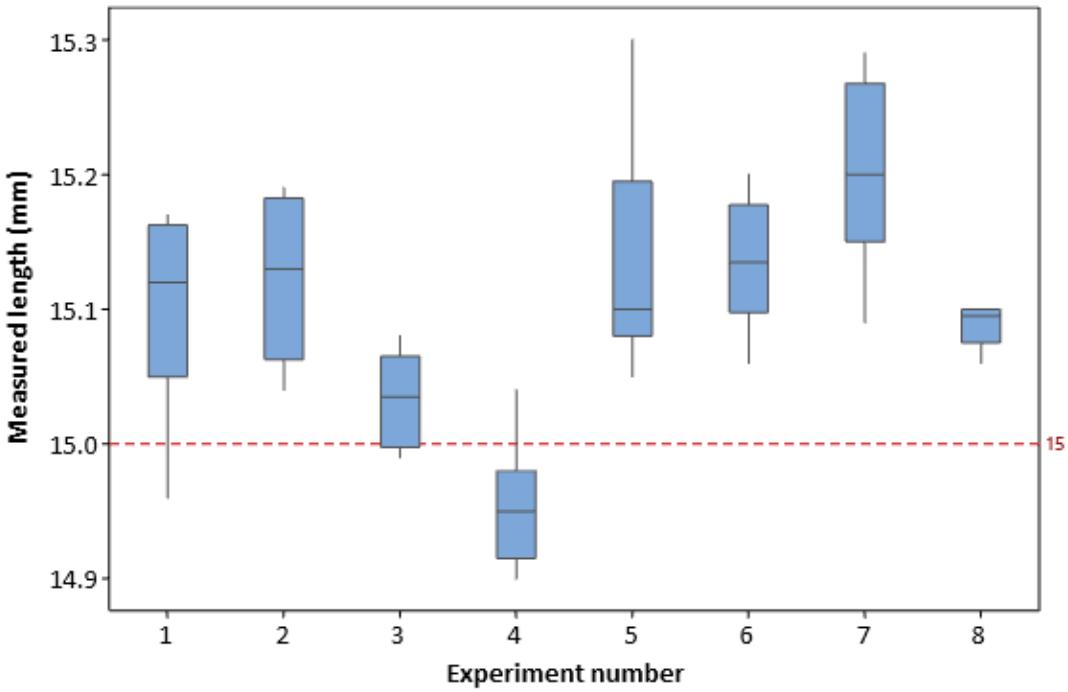

Figure 3.22: Boxplot for sample length produced from each experiment listed on DOE with a targeted sample length of 15 mm, shown as the reference line on the graph.

From this dimensional variation's analysis, it is observed that variations in composite thickness and width follow a very unique pattern compared to sample length which doesn't exhibit any specific pattern when composite samples are printed at different zones on the print head as indicated in Figure 3.21. Among all the dimensional variation results, thickness analysis was deemed more important as it was postulated that the probability of printing polymers containing higher magnetic filler loading was greater in these specific zones.

3.5.3 Analysis of thickness in cured ferromagnetic polymer layers

Results expressed in this section relate to the analysis of ferromagnetic polymer curing behavior. In section 3.5.2, characteristic resin parameters like depth of penetration (D_p) and critical energy of polymerization (E_c) were determines. Utilizing

a fractional factorial design, the influence of experimental parameters on depth of penetration was determined. The fundamental data utilized to determine the resin characteristic parameters is the measured cured depth (or) thickness from grids indicated in Figure 3.22. It is known that every grid was designed to receive a distinct amount of UV exposure. In this section, first we understand the variations in thickness measurements conducted using the CMM. Utilizing the thickness measurements of one single grid, the influence of adopted experimental parameters is evaluated based on the experiment design in Table 3.2.

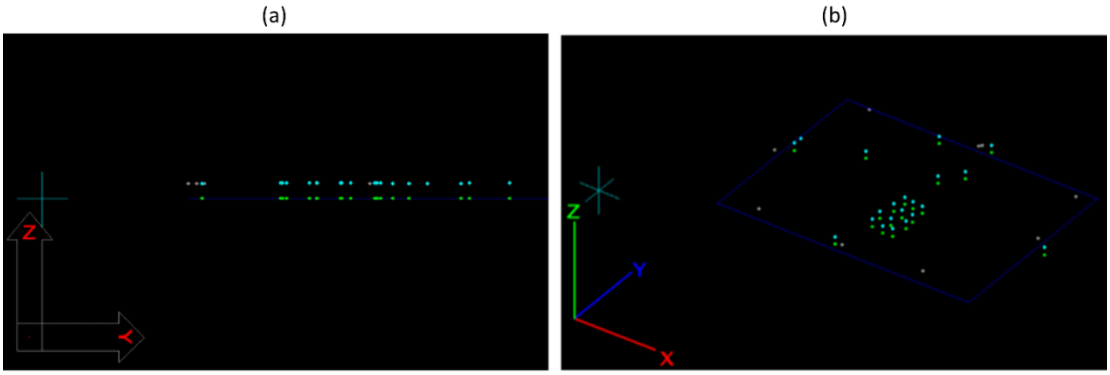

Figure 3.23: Z-Y and X-Y-Z Plane views of thickness measurements recorded on the CMM software (a) Z-Y plane view (b) X-Y-Z plane view. The distance between the green points and the blue points are the thickness of the acrylic sheet.

Figure 3.22 shows an image from the CMM software on how thickness of the cured ferromagnetic polymer layers adhering to the acrylic sheet was measured using the CMM. To understand the capability of the measurements using a CMM, variation of thickness across two grids of a sample are shown in Figure 3.23.

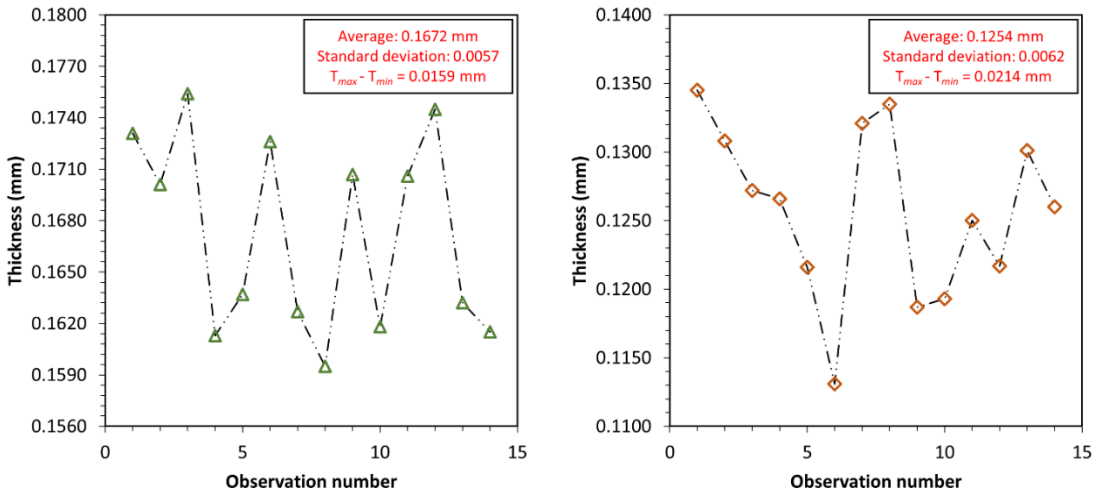

Figure 3.24: Thickness variations across sample grids.

Difference between the maximum and minimum measured thickness in the above mentioned example was observed to be 16 µm and 21 µm. From the above figure, variation in cured layer thickness measured using the CMM which is a contact type measurement is well understood. This additionally exhibits the reliability of the CMM measurements utilized to measure the cured depth and further derive characteristic resin parameters of ferromagnetic polymers.

The design of experiment framework developed and listed in Table 3.2 was evaluated for the obtained cured depth (or) thickness. Even though the thickness data from every single grid was analyzed, cured layer thickness of one single grid (Grid number 2) is expressed to understand the parameter significance. From Figure 3.24, it is evident that moving towards a higher level of filler loading and additive loading the cured thickness drastically reduces. The reason for observing a decrease in cured depth at high filler or additive loading is trivial. The fillers and the additives hinder the UV light penetration i.e the UV light cannot reach to a deeper layer of uncured resin. It was additionally postulated that the initially solidified layer further reduces the penetration

of UV light further deep into the resin. It was observed that the type of magnetic filler does not have a significant impact on cured thickness. Moreover, choosing Disparlon 6900-20X as stabilizing additive or increasing the per projection exposure time yielded a higher cured thickness. The increase in cured thickness at higher exposure time per projection is due to the increased energy absorbed by the uncured resin. The trends in the process parameters are expressed through factorial plot shown in Figure 3.24.

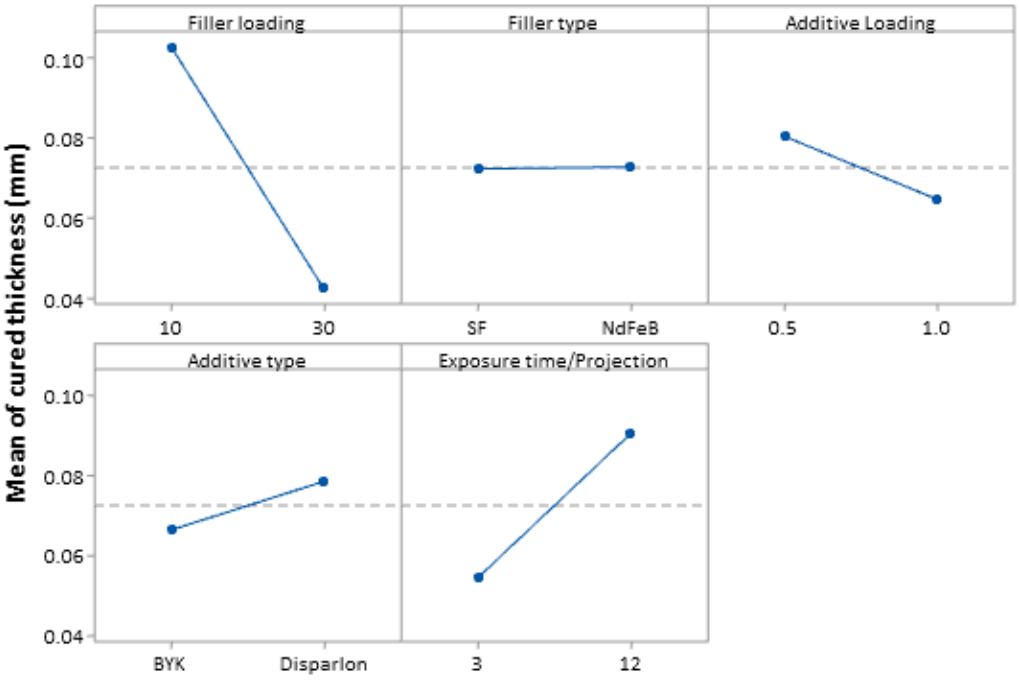

Figure 3.25: Main effects plot for cured thickness (Grid number 2).

Analysis of variance was conducted to understand the significance of process parameters on cured thickness.

Table 3.11: Analysis of variance for cured depth / thickness.

Source	DF	Adj SS	Adj MS	F-Value	P-Value
Model	7	0.0032751	0.0004679	23.72	0.000
Blocks	2	0.000448	0.000224	1.13	0.346
Linear	5	0.032303	0.006461	32.75	0.000
MFL	1	0.022079	0.022079	111.93	0.000
MFT	1	0.000001	0.000001	0.01	0.934
AL	1	0.001499	0.001499	7.60	0.014
AT	1	0.000889	0.000889	4.51	0.050
ET/P	1	0.007834	0.007834	39.72	0.000
Error	16	0.003156	0.000197		
Total	23	0.035907			

A lower P-value ($P < 0.05$) indicates higher parameter significance and from the above table, exposure time per projection, filler loading, additive loading and additive type were observed to influence the cured thickness. The Pareto chart that enables understanding the magnitude of the effects in shown in Figure 3.26.

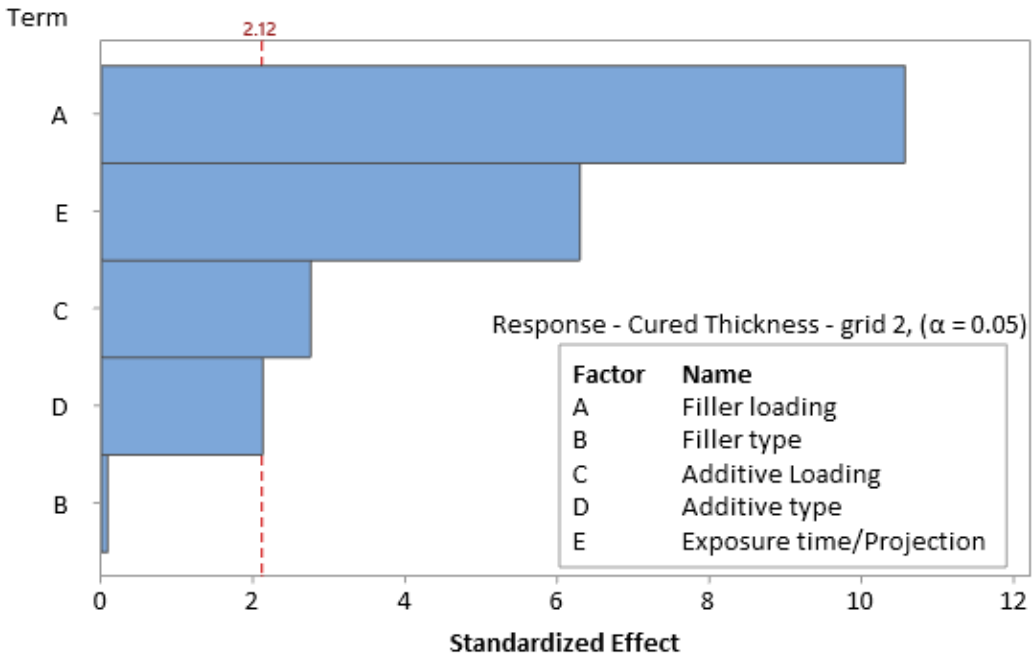

Figure 3.26: Pareto chart for cured thickness for grid 2.

A fundamental difference observed between the analysis of cured depth (C_d)/ thickness and analysis of depth of penetration (D_p) is that, the exposure time is a significant parameter governing the cured depth whereas in the analysis resin characteristic parameter D_p it was observed to be less influential. The pareto chart showcases the absolute value of the effects, but a normal plot of effects is required to understand the parameters that increase or decrease the final response.

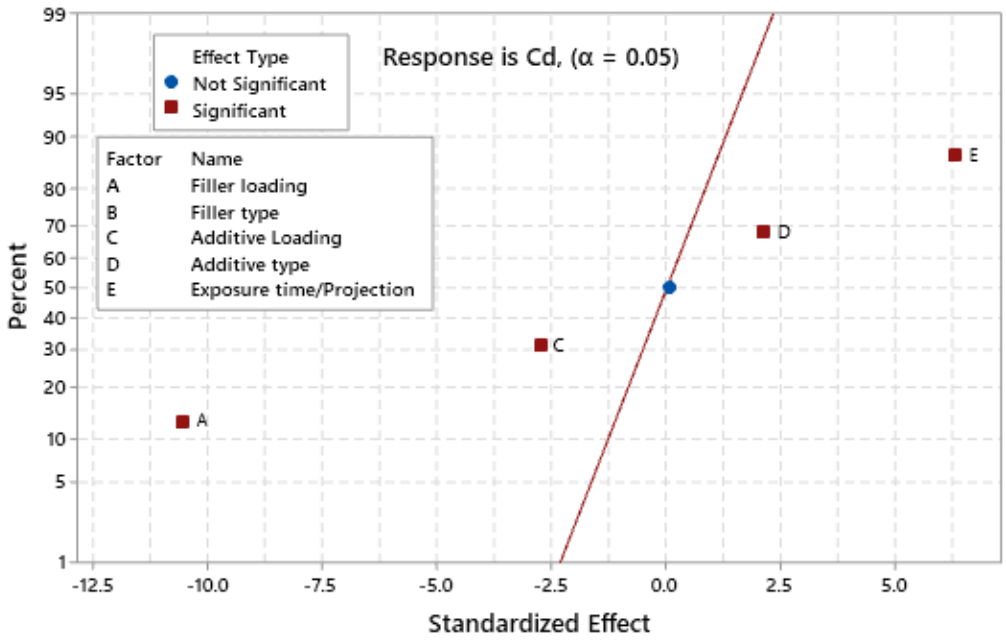

Figure 3.27: Normal plot of standardized effects for cured thickness (Cd).

From the normal plot, it is evident that both the filler loading and additive loading reduce the cured thickness when changing the parameter from a lower level to a higher level. Increasing the exposure time per projection and changing the type of additive utilized were observed to result in increased cured depth/ thickness. It is these thickness measurements that enabled to further determine and evaluate resin characteristic parameters like depth of penetration and critical energy for polymerization.

3.6 Additional observations

This section explains the challenges encountered while printing prepolymers with increased filler loading. In some printing cases, the cured layer was obsered to adhere to the PDMS window as indicated in figure 3.28 hindering the printing process. In such cases, the cured layer was removed and the prepolymer was further filtered using a paint strainer cone inorder to remove additional cured fragments. The prepolymer was mechanically agitated and the resin tray was cleaned prior to subsequent printing trials. Filtering the resin was mandatory as the cured fragments were observed to hinder the printing process.

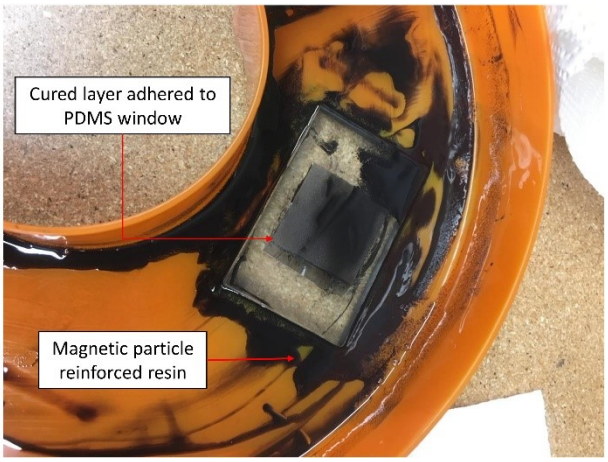

Figure 3.28: Cured layer adhered to the PDMS window

Additionally, attempts towards printing increased filler loadings was accomplished by printing ferromagnetic prepolymer on a cured clear photopolymer layer that acted as a print substrate instead of the aluminum build head as seen in figure 3.29.

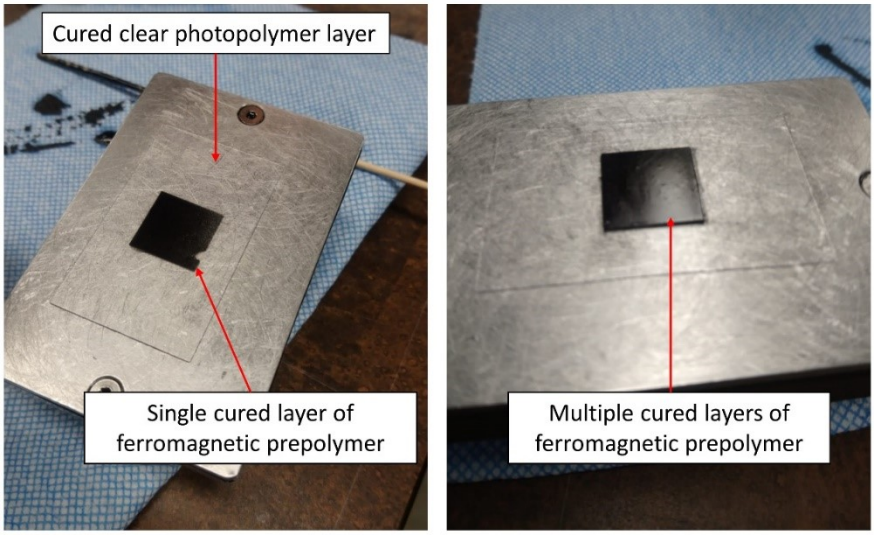

Figure 3.29: Magnetic composite printed on a cured clear photopolymer layer as substrate

Even though, some attempts were successful, layer tearing was still observed in composites printed using resins with higher filler loading.

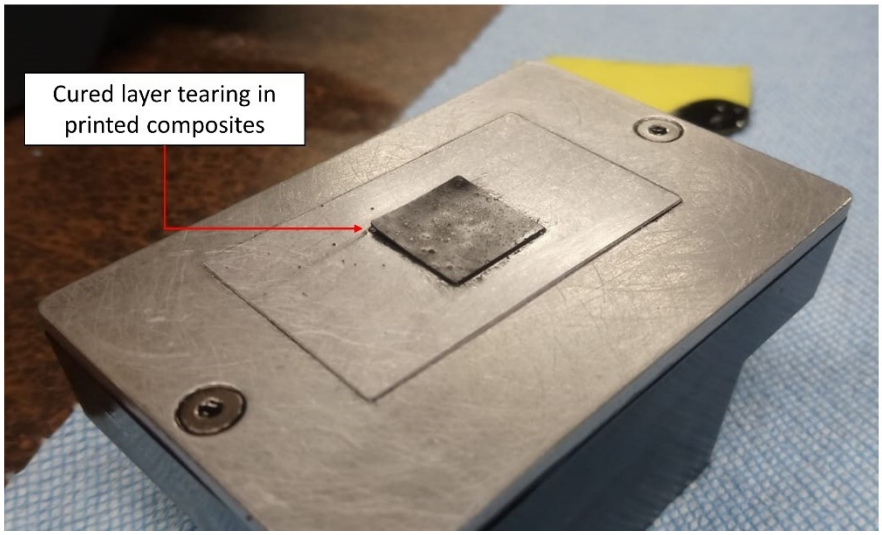

Figure 3.30: Cured layer tearing in printed composite

Additionally, layer sliding was additionally observed in some magnetic composites. This was caused due to process parameter settings that resulted in printer jamming during the printing process.

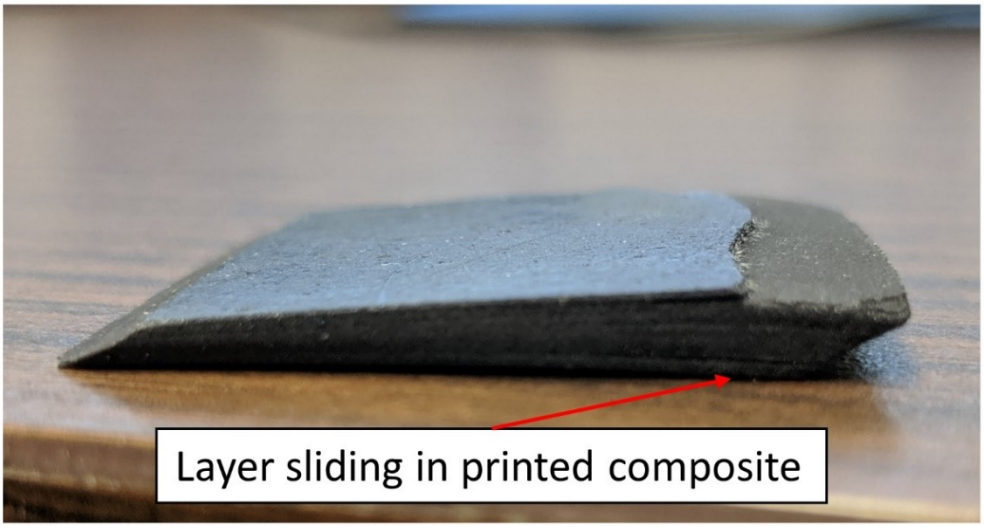

Figure 3.31: Layer sliding observed in printed magnetic composite

Furthermore, removing the cured clear polymer base and the magnetic composite was a significant challenge after the printing process.

3.7 Conclusions

A comprehensive study on the development, characterization, printing and analysis of a magnetic particle reinforced photopolymer resin formulation for a stereolithography 3D printing process was herein presented. Analyzing the thickness variation of magnetic composites printed across different zones on the build head augmented the understanding of the characteristics of the 3D printing equipment and magnetic resin formulations. Based on a Taguchi analysis it was observed that exposure time per projection, layer thickness, and magnetic filler loading significantly influenced the mean thickness of magnetic composites. It was additionally observed that

irrespective of material and process variables, the thickness of printed magnetic composites varied according to a specific pattern, i.e., thickness depended on the printing zone on the build head. Similar to thickness, the width and length of composite parts were additionally evaluated. The width of composite parts was observed to vary in a similar manner as thickness whereas no such pattern was observed for composite part length. The approach adopted to evaluate the curing behavior of ferromagnetic polymer composites enabled understanding the role of constituent materials on curing. The cured depth of photopolymer based ferromagnetic composites was found to increase with increasing UV energy dose. The depth of UV penetration was observed to be highly dependent on magnetic filler loading and additive loading utilized to engineer the formulations suitable for fabrication. The analysis of variance method enabled establishing the order of parameter significance based on Pareto charts and normal plots of standardized effects. This analysis further enabled establishing the critical energy of polymerization required to cure a composite layer of a specific thickness. Utilizing the curing behavior analysis as a reference, exposure parameters were determined for printing formulations engineered with 10 wt% and 25 wt% magnetic filler content. It was observed that for the same filler loading, the exposure time required to cure NdFeB reinforced polymer was less compared to SrFeO reinforced polymer. It was additionally found that a formulation with 25 wt% magnetic filler was printable only by adjusting other machine parameters like the separation/approach slide velocity and Z-axis separation velocity. Even though photopolymer with 25 wt% filler loading was printable, the resulting composites contained defects that elucidate the need for further process parameter analysis in order

to eliminate the observed defects. Tensile tests conducted on samples revealed that NdFeB composites exhibited superior tensile characteristics compared to SrFeO composites at a filler loading of 10 wt%. Utilizing the same exposure parameters for the NdFeB resin, the smallest printable dimensions of the magnetic cantilever structure was 0.13 mm. Overall, this fundamental study enabled understanding the 3D printing characteristics of the developed material formulations and capability of the DLP printer to 3D print magnetic structures with filler loadings up to 25 wt%. Future work will focus on utilizing a robust framework to 3D print magnetic composites eliminating the observed defects and additionally develop strategies to minimize the observed dimensional variations.

3.8 References:

[1] I. Gibson, D. Rosen, and B. Stucker, Additive Manufacturing Technologies. New York, NY: Springer New York, 2015.

[2] P. J. Bartolo, Stereolithography: Materials, Processes and applications. Springer,London, 2011.

[3] J. W. Stansbury and M. J. Idacavage, "3D printing with polymers: Challenges among expanding options and opportunities," Dent. Mater., vol. 32, no. 1, pp. 54–64, 2016.

[4] M. Zarek, M. Layani, I. Cooperstein, E. Sachyani, D. Cohn, and S. Magdassi, "3D Printing: 3D Printing of Shape Memory Polymers for Flexible Electronic Devices (Adv. Mater. 22/2016)," Adv. Mater., vol. 28, no. 22, pp. 4166–4166, Jun. 2016.

[5] A. Mitchell, U. Lafont, M. Hołyńska, and C. Semprimoschnig, "Additive manufacturing — A review of 4D printing and future applications," Addit. Manuf., vol. 24, no. September 2017, pp. 606–626, Dec. 2018.

[6] H. Li, T. J. Flynn, J. C. Nation, J. Kershaw, L. Scott Stephens, and C. A. Trinkle, "Photopatternable NdFeB polymer micromagnets for microfluidics and microrobotics applications," J. Micromechanics Microengineering, vol. 23, no. 6, p. 065002, Jun. 2013.

[7] C. Credi et al., "3D Printing of Cantilever-Type Microstructures by Stereolithography of Ferromagnetic Photopolymers," ACS Appl. Mater. Interfaces, vol. 8, no. 39, pp. 26332–26342, Oct. 2016.

[8] S. J. Leigh, C. P. Purssell, J. Bowen, D. A. Hutchins, J. A. Covington, and D. R. Billson, "A miniature flow sensor fabricated by micro-stereolithography employing a magnetite/acrylic nanocomposite resin," Sensors Actuators A Phys., vol. 168, no. 1, pp. 66–71, Jul. 2011.

[9] N. Löwa, J. Fabert, D. Gutkelch, H. Paysen, O. Kosch, and F. Wiekhorst, "Journal of Magnetism and Magnetic Materials 3D-printing of novel magnetic composites based on magnetic nanoparticles and photopolymers," J. Magn. Magn. Mater., vol. 469, no. September 2018, pp. 456–460, 2019.

[10] R. Domingo-Roca, J. C. Jackson, and J. F. C. Windmill, "3D-printing polymer-based permanent magnets," Mater. Des., vol. 153, pp. 120–128, Sep. 2018.

[11] S. Lantean et al., "3D Printing of Magnetoresponsive Polymeric Materials with Tunable Mechanical and Magnetic Properties by Digital Light Processing," Adv. Mater. Technol., vol. 4, no. 11, p. 1900505, Nov. 2019.

[12] J. J. Martin, B. E. Fiore, and R. M. Erb, "Designing bioinspired composite reinforcement architectures via 3D magnetic printing," Nat. Commun., vol. 6, p. 8641, 2015.

[13] B. Nagarajan, A. F. Eufracio Aguilera, M. Wiechmann, A. J. Qureshi, and P. Mertiny, "Characterization of magnetic particle alignment in photosensitive polymer resin: A preliminary study for additive manufacturing processes," Addit. Manuf., vol. 22, no. May, pp. 528–536, Aug. 2018.

[14] B. Nagarajan, A. F. E. Aguilera, A. Qureshi, and P. Mertiny, “Additive Manufacturing of Magnetically Loaded Polymer Composites: An Experimental Study for Process Development,” in ASME 2017 International Mechanical Engineering Congress and Exposition, 2017, p. V002T02A032-V002T02A032.

[15] B. Nagarajan, M. Arshad, A. Ullah, P. Mertiny, and A. J. Qureshi, “Additive manufacturing ferromagnetic polymers using stereolithography – Materials and process development,” Manuf. Lett., vol. 21, pp. 12–16, Aug. 2019.

[16] P. F. Jacobs, Rapid prototyping & manufacturing: fundamentals of stereolithography. Society of Manufacturing Engineers, 1992.

[17] J. Bennett, “Measuring UV curing parameters of commercial photopolymers used in additive manufacturing,” Addit. Manuf., vol. 18, pp. 203–212, 2017.

[18] A. Boddapati, “Modeling cure depth during photopolymerization of multifunctional acrylates.” Georgia Institute of Technology, 2010.

[19] X. Zhang, X. . Jiang, and C. Sun, “Micro-stereolithography of polymeric and ceramic microstructures,” Sensors Actuators A Phys., vol. 77, no. 2, pp. 149–156, Oct. 1999.

[20] Y. Y. C. Choong, S. Maleksaeedi, H. Eng, P.-C. Su, and J. Wei, “Curing characteristics of shape memory polymers in 3D projection and laser stereolithography,” Virtual Phys. Prototyp., vol. 12, no. 1, pp. 77–84, Jan. 2017.

[21] A. Deka and N. Dey, “Rheological studies of two component high build epoxy and polyurethane based high performance coatings,” J. Coatings Technol. Res., vol. 10, no. 3, pp. 305–315, May 2013.

[22] B. A. Horri, P. Ranganathan, C. Selomulya, and H. Wang, “A new empirical viscosity model for ceramic suspensions,” Chem. Eng. Sci., vol. 66, no. 12, pp. 2798–2806, Jun. 2011.

[23] E. Aznarte Garcia, A. J. Qureshi, and C. Ayranci, “A study on material-process

interaction and optimization for VAT-photopolymerization processes," Rapid Prototyp. J., vol. 24, no. 9, pp. 1479–1485, Nov. 2018.

[24] K. Mostafa, A. J. Qureshi, and C. Montemagno, "Tolerance Control Using Subvoxel Gray-Scale DLP 3D Printing," in Proceedings of the ASME 2017 International Mechanical Engineering Congress and Exposition, 2017.

[25] "ISO 527-1, Plastics — Determination of tensile properties — Part 1: General principles." ISO - International Organization for Standardization, 2019.

[26] V. S. D. Voet et al., "Biobased Acrylate Photocurable Resin Formulation for Stereolithography 3D Printing," ACS Omega, vol. 3, no. 2, pp. 1403–1408, Feb. 2018.

[27] Henderson, G. Robin. Six Sigma Quality Improvement with Minitab, John Wiley & Sons, Incorporated, 2011. ProQuest Ebook Central, https://ebookcentral.proquest.com/lib/ualberta/detail.action?docID=819255.

CHAPTER 4: CHARACTERIZATION OF MAGNETIC PARTICLE ALIGNMENT IN PHOTOSENSITIVE POLYMER RESIN: A PRELIMINARY STUDY FOR ADDITIVE MANUFACTURING PROCESSES

4. Overview of Chapter 4

In Chapter 4, a very fundamental approach is adopted to formulate the needs for developing a material jetting equipment with particle alignment capability. Scientific methods like finite element simulations, optical microscopy coupled with image processing and X-Ray diffraction analysis are utilized to build robust fundamentals towards equipment development. Technical contributions in this chapter include

- Finite element method magnetics simulation to evaluate magnetic flux density distribution for permanent magnet based particle alignment setups
- Development and utilization of an experiment setup to evaluate alignment behavior of magnetic particles dispersed in UV curable polymer in magnetic fields
- Real time optical microscopy coupled with image processing to identify particle alignment strategies and quantify degree of particle alignment
- Characterization of easy axis of magnetization (crystallographic texture) using XRD analysis

4.1 Introduction

Material jetting is an Additive Manufacturing (AM) technique used to create three-dimensional (3D) solid parts by dispensing material from a print head on a substrate. Highly researched areas and most promising materials for future applications

include the printing of polymers, ceramics and metals [1]. Material jetting 3D printing, which is analogous to inkjet printing, is a well-established process utilized to create solid parts by depositing liquid photopolymers using a print head and subsequent curing using ultraviolet (UV) light. Examples of associated printing equipment include the MultiJet (3D Systems, Rock Hill, South Carolina, USA) and PolyJet devices (Stratasys, Eden Prairie, Minnesota, USA), which are capable of depositing materials selectively and subsequent curing to fabricate multi-material parts [2]. In several publications the use of direct inkjet printing for fabricating components from alumina (Al_2O_3) and lead zirconate titanate (PZT) ceramics was demonstrated [3], [4]. Metallic particles suspended in a polymer resin have been used to print components for electrical applications. For example, nano-particulate inks containing gold and copper have been printed successfully utilizing an inkjet printing process [5]. Huang et al. printed gold nanocrystals using an inkjet printer to demonstrate a plastic compatible low resistance conductor technology [6]. Inkjet printing of patterns using copper nanoparticles and subsequent sintering for flexible electronics applications was demonstrated in [7].

Magnetic materials are of great importance for electrical and electronic devices. Inkjet printing of iron oxide (Fe_3O_4) nanoparticles dispersed in a UV curable polymer matrix for electromagnetic applications was reported in [8]. Considering particle alignment, inkjet printing of cobalt-based magnetic nanoparticles with transverse isotropy has already been demonstrated. It has been shown that inkjet printing based AM processes can enable the control of particle orientation in every deposited droplet by the application of a suitable external field. Aligning magnetic particles in the manufacturing process by an external magnetic field promotes the creation of parts with

high permeability. Song et al. utilized an electromagnet type particle alignment configuration to orient magnetic particles in an inkjet printing based AM process [9]. Anisotropy of printed samples and particle orientation along the preferred axis of magnetization were evidenced using hysteresis curve measurements. Similarly, Kokkinis et al. demonstrated the local control of particle orientation in a direct ink writing process using a rotating neodymium permanent magnet [10]. The characterization of anisotropic magnetic particle alignment in the photosensitive polymer resin was accomplished using Fast Fourier Transform (FFT) analysis on time lapsed snapshots of optical microscopic images. Lu and co-workers confirmed the printability of magnetorheological fluid dispersed in UV curable pre-polymers with various particle distributions using a new additive manufacturing process named magnetic field-assisted projection stereolithography [11].

Ferrites belong to the class of hard magnetic materials that are of commercial importance. Ferrites are magnetic metal oxides that contain iron oxide as a principal component. Strontium ferrite ($SrFe_{12}O_{19}$) is a notable permanent magnet material due to its comparatively low cost and wide availability. Apart from making permanent magnets, strontium ferrite finds extensive applications in making inductor cores, magnetic recording media, data storage components and electrical devices operating at microwave/GHz frequencies. Strontium ferrite belongs to the class of M-type hard ferrites, having a hexagonal structure like magnetoplumbite. Strontium ferrite has a preferred axis of magnetization (‘easy axis’) along the crystallographic c-axis, so individual particles will align themselves with the c-axis parallel to an applied magnetic field [12]. Therefore, magnetic measurements yield different values when performed

along the direction of alignment as compared to perpendicular to it. In general, when the magnetic field is applied parallel to the c-axis, saturation magnetization and coercivity are larger at lower applied fields compared to fields applied perpendicular to the c-axis. X-ray diffraction (XRD) can be employed to detect this alignment behavior. Compared to samples with randomly oriented particles, an anisotropic grain or particle orientation in a material is indicated by strong (00*l*) reflections, that is, c-axis alignment in a strontium ferrite composite [13].

In this chapter, the authors delineate the development of a particle alignment configuration using permanent magnets for a material jetting based AM process. The design of the particle alignment setup using Finite Element Method Magnetics (FEMM), the experimental setup development and its capabilities are described in brief. Through experiments with the developed setup, a fundamental understanding of magnetic particle alignment in small droplets of a matrix resin prior to the curing process was established. Anisotropy characterization was performed through image processing and XRD analysis. Furthermore, the behavior of process parameters on anisotropy development was evaluated employing a structured full factorial experiment analysis. Ultimately, the objective of this study is to evaluate the developed particle alignment configuration and provide a fundamental understanding of the fabrication process to ultimately produce cured polymer-based 3D solids with localized particle orientation through a material jetting based AM process.

4.2 Experimental procedures

4.2.1 Materials

For this study, strontium ferrite powder and PR-48 photosensitive polymer resin were purchased from DOWA Electronics Materials Co. Ltd. (Tokyo, Japan) and AUTODESK Inc. (San Rafael, California, USA), respectively. The average particle diameter and volumetric mass density of the magnetic filler as specified by the manufacturers are correspondingly 1.41μm and 3.41g/cm^3.

4.2.2 Scanning electron microscopy

The morphology of the strontium ferrite powder was observed employing scanning electron microscopy (SEM) in a Zeiss EVO M10 SEM (Carl Zeiss AG, Oberkochen, Germany) equipped with a tungsten source thermionic emission unit at an acceleration voltage of 20kV and magnification of 4.52KX. Figure 4.1 shows an SEM image of magnetic filler particles, which do not exhibit any characteristic geometric shape.

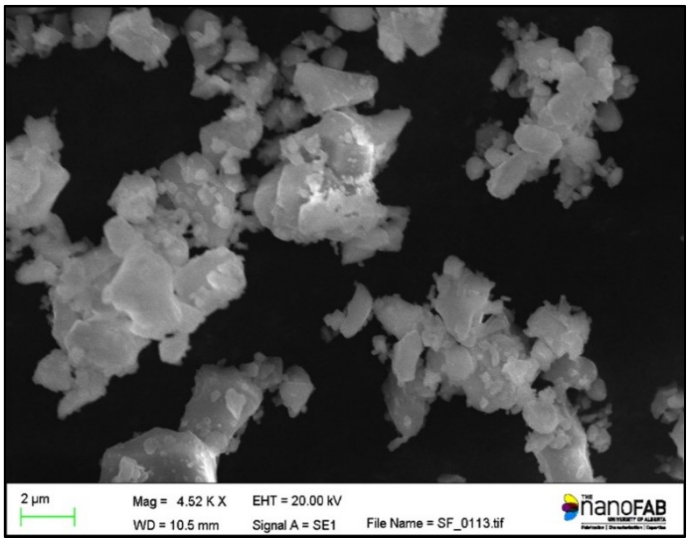

Figure 4.1: SEM image of strontium ferrite powder.

4.2.3 Magnetic field simulation for particle alignment setup

Strontium ferrite particles were aligned within the resin using a pair of cube-shaped N52 grade neodymium permanent magnets purchased from K&J Magnetics Inc. (Pipersville, Pennsylvania, USA). The dimensions of the cube magnets are 9.5mm. The surface field of the sintered cube magnets as specified by the manufacturer is 0.6 Tesla (T). The FEMM software developed by Meeker at QinetiQ North America (Waltham, Massachusetts, USA) was used to simulate the approximate magnetic flux density at the center between the two cube magnets [14]. The input parameters for the analysis were the type and dimension of the cube magnets, the magnetization direction, the distance of separation, and the surrounding medium. The analysis was performed applying open boundary conditions. The alignment configuration using two cube magnets is depicted in Figure 4.2.

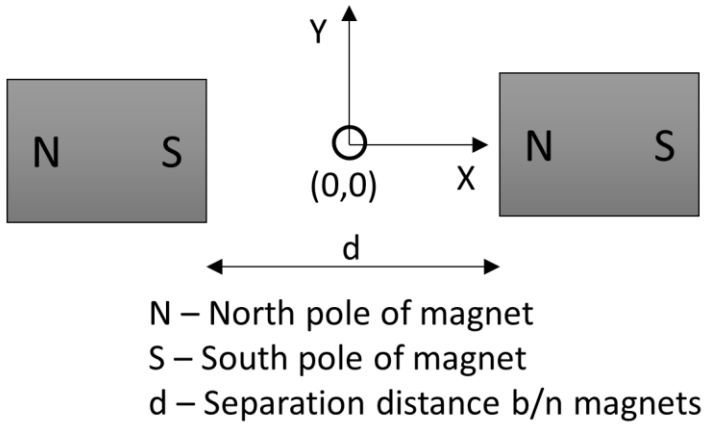

Figure 4.2: Alignment configuration using two cube magnets.

4.2.4 Experimental setup

To carry out the experimental research on filler orientation for additive manufacturing, an experimental setup was developed to enable orientation control of magnetic particles within the photosensitive resin. A computer control system with a

graphical user interface was programmed enabling the operation of the mechanical and electrical components of the setup. The system was based on an Arduino Mega, a printed circuit board manufactured by Arduino (Scarmagno, Italy). Three stepper motors NEMA 14 from Changshou Songyang Machinery & Electronics (Changshou, Jiangsu, China) were used to adjust the distance between the cube magnets and their orientation. Limit switches were used to provide the system with reference positions. In addition, the pair of cube magnets is positioned about a fixed center of rotation. This rotation point is considered with respect to the horizontal plane of the transparent build platform made from pressed polished polyvinyl chloride used to hold the specimen. This enables the magnet faces to be parallel and point toward the center of the specimen tray, irrespective of the angular orientation and the distance that is set between the magnets. For specimen curing, two 10W ultraviolet light-emitting diode emitters with a light wavelength of 405nm were used (model LZA-00UA00, LED Engin Inc., San Jose, California, USA). The developed test setup offers an accuracy of 1mm regarding the distance between the magnets and 2° in terms of rotation.

The conditions for an experiment are set using the graphical user interface. The following parameters are adjustable: distance between the cube magnets, their angular position, time for positioning the magnets to their position, and duration of LED activation. The time parameters were selected to allow for filler particle alignment in the magnetic field and specimen curing.

4.2.5 Filler alignment characterization experiments using real time optical microscopy

To study the effect of the magnetic field on the count of oriented structures and angular orientation, 1wt% strontium ferrite powder was dispersed in PR-48 resin through mechanical mixing at 500 rpm for 10 minutes using an impeller agitator from Calframo Ltd. (Georgian Bluffs, Ontario, Canada). No other additives were added into the particle resin mixture. The strontium ferrite powder was anisotropic and non-magnetized prior to the experiments. Nylon plastic washers with an inner diameter of 5.3mm were placed at the center of the specimen tray to hold the liquid resin mixture within a confined space. The resin mixture was manually deposited using a syringe. The filler alignment prior to resin curing was evaluated by varying the separation distance between the cube magnets and maintaining a constant magnetization time (i.e. the time the cube magnets remained at a specific distance of separation). The components of the experimental setup are detailed in Figure 4.3.

Three different horizontal alignment configurations were studied, denoted as ‘direct cardinal orientation’ (i.e. 0°, see Figure 4.3b), ‘direct angular orientation’, and ‘magnetize and rotate’ (e.g. 30° as shown in Figure 4.3c). For direct cardinal orientation, experiments were conducted for different cube magnet separation distances ranging between 30mm and 60mm. For direct angular orientation, the angular position of the cube magnets was adjusted first, followed by moving the magnets to the desired proximity to the sample. The magnetization time was kept constant at 20 seconds for the cases of direct cardinal orientation and direct angular orientation. For the magnetize and rotate configuration, particles were first magnetized using the direct cardinal

orientation setup at a separation distance of 30mm for 15 seconds, followed by retracting the cube magnets to a separation distance of 90mm. Then, the cube magnets were rotated to the desired angular orientation, and lastly, moved to the final separation distance. The magnetization time after rotation was five seconds. Due to restrictions of the experimental setup, the minimum cube magnet separation distance for all angular orientation configurations was 40mm; the selected maximum distance was 60mm, as for the case of direct cardinal orientation.

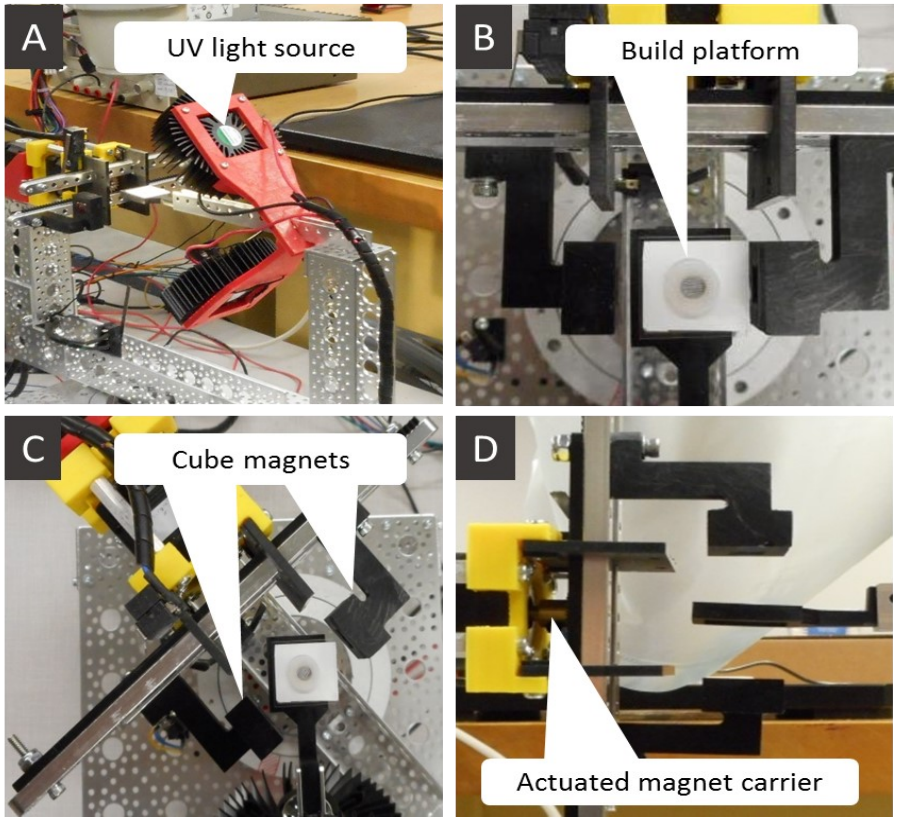

Figure 4.3: Sample fabrication device (A), build platform with cube magnet carrier in direct cardinal orientation (B), 30° angular orientation (C), and vertical orientation to build platform (D).

Real-time optical microscopy was employed to capture images of the samples at 4X magnification. Digital images were enhanced and processed using the 'directionality' feature available in the ImageJ software (National Institute of Mental

Health, Bethesda, Maryland, USA) [15]. The directionality analysis algorithm determines oriented structures in an image using either Fourier component analysis or local gradient orientation techniques.

Resulting data can be compiled to create charts and be used for statistical analyses for the observed oriented structures. Images were acquired with a constant size of 3488x2616 pixels, cropped to 2500x2500 pixels with respect to the image center, converted to grayscale, enhanced, and analyzed for directionality using the local gradient orientation technique implemented in the ImageJ software [16], which employs a 5x5 pixel Sobel filter to derive the local gradient orientation. Resulting data was compiled into graphs with abscissa values ranging from negative 90° to positive 90° for the particle orientation, and an ordinate displaying the count of oriented structures. Presumably, the image analysis of oriented structures exposes a peak in a depicted curve at the respective orientation angle whereas isotropic samples produce results in the form of a flat curve. Hence, for the present study, the degree of directionality was assessed from the presence of a peak and its broadness in plotted curves.

4.2.6 XRD analysis for c-axis alignment

In addition to image analysis, anisotropy characterization was performed through preferred orientation analysis using XRD. For this analysis, 2wt% strontium ferrite filler was dispersed in the resin by mechanical mixing. Samples were prepared by manually dispensing a single droplet of the mixture within a washer, followed by curing for 180 seconds under ultraviolet light. Particle alignment in specimens prepared for XRD analysis occurred in vertical direction, i.e. perpendicular to the build platform,

employing the direct angular orientation conditions and separation distances of 30mm, 40mm and 50mm (see Figure 4.3d). XRD measurements were performed by a Geigerflex 2173 diffractometer (Rigaku Corporation, Tokyo, Japan). The diffractometer is fitted with a Co-tube as an X-ray source and a graphite monochromator to filter K-beta wavelength. Tests were performed at 38kV and 38mA, and samples were scanned over 2θ ranging from 30° to 70° at a rate of 2°/min. First, bulk magnetic powder was analyzed, in part, to find the incident angles for the (008) crystallographic plane. Three samples were cured at separation distances as specified above. For comparison, a single sample, designated as 'isotropic specimen', was cured without applying the magnetic field. In another study [17], XRD measurements of thin films revealed that the (008) peak is most prominent for films with strontium ferrite crystals oriented normal to the film surface, while it is shallow for randomly oriented specimens. In randomly oriented strontium ferrite thin films, the (114) and (203) peaks were significantly enhanced compared to the (008) peak. In the present work, the intensity, *I*, of the (008) peak for samples oriented at different separation distances was assessed with respect to the isotropic sample using the intensity ratio *R* defined in Eq.4.1.

$$R_{008} = \frac{I_{008}(aligned)}{I_{008}(isotropic)} \tag{4.1}$$

4.2.7 Influence of process parameters: Full factorial combination experiments

Once a basic understanding of the anisotropy characteristics of fabricated samples was obtained through image processing and XRD, an assessment of the influence of process parameters, i.e., separation distance between cube magnets and magnetization time, was performed constructing a full factorial experiment design

using the Minitab statistical software (State College, Pennsylvania, USA). By varying both the separation distance between the cube magnets and the magnetization time, experiments were conducted to evaluate the count of oriented structures for the case of direct cardinal orientation using the described digital image filler alignment characterization method. Table 4.1 shows the process parameters and corresponding selected levels.

Table 4.1: Factors and levels selected for experimental analysis.

Level	Magnetization time (s)	Separation distance (mm)
1	3	30
2	6	37
3	9	44
4	12	51

Using the Minitab software, different process parameter combinations were generated. Considering two process parameters and four levels, the total number of experiments in this setup was 16. Experiments were performed randomly in triplicate. The objective of the experiments was to explore the effects of individual process parameters and to identify the process parameter combination that resulted in the higher count of oriented structures. The main effects plot derived from the average of the responses was used to elucidate the behavior of the process parameters. In this research, a high value for the count of oriented structures was desired and ultimately used as the criterion to select the final process parameters.

4.3 Results and discussion

4.3.1 Particle alignment configuration design and analysis using FEMM

In this section, results from the FEMM software used to design and evaluate the particle alignment configuration are described. The FEMM simulation indicated the existence of a dipole field between the two cube magnets. Results from the FEMM simulation, depicted in Figure 4.4, indicate an exponential decrease in magnetic flux density with increasing separation distance between the cube magnets.

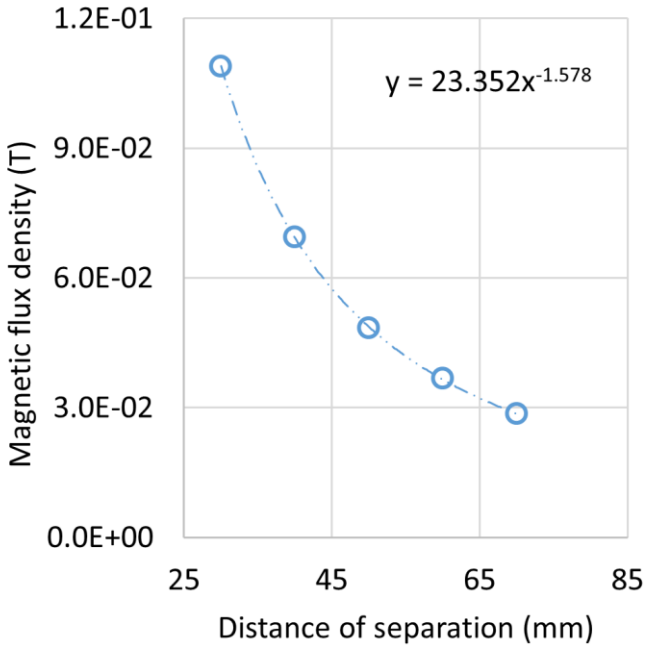

Figure 4.4: FEMM predictions for magnetic flux density at the center between two cube magnets with respect to their separation distance.

For example, the magnetic flux density at a separation distance of 70mm is reduced by 74% compared to the flux density at 30mm. From the simulation results, a correlation between the cube magnet separation distance, d (in millimeters), and the approximate magnitude of magnetic flux density, B (in Tesla), acting on a droplet sample location was established, as described by Eq. 4.2. Values for the magnetic flux

density along the *x*- and *y*-axes were derived from the simulation results starting from the center point O (see Figure. 4.2 for coordinates).

It was presumed that the magnetic flux density reaches a value equivalent to the surface flux density of the cube magnet along the *x*-axis and reduces to zero at a point along the *y*-axis. As depicted in Figure 4.5, the FEMM simulation confirmed this presumption, i.e. along the *x*-axis, the magnetic flux density between two cube permanent magnets increases from 0.1 Tesla at the center point O to 0.6 Tesla near the magnet face. The latter is equivalent to the cube magnet surface field. Along the *y*-axis, the magnetic flux density decreases from 0.1 Tesla at the center point O to zero at approximately 22mm.

$$B = 23.352\ (d)^{-1.578} \tag{4.2}$$

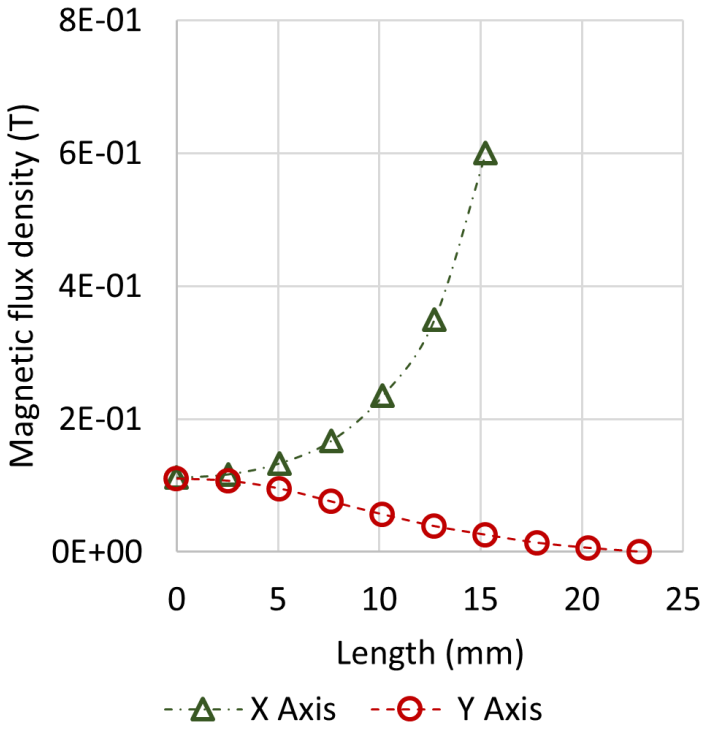

Figure 4.5: FEMM predictions for magnetic flux density along the x- and y-axes for a cube magnet separation distance of 30mm.

4.3.2 Optical microscopy study of aligned filler morphology

In this study, fundamental capabilities of the experimental setup were evaluated using optical microscopy, image processing and XRD analysis. Using real-time optical microscopy, it was possible to capture and assess the magnetic filler alignment within the resin prior to the curing process. Observed microstructures for direct cardinal orientation (i.e.~ 0°) are presented in the images in Figure 4.6.

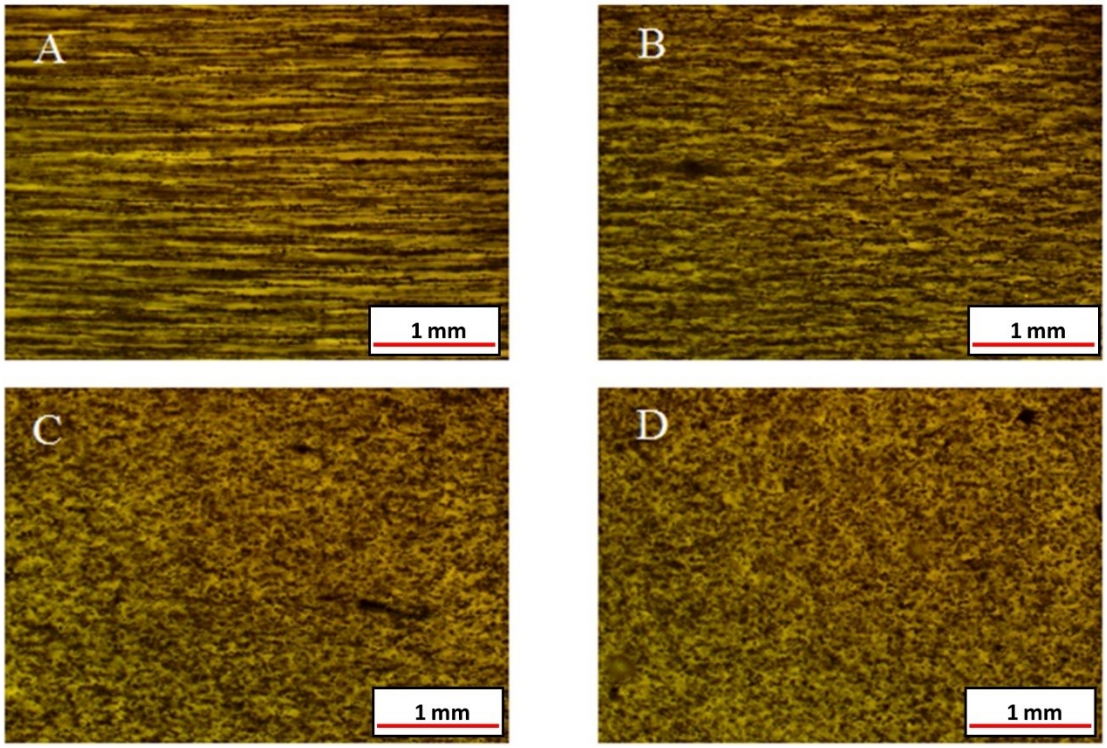

Figure 4.6: Micrographs of filler particles in liquid resin at a separation distance of (A) 30mm (~0.11 T), (B) 40 mm (~0.07 T), (C) 50 mm (~0.05 T), and (D) 60mm (~0.04 T), for case direct cardinal orientation (0°).

Presumably, the strontium ferrite particles behaved like individual magnetic dipoles under the influence of the applied magnetic field, and hence, the particles formed chain-like microstructures. The development of distinct chain structures depended on the magnetic flux density that varied with separation distance. For the

case of direct cardinal orientation, the separation distance was varied from 30 mm to 60 mm in steps of 10 mm. The formation of continuous chains was observed in the form of distinct striations at the closest separation distance of 30mm. The linkage of particles and formation of distinct continuous chains diminished with increasing cube magnet separation distance, and thus, magnetic flux density. Conducting image analysis using the 'directionality' feature in the ImageJ software yielded the directionality graph shown in Figure 4.7.

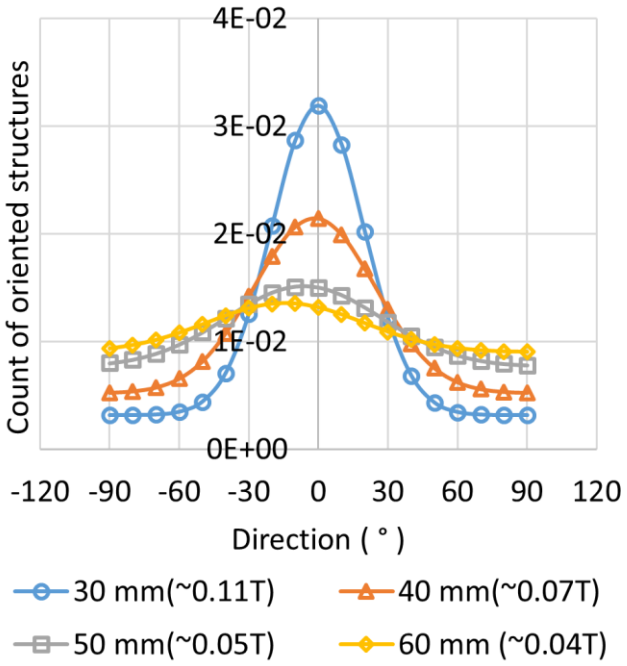

Figure 4.7: Filler directionality analysis data for the case direct cardinal orientation.

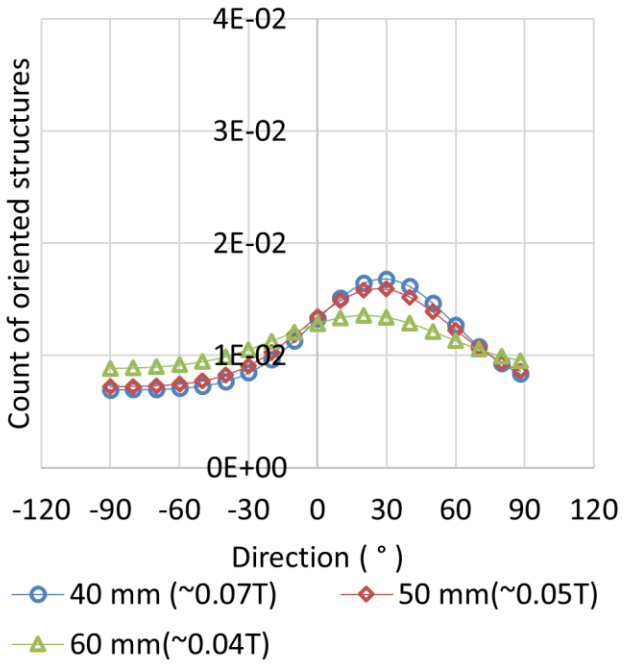

Figure 4.8: Filler directionality analysis data for the case direct angular orientation.

The data, following a bell curve shape, indicates a significant influence of the magnetic flux density, being a function of cube magnet separation distance, on particle alignment; that is, a greater number of particles is aligned in the 0° direction along with a decreasing deviation from the mean. Similar tests were conducted for the case of direct angular orientation (i.e. the cube magnets were rotated to the desired angular position of 30°, followed by setting the separation distance). The experimental results shown in Figure 4.8 exhibit similarities to the case of direct cardinal orientation; that is, with increasing magnetic flux density a greater number of particles aligned in the set magnet direction (30° in this case).

Finally, the case of magnetize and rotate was studied for a final angle of rotation of 30° and separation distances of 40 mm, 50 mm and 60 mm. Notably, it appears that

the magnetize and rotate process yielded significant enhancements in filler alignment compared to the case of direct angular orientation.

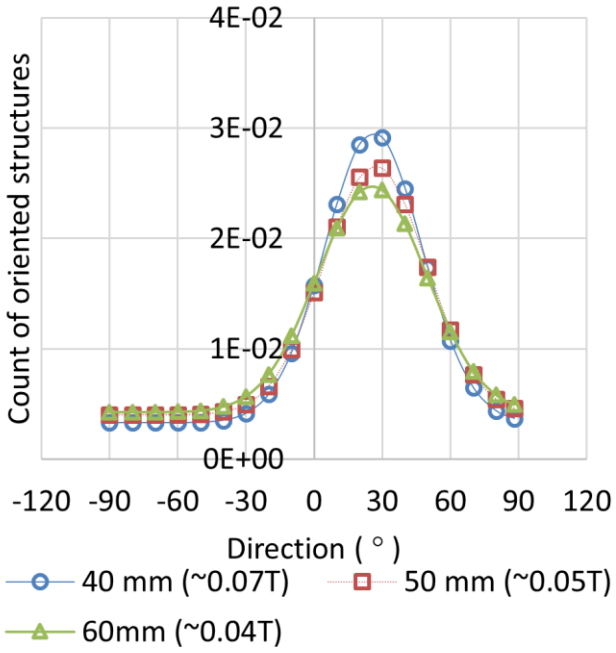

Figure 4.9: Filler directionality analysis data for the case magnetize and rotate.

As shown in Figure 4.9, the case of magnetize and rotate yielded a greater count of oriented structures in the set direction of 30° with a decreased deviation from the mean as compared to the case of direct angular orientation. Moreover, the data depicted in Figure 4.9 indicates a comparatively small decrease in the count of oriented structures with increasing separation distance of the cube magnets.

To further explore the differences between the cases of direct angular orientation and magnetize and rotate, respective microstructures of fillers in resin are presented in Figure 4.10 for alignment angles of 30°, -30°, 45° and -45°. It can be observed that striations formed by aligned particles are more distinct and prominent for magnetize and rotate than direct angular orientation. Directionality curves for the above

alignment angles for the cases of magnetize and rotate and direct angular orientation are shown in Figure 4.11 and 4.12, respectively. Comparatively sharp peaks can be observed for the case of magnetize and rotate while peaks for the direct angular orientation case are rather broad. These observations suggest that in the magnetize and rotate case, strong particle alignment was achieved during the initial magnetization phase at a high magnetic flux density (at 0° and low separation distance of 30mm), which was preserved during the subsequent field reorientation with a reduced magnetic field strength.

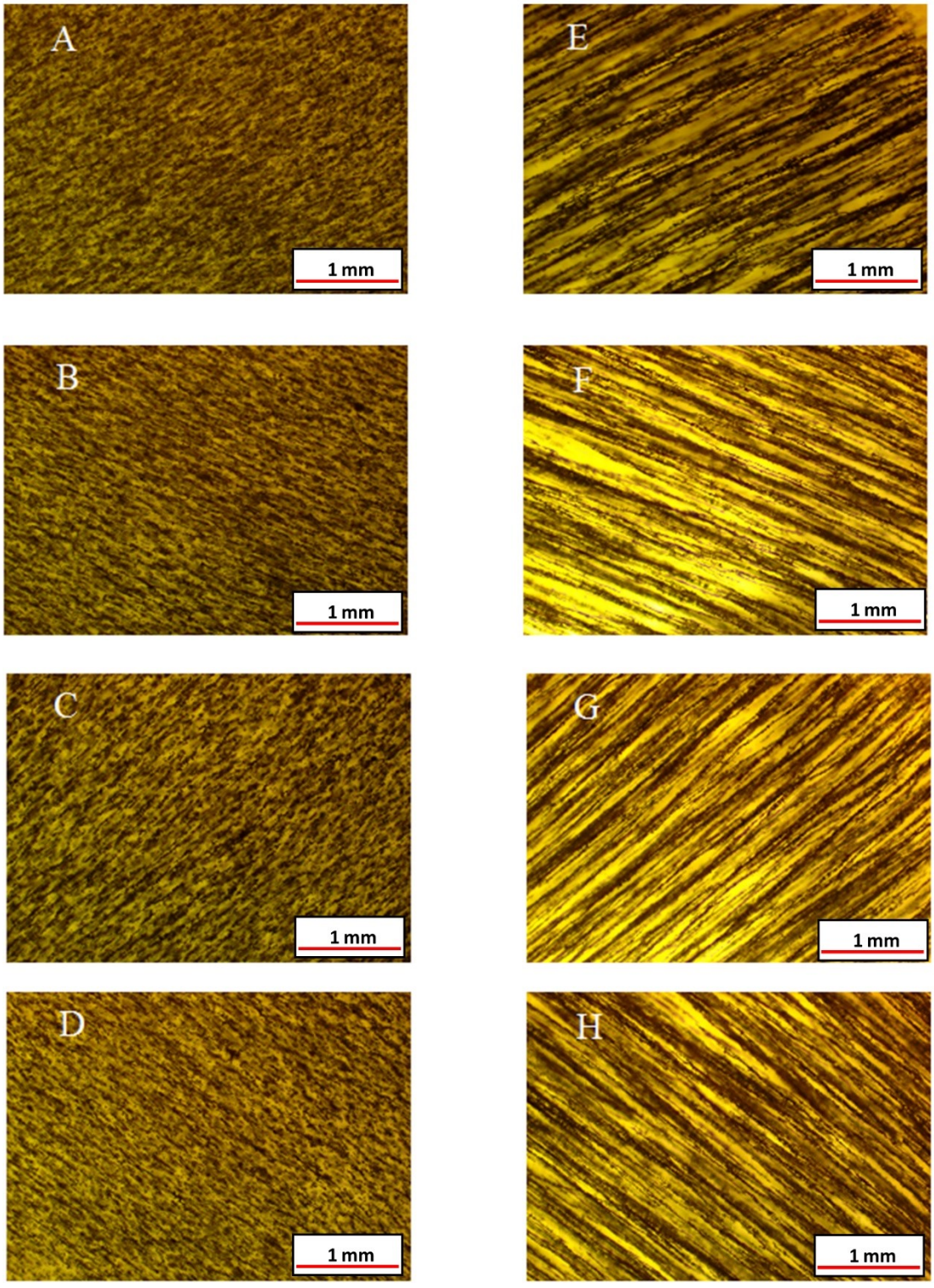

Figure 4.10: Micrographs of filler particles in liquid resin for the cases direct angular orientation (left column) and magnetize and rotate (right column) with angular orientations of 30° (A,E), -30° (B,F), 45° (C,G), -45° (D,H).

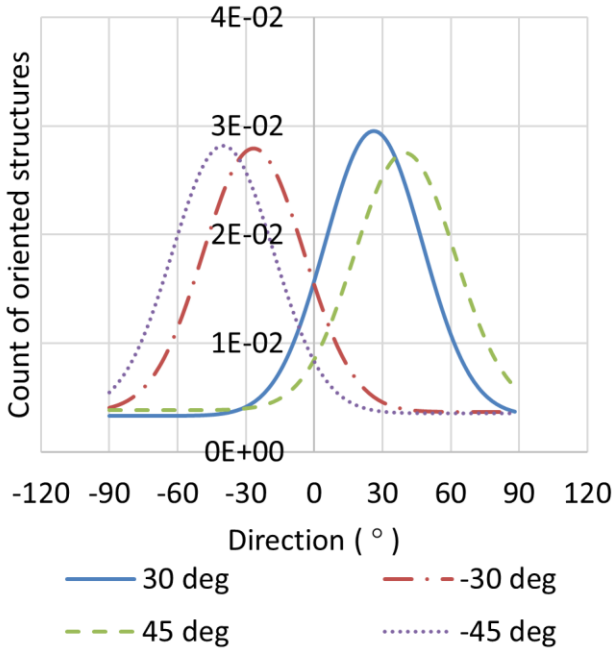

Figure 4.11: Filler directionality analysis data for multiple angle orientations for the magnetize and rotate configuration.

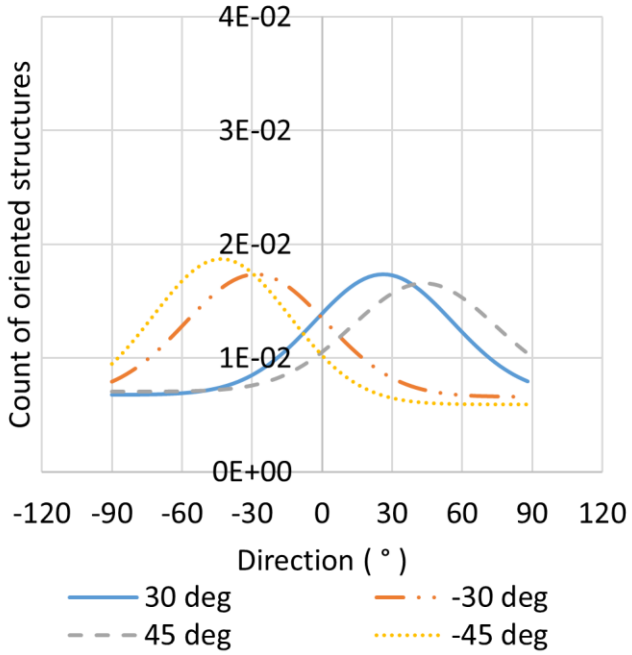

Figure 4.12: Filler directionality analysis data for multiple angle orientations for the direct angular orientation configuration.

4.3.3 XRD analysis of bulk magnetic filler and filler modified composites

The XRD diffraction peaks obtained for bulk magnetic powder confirmed the material to be strontium iron oxide (also known as strontium dodecairon nonadecaoxide) with $SrFe_{12}O_{19}$ as the chemical formula. The diffraction peak for (008) crystallographic plane was observed at a 2θ incident angle of 36.18°. XRD results for 2θ incident angles ranging between 30° and 45° are presented in Figures 4.13 and 4.14 for resin specimens that were cured with fillers being aligned perpendicular to the build platform and an isotropic sample, respectively. Intensity ratios as defined by Eq.4.1 are depicted in Figure 4.15, which indicate a decrease in intensity ratio for increasing cube magnet separation distance.

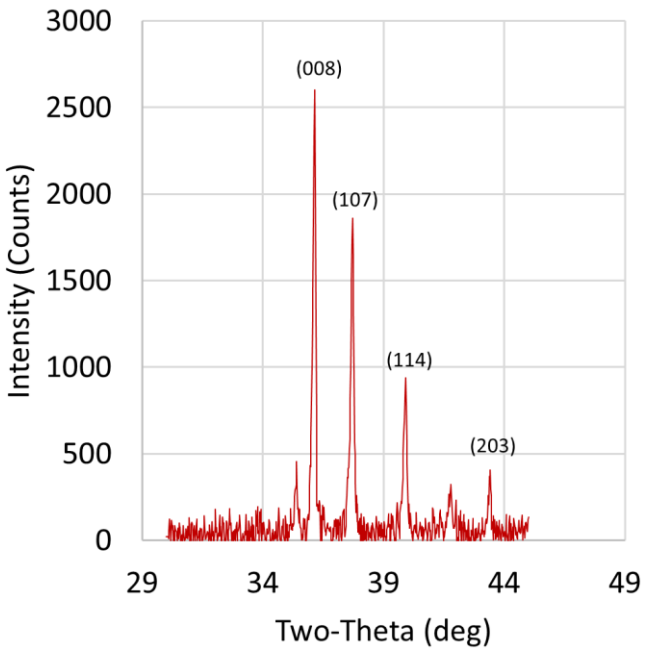

Figure 4.13: XRD analysis data for the anisotropic filler composite sample.

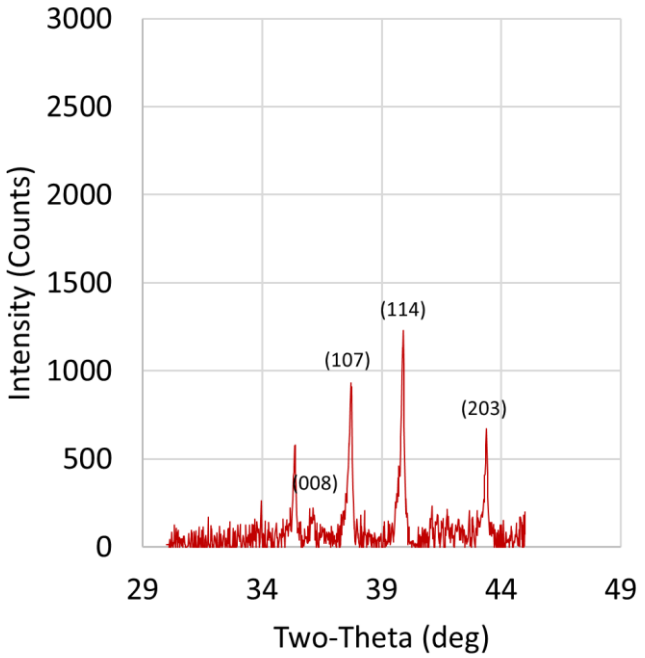

Figure 4.14: XRD analysis data for the isotropic filler composite sample.

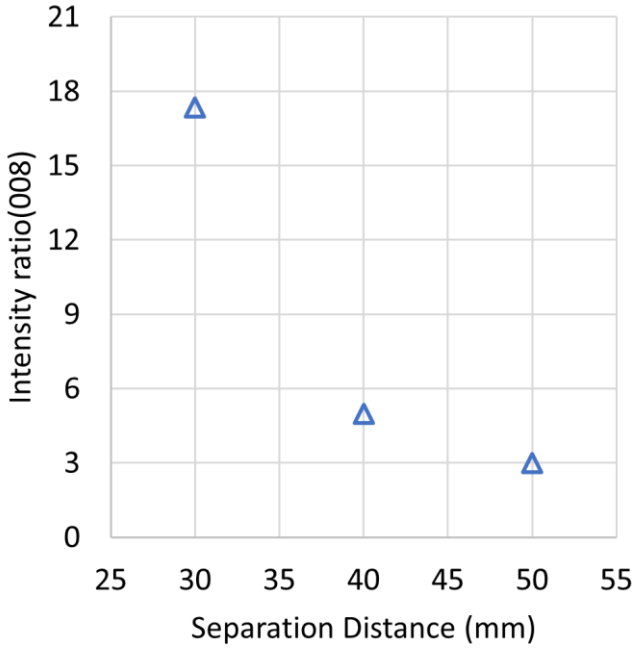

Figure 4.15: (008) peak intensity ratios for different cube magnet separation distances.

The (008) peak in Figure 4.13 for the anisotropic sample is approximately 17 times greater than the corresponding peak for the isotropic sample in Figure 4.14, as

determined using Eq.4.1. The strongly increased (008) peak intensity of the anisotropic sample is indicative of significant filler c-axis alignment in the magnetization direction. For the isotropic sample (with randomly oriented particles), greater intensity of the (114) and (203) peaks can be observed as compared to the anisotropic sample, which is congruent to observations by Koleva and co-workers [11]. XRD results thus corroborate that significant filler alignment is achievable with the developed experimental setup.

4.3.4 Influence of process parameters: Full factorial experiments

This section presents the combined effect of process parameters listed in Table 4.1 on the count of oriented structures for the case direct cardinal orientation. The objective of the analysis was to find the process parameter combination that resulted in higher count of oriented structures in directionality analysis, therefore defined as the response variable. The fitted means from the experimental results were used to create the main effects plot using the Minitab statistical software as shown in Figure 4.16. An approximately linear increase in the count of oriented structures with comparatively low gradient was observed with increasing magnetization time, *t*, which indicates that there is adequate time for particles to rotate and interact to form chain structures. With respect to separation distance, the count of oriented structures decreased greatly with the increase of this parameter, given that separation distance is associated with an exponential decrease in magnetic flux density. From the main effects plot, it was concluded that cube magnet separation distance, that is, the magnetic flux density acting on the magnetic filler particles, is the most important process parameter influencing the response variable. It was further established that a cube magnet

separation distance of 30mm and a magnetization time of 12 seconds provide the greatest effect on the count of oriented structures for the developed experimental setup.

A Pareto chart was derived considering the individual process parameters and a single interaction term to determine the magnitude of their effects on the count of oriented structures, *C*. The Pareto chart shown in Figure 4.17 indicates that the separation distance, *d* (factor B in this chart indicated by the acronym 'SDS') between the cube magnets has the maximum influence on count of oriented structures followed by magnetization time, *t* (factor A 'MTS') and the interaction between the two process parameters (factor AB). Bars crossing the (red) reference line at 2.04 indicates that all included terms have statistically significance on the count of oriented structures (factors are significant at a 0.05 level).

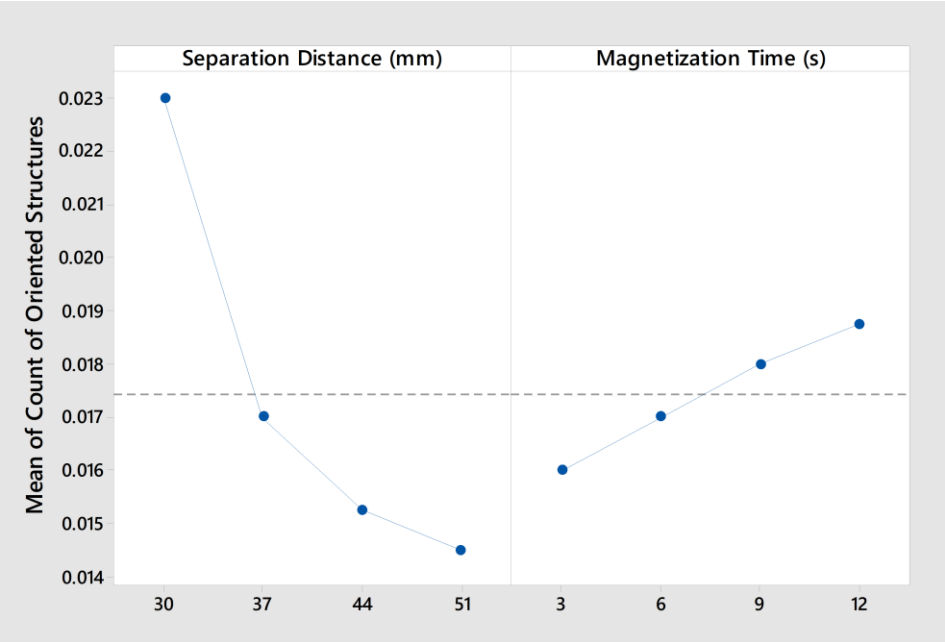

Figure 4.16: Main effects plot for count of oriented structures (fitted means) with respect to magnetization time and separation distance.

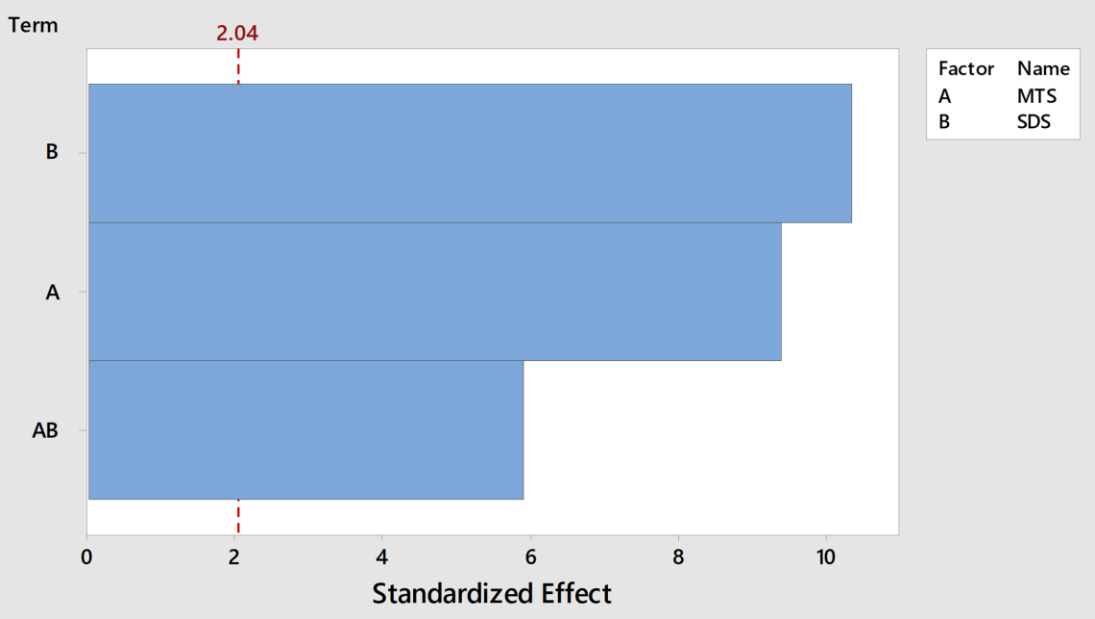

Figure 4.17: Pareto chart depicting absolute values of the standardized effects. The response is the count of oriented structures. Factors are significant at a 0.05 level.

The resultant data of the full factorial experiment was fitted to an equation including interaction and quadratic terms as shown in Eq.(4.3).

$$C = 6.228 \times 10^{2} + t \times 1.481 \times 10^{-3} - d \times 2.239 \times 10^{-3} + d^{2} \times 2.5 \times 10^{-5} - d \times t \times 2.8 \times 10^{-5} \quad (4.3)$$

The coefficient of determination (R^2) for the above equation was observed to be 93.7%. Considering a model equation without interaction terms the coefficient of determination (R^2) was 78.4%, which is 15.3% lower than the model with interaction terms. This signifies that the count of oriented structures is additionally influenced by the interaction among the two process parameters considered in this initial experiment. A detailed design of experiment analysis studying the statistical significance of the process parameters will be undertaken in future studies.

4.4 Additional results

4.4.1 Development of a permanent magnet array and comparison with two cube system

Alignment configurations to orient magnetic particles were designed using cube shaped N52 grade neodymium permanent magnets. The dimensions of the selected cube magnets were 9.5 mm. The surface field of the sintered cube magnets as specified by the manufacturer is 0.6 Tesla (T). The Finite Element Method Magnetics (FEMM) software developed by David Meeker at QinetiQ North America (Waltham, Massachusetts, USA) was used to evaluate the approximate magnetic flux density at the center between the cube magnets.

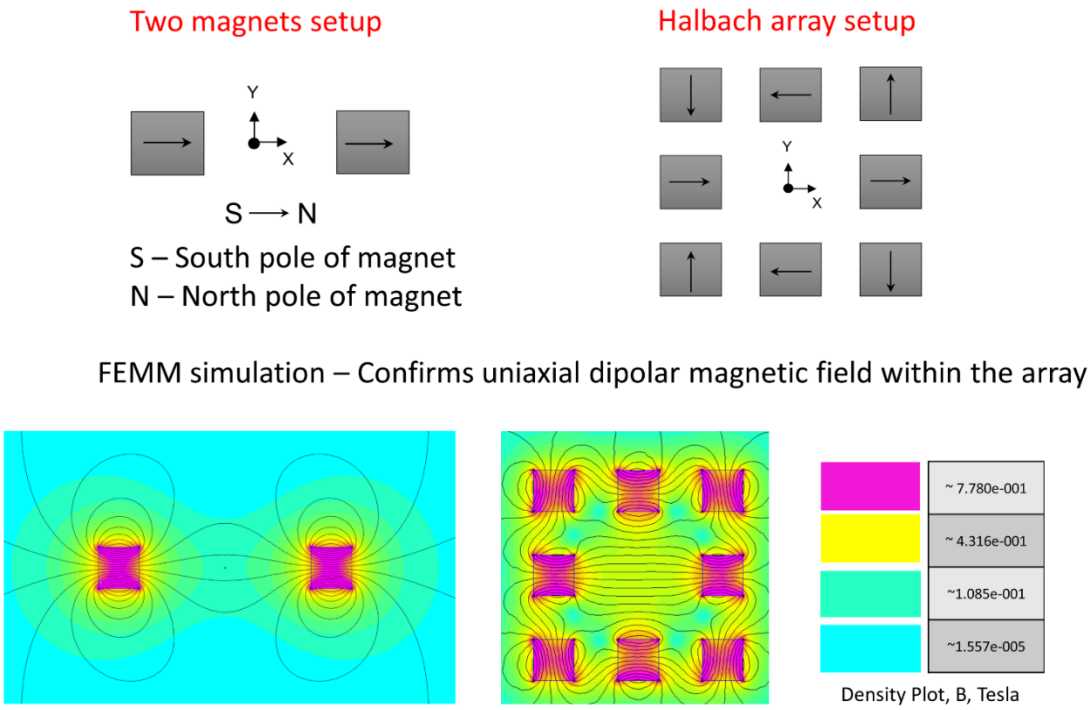

Figure 4.18: Developed alignment configurations and FEMM modelling results.

Two different alignment configurations were modelled and analyzed. The Type 1 configuration was a two-cube shaped permanent magnet system with opposite polarities of the magnets facing each other, whereas the Type 2 configuration was a

combination of eight magnets placed in a Halbach array [1]. Input parameters for the analysis were the type and dimension of the cube magnets, magnetization direction, distance of separation, and properties of the surrounding medium. The alignment configurations designed and analyzed using FEMM software are depicted in Figure 4.18. FEMM simulation results indicated the existence of a dipolar field in both the alignment configurations. Then, magnetic flux density at the center within the Halbach array was compared to the two-cube magnet alignment configuration for a separation distance of 30 mm. The Halbach array configuration provides a flux density enhancement by 0.21 Tesla over the two-cube magnet alignment configuration. The flux density predictions are presented in Figure 4.19

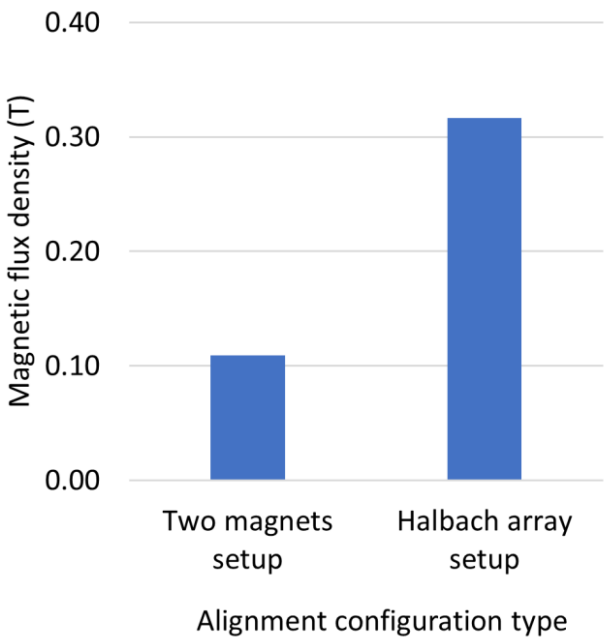

Figure 4.19: FEMM comparison for two-cube and Halbach array.

4.4.2 Proof of concept optical microscopy within magnetic array

Permanent magnets were embedded inside a 3D printed fixture according the orientation configuration observed in Figure 4.20.

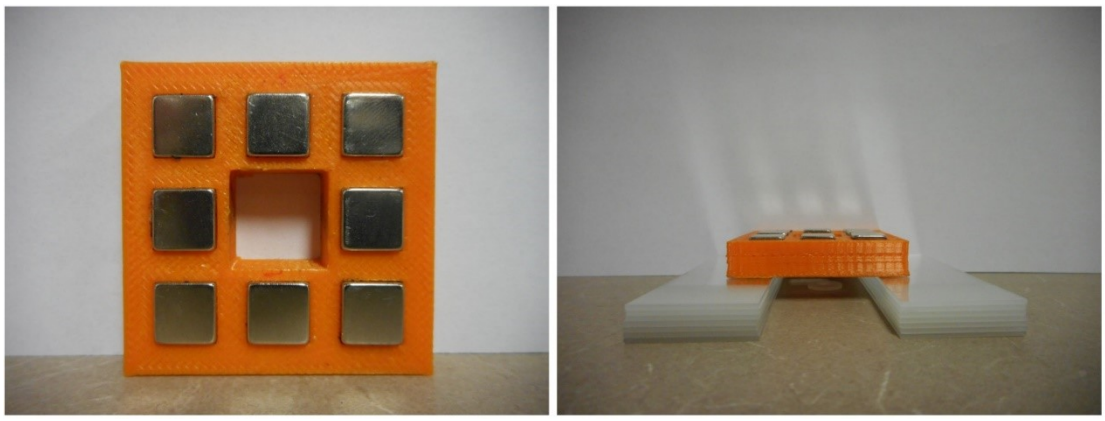

Figure 4.20: Magnetic array developed using permanent magnets embedded in 3D printed fixture.

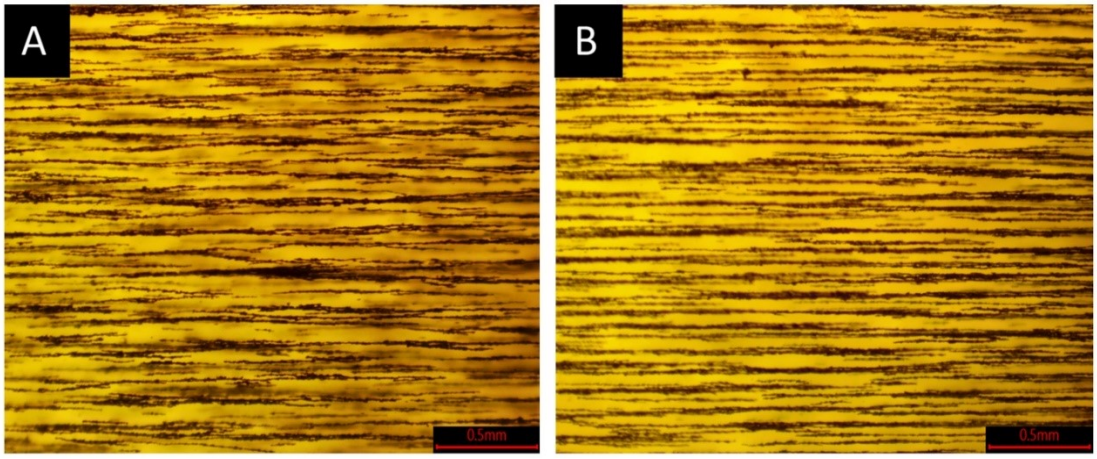

Figure 4.21: Proof of concept optical microscopy within the magnetic array A) height from substrate is 5 mm B) height from substrate is 15 mm.

4.4.3 Realization of another additive to mitigate particle settling

Apart from BYK 7410 ET which enabled controlling particle settling in UV curable formulation, another additive Disparlon 6900-20X was additionally tested for its capability.

Figure 4.22: Photographs of magnetic filler settling experiments, taken at (1) immediately, (2) 3 hours, and (3) 24 hours after filling the test tubes. (A) 0wt% rheological additive, (B) 0.5wt% BYK 7410 ET, (C) 2wt% BYK7410 ET, (D) 0.5wt% Disparlon 6900-20X, (E) 2wt% Disparlon 6900-20X.

4.5 Conclusions

In this fundamental study, an experimental setup was built to investigate the alignment and orientation of randomly shaped hard magnetic particles in a photosensitive polymer matrix using an external magnetic field created by a pair of

permanent (cube) magnets. The experiments successfully demonstrated that alignment and orientation of strontium ferrite particles in the polymer can be achieved in a controlled manner using the permanent magnet dipole field. Using real-time optical microscopy, the interaction of magnetic fillers and the formation of continuous chain like microstructures was evidenced. Image analysis of liquid resin composites subjected to constant magnetization time demonstrated a significant increase in the count of oriented structures with decreasing separation distance between the permanent magnets. FEMM predicted an exponentially diminishing magnetic flux density with increasing magnet pair separation distance. It was demonstrated that an initial particle magnetization at the minimum permanent magnet proximity and thus maximum magnetic flux density, followed by particle reorientation at a high magnet separation distance yielded superior results as compared to reorienting particles directly for a range of intermediate field strengths. Particle interactions and the formation of chain-like microstructures created during the initial magnetization phase was significant and enabled the rotation of formed chains even at low magnetic flux densities. In magnetized and cured polymer composite samples, XRD analyses confirmed significant c-axis alignment of strontium ferrite particles as compared to samples with randomly oriented filler. A main effects analysis employing a full factorial design revealed that the permanent magnet separation distance had the most significant influence on filler alignment rather than magnetization time. From the information gathered through the present study, it was concluded that a permanent magnet dipole field is a suitable means for constructing a device for aligning magnetic particles for material jetting 3D printing.

4.6 References

[1] I. Gibson, D. Rosen, and B. Stucker, *Additive Manufacturing Technologies*. New York, NY: Springer New York, 2015.

[2] Y. L. Yap, C. Wang, S. L. Sing, V. Dikshit, W. Y. Yeong, and J. Wei, "Material jetting additive manufacturing: An experimental study using designed metrological benchmarks," *Precis. Eng.*, vol. 50, pp. 275–285, Oct. 2017.

[3] C. Ainsley, N. Reis, and B. Derby, "Freeform fabrication by controlled droplet deposition of powder filled melts," *J. Mater. Sci.*, vol. 37, no. 15, pp. 3155–3161, 2002.

[4] T. Wang and B. Derby, "Ink-jet printing and sintering of PZT," *J. Am. Ceram. Soc.*, vol. 88, no. 8, pp. 2053–2058, 2005.

[5] G. M. Hutchings, Ian M., "Inkjet Technology for Digital Fabrication," in *John Wiley & Sons*, 2012.

[6] D. Huang, F. Liao, S. Molesa, D. Redinger, and V. Subramanian, "Plastic-Compatible Low Resistance Printable Gold Nanoparticle Conductors for Flexible Electronics," *J. Electrochem. Soc.*, vol. 150, no. 7, p. G412, 2003.

[7] S. Jang, Y. Seo, J. Choi, T. Kim, J. Cho, S. Kim, and D. Kim, "Sintering of inkjet printed copper nanoparticles for flexible electronics," *Scr. Mater.*, vol. 62, no. 5, pp. 258–261, Mar. 2010.

[8] E. Saleh, P. Woolliams, B. Clarke, A. Gregory, S. Greedy, C. Smartt, R. Wildman, I. Ashcroft, R. Hague, P. Dickens, and C. Tuck, "3D inkjet-printed UV-curable inks for multi-functional electromagnetic applications," *Addit. Manuf.*, vol. 13, pp. 143–148, Jan. 2017.

[9] H. Song, J. Spencer, A. Jander, J. Nielsen, J. Stasiak, V. Kasperchik, and P. Dhagat, "Inkjet printing of magnetic materials with aligned anisotropy," *J. Appl. Phys.*, vol. 115, no. 17, p. 17E308, May 2014.

[10] D. Kokkinis, M. Schaffner, and A. R. Studart, "Multimaterial magnetically assisted 3D printing of composite materials," *Nat. Commun.*, vol. 6, p. 8643, 2015.

[11] L. Lu, E. Baynojir Joyee, and Y. Pan, "Correlation Between Microscale

Magnetic Particle Distribution and Magnetic-Field-Responsive Performance of Three-Dimensional Printed Composites," *J. Micro Nano-Manufacturing*, vol. 6, no. 1, p. 10904, Dec. 2017.

[12] R. C. Pullar, "Hexagonal ferrites: A review of the synthesis, properties and applications of hexaferrite ceramics," *Prog. Mater. Sci.*, vol. 57, no. 7, pp. 1191–1334, Sep. 2012.

[13] M. Sardela, *Practical Materials Characterization*. New York, NY: Springer New York, 2014.

[14] "Meeker, David. 'Finite element method magnetics.' FEMM 4 (2010): 32. http://www.femm.info/wiki/Documentation/," vol. 4, p. 2010, 2010.

[15] J.-Y. Tinevez, "Directionality plugin for Fiji ImageJ." [Online]. Available: https://imagej.net/Directionality.

[16] J. Schindelin, I. Arganda-Carreras, E. Frise, V. Kaynig, M. Longair, T. Pietzsch, S. Preibisch, C. Rueden, S. Saalfeld, B. Schmid, J.-Y. Tinevez, D. J. White, V. Hartenstein, K. Eliceiri, P. Tomancak, and A. Cardona, "Fiji: an open-source platform for biological-image analysis," *Nat. Methods*, vol. 9, no. 7, pp. 676–682, Jun. 2012.

[17] M. E. Koleva, S. Zotova, P. A. Atanasov, R. I. Tomov, and C. Ristoscu, "Sr-ferrite thin films grown on sapphire by pulsed laser deposition," *Appl. Surf. Sci.*, vol. 168, pp. 108–113, 2000.

CHAPTER 5: RHEOLOGY ASSISTED MICROSTRUCTURE CONTROL FOR PRINTING MAGNETIC COMPOSITES – MATERIAL AND PROCESS DEVELOPMENT

5. Overview of Chapter 5

In the present chapter, a scientific approach was carefully implemented to create magnetic polymer composite structures with desired microstructure by engineering material formulations. The material formulations were engineered to suit material jetting additive manufacturing process and tested for their capability to enable fabricating magnetic composites with isotropic and anisotropic magnetic particle distributions. Rheometry, optical microscopy and magnetic characterization were utilized to characterize the developed formulations and composites. Technical contributions in this chapter include

- Characterization of rheological and thixotropic properties of the developed formulations
- Utilizing models from the technical literature to derive formulation properties
- Analyzing particle aggregation in photopolymer suspensions and providing solutions to mitigate particle aggregation
- Development of new manufacturing schemes through component re-designs, and programming new printing and curing schemes
- Evaluation of particle alignment as a function of formulation viscosity
- Characterization of magnetic properties along and perpendicular to the direction of particle structuring

5.1 **Introduction**

Material jetting is an additive manufacturing process where three-dimensional solid parts are manufactured by dispensing polymeric material from a print head and subsequently solidifying them utilizing ultraviolet light or thermal curing methodologies. Material jetting employing photopolymerization is similar to stereolithography, where acrylate type photopolymers are deposited and exposed to ultraviolet light. Promising material systems for future applications include polymers, ceramics and metals. Factors that mutually influence the material jetting process are machine and material parameters, including liquid material viscosity, shear thinning effects and surface tension, print head nozzle design, speed, and droplet velocity and droplet frequency. The development of fabrication processes includes the fine tuning of material and machine parameters in order to achieve robust and effective material jetting based additive manufacturing [1].

Field structured magnetic composites are manufactured by aligning magnetic particles within a polymer matrix by applying an external magnetic field. The concept of field structuring is illustrated in Figure 5.1.

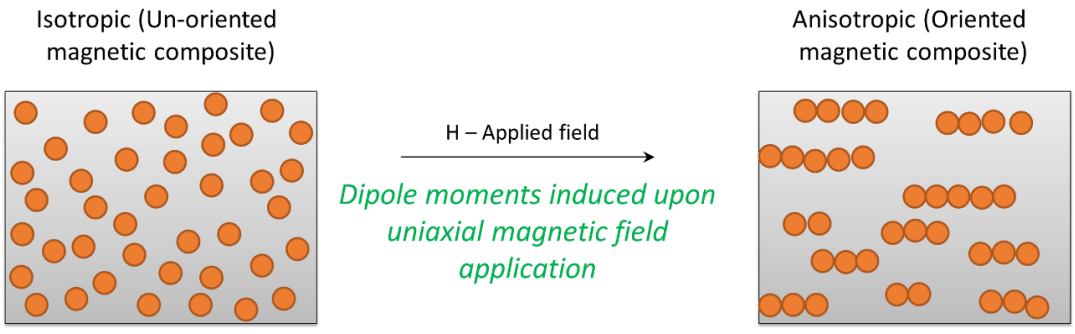

Figure 5.1: Schematic of magnetic field induced particle structuring in magnetic polymer composites

The external magnetic field produces particle chaining that enhances magnetic properties like remanence and susceptibility along the direction of field structuring [2]. Such field structured magnetic materials are of significant interest in applications like magnetic sensors and data storage systems [3], [4]. Anisotropy in thermal conductivity was achieved by orienting ferromagnetic particles in epoxy resin applying an external magnetic field where the chain like microstructures served as enhanced heat flow paths [5]. Inkjet printed one-dimensional arrays of monodisperse Fe_3O_4 nanoparticles with high anisotropic magnetization with possible applications for magnetic field sensing was demonstrated in the technical literature [6]. Among the available magnetic materials, ferrite based magnetic materials have become particularly important for a multitude of applications. Strontium ferrite is one such material, having a hexagonal structure like magnetoplumbite [7]. Under the influence of an external magnetic field, dipole moments induced in the particles along the crystallographic C-axis orients the particles along the direction of applied magnetic field. Additive manufacturing of magnetorheological fluid-dispersed photopolymers using magnetic field assisted stereolithography has been studied and reported in the technical literature [8]. The influence of applied magnetic flux density on the degree of particle alignment and orientation behavior at multiple angles has already been reported in previous work by the present author [9]. Finite Element Method Magnetics (FEMM) simulation for a two-cube magnet particle alignment system indicated an exponential reduction in magnetic flux density with increasing separation distance between the magnet faces. Simulations additionally showed that the magnetic flux density was enhanced by 0.21 Tesla in a magnetic array type particle alignment system compared to a two-cube

permanent magnet system [10]. The developed particle alignment systems were integrated with an in-house developed material jetting 3D printer which in addition to material deposition enabled particle structuring during the manufacturing process [11]. Moreover, the effectiveness of utilization of additives to mitigate particle settling in polymers using two different additive systems has been reported in the technical literature [12], [13].

The present study investigates the capabilities of polymer formulations engineered with magnetic fillers and additives for the material jetting additive manufacturing process. First, the developed formulations were characterized for their rheological behavior, and mathematical models were utilized to derive suspension properties. Derived properties were utilized to correlate different aspects of material and process behavior observed at various manufacturing process stages. The role of additives toward controlling particle aggregation and enabling particle alignment was evaluated using optical microscopy. Optical microscopy coupled with directionality analysis using image processing enabled quantifying particle alignment within the dispensed photopolymers. The fundamental understanding thus obtained for developed materials and process scenarios permitted the fabrication of field structured composites using a suspension engineered with 10 wt% magnetic particle loading. Magnetic characterization of field structured composites was conducted using a SQUID (superconducting quantum interference device) magnetometer. The goal of this work was to scientifically rationalize material behavior and utilizing this knowledge for developing magnetic composite structures with controllable microstructures. Ultimately, this research seeks to provide an in-depth understanding of the role of

material formulations, magnetic alignment setup and manufacturing process methods, in order to further evolve processes to produce 3D magnetic solids using the material jetting based additive manufacturing process.

5.2 Experimental procedures

5.2.1 Materials

For this study, strontium ferrite (SrFeO) powder with an average particle size of 1.41 μm was purchased from DOWA Electronics Materials Co. Ltd (Tokyo, Japan). Photosensitive polymer resin PR-48 was purchased from Colorado Photopolymer Solutions (Boulder, Colorado, United States) and rheological additive BYK 7410ET was obtained from BYK-Chemie GmbH (Wesel, Germany).

5.2.2 Magnetic filler dispersion methodology

Dispersion of magnetic fillers in the UV curable prepolymer was accomplished using a combination of mechanical mixing and sonication techniques. Strontium ferrite powder was added in the desired quantity to the PR-48 resin and the resultant combination was agitated using an impellor agitator from Calframo Ltd (Georgian Bluffs, Ontario, Canada). After mechanical agitation, ultrasonic mixing was initiated using a Branson model S-75 sonicator (Branson Ultrasonics Corporation, Danbury, Connecticut, USA) adopting 15-second pulsed on/off mode for 15 minutes. The suspension was allowed to rest for a day. The suspensions were again mechanically agitated to enhance the efficiency of the rheological additive. Any air that was entrapped during the mixing processes was degassed in vacuum.

5.3 Characterization methods

5.3.1 Rheological behavior – Viscosity and flow curve analysis

Rheological analysis of magnetically loaded prepolymer suspensions containing ferromagnetic particles and rheological additive materials was performed using a rotational rheometer (Rheolab QC, Anton Parr GmbH, Graz, Austria) equipped with double gap type measuring system. Table 5.1 lists the material formulations that were characterized for their rheological properties.

Table 5.1: Materials characterized for rheological properties.

Material code	Magnetic filler	Additive type	Additive loading
Base Resin	-	-	-
10SF	10	-	-
10SF-0.5BYK	10	BYK-7410ET	0.5
10SF-2.0BYK	10	BYK-7410ET	2

Flow curves derived from rheological characterization experiments for the magnetic suspensions were used to interpret the suspension behavior. In material jetting processes, extrusion of the developed formulation is driven by an applied pressure. Shear forces break the network structure developed resin material by the rheological additive. Flow of the liquid formulation that is ejected from the nozzle is primarily governed by equations for incompressible, laminar flow through a circular tube of constant cross-section. The Hagen Poiseuille equation defines the pressure drop as indicated in Eq.5.1.

$$\Delta p = \left(\frac{8\eta QL}{\pi r^4}\right) \tag{5.1}$$

where Δp is the pressure drop, Q is the volumetric flow rate, η is the formulation viscosity, r and L are the radius and length of a circular tube, respectively. The shear stress at any point inside the circular tube is given by Eq.5.2.

$$\tau = -\frac{\Delta p}{2L} r \tag{5.2}$$

The wall shear rate, $\dot{\gamma}_{\mathrm{w}}$, in terms of pressure drop is given by Eq.5.3.

$$\dot{\gamma}_w = -\frac{\Delta p}{\eta L}\frac{r}{2} \tag{5.3}$$

The volumetric flow rate Q is expressed as [14]:

$$Q = \pi r^2 V = \pi \left(\frac{n}{3n+1}\right)\left(-\frac{\Delta p}{2mL}\right)^{\frac{1}{n}} r^{\frac{3n+1}{n}} \tag{5.4}$$

In Eq.5.4, n is the power law index and m is the consistency index (or) viscosity obtained from mathematical analysis of rheological data through a power law model. From the theoretical equations, we interpret that $-\nabla p \; \alpha \; Q^n$, i.e., the pressure gradient is less sensitive for a shear thinning fluid than for a Newtonian fluid [14]. The dependence of fluid viscosity on shear rate is expressed utilizing a power law as indicated in Eq.5.5.

$$\eta = m\dot{\gamma}^{n-1} \tag{5.5}$$

Here, n is the power law index or shear thinning exponent and m is the consistency index (or) viscosity [15]. The magnitude of power law index n indicates the degree of pseudoplasticity in the characterized material. The power law model is a two parameter model and is used extensively to enable fundamental understanding of fluid behavior. An expression for the actual shear rate experienced by the fluid inside the cylinder as expressed in technical literature is indicated by Eq.5.6 [16]

$$\dot{\gamma} = \frac{V r^{(2+n)}}{\left(\frac{n}{3n+1}\right) r^{\frac{3n+1}{n}}} \tag{5.6}$$

It was additionally observed that a formulation with low viscosity experiences higher shear rates during the dispensing process [16]. Overall, from the above theoretical equations, the importance of rheological modification of formulations is well established. Yield strength of the magnetic suspension that characterizes the behavior of material at rest was determined using the Herschel-Bulkley equation that is well suited for Non-Newtonian fluids. The Hershel-Bulkley model equation is expressed as follows:

$$\tau = \tau_0 + C\dot{\gamma}^n \tag{5.7}$$

where τ_0 is the yield point or yield strength, C is the consistency index, τ is shear stress, $\dot{\gamma}$ is shear rate and n is the Herschel-Bulkley index. The Herschel-Bulkley index primarily determines the behavior of the suspension as follows: $n < 1$ for shear thinning behavior, $n > 1$ for shear thickening behavior and $n = 1$ for Bingham behavior [17], [18].

5.3.2 Thixotropic flow behavior analysis

Thixotropy refers to reversible changes in fluid behavior from a flowable liquid to a solid elastic gel. Liquids with a microstructure exhibit thixotropy and it reflects on the time taken to move from one microstructural state to another and back to the original microstructure. These materials exhibit structural decomposition at high shear rates and structural regeneration at low shear rates. Stresses experienced by the fluid play a dominant role in breakdown of the thixotropic network structures [19]. The

influence of rheological additives on thixotropic behavior of magnetic suspensions was characterized using a step test consisting of three intervals. Low shear rate conditions simulate the sample behavior under stationary conditions and high shear rate conditions simulate sample behavior under the influence of external forces. Experiments were conducted using controlled shear rate conditions. In the first interval, viscosity was measured at $\dot{\gamma}$ = 1 s^{-1} for 20 seconds followed by viscosity measurement at $\dot{\gamma}$ = 300 s^{-1} for 50 seconds and finally viscosity was measured again at $\dot{\gamma}$ = 1 s^{-1} for 40 seconds. This test was used to characterize the structural decomposition and regeneration behavior of the magnetic suspensions incorporated with rheological additives. The thixotropy index that characterizes time dependent viscosity recovery was calculated using Eq.5.8

$$Thixotropy\ index = \frac{\eta_2 - \eta_1}{t_2 - t_1} = \frac{\Delta\eta}{\Delta t} \tag{5.8}$$

where η_2, η_1 are viscosities in the recovery phase at two different times t_1 and t_2.

5.3.3 Magnetic particle reinforced resin behavior in magnetic field

To carry out experimental research on stability of magnetic particle loaded polymer resin droplets in the magnetic field, an in-house developed experimental system was utilized [9]. A computer control system programmed with a graphical user interface was used to control the mechanical and electrical components of the system. Conditions for the experiments were set using the graphical user interface. The experimental system allowed adjusting the separation distance between alignment magnets and the magnetization time. Droplets were deposited using a Ultimus V deposition system (Nordson EFD, East Providence, RI, USA). Real time optical microscopy was used as a tool to capture droplet behavior on the substrate.

5.3.4 Magnetic particle aggregation control in photopolymers

To evaluate the behavior of magnetic particles dispersed in the UV curable polymer, optical microscopy was utilized. The magnetic filler loading in the formulations was maintained at 0.5 wt% to enable light optical microscopy. Particle aggregation due to interparticle magnetic interactions, degree of particle alignment as a function of resin viscosity and particle chain misorientations were captured and understood in this analysis. Magnetic particles dispersed in a suspension aggregate due to the magnetic forces that are a function of particle size and magnetization of the particle [20]. Mathematically, the interaction between particles is expressed as follows:

$$W_{mag} = \mu_0 M^2 a^3 \tag{5.9}$$

where W_{mag} is the interaction energy between two magnetic particles, M is the particle magnetization, a is the particle radius and μ_0 is the permeability of vacuum. To understand the role of additives in controlling particle aggregation, a droplet of the prepared suspension was dispensed within a nylon washer. The state of the particles within the dispensed droplet was captured after 15 minutes using an optical microscope.

5.3.5 Manufacturing scenarios for particle structuring, and influence of resin viscosity on particle alignment

During the process of magnetic particle structuring applying an external magnetic field, the dispersed magnetic particles experience forces that are a function of several parameters, i.e., magnetic, gravity and viscous drag forces. The particle motion is expressed mathematically as follow [21]–[23]:

$$\left(\frac{4}{3}\pi a^3 \rho_p\right)\frac{dV_p}{dt} = \left[\, F_m + F_d + F_g \,\right] \tag{5.10}$$

where the individual force terms are expressed as indicated in the following equations:

$$Magnetic\ force: F_m = \mu_0 \left(\frac{4}{3}\pi a^3\right)\chi \frac{1}{2}\,\nabla(H.H) \tag{5.11}$$

$$Viscous\ drag\ force: F_d = 6\pi a \eta V_p \tag{5.12}$$

$$Gravity\ forc: F_g = \left(\frac{4}{3}\pi a^3\right)\left(\rho_p - \rho_l\right)g \tag{5.13}$$

In the above equations, H is the magnetic field, a is particle radius, χ is magnetic susceptibility, g is acceleration due to gravity, V_p is the particle velocity, ρ_p and ρ_l are the particle and fluid densities, η is the fluid viscosity respectively. The equations enable understanding the mechanics of particle alignment where some of the most important variables that can be manipulated are the magnetic field (H) and resin viscosity (η). In previous work, the influence of a magnetic field and novel methods of particle alignment were already investigated [9]. Simple design changes in the material jetting equipment and alignment methodology were illustrated adopting two different manufacturing scenarios. Note that in the original design of the 3D printer, the deposition of the magnetic resin and particle alignment was coupled [11]. Moreover, UV curable resin would cure at the nozzle tip hindering the deposition process. In the present work, the need for de-coupling printing processes through simple component design changes and manufacturing methodology is described. To understand the influence of resin viscosity on particle alignment, a single layer of the designed sample geometry (15 mm by 15 mm by 1 mm) was dispensed using the material jetting printer and subsequently cured using UV light. The height of the magnetic alignment jig from

the substrate was maintained at around 10 mm as further lowering the jig would interfere with the substrate. Optical microscopy was used as a tool to investigate aforementioned aspects of the experiments. Directionality analysis using ImageJ software (National Institute of Mental Health, Bethesda, Maryland, USA) was used to quantify the degree of particle alignment in field structured composites [24].

5.3.6 Additive manufacturing of magnetic polymer composites and magnetic characterization

To manufacture field structured magnetic composites, a material jetting 3D printer was utilized to deposit the ferromagnetic resin on the substrate. An in-house developed material jetting 3D printer controlled using the Labview programming environment (National Instruments, Austin, TX, USA) was employed to deposit the material to the designed geometry. Apart from the material jetting that is controlled in 3 axis (X,Y and Z axis of the printer), the alignment of the particle is additionally controlled in the X-Y plane (2D alignment control using magnetic jig) resulting in a complex 5D control of the whole manufacturing process. A graphical user interface enabled controlling the different movements of the 3D printer. The sample geometry (15 mm by 15 mm by 1 mm) was designed in SolidWorks (Dassault Systems, Vélizy-Villacoublay, France), and the open source Sli3cr software was used to generate the G-code for the nozzle deposition path [25]. The generated G-code was further modified for proper positioning of the magnetic alignment jig above the deposited material and subsequently curing every deposited layer.

The field structured magnetic composite was characterized for its magnetic properties using a SQUID magnetometer (MPMS XL-7 Evercool, Quantum Design,

San Diego, CA, USA) for its in-plane and out-of-plane magnetic characteristics, i.e., magnetic properties were measured along and perpendicular to the direction of particle structuring. A small piece from a 3D printed part was first weighed, placed in a gelatin capsule and further inserted into a transparent diamagnetic plastic straw. Measurements were performed applying magnetization reversal loops in a magnetic field with strength of $\mu_0 H = \pm 7$ Tesla at a temperature of 300 K. Saturation magnetization was determined at an applied field strength of 7 T. Remanence and coercivity were obtained through linear interpolation of magnetization at zero applied field and applied field at zero magnetization. The magnetic properties were determined by averaging the values obtained through both magnetization and de-magnetization cycles.

5.4 Results and discussion

5.4.1 Rheological behavior analysis of ferromagnetic polymers

Rheological properties of filler modified resin formulations have great significance in extrusion based additive manufacturing process [26], [27]. In the present rheological study, changes in material behaviour as a result of two different additive loadings were investigated. Materials developed and utilized for additive manufacturing processes are subjected to various types of shear rates and deformations during storage and during the manufacturing process. The study of viscosity properties at different shear rates provides useful information on the properties of the developed formulations. It is well known that the rheological properties of the polymer formulations are strongly dependent on the characteristics of the fillers, volume fraction of fillers, dispersion quality, and network structure within the polymer [28], [29]. As observed in Figure 5.2, apart from the base resin (pure PR-48) that exhibits Newtonian behaviour (viscosity independent of shear rate), all other formulations exhibit non-

Newtonian behaviour, which is confirmed by observing a decrease in viscosity with increasing shear rates.

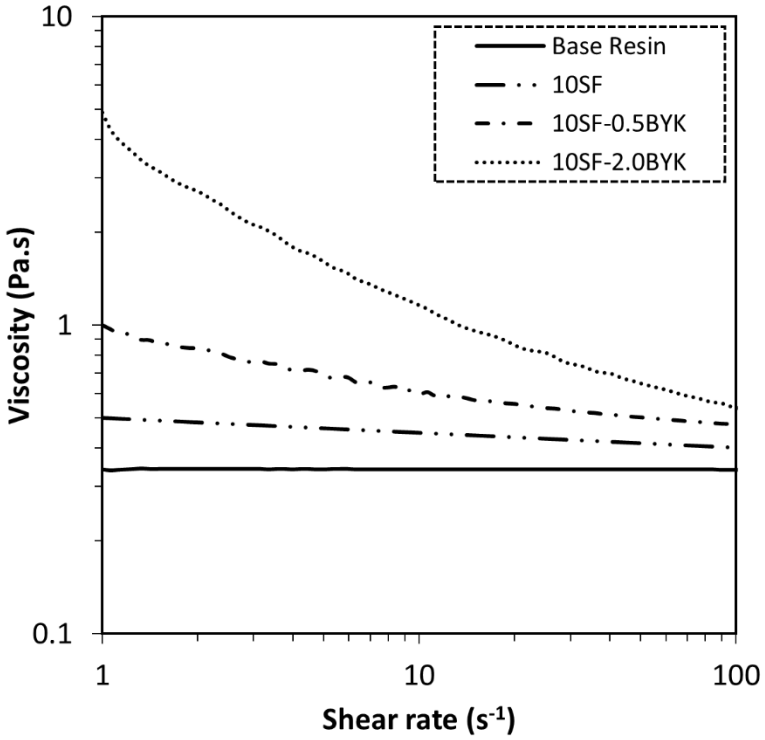

Figure 5.2: Viscosity as a function of shear rate for material formulation listed in Table 5.1.

First, adding strontium ferrite fillers to the base polymer increased the viscosity of the suspensions rendering an initial non-Newtonian material behaviour. Additionally, an increase in the low shear viscosity was observed in suspensions modified using the rheological additive. It was observed that the additive loading significantly influenced the magnitude of increase in low shear viscosity. Such observations where changes in the mechanical behaviour are imposed on the resin system by introducing additives, are deemed important for extrusion-based additive manufacturing processes [30]. The additive BYK 7410ET is a polyurea based thixotropic additive material system. Such material, when dispersed in a polymeric matrix, results in the formation of a gel

structure by hydrogen bonding with the polar hydroxyl group of the resin binder [31]. The development of a structural network within the polymeric binder is supported by the enhancement in low shear viscosity observed in Figure 5.2. With increasing shear rate, the viscosity decreases due to the disruption of this structural network. Utilizing Eq.5.5, the properties of the formulations like the power law index and viscosity were derived to understand the influence of additive loading.

Table 5.2: Rheological properties derived using Eq.5.5.

Material code	*n* – power law index	*m* - viscosity (Pa.s)
Base resin	-	-
10SF	0.95	0.50
10SF-0.5BYK	0.87	0.88
10SF-2.0BYK	0.61	3.23

As observed in Table 5.2, curve fitting using the power law model for all the formulations except for the base resin confirms shear thinning or pseudoplastic material behaviour. Additionally, it was observed that the additive loading significantly influenced the degree of pseudoplasticity. The formulation with the lowest power law index exhibited the highest material viscosity, which is advantageous for extrusion based additive manufacturing.

Yield point or yield stress defined as the shear stress at zero shear rate derived using Eq.5.7 are listed in Table 5.3. With Herschel-Bulkley indices being less than unity, it is additionally confirmed that all suspensions exhibit pseudoplastic behaviour. As far as the yield strengths of the suspensions are concerned, they were observed to be dependant on additive loading. The additive was found to be particular efficient in terms of yield strength enhancement as indicated by the results shown in Table 5.3. The

enhancement in yield strength was caused by the thixotropic network structure as a result of additive incorporation within the magnetic particle reinforced formulations.

Table 5.3: Yield stress predictions using Herschel-Bulkley model (Eq.5.7).

Material code	Herschel-Bulkley model		
	τ_0 (Pa)	C (Pa. s)	n
Base resin	-	-	-
10SF	0.26	0.45	0.97
10SF-0.5BYK	0.65	0.59	0.93
10SF-2.0BYK	3.07	1.18	0.81

5.4.2 Thixotropic flow behavior analysis

In material jetting AM processes, the material experiences various forces at different processing stages, i.e., forces are imposed on the material during handling, pressure induced material dispensing, and magnetic field exposure during particle structuring. Thixotropy analysis was further utilized to understand and determine the viscosity recovery in the magnetic suspensions. Results of the step test consisting of three intervals shown in Figure 5.3 indicate high initial suspension viscosity at $\dot{\gamma}$ = 1 s^{-1}, followed by instantaneous viscosity reduction when the shear rate was increased to $\dot{\gamma}$ = 300 s^{-1}. Finally, in the recovery phase when the shear rate was again reduced to $\dot{\gamma}$ = 1 s^{-1}, the magnetic suspensions exhibited time-dependent viscosity recovery behavior. The observed phenomena relate to the processes of structural decomposition at high shear rates and structural regeneration at low shear rates that are mainly controlled by the rheological additives. From this analysis, it is well understood that the additive impart thixotropic properties to the magnetic suspension. Thixotropy indices calculated using Eq.5.8 are listed in Table 5.4.

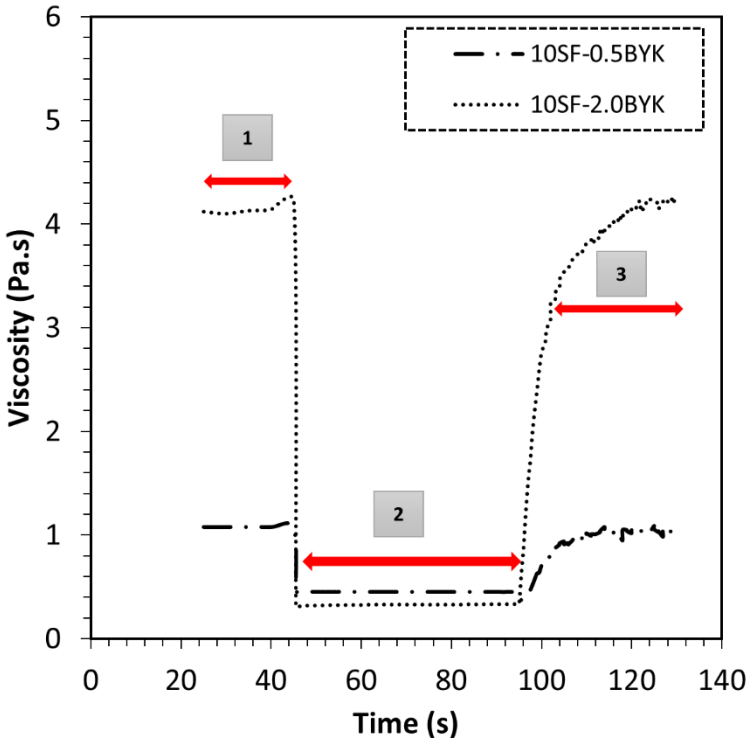

Figure 5.3: Three interval thixotropy test for developed material formulations [1: Low shear phase $\dot{\gamma} = 1\ s^{-1}$; 2: High shear phase $\dot{\gamma} = 300\ s^{-1}$; 3: Low shear phase $\dot{\gamma} = 1\ s^{-1}$].

Table 5.4: Thixotropy index of developed magnetic suspensions

Material code	Thixotropy index
10SF-0.5BYK	0.05
10SF-2.0BYK	0.32

The step test data indicates a strong influence of rheological additive content on the magnitude of viscosity recovery. This type of structural decomposition and regeneration is deemed to be one of the fundamental requirements for a material to be considered for material jetting based additive manufacturing. Present results corroborate findings in the technical literature [16].

5.4.3 Magnetic particle reinforced resin behavior in magnetic field

In this study, the behavior of magnetically loaded polymer droplets was evaluated as a function of time at a magnet separation distance of 30 mm where the magnetic flux density at the center between two magnets is 0.10 Tesla. From particle alignment experiments it was evident that the degree of particle alignment was higher at a separation distance of 30 mm between the cube magnets [9]. However, it was observed that droplets dispensed on the substrate deformed significantly under the influence of the magnetic field. Experiments were conducted using the base resin reinforced with just 10 wt% SrFeO particles to determine the time at which a droplet loses its stability on the substrate. Deformation of magnetic particle reinforced polymer droplets obtained from experiments conducted varying the time at a separation distance of 30 mm are depicted in Figure5.4.

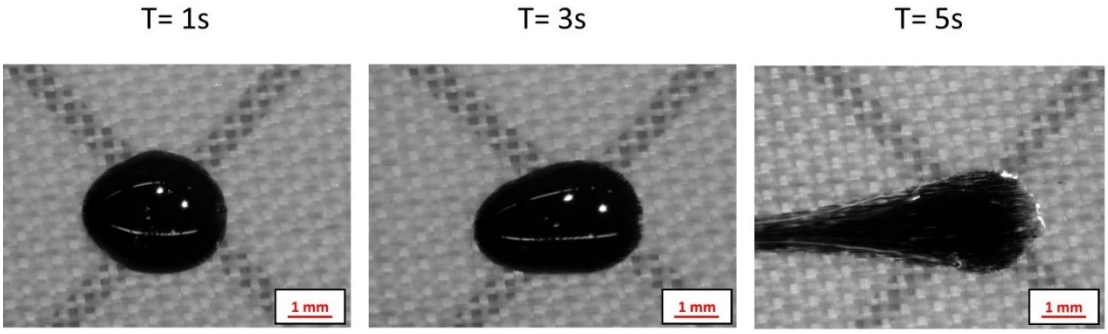

Figure 5.4: Optical microscopy images of droplet deformation w.r.t. magnetization time at separation distance of 30 mm.

The magnetic particle reinforced resins engineered with 10 wt% magnetic particles loading and 0.5 wt% and 2 wt% of BYK 7410ET were tested for their stability on the substrate. As observed in Figure 5.5, the resin engineered with higher additive loading (2 wt%) was stable on the substrate in the presence of a magnetic field. This observed behavior corresponds well with the rheological analysis results where the

formulation engineered using 2 wt% of the additive exhibited enhanced low shear viscosity, yield strength and thixotropic properties.

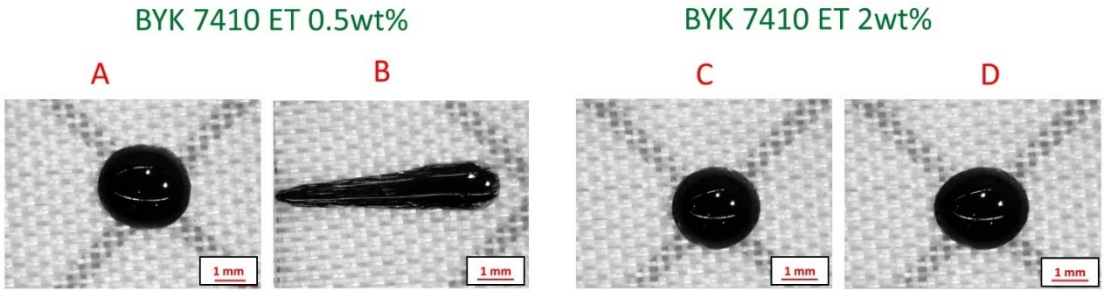

Figure 5.5: Droplet images show the influence of rheological additive loading (A & C – Droplet images before magnetic field application; B & D Droplet image after field application).

5.4.4 Magnetic particle aggregation control in photopolymers

The present study also investigates the ability of magnetic particle reinforced formulations to control particle aggregation due to interparticle interactions. To enable optical microscopy, the magnetic filler loading was kept low at 0.5 wt%. Table 5.5 lists the formulations prepared for evaluating the magnetic particle behaviour in the prepared formulations.

Table 5.5: Suspensions prepared for optical microscopy analysis.

Sample identifier	Magnetic filler	BYK 7410ET additive loading
A	0.5	0
B	0.5	0.5
C	0.5	1.0
D	0.5	2.0

First, the influence of additive loading toward mitigating particle aggregation was taken into consideration. According to Eq.5.9, magnetic particles attract each other due to the interaction energy and tend to form aggregates. The formation of aggregates is evident in the micrographs shown in Figures 5.6A and B. Aggregation was observed to reduce

with increasing additive content in the base resin. Even though the micrograph in Figure 5.6B shows particle aggregation, randomized chaining of magnetic particles is not as profound as the formulation without any additive (Figure 5.6A). Micrographs in Figures 5.6C and D exhibit uniform particle dispersion as the viscous drag due to the additive inhibits magnetic particle motion. This viscous drag is a result of thixotropic network formation within the formulation. The plastic fluidity which is a result of additive incorporation ensures good dispersion of the magnetic particles within the developed photopolymer formulation.

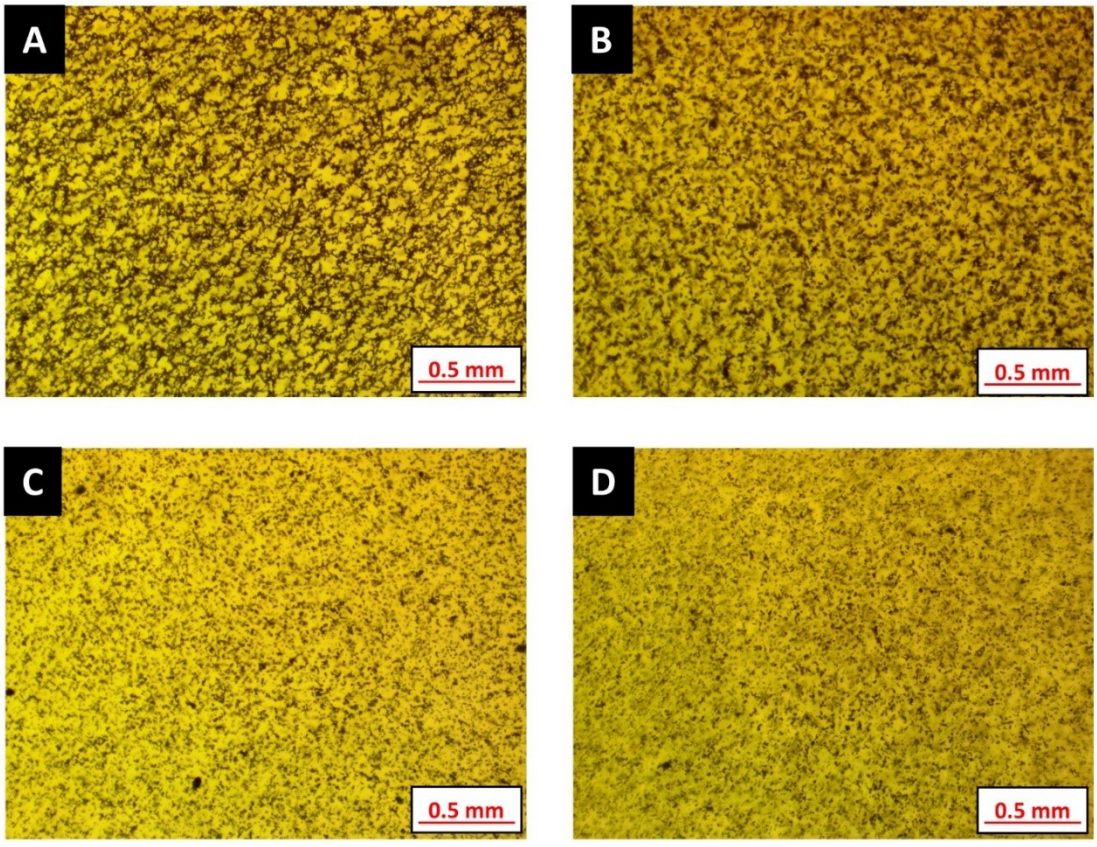

Figure 5.6: Particle aggregation in photosensitive polymer formulations listed in Table 5.5.

5.4.5 Manufacturing scenarios and influence of resin viscosity on particle alignment

To manufacture field structured magnetic composites, two different manufacturing scenarios were tested. In scenario A represented in Figure 5.7A, the permanent magnet alignment system is coupled along with the dispensing system. Once dispensed, the curing source moves right ahead of the dispensed material and solidifies the resin. In scenario B in Figure 5.7B, the alignment is coupled with the curing system. All machine movements were accomplished programming appropriate G-codes with the respective wait times prior to the curing process. From the micrograph shown in Figure 5.8, it is understood that the alignment system coupled with the curing source enhances particle structuring (A) whereas removing the field structuring setup during the curing process (B) results in chain misalignment and a reconfigured microstructure.

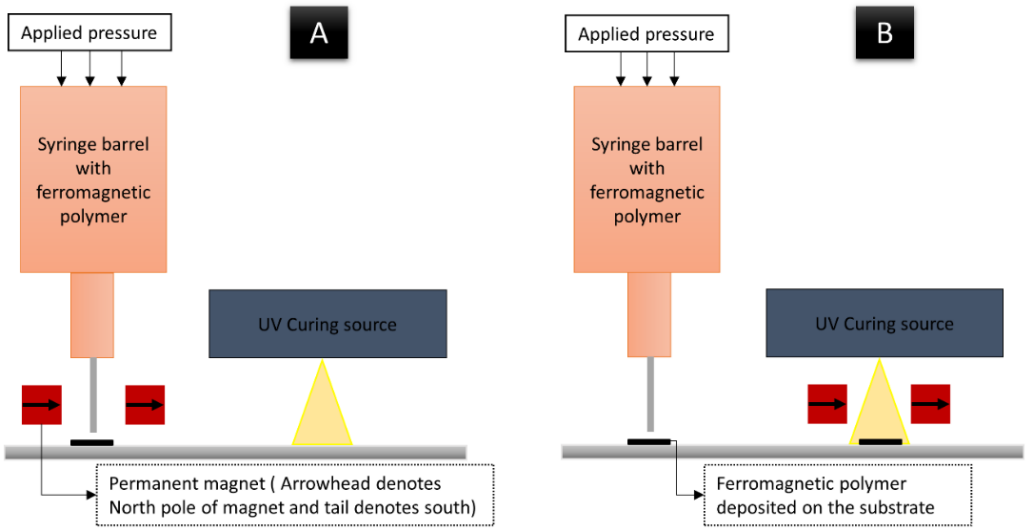

Figure 5.7: Graphical representation of the adopted manufacturing scenarios.

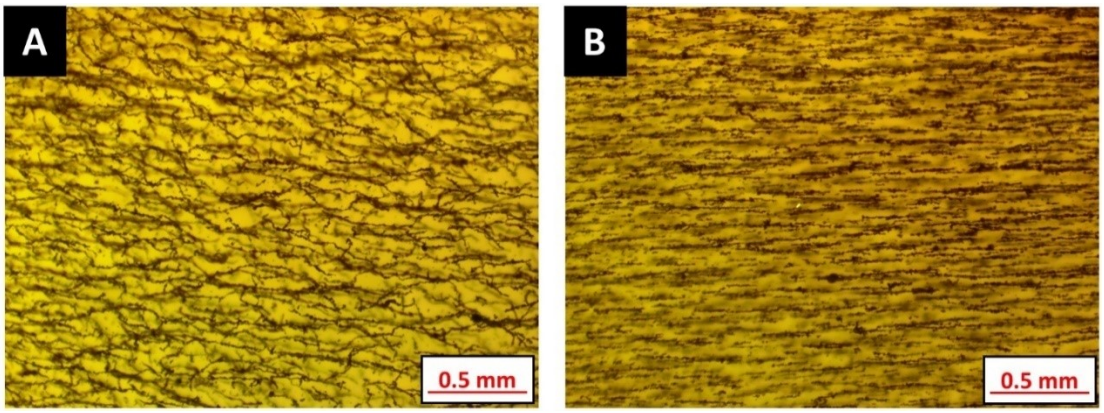

Figure 5.8: Micrographs obtained from experiments adopting machine configuration scenarios as indicated in Figure 5.7.

Furthermore, the influence of additives on the degree of particle alignment was studied adopting scenario B as the machine setting and dispensing one single layer of the designed sample geometry. The height of the magnetic alignment jig was maintained at around 10 mm from the substrate. Maintaining this height required increasing the time to allow particle chaining to occur prior to UV curing. The wait time prior to curing was maintained at 60 seconds. Optical micrographs obtained for samples manufactured using the formulations listed in Table 5.5 are shown in Figure 5.9. Results from directionality analysis shown in Figure 5.10 indicate that increasing the additive loading decreased the particle chaining effect. The count of oriented structures, which enables quantification of filler directionality and the degree of filler orientation, was observed to decrease with increasing additive content. Furthermore, the observed behaviour emphasizes that magnetic field strength along with resin viscosity are critical aspects for the manufacturing process especially concerning the degree of particle alignment.

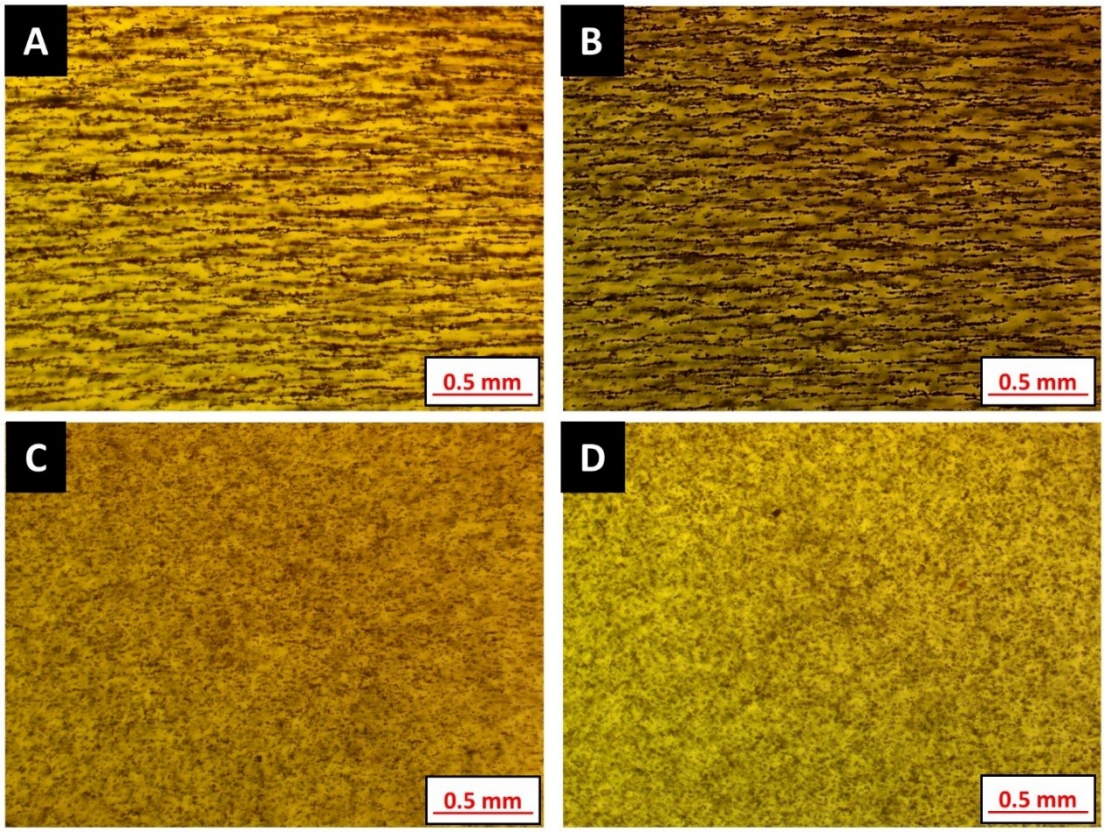

Figure 5.9: Influence of additive loading on particle alignment.

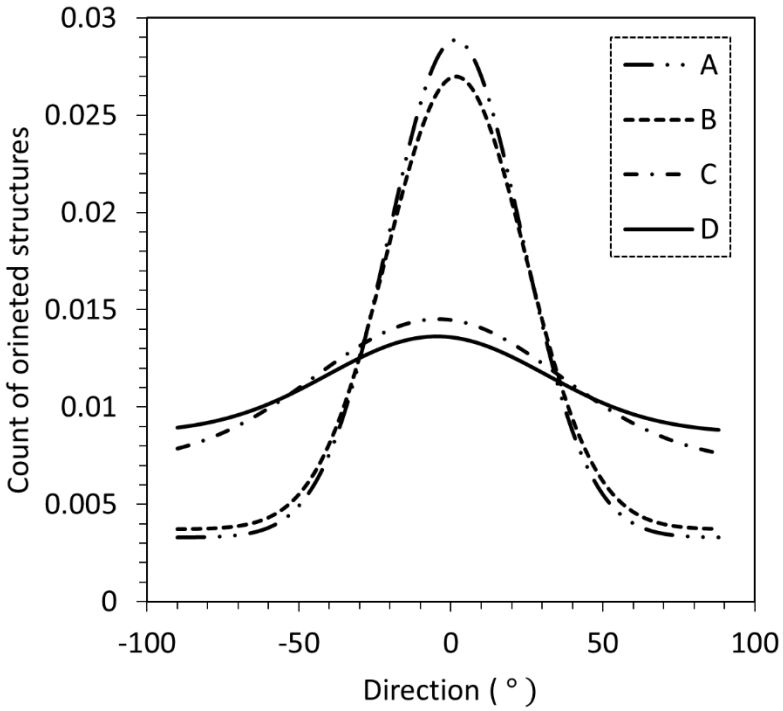

Figure 5.10: Particle alignment orientation obtained using image analysis.

5.4.6 Additive manufacturing of field structured composites and magnetic characterization

Magnetic field structured composites were printed using a formulation engineered with 10 wt % magnetic filler and 0.5 wt% BYK 7410ET additive. The extrusion pressure was set at 2.5 psi; layer thickness and deposition speed were 0.2 mm and 10 mm/s, respectively. Printer settings were modified to position the magnetic alignment jig and the curing source right above the deposited material. Such modifications were done to fabricate composite samples with three print layers of the deposited material. The time of magnetic field application and UV irradiation were maintained at 60 seconds time and 20 seconds for every layer, respectively. As shown in Figure 5.11, small deformations due to the magnetic field during the alignment process prior to curing were observed.

Figure 5.11: 3D printed magnetic composite with observed deformation artefact due to the magnetic field.

The observed deformations occurred due to a non-uniform magnetic flux density within the magnetic jig, which was already reported in previous work [9]. The field structured magnetic composite was tested for its magnetic properties along the direction of field structuring (in-plane) and perpendicular to it (out of plane).

Magnetic composites are characterized by properties like saturation magnetization, magnetic remanence and coercivity. These magnetic characteristics are derived from magnetization and de-magnetization loops obtained in the form of hysteresis graphs. Figure 5.12A shows the hysteresis data obtained for a sample characterized along and perpendicular to the direction of particle structuring. From the magnified views expressed in Figures 5.12B, C and D, properties along the direction of field structuring were observed to be higher compared to properties perpendicular to it. Along the direction of field structuring, saturation magnetization was observed to increase by 0.10 emu/g, magnetic remanence by 0.13 emu/g and coercivity by 0.55 KOe. The area enclosed by the hysteresis curve for measurements along the direction of particle structuring was greater by 5.13% compared to the hysteresis curve obtained for the direction perpendicular to the direction of field structuring. The observed graphical patterns and results are congruent to observations in the technical literature for magnetic composites with aligned magnetic fillers [21], [32]. This enhancement further confirms the alignment of the easy axis of magnetization of individual particles by orienting the fillers, resulting in chain like microstructures. Overall, magnetic composite structures printed by orienting ferromagnetic particles exhibit anisotropic magnetic properties due to particle assembly through the external magnetic field, which has the potential unlock innovative approaches to build magnetic structures for a multitude of applications.

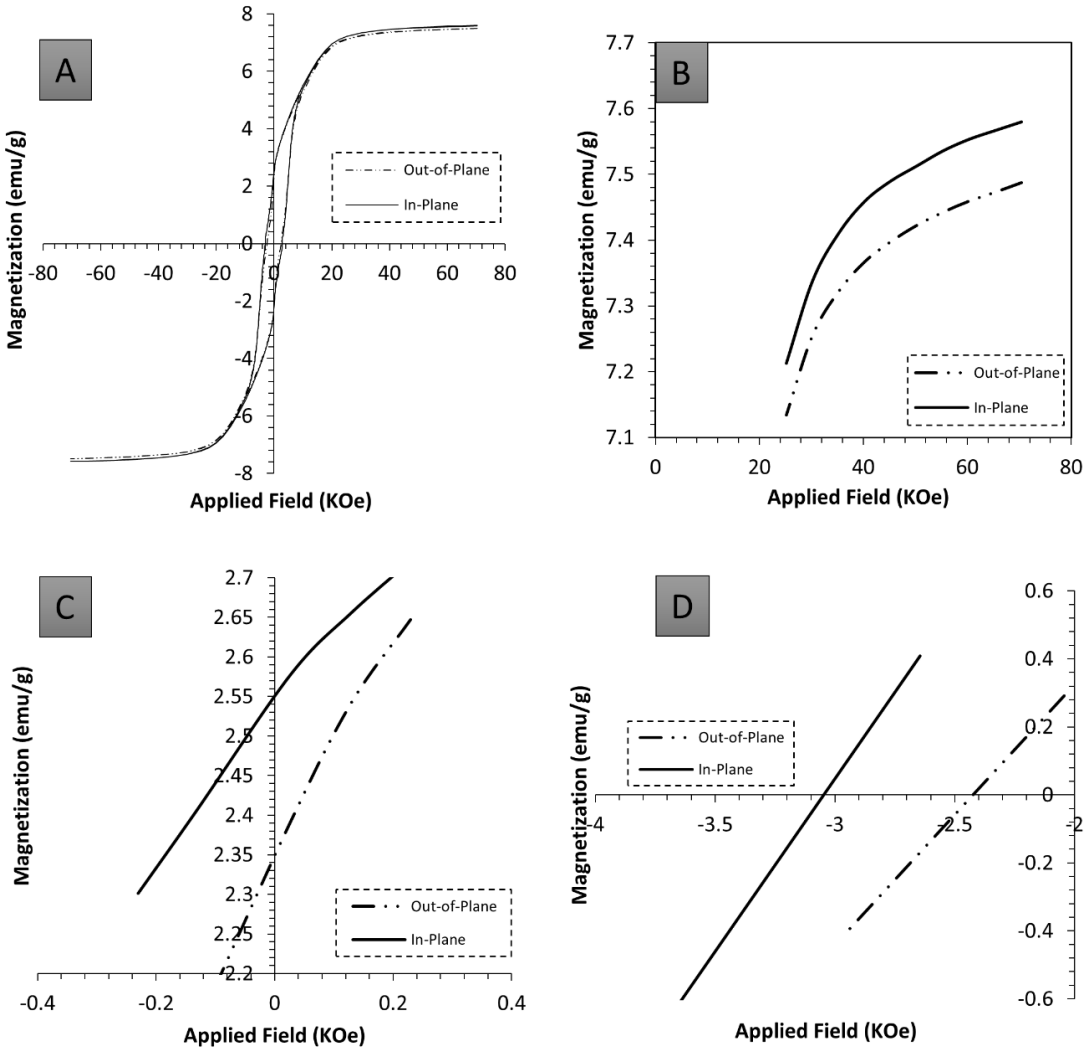

Figure 5.12: A: Hysteresis data for magnetization versus applied magnetic field; B, C and D: Magnified views of hysteresis graph for saturation magnetization, magnetic remanence, coercivity.

5.5 Conclusions

The present study expanded the understanding of formulation materials for magnetic polymer composites in a multidisciplinary context. Rheology studies enabling microstructure control, field structured composite manufacturing scenarios, and magnetic characterization of field structured composites were successfully performed. It was observed that the rheological additive materials enabled enhancing

the low shear viscosity and yield strength through the formation of a thixotropic network within the prepared formulations. Mathematical analysis of rheological data enabled interpreting the formulation properties like flow index and yield strength. A flow index of less than unity for all formulations provided strong evidence for pseudoplastic material behaviour. Additionally, a step test consisting of three intervals demonstrated the time dependent viscosity recovery in the magnetic suspensions. It was observed that fluid properties like flow index, yield strength and thixotropy index were dependent on the additive loading in the developed formulations. Experiments conducted using a formulation engineered with BYK 7410ET additive revealed that at the highest additive loading of 2 wt% the deposited resin material was stable on the substrate in the presence of a magnetic field. However, optical microscopy at lower magnetic filler loading revealed that an increase in additive loading, while suppressing aggregation of magnetic particles, severely reduced the desired chaining effect in the presence of an applied magnetic field due to enhanced viscous drag in the magnetic formulations. Optical microscopy coupled with image processing enabled quantifying the degree of particle orientation in the polymer formulations. These fundamental studies were critical for providing the understanding of the role of material formulations in achieving a variety of material and manufacturing process related goals for the additive manufacturing process in order to create magnetic particle reinforced composites. Composites characterized using SQUID magnetometry revealed an enhancement in magnetic properties along the direction of particle structuring. Compared to the out-of-plane magnetic characteristics, the in-plane magnetic saturation, remanence and coercive fields were observed to be enhanced. Ultimately,

this research work provides the basis for devising robust material formulations and manufacturing processes to effectively form magnetic polymer composites with desired microstructure distribution during material jetting based additive manufacturing.

5.6 References

[1] I. Gibson, D. Rosen, and B. Stucker, *Additive Manufacturing Technologies*. New York, NY: Springer New York, 2015.

[2] J. Martin, E. Venturini, J. Odinek, and R. Anderson, "Anisotropic magnetism in field-structured composites," *Phys. Rev. E*, vol. 61, no. 3, pp. 2818–2830, Mar. 2000.

[3] S. Xia, E. Metwalli, M. Opel, P. A. Staniec, E. M. Herzig, and P. Müller-Buschbaum, "Printed thin magnetic films based on diblock copolymer and magnetic nanoparticles," *ACS Appl. Mater. Interfaces*, vol. 10, no. 3, pp. 2982–2991, 2018.

[4] D. Speliotis, "Magnetic recording beyond the first 100 years," *J. Magn. Magn. Mater.*, vol. 193, no. 1–3, pp. 29–35, 1999.

[5] K. Goc *et al.*, "Influence of magnetic field-aided filler orientation on structure and transport properties of ferrite filled composites," *J. Magn. Magn. Mater.*, vol. 419, pp. 345–353, Dec. 2016.

[6] M. Gao, M. Kuang, L. Li, M. Liu, L. Wang, and Y. Song, "Printing 1D Assembly Array of Single Particle Resolution for Magnetosensing," *Small*, vol. 14, no. 19, p. 1800117, May 2018.

[7] R. C. Pullar, "Hexagonal ferrites: A review of the synthesis, properties and applications of hexaferrite ceramics," *Prog. Mater. Sci.*, vol. 57, no. 7, pp. 1191–1334, Sep. 2012.

[8] L. Lu, P. Guo, and Y. Pan, "Magnetic-Field-Assisted Projection Stereolithography for Three-Dimensional Printing of Smart Structures," *J. Manuf. Sci. Eng.*, vol. 139, no. 7, p. 071008, Mar. 2017.

[9] B. Nagarajan, A. F. Eufracio Aguilera, M. Wiechmann, A. J. Qureshi, and P.

Mertiny, “Characterization of magnetic particle alignment in photosensitive polymer resin: A preliminary study for additive manufacturing processes,” *Addit. Manuf.*, vol. 22, no. May, pp. 528–536, Aug. 2018.

[10] B. Nagarajan, A. F. E. Aguilera, A. Qureshi, and P. Mertiny, “Additive Manufacturing of Magnetically Loaded Polymer Composites: An Experimental Study for Process Development,” in *ASME 2017 International Mechanical Engineering Congress and Exposition*, 2017, p. V002T02A032-V002T02A032.

[11] A. F. Eufracio Aguilera, B. Nagarajan, B. A. Fleck, and A. J. Qureshi, “Ferromagnetic particle structuring in material jetting - Manufacturing control system and software development,” *Procedia Manuf.*, vol. 34, pp. 545–551, 2019.

[12] B. Nagarajan, A. F. Eufracio., A. Qureshi., and P. Mertiny, “Additive manufacturing of magnetically loaded polymer composites: An experimental study for process development,” *Proc. 17th Int. Mech. Eng. Congr. Expo. IMECE17. Am. Soc. Mech. Eng. Tampa, FL, USA, 3-9 Novemb. 2017*, pp. 1–9, 2017.

[13] B. Nagarajan, M. Arshad, A. Ullah, P. Mertiny, and A. J. Qureshi, “Additive manufacturing ferromagnetic polymers using stereolithography – Materials and process development,” *Manuf. Lett.*, vol. 21, pp. 12–16, Aug. 2019.

[14] R. P. Chhabra and J. F. Richardson, *Non-Newtonian flow and applied rheology: engineering applications*. Butterworth-Heinemann, 2011.

[15] U. Eberhard *et al.*, “Determination of the Effective Viscosity of Non-newtonian Fluids Flowing Through Porous Media,” *Front. Phys.*, vol. 7, no. MAY, pp. 1–9, May 2019.

[16] A. K. Bastola, M. Paudel, and L. Li, “Development of hybrid magnetorheological elastomers by 3D printing,” *Polymer (Guildf).*, vol. 149, pp. 213–228, Aug. 2018.

[17] T. G. Mezger, “The Rheology Handbook,” *Pigment Resin Technol.*, vol. 38, no. 5, p. prt.2009.12938eac.006, Sep. 2009.

[18] B. Nagarajan *et al.*, “Development and Characterization of Stable Polymer

Formulations for Manufacturing Magnetic Composites," *J. Manuf. Mater. Process.*, vol. 4, no. 1, p. 4, Jan. 2020.

[19] H. A. Barnes, "Thixotropy—a review," *J. Nonnewton. Fluid Mech.*, vol. 70, no. 1–2, pp. 1–33, May 1997.

[20] M. T. López-López, P. Kuzhir, G. Bossis, and P. Mingalyov, "Preparation of well-dispersed magnetorheological fluids and effect of dispersion on their magnetorheological properties," *Rheol. Acta*, vol. 47, no. 7, pp. 787–796, Sep. 2008.

[21] K. N. Al-Milaji, R. L. Hadimani, S. Gupta, V. K. Pecharsky, and H. Zhao, "Inkjet Printing of Magnetic Particles Toward Anisotropic Magnetic Properties," *Sci. Rep.*, vol. 9, no. 1, p. 16261, Dec. 2019.

[22] U. Banerjee, P. Bit, R. Ganguly, and S. Hardt, "Aggregation dynamics of particles in a microchannel due to an applied magnetic field," *Microfluid. Nanofluidics*, vol. 13, no. 4, pp. 565–577, Oct. 2012.

[23] Ganguly and Puri, "Field-Assisted Self-Assembly of Superparamagnetic Nanoparticles for BioMEMS.," *Sciencedirect.Com*, vol. 41, no. 06, pp. 293–335, 2007.

[24] J. Schindelin *et al.*, "Fiji: an open-source platform for biological-image analysis," *Nat. Methods*, vol. 9, no. 7, pp. 676–682, Jun. 2012.

[25] A. Ranellucci, "Slic3r." 2011.

[26] C. Ajinjeru *et al.*, "Rheological survey of carbon fiber-reinforced high-temperature thermoplastics for big area additive manufacturing tooling applications," *J. Thermoplast. Compos. Mater.*, p. 089270571987394, Sep. 2019.

[27] C. Ajinjeru *et al.*, "Rheological evaluation of high temperature polymers to identify successful extrusion parameters," Oak Ridge National Lab.(ORNL), Oak Ridge, TN, USA, 2017.

[28] M. Kamkar, S. M. Nourin Sultana, S. Patangrao Pawar, A. Eshraghian, E. Erfanian, and U. Sundararaj, "The key role of processing in tuning nonlinear viscoelastic properties and microwave absorption in CNT-based polymer nanocomposites," *Mater. Today Commun.*, vol. 24, no. February, p. 101010,

Sep. 2020.

[29] A. H. A. Hoseini, M. Arjmand, U. Sundararaj, and M. Trifkovic, “Significance of interfacial interaction and agglomerates on electrical properties of polymer-carbon nanotube nanocomposites,” *Mater. Des.*, vol. 125, pp. 126–134, 2017.

[30] V. Kunc, A. Lee, M. Mathews, and J. Lindahl, “Low Cost Reactive Polymers for Large Scale Additive Manufacturing,” *CAMX 2018*, pp. 15–18, 2018.

[31] A. Deka and N. Dey, “Rheological studies of two component high build epoxy and polyurethane based high performance coatings,” *J. Coatings Technol. Res.*, vol. 10, no. 3, pp. 305–315, May 2013.

[32] H. Song *et al.*, “Inkjet printing of magnetic materials with aligned anisotropy,” *J. Appl. Phys.*, vol. 115, no. 17, p. 17E308, May 2014.

CHAPTER 6: DEVELOPMENT AND CHARACTERIZATION OF STABLE POLYMER FORMULATIONS FOR MANUFACTURING MAGNETIC COMPOSITES

6. Overview of Chapter 6

The present chapter describes the engineering of magnetic particle reinforced formulations to fabricate permanent magnets suitable for electro-mechanical applications. Materials are engineered primarily for material jetting based additive manufacturing process. The overall goal is to utilize engineered material formulations and evaluate how different process issues are tackled using engineered material formulations. Technical contributions in this chapter include

- Characterization of basic and complex rheological properties of additive modified and hybrid magnetic particle reinforced formulations
- Determination of properties like yield strength, storage and loss modulus of formulation materials
- Magnetic characterization of magnetic composites and determine properties like magnetic saturation, remanence and coercive field.

6.1 Introduction

Permanent magnets are used in a wide range of consumer and industrial applications that involve the conversion of mechanical energy to electrical energy, and vice versa. Permanent magnets find applications in areas like factory automation, medical devices, household appliances, consumer electronics and automotive systems. Permanent magnets are utilized in electro-mechanical devices such as microwave generators, motors, dynamos, actuators, speakers and magnetic couplings [1,2]. Among

many permanent magnet materials, alnico, ferrites, samarium cobalt, and neodymium iron boron ($Nd_2Fe_{14}B$, abbreviated herein as NdFeB) are predominantly used in the industry. The hard-magnetic properties of these materials make them attractive for selective applications over other magnetic material options. A permanent magnet where the magnetic powder is mixed with a polymeric binder is called a bonded magnet. Commonly utilized magnetic powders include the aforementioned magnetic materials and hybrid mixtures thereof. The binders include polyamide (PA), polytetrafluoroethylene, epoxies, polyester and polyphenylene sulphide. Four traditional processes utilized to manufacture bonded magnets are extrusion, compression molding, injection molding and calendaring [3]. The properties of the polymer bonded magnets depend on the type of magnetic filler used, the polymer binder and the distribution of the filler [4].

Magnetic composites with magnetically hard and soft fillers find applications in electrical machines due to their favorable mechanical, magnetic and physical properties. Electric motors are devices utilized to convert electrical energy to mechanical energy with high conversion efficiency [5]. One such application is a flywheel energy storage system (FESS), which utilizes an electrical machine that functions both as a motor and generator [6]. Edwards et al. developed fiber-reinforced polymer composite laminates with both mechanical and magnetic functionality for use in electromechanical applications [7]. Mechanically stiff magnetic composites with high tensile elasticity and electrical resistivity were developed using bidisperse iron particles for flywheel lift magnet applications [8]. With the motive of developing anisotropic magnetic polymer composites with enhanced magnetic characteristics,

particle structuring using uniaxial and biaxial fields has been adopted to fabricate composites with chain and sheet like particle structures, respectively. To prevent the sedimentation of magnetic particles during fabrication, a magnetic field supplied by permanent magnets during the room temperature gelling of resin combined with a multistage curing methodology was utilized [9].

Additive manufacturing (AM) is a rapid prototyping technique where parts are constructed by adding materials in layers, where each layer of the part is a thin cross-section derived from a computer-aided design (CAD) file. AM enables the production of complex three-dimensional (3D) objects directly from CAD data without having to consider tooling [10]. AM of magnetic components has been an extensive field of research to develop components for the electrical and electronic industry. Researchers have studied both metal and polymer-based AM systems to manufacture magnetic functional materials. Mikler et al. demonstrated laser additive processing of three soft magnetic alloys using direct energy deposition [11]. Nilsen et al. utilized powder bed fusion to develop ferromagnetic nickel–manganese–gallium alloy and studied the influence of process parameters using structured experimental design [12]. A commercial multi-extruder 3D printer was utilized by Yan et al. for fabricating magnetic components in an effort to simplify integration processes in power electronic circuits [13]. The feasibility of AM processes to fabricate complex magnetic components by printing a conductive winding along with a magnetic core has been reported in the technical literature [14]. Additionally, improvements in magnetic properties were reported by adjusting the feed paste formulation, its flow characteristics and AM process parameters. Direct-write AM of NdFeB polymer bonded permanent

magnets using epoxy as a binder was demonstrated by Compton et al. [15]. In other research, big area additive manufacturing of isotropic NdFeB powder in PA binder enabled the manufacturing of magnets with enhanced remanence and coercive field compared to traditional injection-molded magnets [16]. Polymer bonded permanent magnets with anisotropic properties were developed by applying an external magnetic field with intensities varying from 5 kOe to 50 kOe using an electromagnet as a part of the post printing process [17]. Methodologies to orient ferromagnetic particles at user defined angles and the influence of external magnetic field strength on degree of particle alignment at lower filler loadings for AM process have been reported in the technical literature [18]. Magnetic products based on strontium ferrite ($SrFe_{12}O_{19}$, abbreviated herein as SrFeO) and NdFeB were fabricated using the extrusion of developed strips and filaments using ethylene ethyl acrylate as a binder [19]. Stainless steel microparticles in an acrylonitrile butadiene styrene polymer matrix were 3D printed with the motive of utilizing the resulting parts in the application of passive magnetic sensors and actuators [20]. Magnetic composites using a NdFeB/PA magnetic filament were printed for the prototype of a rotary blood pump and successfully integrated [21]. Research related to 3D printing polymer bonded magnets has mainly been focused on thermoplastic polymers and enhancing magnetic filler loading and efficiency. Thermoplastic filaments with engineered magnetic particle content for AM have already been reported in the technical literature [20]. In contrast, developing a methodology to engineer magnetic particle content in 3D printed thermoset composites has received limited attention and is thus one of the many challenges addressed in the present work.

In this research, the authors develop and engineer magnetic pastes for in-situ polymerization and material jetting-based AM processes. First, magnetic pastes were engineered to prevent particle settling at room temperature and at elevated curing temperatures. X-ray diffraction (XRD) analysis was utilized to validate the ability of the material formulations to resist gravitational particle settling after the thermal curing process. The rheological properties of the magnetic pastes with multi modal magnetic particles and an additive material were characterized. These results were utilized to elucidate the material behavior encountered in different stages of the manufacturing process. Developed magnetic pastes were further used to print 3D magnetic structures using an in-house developed material jetting 3D printer. Initial material deposition trials were conducted to observe uncertainties and also tune the deposition parameters for a stable deposition. Tailoring the paste rheology enabled the printing of magnetic composites with engineered magnetic particle loading without significant deformation after the curing process. The particle distribution in 3D-printed magnetic composites was characterized using scanning electron microscopy (SEM). Magnetic characterization of 3D-printed composites was conducted using a SQUID (superconducting quantum interference device) magnetometer. The results from this research enable an in-depth understanding of the role that engineered material formulations play in overcoming several manufacturing process issues and demonstrate the clear benefits of utilizing tailored rheology to one's advantage.

6.2 Materials and methods

6.2.1 Material utilized

For this study, anisotropic NdFeB powder (type MQA-38-14) was purchased from Magnequench Inc. (Singapore), and SrFeO powder was purchased from Dowa

Electronics Materials Co. Ltd. (Tokyo, Japan). For the pre-polymer, a bisphenol A based epoxy resin, EPON 826, with an aromatic amine curing agent, EPICURE W, were used (Hexion Inc., Columbus, OH, USA). Disparlon 6900-20X obtained from King Industries (Norwalk, CT, USA) was used as an anti-settling additive and shear thinning agent. Table 6.1 lists the physical properties of the magnetic particles and the epoxy resin.

Table 6.1: Physical properties of materials utilized (as obtained from manufacturers).

Material Type	Average Particle Size	Density [g/cm^3]
MQA-38-14 (NdFeB)	90 μm	7.51
SF-500 (SrFeO)	1.41 μm	3.41
EPON 826	-	1.16

6.2.2 Scanning Electron Microscopy

The morphology of the magnetic particles and the magnetic particle-reinforced composites was studied using a Zeiss Sigma 300 VP field-emission scanning electron microscope (Oberkochen, Germany) equipped with secondary and backscattered electron detectors. Prior to imaging, the composite samples were cut, polished, and finally coated with carbon using a Leica EM SCD005 evaporative carbon coater (Wetzlar, Germany) to prevent the charging of the composite surface.

6.2.3 Preparation of magnetic paste formulations

The composite mixtures were prepared from epoxy resin, which in some cases was modified with the rheological additive, and magnetic particles by mechanical mixing using an impeller agitator from Calframo Ltd. (Georgian Bluffs, ON, Canada).

The additive material was premixed with the epoxy resin to create a pre-polymer base (additive modified epoxy is herein abbreviated as aZEPX where 'Z' indicates the additive weight fraction). For rheological studies, the magnetic particles were then added in increments to the pre-polymer base to meet the desired filler loading. For the 3D-printed and cured samples used in the magnetic characterization, the required quantity of the curing agent was included in the amount of base pre-polymer when determining the mass of magnetic filler to ensure the desired filler loading was achieved. Acetone was used to aid in the dispersion process. The curing agent, when needed, was added as the last component of the magnetic paste formulation. After blending, the composite mixtures were degassed in vacuum to remove entrapped volatiles.

6.2.4 Rheological characterization

The rheological behavior of magnetic paste formulations was assessed using an Anton–Parr MCR 302 rheometer equipped with a 25 mm diameter parallel plate geometry. Table 6.2 lists the material formulations that were characterized for their rheological properties. For all the rheological tests, the magnetic filler loading in the magnetic paste formulations was maintained at 50 wt%. Hy-EPX sample, which is a hybrid formulation, containing 30 wt% of NdFeB and 20 wt% of SrFeO.

The viscosity of the magnetic pastes was monitored as a function of shear rate at room temperature. A single rheological experiment was performed for each of the materials listed in Table 6.2. The resulting flow curve data were constructive for deriving a fundamental understanding of how rheological properties are influenced by magnetic particle size and additive loading. The yield stress, defined as the shear stress

at zero shear rate, was estimated by curve fitting of the Herschel–Bulkley model (as shown in Eq.6.1) to flow curve data.

Table 6.2: Materials characterized for rheological properties.

Sample Name	Material Type	Magnetic Filler Loading
EPX	Pure epoxy	-
NdFeB-EPX	NdFeB + epoxy	50 wt%
SrFeO-EPX	SrFeO + epoxy	50 wt%
Hy-EPX	NdFeB + SrFeO + epoxy	50 wt%
NdFeB-a5EPX	NdFeB + epoxy modified with 5 wt% additive	50 wt%
NdFeB-a10EPX	NdFeB + epoxy modified with 10 wt% additive	50 wt%

$$\tau = \tau_0 + \mathrm{C}\dot{\gamma}^n \tag{6.1}$$

Here, τ_0 is the yield stress, C is the consistency index, τ is the shear stress, $\dot{\gamma}$ is the shear rate and n is the flow index. The value of the flow index enabled the classification of material behavior as shear thinning ($n < 1$), shear thickening ($n > 1$), or Bingham fluid ($n = 1$) [22]. The shear thinning index (STI)—the ratio of viscosity at two different shear rates—was used to estimate the extent of non-Newtonian behavior exhibited by the magnetic paste formulations [23]. Rheological analysis of magnetic pastes is essential for understanding the paste behavior at different shear rates experienced by the paste inside the cylinder barrel and nozzle for 3D printing processes [24]. Moreover, to understand the influence of temperature on flow behavior, the viscosity of the magnetic pastes was measured at different temperatures (i.e. 60, 80 and 100 °C) with

increasing shear rates. The Arrhenius equation is widely used to describe the relationship between viscosity and temperature, i.e.,

$$\eta = A \cdot \mathrm{e}^{E_\eta / RT} \tag{6.2}$$

where E_η is the flow activation energy, R is the ideal gas constant, T is the absolute temperature, A is the regression coefficient and η is viscosity [25,26].

Oscillatory rheology measurements (e.g., frequency sweep tests at amplitude γ = 1%) were also conducted on the magnetic pastes to determine the viscoelastic properties, such as storage modulus (G'), loss modulus (G") and damping factor (tan δ) of the samples. Studying the viscoelastic response of the samples provided the opportunity of identifying whether the magnetic pastes exhibited liquid like or solid like behavior, which enabled the evaluation of the effects of the particulate microstructure in the pre-polymeric matrix. Frequency sweep tests have previously been utilized to evaluate the material consistency at rest, storage stability, sedimentation, synergies and phase separation of polymeric dispersions [22].

6.2.5 Particle settling evaluation in uncured and cured magnetic polymer composites

The capability of the rheological additive to mitigate particle settling at room temperature was assessed using simple sedimentation experiments, where particle settling effects were captured using digital photographs. The magnetic paste formulations listed in Table 6.2 were utilized for the experiments. The prepared pastes were transferred into transparent glass beakers where settling assessment experiments were conducted. To evaluate the capability of the material formulation to withstand particle settling at elevated curing temperatures, a measured quantity of the magnetic paste formulation was transferred to a small aluminum cuvette and subsequently cured

in an oven at 80 °C for 4 hours. Additionally, particle settling was evaluated using XRD tests. XRD measurements were performed using a Geigerflex 2173 diffractometer (Rigaku Corporation, Tokyo, Japan) fitted with a Co-tube X-Ray source (λ = 1.789 Å; 38 kV and 38 mA) and a graphite monochromator to filter the Co K-β wavelength. The samples were scanned over 2θ, ranging from 30° to 90° at a rate of 2 °/min. Both the top and bottom surface of the cured samples were analyzed. The cured samples were also analyzed over their cross-section via SEM to corroborate findings derived from XRD testing.

6.2.6 Additive manufacturing of magnetic polymer composites

A material jetting-based additive manufacturing technique was utilized to deposit the magnetic pastes and fabricate the magnetic composites. For this purpose, an in-house developed material jetting platform was equipped with a precision dispensing system (Ultimus V, Nordson EFD, East Providence, RI, USA), controlled using the Labview software environment [27] (National Instruments, Austin, TX, USA). A graphical user interface enabled the adjusting of the dispensing pressure and deposition speed. The open source software Sli3cr was used to generate the g-code for the tool path based on given input parameters like layer thickness, extruded material width and infill pattern [28]. Deposition trials were conducted to determine the feasible parameter combinations prior to actual composite fabrication.

6.2.7 Magnetic characterization

The materials listed in Table 6.3 were mixed, 3D printed, cured and then used for magnetic characterization. The target magnetic filler loading was 80 wt% for NdFeB80-a10EPX-C, SrFeO80-a10EPX-C and Hy80-a10EPX-C, and 50 wt% for NdFeB-a10EPX-C, with the base pre-polymer for all samples comprising 10 wt%

rheological additive ('C' in the material identifier indicates cured epoxy pastes). Small pieces from the 3Dprinted, not pre-magnetized samples were weighed and then placed in gelatin capsules, which were themselves inserted into clear and diamagnetic plastic straws. The magnetic properties of the polymer composites were measured using a SQUID magnetometer (MPMS XL-7 Evercool, Quantum Design, San Diego, CA, USA). Magnetization reversal loops were measured for each composite listed in Table 6.3 in magnetic field strengths of $\mu_0 H = \pm 7$ Tesla at temperatures of 325, 350, 375 and 395 K. The saturation magnetization was determined at a field of 7 T. The remanence and coercivity were quantified by the linear interpolation of the magnetization at zero applied field, and the applied field at zero magnetization, respectively. The magnetic parameters were determined by averaging the values for both field sweep directions.

Table 6.3: Materials 3D printed and characterized for magnetic properties.

Material Number	**Material Type**	**Magnetic Filler Loading**
NdFeB80-a10EPX-C	NdFeB + epoxy modified with 10 wt% additive	80.2 wt%
SrFeO80-a10EPX-C	SrFeO + epoxy modified with 10 wt% additive	80.1 wt%
Hy80-a10EPX-C	NdFeB + SrFeO + epoxy modified with 10 wt% additive	80.8 wt%
NdFeB-a10EPX-C	NdFeB + epoxy modified with 10 wt% additive	50.1 wt%

6.3 Results

6.3.1 SEM characterization of magnetic fillers

Figure 6.1 shows the morphological features of magnetic particles investigated via SEM. The images of NdFeB and SrFeO particles indicate irregular morphology. Even though particle size data was obtained from material data sheets, particles dimensions were measured in the SEM images using the ImageJ software (National Institutes of Health, Bethesda, MD, USA) [29]. Particle linear dimensions ranging from 5 to 120 μm were observed for anisotropic NdFeB, and 0.5 to 5 μm for anisotropic SrFeO, indicating a wide particle size distribution of the magnetic fillers. It is assumed that smaller particles enabled the enhancing of the loading fraction by filling in gaps between larger particles.

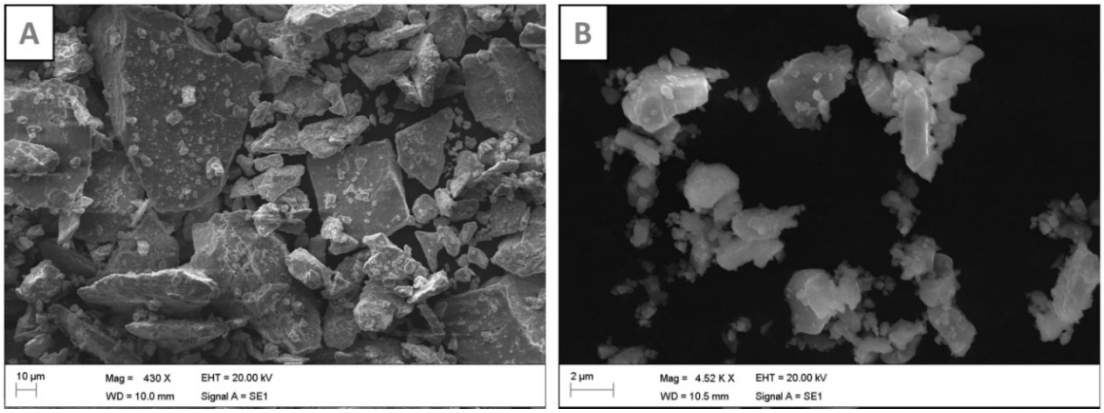

*Figure 6.1: SEM images of magnetic particles: (**A**) NdFeB and (**B**) SrFeO.*

6.3.2 Viscosity and flow curve analysis

Rheological properties of magnetic pastes play a significant role in controlling and optimizing the manufacturing process conditions. The rheological behavior of complex material systems depends on a multitude of parameters, including particle size, shape, filler volume fraction, inter-particle and filler-matrix interactions [30]. The rheological

properties of the samples under rotational and oscillatory flow fields were analyzed to study the effects of particle size and rheological additive on flow behavior and network structure of the magnetic pastes.

Apart from the pure epoxy that exhibits a Newtonian flow behavior (shear rate independent), all magnetic pastes exhibit non-Newtonian behavior, which can be identified by a decrease in the viscosity of the magnetic pastes with increasing shear rate (see Figure 6.2). Utilizing Eq.6.1, the rheological properties of the magnetic pastes (i.e., yield strength, flow index and consistency index, listed in Table 6.4) were derived in order to investigate the influence of the constituent materials utilized to formulate the magnetic pastes. In general, for all the magnetic paste formulations, the flow index, which represents the degree of pseudo-plasticity, was found to be less than unity (i.e., $n < 1$), indicating shear thinning behavior. Additionally, STI values greater than unity confirm pseudo-plastic behavior, and the magnitude of the STI values for all the magnetic pastes enabled us to understand the extent of pseudo-plasticity within the probed range of shear rate window. It was observed that fine SrFeO particles and rheological additives significantly enhanced the yield strength of the magnetic paste formulations. To elaborate on this observation, NdFeB-EPX sample, compared to SrFeO-EPX sample, exhibits lower viscosity at low shear rates (see Figure 6.2), which is attributed to the higher surface area to volume ratio of SrFeO as compared to NdFeB. Hence, for the same filler loading in the magnetic pastes, SrFeO particles feature a considerably greater surface area compared to NdFeB. The effect of fine SrFeO particles is clearly observed in the yield strength of the magnetic pastes, which is 30 times higher than that of samples containing NdFeB particles. The hybrid magnetic

paste (Hy-EPX) exhibited significant enhancement in low-shear viscosity and yield strength compared to NdFeB-EPX sample. Again, this enhancement is attributed primarily to the presence of fine SrFeO particles. A decrease in flow index for materials SrFeO-EPX and Hy-EPX compared to NdFeB-EPX is congruent to findings in the technical literature, where a reduction in flow index was observed with decreasing particle size [26].

Referring to Figure 6.2 and Table 6.4, comparing sample NdFeB-EPX with NdFeB-a5EPX and NdFeB-a10EPX reveals that the addition of the rheological additive (Disparlon 6900-20X) significantly increased the low shear viscosity and yield strength of the magnetic pastes.

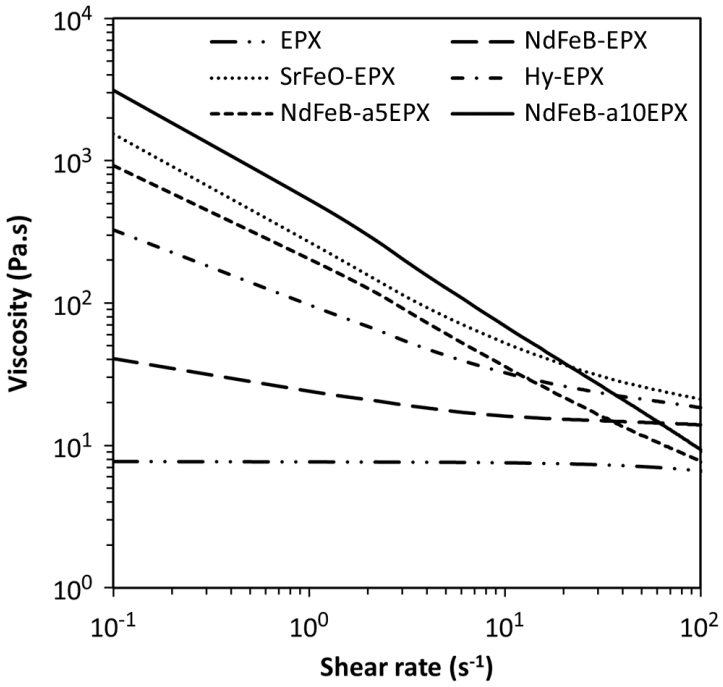

Figure 6.2: Viscosity as a function of shear rate for the magnetic pastes as listed in Table 6.2

This rheological additive is known to create a 3D network through hydrogen bonding with epoxy pre-polymer chains resulting in a gel-like structure. Epoxy resins containing

the rheological additive exhibit shear thinning behavior through the disruption of the network structure, while the formation of hydrogen bonds imparts thixotropic properties, enabling time-dependent changes in viscosity [31]. Comparing flow behavior of samples NdFeB-a5EPX and NdFeB-a10EPX, it can be concluded that an increase in rheological additive content fostered strong shear thinning behavior, which is supported by a low flow index value. Overall, the addition of fine SrFeO particles and the rheological additive raised the yield strength compared to samples containing only NdFeB particles, which is highly desirable for the considered 3D printing processes.

Table 6.4: Derived rheological properties of the magnetic pastes as listed in Table 6.2

Material Number	**Yield Strength [Pa]**	**Flow Index-*n***	**Consistency Index-*C***	**STI**
EPX	-	-	-	1
NdFeB-EPX	7.87	0.96	17.02	3
SrFeO-EPX	235.16	0.82	43.48	30
Hy-EPX	67.77	0.84	36.92	10
NdFeB-a5EPX	159.40	0.49	63.24	26
NdFeB-a10EPX	232.66	0.19	302.37	46

6.3.3 Influence of temperature on viscosity

The temperature dependence of viscosity must be carefully considered to control particle settling at elevated curing temperature in in-situ polymerization and to ensure geometric stability in material jetting processes. As is observed in Figure 6.3A, the viscosity of all the magnetic paste formulations decreased with increasing temperature.

It is clearly observed that rheological additives in samples NdFeB-a5EPX and NdFeB-a10EPX enabled maintaining higher shear viscosity up to 100 °C compared to formulations without an additive. The observed material behavior is consistent with the Arrhenius law presented in Eq.6.2 where viscosity has a negative correlation with temperature. Modifying Eq.6.2, it can be shown that ln(η) has a linear relationship with 1/T. For example, the magnetic pastes containing NdFeB (samples NdFeB-EPX, Hy-EPX and NdFeB-a10EPX) exhibit such a linear relation with good agreement, as indicated by Figure 6.3B. It can be observed that the rate of viscosity decrease is substantially lower for the formulation engineered with the rheological additive (NdFeB-a10EPX) as compared to the other NdFeB composites (NdFeB-EPX and Hy-EPX), confirming that formulations engineered with the rheological additive are less susceptible to temperature changes. Furthermore, the activation energy was calculated from the slope of ln (η)–(1/T) curves with the known R value according to Eq.6.2. The activation energies (E_η) obtained for NdFeB-EPX, Hy-EPX and NdFeB-a10EPX are 72.2 kJ/mol, 54.9 kJ/mol and 34.9 kJ/mol, respectively. It is observed that the formulation engineered with rheological additive (NdFeB-a10EPX) exhibited a lower activation energy compared to the formulation without additive (NdFeB-EPX). Activation energy is an indicator used to characterize the thermal susceptibility of materials. Materials with low activation energy were observed to be less susceptible to temperature changes [26,32]. Additionally, the chosen rheological additive (Disparlon 6900-20x) is PA based with a high melting point, which extends its activity to high temperature ranges [33].

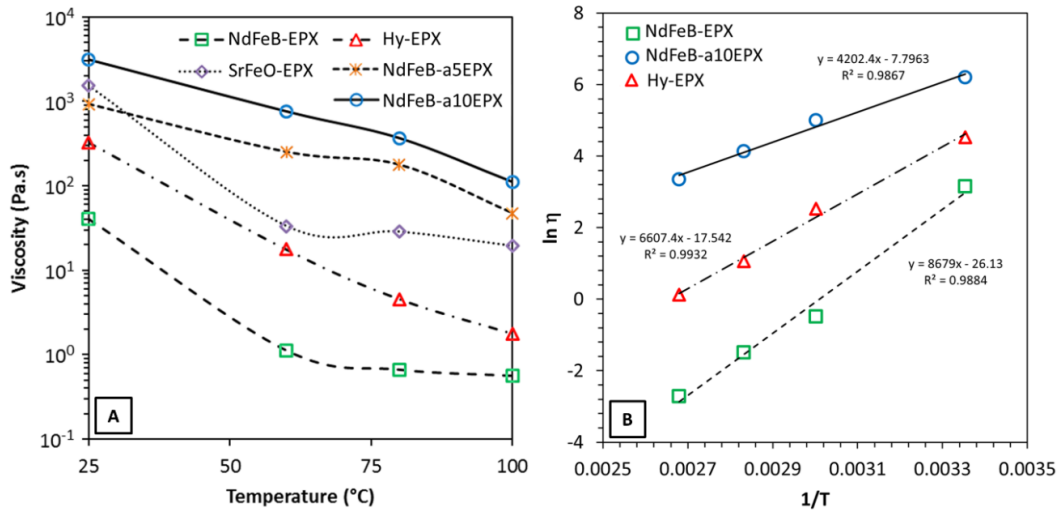

*Figure 6.3: (**A**) Viscosity as a function of temperature at shear rate of 1 s^{-1} for magnetic paste materials listed in Table 6.2. (**B**) Viscosity–temperature data linear curve fitting with linearized Arrhenius equation (Eq.6.2) for NdFeB based magnetic paste materials NdFeB-EPX, Hy-EPX and NdFeB-a10EPX (as per Table 6.2).*

6.3.4 Oscillatory rheology analysis of magnetic paste formulations

Oscillatory frequency sweeps have been widely used to characterize pre-polymer filled samples (polymer composites, polymer solutions, etc.) [34,35]. Information about a sample's rigidity and network structure can be obtained by studying viscoelastic parameters, such as the storage modulus (G'), loss modulus (G'') and damping factor (tan δ) [36]. The storage and loss moduli are indicative of the energy that is stored and dissipated in the material, respectively. In the present study, the viscoelastic characteristics of the pastes were probed using frequency sweep tests conducted over an angular frequency (ω) ranging from 0.1 to 100 rad/s at a constant shear strain γ_0 = 1%. Figure 6.4 A, B depict the frequency dependence of G' and G'' on ω, respectively. For samples NdFeB-EPX, SrFeO-EPX and Hy-EPX, the loss modulus was greater than the storage modulus (G'' > G') for the entire range of probed frequencies, which indicates that the viscous character is dominant.

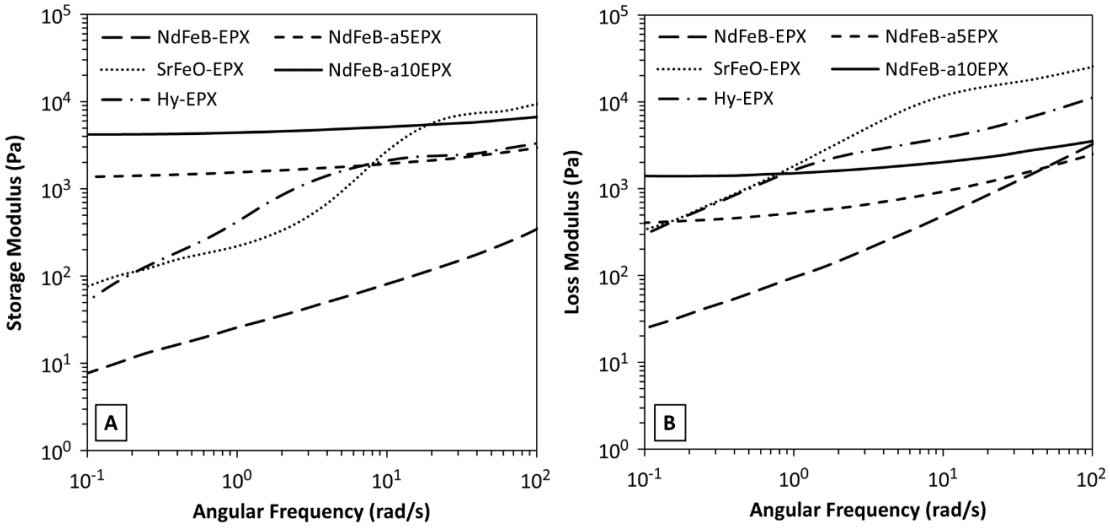

*Figure 6.4: (**A**) Storage modulus G' and (**B**) loss modulus G'' as a function of angular frequency for magnetic paste materials listed in Table 6.2.*

For samples NdFeB-a5EPX and NdFeB-a10EPX, which contain the rheological additive, the opposite behavior was observed, i.e., the storage modulus was higher than the loss modulus ($G' > G''$), signaling a solid-like behavior. This change in the material behavior is imparted by the rheological additive due to the formation of a gel character via hydrogen bonding. Moreover, it is observed that the gradient in modulus curves over the frequency range for magnetic pastes with the rheological additive is considerably less than for the pastes without additive. At higher frequencies, the material response time is considerably lower that has resulted in higher storage and loss modulus values. This characteristic indicates reduced material flowability, which further corroborates the existence of gel-like behavior in pastes containing the rheological additive. Given the observations made for the storage and loss moduli, the ratio of loss modulus to storage modulus ($\tan \delta = G''/G'$) is less than unity for magnetic paste formulations containing the rheological additive (NdFeB-a5EPX and NdFeB-a10EPX) whereas $\tan \delta > 1$ for the other paste formulations. As such, the findings are

congruent with the notion that higher tan δ values are indicative of greater energy dissipation, as in the case of the magnetic paste formulations without rheological additive. Hence, oscillatory and rotational rheometry confirm that the used additive confers the vital prerequisites for 3D-printing of the magnetic pastes.

6.3.5 Particle settling at stationary conditions

Magnetic particle settling in pre-polymers is primarily due to gravity and affects the stability of the paste formulation. In the case of material jetting processes, where paste deposition through a nozzle is driven by pressure, additional inertia is exerted on particles, typically in the downward direction, which may further intensify particles' settling effects. Moreover, particle settling may lead to the clogging of the nozzle and thus create a disruption in the manufacturing process. In this study, the means to address particle settling was adding the rheological additive to the magnetic paste formulations. Figure 6.5 shows the ability of the rheological additive to mitigate gravitational particle settling. Eight hours after filling the beaker, filler sedimentation and a clear supernatant is visible for material NdFeB-EPX, while NdFeB-a5EPX and NdFeB-a10EPX are still uniformly mixed, exhibiting an anti-settling characteristic. The rheological tests indicated that the additive causes a gelling effect in the magnetic paste formulations, presumably due to the development of a thixotropic network structure. Hence, the rheological additive, providing high viscosity at low shear rates, high yield strength, and a greater storage modulus, effectively mitigated particle settling and promoted a stable paste formulation in stationary conditions.

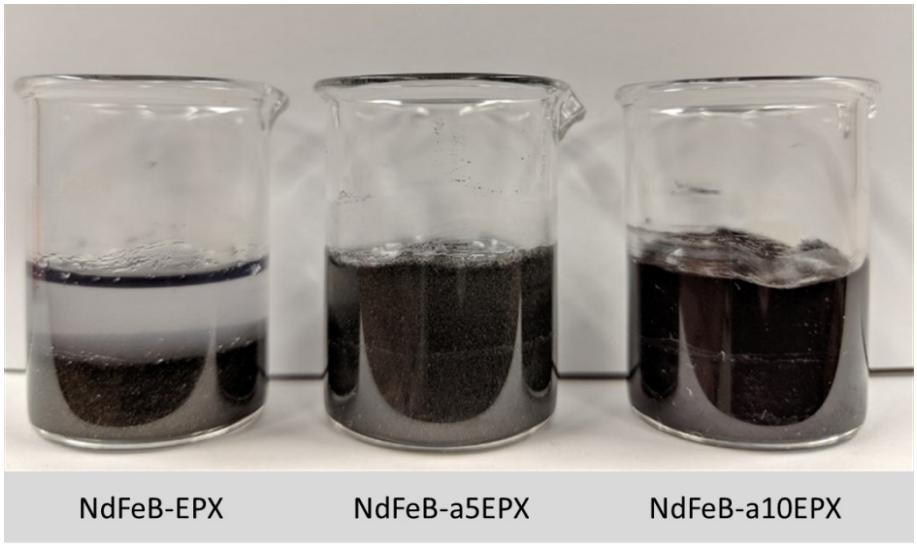

Figure 6.5: Photograph of clear supernatant in material NdFeB-EPX, while NdFeB-a5EPX and NdFeB-a10EPX exhibit an anti-settling characteristic

6.3.6 Particle settling in cured magnetic polymer composites—in-situ polymerization

Magnetic particle settling during the thermal curing process was investigated in samples manufactured using in situ polymerization, where the magnetic paste was transferred to a cuvette and cured at 80 °C. Paste formulations NdFeB-a5EPX and NdFeB-a10EPX were utilized in this set of experiments. The top and bottom surfaces of the cured samples were examined via XRD (see Figure 6.6). Strong XRD peaks of crystalline NdFeB were obtained from the bottom surfaces of the samples fabricated using both NdFeB-a5EPX and NdFeB-a10EPX, suggesting the presence of near-surface NdFeB particles (Figure 6.6 B).

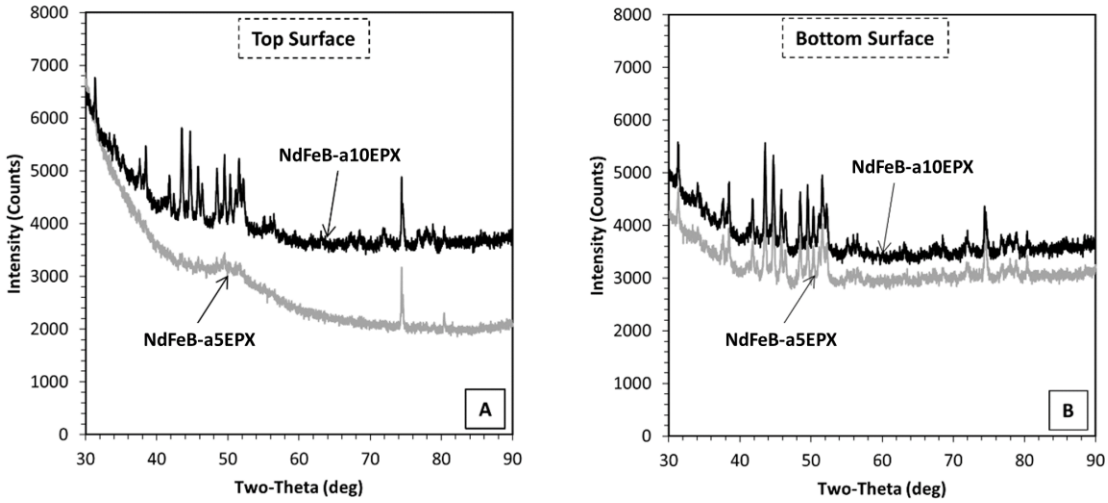

*Figure 6.6: XRD diffractograms from (**A**) top surface (**B**) bottom surface of cured materials NdFeB-a5EPX and NdFeB-a10EPX (as per Table 6.2).*

Similarly, the top surface of the sample fabricated from NdFeB-a10EPX also exhibited strong crystalline peaks (Figure 6.6 A). In contrast, the amorphous polymer peak dominants for the top surface of the NdFeB-a5EPX sample with other peaks having markedly reduced intensity, which suggests that near-surface NdFeB particles are largely absent due to settling. The XRD results thus reflect the effectiveness of the rheological additive to mitigate particle settling during the thermal curing process.

Cross-sections of the cured samples were further studied via SEM to validate the suppositions derived from the XRD study. In Figure 6.7, the sample fabricated using material NdFeB-a5EPX features a polymer-rich layer devoid of particles with an approximate thickness of 200 μm; in the sample made from NdFeB-a10EPX, particles are visible at and near the sample surface. It thus appears that some particle settling occurred in the material NdFeB-a5EPX sample, causing the observed suppression of XRD peaks

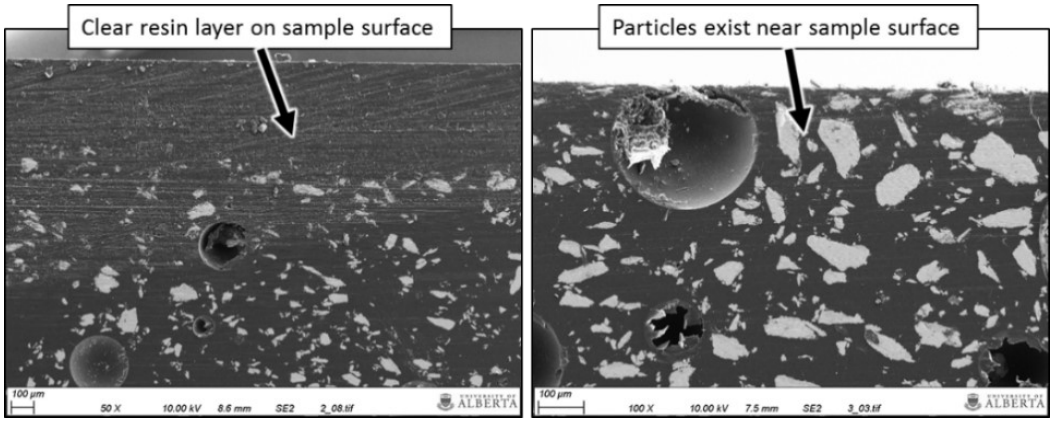

Figure 6.7: SEM cross-section images illustrating reduced particle settling in a sample of cured material NdFeB-a10EPX (right) compared to NdFeB-a5EPX (left) (as per Table 6.2). The top of the micrographs corresponds to the sample's upper surface. Some entrapped air bubbles are visible as well

6.4 Additive manufacturing and characterization of magnetic composites

6.4.1 Geometric stability observations in 3d printed magnetic composites

One of the fundamental goals of this work was to print magnetic composites using engineered paste formulations containing magnetic particles. Magnetically loaded polymer composites were thus fabricated from the developed paste formulations using an in-house developed material jetting 3D printer. For composites with 80 wt % magnetic particles, the epoxy resin with the additive was prepared as a premix where the base resin was additive mixed epoxy to which the magnetic fillers were added. It was additionally observed that for composite with 50wt% magnetic particles, both additive mixed epoxy as the resin base and additive mixed based on total formulation weight were observed to work effectively. Prior to 3D printing, trials were conducted to determine the apt printing parameters, including deposition pressure, layer thickness and deposition speed. The utilized layer thickness setting varied between 0.5 and 1.2 mm and the adopted printing speed range was between 5 and 10 mm/s. The deposition pressure for printing composites was observed to depend on the printed

magnetic pastes. The formulations containing SrFeO demanded high deposition pressures, ranging from 137 to 275 kPa; for the NdFeB formulations, the required deposition pressures were between 21 and 103 kPa. In some cases, it was required to adjust the deposition pressure and layer thickness settlings during part fabrication, as adopting the same parameters for multilayer structures resulted in gaps between the deposited layers and discontinuous prints.

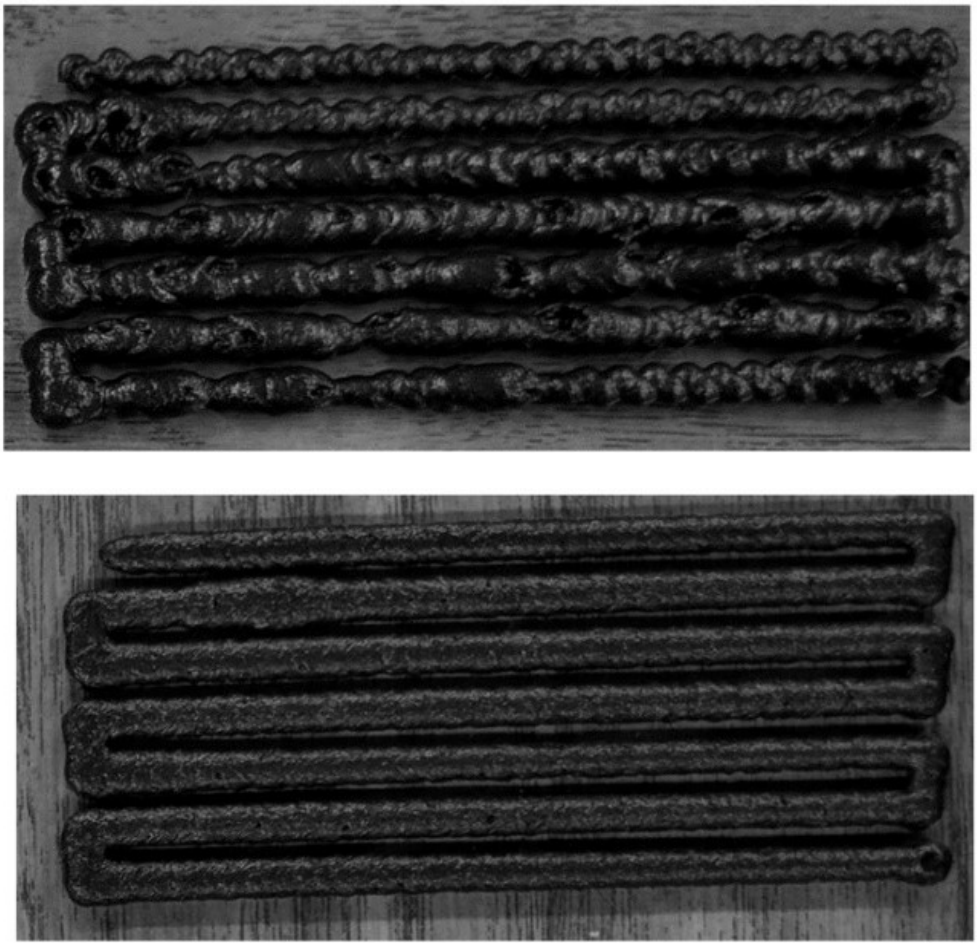

Figure 6.8: Initial deposition trials conducted to evaluate process parameters

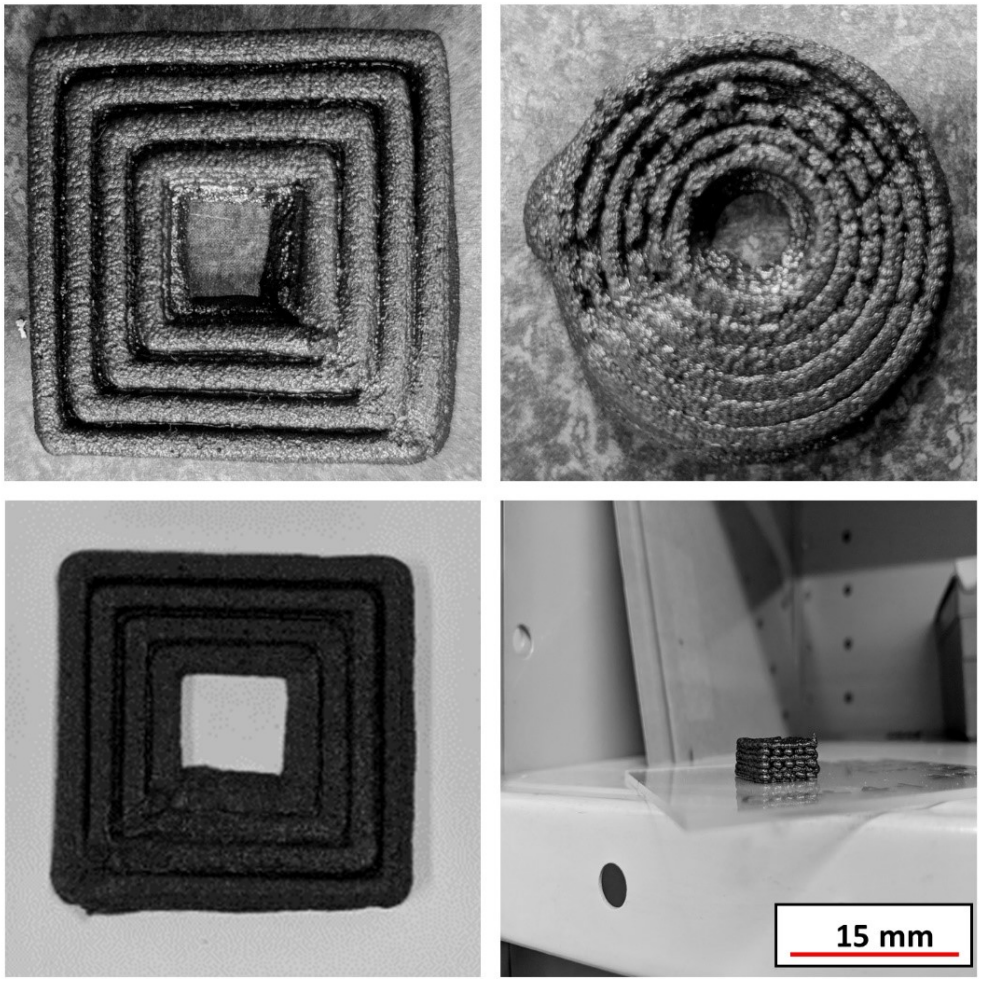

Figure 6.9: Observed gaps and discontinuities in material deposition during material jetting process

The observed deposition deficiencies in terms of gaps and discontinuous material flow are primarily due to non-uniform filling of prepolymer in the resin barrel, high prepolymer viscosity, uneven surface of the substrate material, and air entrapments in the prepolymer due to the mixing process. Additionally, laser confocal microscopy was used as tool to observe the profile shapes of material deposits and also evaluate the surface roughness in the manufactured composites

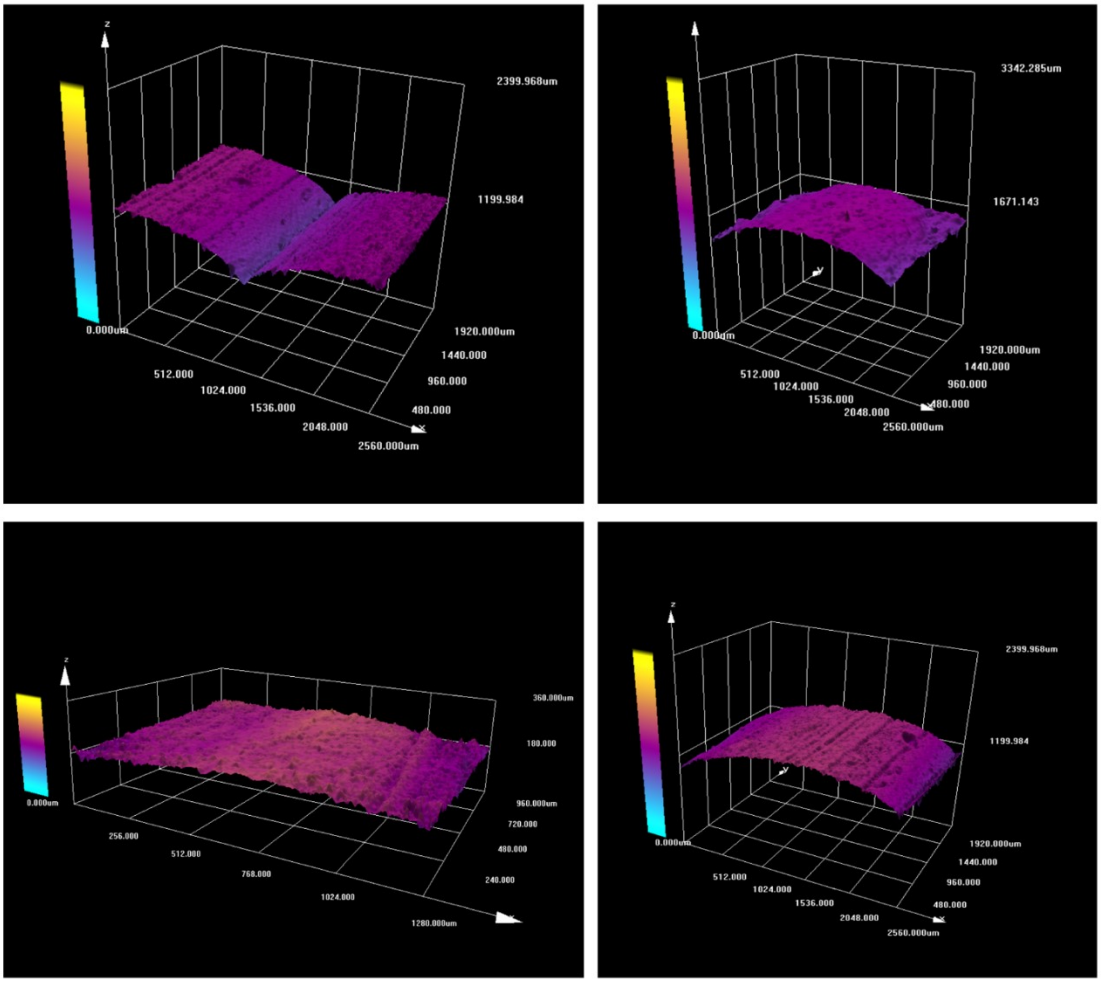

Figure 6.10: Laser confocal microscopy images of manufactured composites.

The surface roughness (R_a values) of the composites manufactured using NdFeB-EPX, SrFeo-EPX, Hybrid-EPX and NdFeB-50-EPX were observed to be 5.51, 3.41, 4.05 and 3.49 µm, respectively. Initially, samples were manufactured using materials NdFeB-EPX, NdFeB-a5EPX and NdFeB-a10EPX. Figure 6.11 shows the final shapes of the 3D-printed magnetic composites after thermal curing. It can be observed that only the paste formulations engineered using the rheological additive (NdFeB-a5EPX and NdFeB-a10EPX) retained the printed shape adequately. From rheological measurements, the formulation without the rheological additive (NdFeB-EPX) had low yield strength and exhibited viscoelastic fluid behavior, in contrast to

materials NdFeB-a5EPX and NdFeB-a10EPX. The ability of the rheologically modified resin to maintain a comparatively high viscosity over a broad temperature range, especially at curing temperatures, enabled the materials to maintain the printed geometry.

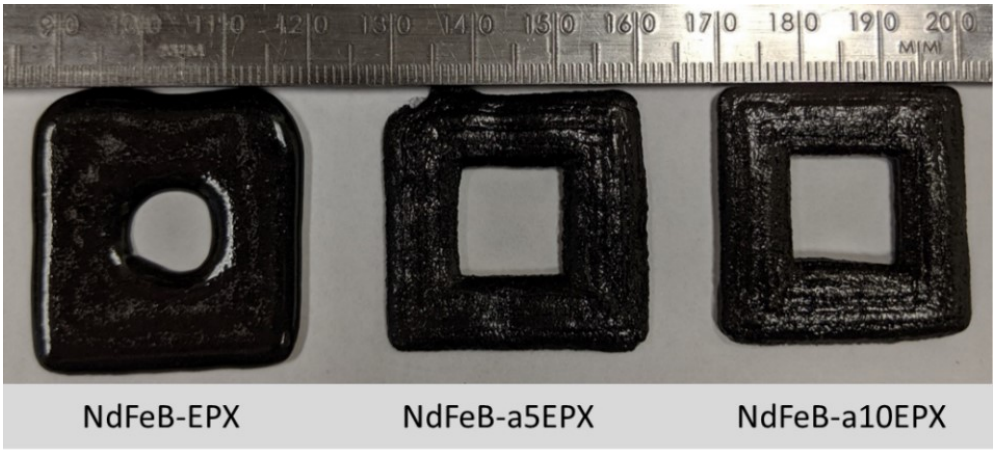

Figure 6.11: Geometry of 3D-printed composites (30 mm by 30 mm CAD dimensions) after thermal curing for paste formulations NdFeB-EPX, NdFeB-a5EPX and NdFeB-a10EPX (as per Table 6.2).

6.4.2 SEM and magnetic characterization of 3d printed composite magnets

Using SEM and the SQUID magnetometer, composites printed using the material jetting process were characterized for their microstructure and magnetic properties (e.g., saturation magnetization, remanence and coercivity), respectively. Note that even though the deformation of the deposited pastes was adequately controlled using 5 wt% rheological additive, 10 wt% additive was employed for the analyses, as this additive loading was more effective in controlling particle settling. The SEM images from the (cut and polished) surface of the printed magnetic composites exhibit a homogenous microstructure with well distributed particles, as seen in Figure 6.12. The presence of

resin-rich regions in sample NdFeB80-a10EPX-C (80.2 wt% NdFeB) is an indication that the magnetic filler loading can be further enhanced to fill gaps between particles.

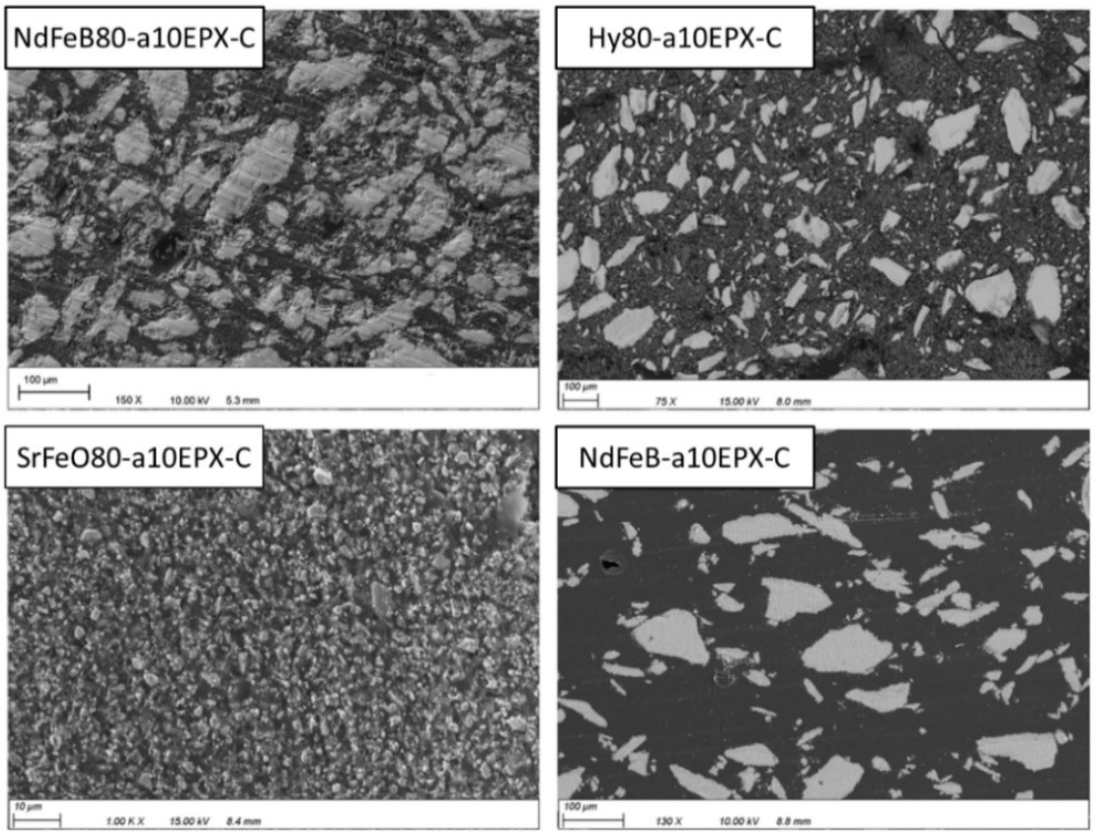

Figure 6.12: SEM images of magnetic composites listed in Table 6.3

Some porosity is also observed in the composites. The presence of porosities indicates an opportunity to improve mixing and degassing processes. Less porosity could be observed for composite SrFeO80-a10EPX-C, which features the smaller SrFeO particles. Material Hy80-a10EPX-C, which is a mixture of 60.1 wt% NdFeB and 20.7 wt% SrFeO, indicates good distribution of smaller and larger particles in the composite. Material NdFeB-a10EPX-C, which has the lower NdFeB filler loading of 50 wt%, exhibits good distribution of magnetic particles; no signs of particle agglomeration are observed. Utilizing the ImageJ software, the sizes of the NdFeB and

SrFeO particles were derived from SEM images of composite samples. The measured linear dimensions of particles, expressed in the histograms in Figure 6.13, indicate a wide particle size distribution, as indicated by the powder manufacturers.

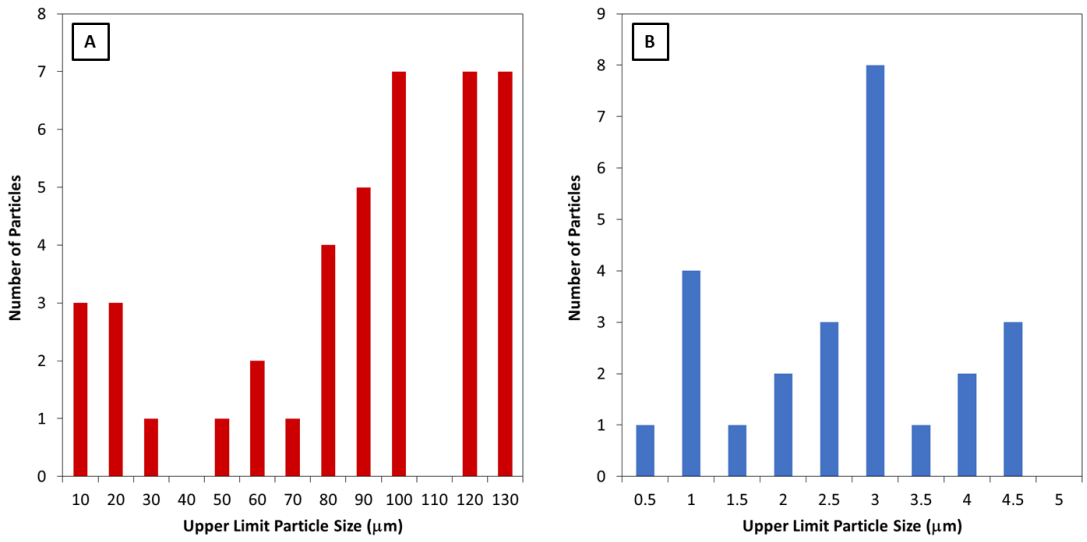

*Figure 6.13: Size distribution of (**A**) NdFeB and (**B**) SrFeO particles in manufactured magnetic composites obtained from SEM micrographs.*

Permanent magnets are characterized by remanence and coercivity, i.e., their ability to supply sufficient magnetic flux, and withstand demagnetization, respectively. High values of remanence and coercivity indicate strong magnetic performance. Figure 6.14 shows the hysteresis data obtained for the powder and magnetic composite samples fabricated in this research. Obtained hysteresis loops were observed to be similar to the ones reported in technical literature for isotropic bonded magnets [15,37].

Figures 6.15 and 6.16 show, respectively, the saturation magnetization (M_s), remanence (M_r) and coercive field (H_c) extracted from hysteresis loops at temperatures between 300 and 400 K for the composite samples and powders. In these figures, the extracted data from the hysteresis loops are depicted with best linear fits to ease

understanding the overall influence of temperature on magnetic properties. The errors are estimated to be ±5 emu/g for remanence and saturation magnetization and ±0.1 kOe for the coercive field for all samples. The values of magnetic saturation for all the composite samples match within the error band of the loading-adjusted powder saturation magnetization, which indicates that the saturation magnetization is not influenced by the composite fabrication process. Remanence for samples containing NdFeB (NdFeB80-a10EPX-C, Hy80-a10EPX-C and NdFeB-a10EPX-C) behaves similarly and follows the loading adjusted powder remanence. The composite containing only the SrFeO filler (SrFeO80-a10EPX-C), however, exhibited a decrease in remanence that exceeds the expected decrease due to the loading factor. It is thus deduced that magnetic properties not only depend on the magnetic characteristics of the powder but are also a function of filler distribution and dispersion within the epoxy polymer. In general, the measured values of remanence are comparable with the values reported in the technical literature for NdFeB- and SrFeO-bonded magnets [19].

The remanence to saturation ratio, which determines the degree of anisotropy, varies between 0.35 and 0.59 for all samples in the studied temperature range. Note that a remanence to saturation ratio greater than 0.5 indicates the transition in magnetic properties from isotropic to anisotropic [37]. It is unclear whether ratios greater than 0.5, as observed herein, are caused by interparticle interactions. In terms of temperature, an increase resulted in reductions in saturation, remanence and coercivity (see Figures 6.14–6.16). Within the given error band, composites and powders exhibited similar temperature dependencies. Note that a reduction in M_s, M_r and H_c with increasing temperature is commonly observed in magnetic materials. Notably,

material SrFeO80-a10EPX-C was the most stable of the magnetic composites over the temperature range, which is consistent with the properties of the powder. It was observed that material NdFeB80-a10EPX-C exhibited a stronger dependence on temperature with respect to magnetic saturation and remanence compared to all other materials. It is noted from the technical literature that the NdFeB phase undergoes spin reorientations due to the temperature dependence of anisotropy [38]. In general, magnetic filler loading is observed to influence the coercive field. Material NdFeB-a10EPX-C (50.1 wt% magnetic filler) exhibited lower coercivity compared to NdFeB80-a10EPX-C (80.2 wt% magnetic filler).

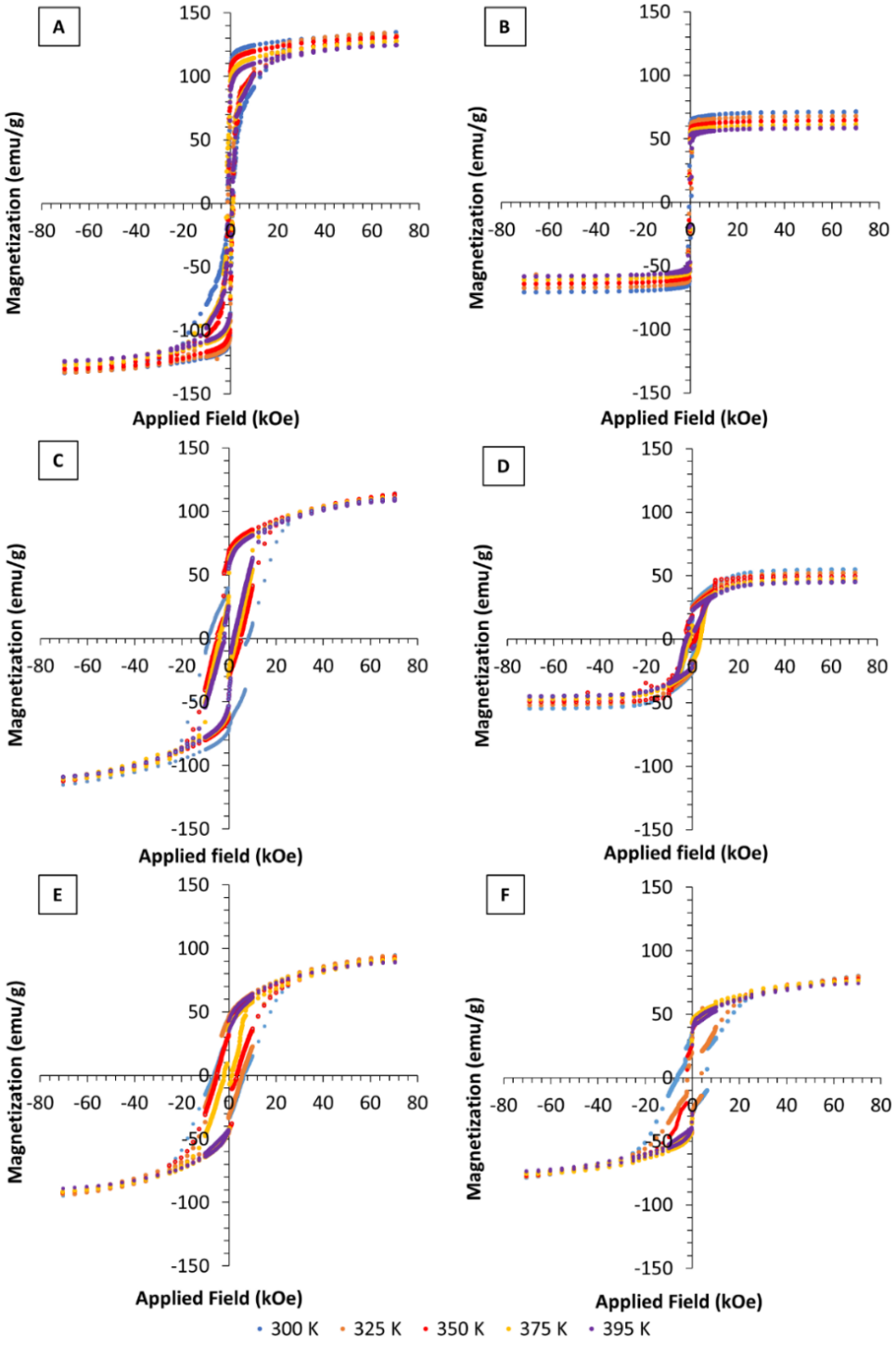

*Figure 6.14: Hysteresis data for magnetization versus applied magnetic field, for (**A**) NdFeB powder, (**B**) SrFeO powder, cured materials: (**C**) NdFeB80-a10EPX-C, (**D**) SrFeO80-a10EPX-C, (**E**) Hy80-a10EPX-C and (**F**) NdFeB-a10EPX-C (as per Table 6.3).*

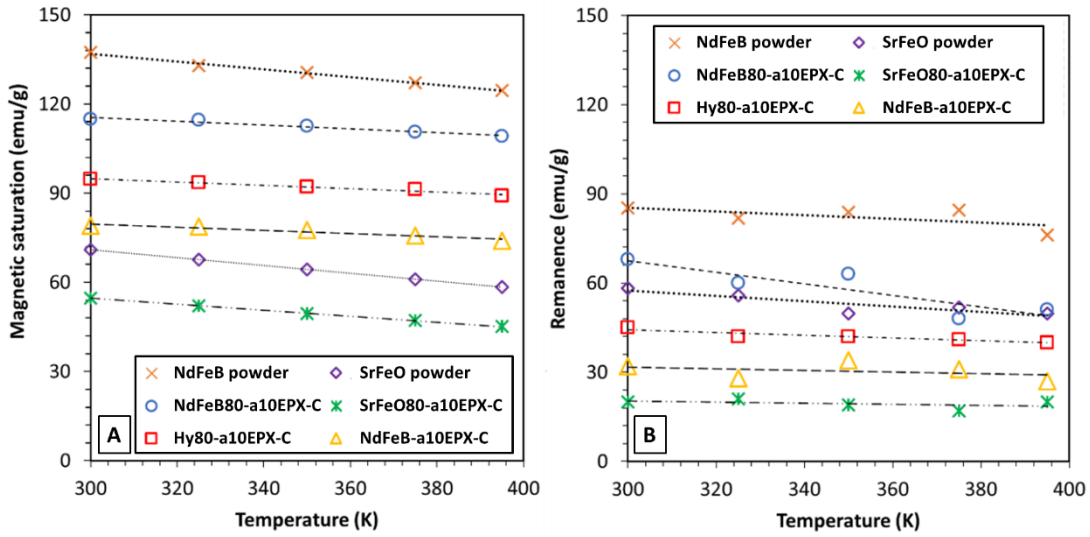

*Figure 6.15: (**A**) Saturation magnetization and (**B**) remanence of magnetic fillers and 3D-printed magnetic composites (as per Table 6.3).*

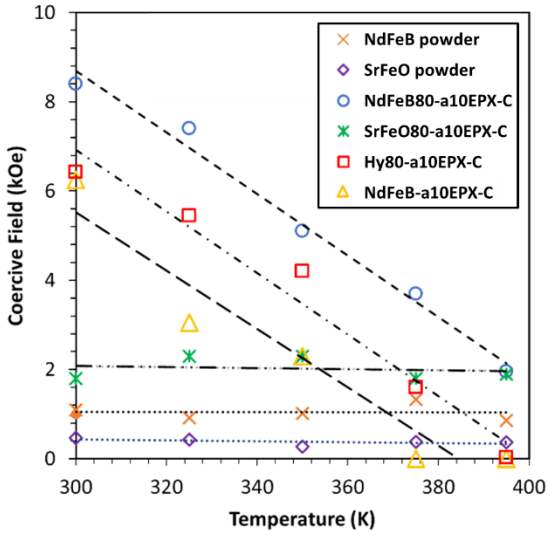

Figure 6.16: Coercive field of magnetic fillers and 3D-printed magnetic composites (as per Table 6.3).

Overall, the latter magnetic composite (NdFeB80-a10EPX-C) exhibited the best magnetic characteristics among the tested material formulations. Notably, the coercive field of NdFeB80-a10EPX-C at room temperature exceeds the properties of injection molded magnets from the same powder as mentioned in technical data sheets. No

benefits in terms of M_s and M_r could be ascertained by mixing SrFeO with NdFeB powders (Hy80-a10EPX-C), as this material behaved as expected from a simple mass weighted addition of constituents' properties. This extends to the behavior for H_c, where the addition of SrFeO did not achieve an increase at high temperatures. These findings are consistent with other research [39].

6.5 Conclusions

In this study, stable magnetic powder-based material formulations were developed and tested that can be utilized for in situ polymerization and material jetting-based additive manufacturing processes. It was observed that the addition of a rheological additive into epoxy enhanced the desired rheological properties, i.e., viscosity at low shear rates, yield strength, degree of shear thinning and storage modulus of the magnetic paste formulation. A transition in the material behavior from viscoelastic fluid to viscoelastic solid was observed in formulations that contained the rheological additive. The material modified with fine strontium ferrite particles, while having favorable rheological properties, exhibited undesirable viscoelastic fluid behavior. All the magnetic paste formulations experienced reductions in viscosity with an increase in temperature, yet the formulation modified with the highest amount of rheological additive resulted in a viscosity for low shear rates at the epoxy curing temperature that was over 500 times greater in magnitude compared to the comparable paste without additive. The ability of the material to maintain high viscosity at low shear rates at curing temperatures enabled the control of particle settling, which was validated using XRD and SEM analyses. A rheological additive loading of 10 wt% was observed to be efficient in controlling magnetic particle settling. The developed material formulation enabled the printing of magnetic composites with a filler loading of 50 wt% and 80

wt% using a material jetting based 3D printer. It was observed that the formulations engineered with the additive maintained the printed shape, whereas significant material deformation was observed in unmodified resins. SEM images indicated good distribution and dispersion of magnetic particles within the composite. Magnetic characterization enabled understanding that the resultant magnetic properties are highly dependent on the magnetic powder characteristics, filler loading and the distribution of magnetic particle within the composite. Coercivity was observed to notably decrease with increasing temperature, whereas only a moderate decrease was observed in magnetic remanence. Even through the addition of strontium ferrite enhanced certain rheological characteristics, the magnetic performance was found to be inferior. Overall, this fundamental work yielded thermally stable magnetic material formulations, which enabled the solving of fundamental material and process issues related to additive manufacturing. Future work will include utilizing the developed material formulations to print magnetic composites and characterize cure and mechanical (elastic, fracture) behavior. Additionally, blending processes shall be optimized to reduce porosity and further engineer formulations to reach higher magnetic filler loadings.

6.6 References

[1] J. Ormerod and S. Constantinides, "Bonded permanent magnets: Current status and future opportunities (invited)," *J. Appl. Phys.*, vol. 81, no. 8, pp. 4816–4820, Apr. 1997.

[2] D. Brown, B.-M. Ma, and Z. Chen, "Developments in the processing and properties of NdFeb-type permanent magnets," *J. Magn. Magn. Mater.*, vol. 248, no. 3, pp. 432–440, Aug. 2002.

[3] J. Ormerod and S. Constantinides, "Bonded permanent magnets: Current status and future opportunities (invited)," *J. Appl. Phys.*, vol. 81, no. 8, pp. 4816–

4820, Apr. 1997.

[4] J. Xiao and J. U. Otaigbe, “Polymer-bonded magnets: Part I. Analytic thermogravimetry to determine the effect of surface modification on dispersion of Nd–Fe–B fillers,” *J. Mater. Res.*, vol. 14, no. 7, pp. 2893–2896, Jul. 1999.

[5] M. Najgebauer, J. Szczygłowski, B. Ślusarek, M. Przybylski, A. Kapłon, and J. Rolek, “Magnetic Composites in Electric Motors,” in *Analysis and Simulation of Electrical and Computer Systems*, D. Mazur, M. Goł\kebiowski, and M. Korkosz, Eds. Cham: Springer International Publishing, 2018, pp. 15–28.

[6] G. Ertz, T. Hrynik, D. Lafleur, P. Mertiny, M. Secanell, and N. Wagner, “Design of Low-Cost Fly Wheel Energy Storage Systems,” *SAMPE J.*, vol. 53, no. 6, pp. 18–26, 2017.

[7] L. Edwards, J. Yon, I. Bond, and P. Mellor, “STRUCTURAL MAGNETIC COMPOSITES FOR USE IN ELECTRO-MECHANICAL APPLICATIONS,” in *ICCM 20 20th International Conference on Composite Materials (pp. 1–8)*, 2015.

[8] J. E. Martin, L. E. S. Rohwer, and J. Stupak, “Elastic magnetic composites for energy storage flywheels,” *Compos. Part B Eng.*, vol. 97, pp. 141–149, Jul. 2016.

[9] J. Martin, E. Venturini, J. Odinek, and R. Anderson, “Anisotropic magnetism in field-structured composites,” *Phys. Rev. E*, vol. 61, no. 3, pp. 2818–2830, Mar. 2000.

[10] I. Gibson, D. Rosen, and B. Stucker, *Additive Manufacturing Technologies*. New York, NY: Springer New York, 2015.

[11] C. V. Mikler *et al.*, “Laser Additive Manufacturing of Magnetic Materials,” *JOM*, vol. 69, no. 3, pp. 532–543, Mar. 2017.

[12] F. Nilsén, I. F. Ituarte, M. Salmi, J. Partanen, and S.-P. Hannula, “Effect of process parameters on non-modulated Ni-Mn-Ga alloy manufactured using powder bed fusion,” *Addit. Manuf.*, vol. 28, no. November 2018, pp. 464–474, Aug. 2019.

[13] Y. Yan *et al.*, “Additive manufacturing of magnetic components for heterogeneous integration,” in *2017 IEEE 67th Electronic Components and*

Technology Conference (ECTC), 2017, pp. 324–330.

[14] Y. Yan, J. Moss, K. D. T. Ngo, Y. Mei, and G.-Q. Lu, "Additive Manufacturing of Toroid Inductor for Power Electronics Applications," *IEEE Trans. Ind. Appl.*, vol. 53, no. 6, pp. 5709–5714, Nov. 2017.

[15] B. G. Compton *et al.*, "Direct-write 3D printing of NdFeB bonded magnets," *Mater. Manuf. Process.*, vol. 0, no. 0, pp. 1–5, Aug. 2016.

[16] L. Li *et al.*, "Big Area Additive Manufacturing of High Performance Bonded NdFeB Magnets," *Sci. Rep.*, vol. 6, no. October, pp. 1–7, 2016.

[17] K. Gandha *et al.*, "Additive manufacturing of anisotropic hybrid NdFeB-SmFeN nylon composite bonded magnets," *J. Magn. Magn. Mater.*, vol. 467, no. April, pp. 8–13, 2018.

[18] B. Nagarajan, A. F. Eufracio Aguilera, M. Wiechmann, A. J. Qureshi, and P. Mertiny, "Characterization of magnetic particle alignment in photosensitive polymer resin: A preliminary study for additive manufacturing processes," *Addit. Manuf.*, vol. 22, no. May, pp. 528–536, Aug. 2018.

[19] E. M. Palmero *et al.*, "Magnetic-Polymer Composites for Bonding and 3D Printing of Permanent Magnets," *IEEE Trans. Magn.*, vol. 55, no. 2, pp. 1–4, Feb. 2019.

[20] B. Khatri, K. Lappe, D. Noetzel, K. Pursche, and T. Hanemann, "A 3D-Printable Polymer-Metal Soft-Magnetic Functional Composite—Development and Characterization," *Materials (Basel).*, vol. 11, no. 2, p. 189, Jan. 2018.

[21] K. von Petersdorff-Campen *et al.*, "3D Printing of Functional Assemblies with Integrated Polymer-Bonded Magnets Demonstrated with a Prototype of a Rotary Blood Pump," *Appl. Sci.*, vol. 8, no. 8, p. 1275, Aug. 2018.

[22] T. G. Mezger, "The Rheology Handbook," *Pigment Resin Technol.*, vol. 38, no. 5, p. prt.2009.12938eac.006, Sep. 2009.

[23] "ASTM E3070-18, Standard Test Method for Shear Thinning Index of Non-Newtonian Liquids Using a Rotational Viscometer, ASTM International, West Conshohocken, PA, 2018,." 18AD.

[24] M. Elbadawi, J. L. Rivera-Armenta, and B. A. S. Cruz, "Polymeric Additive Manufacturing: The Necessity and Utility of Rheology," in *Polymer Rheology*,

IntechOpen Rijeka, 2018, pp. 43–63.

[25] S. Burlawar, D. J. Klingenberg, T. W. Root, K. Schlafmann, and C. Tim Scott, "Effect of temperature on the rheology of concentrated fiber suspensions," *J. Rheol. (N. Y. N. Y).*, vol. 63, no. 4, pp. 677–691, Jul. 2019.

[26] M. E. Sotomayor, A. Várez, and B. Levenfeld, "Influence of powder particle size distribution on rheological properties of 316L powder injection moulding feedstocks," *Powder Technol.*, vol. 200, no. 1–2, pp. 30–36, Jun. 2010.

[27] A. F. Eufracio Aguilera, B. Nagarajan, B. A. Fleck, and A. J. Qureshi, "Ferromagnetic particle structuring in material jetting - Manufacturing control system and software development," *Procedia Manuf.*, vol. 34, pp. 545–551, 2019.

[28] A. Ranellucci, "Slic3r." [Online]. Available: https://slic3r.org/.

[29] C. A. Schneider, W. S. Rasband, and K. W. Eliceiri, "NIH Image to ImageJ: 25 years of image analysis," *Nat. Methods*, vol. 9, no. 7, p. 671, 2012.

[30] M. Kamkar, E. Aliabadian, A. Shayesteh Zeraati, and U. Sundararaj, "Application of nonlinear rheology to assess the effect of secondary nanofiller on network structure of hybrid polymer nanocomposites," *Phys. Fluids*, vol. 30, no. 2, p. 023102, Feb. 2018.

[31] K. B. Manning *et al.*, "Self Assembly–Assisted Additive Manufacturing: Direct Ink Write 3D Printing of Epoxy–Amine Thermosets," *Macromol. Mater. Eng.*, vol. 304, no. 3, p. 1800511, Mar. 2019.

[32] H. Wang, X. Liu, P. Apostolidis, and T. Scarpas, "Rheological Behavior and Its Chemical Interpretation of Crumb Rubber Modified Asphalt Containing Warm-Mix Additives," *Transp. Res. Rec. J. Transp. Res. Board*, vol. 2672, no. 28, pp. 337–348, Dec. 2018.

[33] R. Berndlmaier, "Rheology additives for coatings," in *Handbook of coating additives*, D. J. M. John J. Florio, Ed. Marcel Dekker Inc, pp. 363–403.

[34] M. Kamkar, S. Sadeghi, M. Arjmand, and U. Sundararaj, "Structural Characterization of CVD Custom-Synthesized Carbon Nanotube/Polymer Nanocomposites in Large-Amplitude Oscillatory Shear (LAOS) Mode: Effect of Dispersion Characteristics in Confined Geometries," *Macromolecules*, vol.

52, no. 4, pp. 1489–1504, Feb. 2019.

[35] E. Aliabadian, S. Sadeghi, M. Kamkar, Z. Chen, and U. Sundararaj, “Rheology of fumed silica nanoparticles/partially hydrolyzed polyacrylamide aqueous solutions under small and large amplitude oscillatory shear deformations,” *J. Rheol. (N. Y. N. Y).*, vol. 62, no. 5, pp. 1197–1216, Sep. 2018.

[36] A. Rezvani Moghaddam, M. Kamkar, Z. Ranjbar, U. Sundararaj, A. Jannesari, and B. Ranjbar, “Tuning the Network Structure of Graphene/epoxy nanocomposites by Controlling Edge/Basal Localization of Functional Groups,” *Ind. Eng. Chem. Res.*, 2019.

[37] I. C. Nlebedim *et al.*, “Studies on in situ magnetic alignment of bonded anisotropic Nd-Fe-B alloy powders,” *J. Magn. Magn. Mater.*, vol. 422, pp. 168–173, Jan. 2017.

[38] K. P. Su, Z. W. Liu, D. C. Zeng, D. X. Huo, L. W. Li, and G. Q. Zhang, “Structure and size-dependent properties of NdFeB nanoparticles and textured nano-flakes prepared from nanocrystalline ribbons,” *J. Phys. D. Appl. Phys.*, vol. 46, no. 24, p. 245003, Jun. 2013.

[39] X. F. Wang, D. Lee, and Z. L. Jiang, “Magnetic properties of hybrid polymer bonded Nd–Fe–B/ferrite magnets,” *J. Appl. Phys.*, vol. 99, no. 8, p. 08B513, Apr. 2006.

CHAPTER 7: OTHER EXPERIMENT TRIALS AND ASSOCIATED RESULTS

7. Overview of Chapter 7

This chapter is dedicated to present the results of experimental trails conducted as a part of this research work. Some of the results expressed in this section will be utilized as base results for future work. The results comprise of a collection of magnetic composites fabricated using epoxy resins and UV curable acrylate formulations. The following aspects are discussed in this section

- Fabrication of milled glass fiber reinforced magnetic composites and composites with plate like magnetic particles using material jetting process
- Development of dual cure (UV/thermal) acrylate resin to print permanent magnets using in-situ polymerization and material jetting
- Processing and analysis of magnetic composites developed using in-situ polymerization in the presence of magnetic fields

7.1 Milled glass fiber reinforced magnetic composite using material jetting

Manufacturing fiber reinforced magnetic composites using approaches like filament winding and simple layup techniques has been reported in technical literature. Composite structures were developed with tunable mechanical and magnetic properties using traditional approaches [1] [2]. In this section, magnetic composites reinforced with milled glass fibers are manufactured using the material jetting process. The magnetic material formulation was prepared using epoxy resin (Epon 826) reinforced with 5wt % of Disparlon 6900-20X and 5 wt% of the milled glass fiber. The formulation was prepared with 70wt% Anisotropic MQA powder. Scanning electronn

microscopy (SEM) analysis conducted on printed samples enabled finding out alignment of milled glass fibers in printed composites. Figure 7.1 shows SEM images of sample surface in two different magnifications obtained after cutting, grinding and polishing the 3D printed samples.

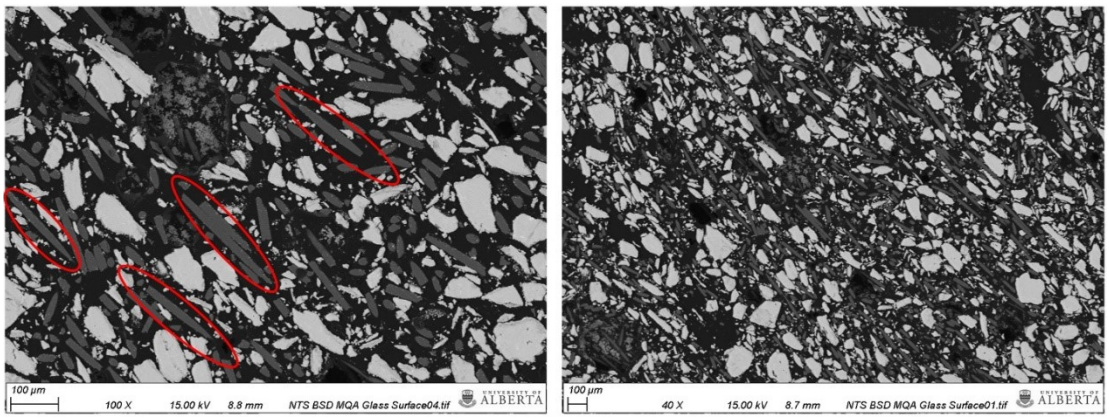

Figure 7.1: SEM images of milled glass fiber reinforced composite (Marked regions exhibit fiber alignment)

7.2 Additive manufacturing of isotropic NdFeB magnetic composites using material jetting

This section deals with the fabrication of plate like isotropic NdFeB particles using material jetting process. Isotropic NdFeB magnetic powder MQP-B2 (Magnequench Inc) was used as the magnetic material. Epon 826, Epicure W and Disparlon 6900-20X were used as the resin, curing agent and the rheological additive. The average particle size as indicated by the manufacturer is around 200 µm. SEM analysis was used to identify the characteristics of the magnetic particles. As observed in Figure 7.2, the particles exhibit plate like morphology.

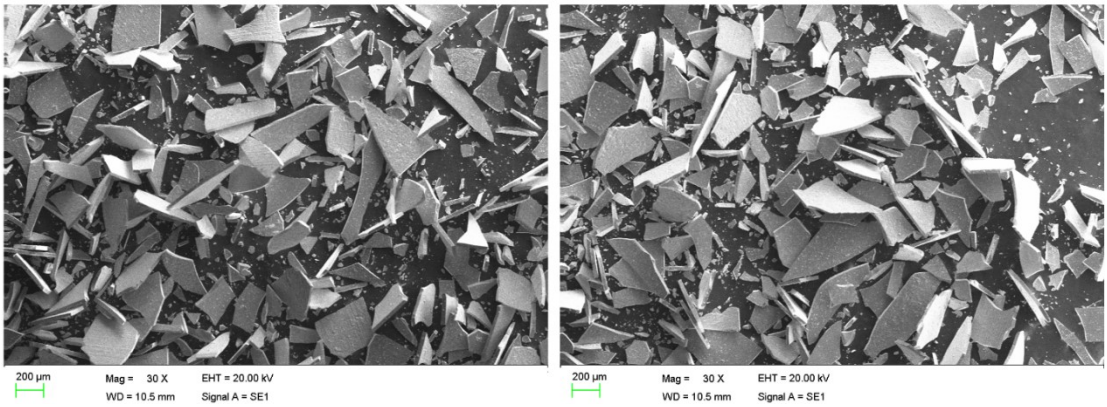

Figure 7.2: SEM images of isotropic NdFeB particles (MQP-B2)

For fabricating magnetic composites, the epoxy resin was blended with 10wt% of Disparlon 6900-20X additive to provide the required shear thinning behavior and additional properties to retain the shape of the deposited material. The magnetic particle loading was maintained at 80 wt%. Cured magnetic polymer composites were cut and polished for SEM observations.

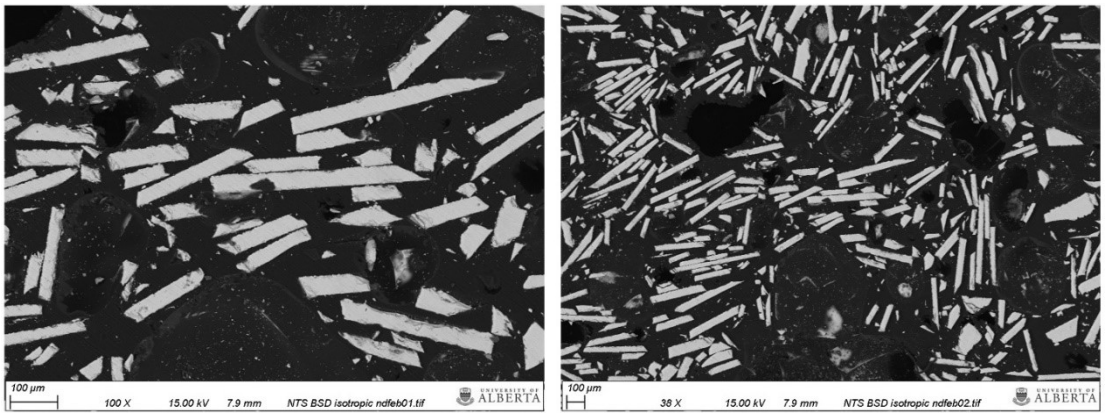

Figure 7.3: SEM observation of isotropic NdFeB composite shown at two different magnifications

In the SEM images, apart from the magnetic particles many pores and empty spaces were observed. The pores are due to the additives which made the degassing step extremely difficult. Such bubbles left over after the degassing process created significant porosities in the manufactured composites. Empty spaces or resin rich

spaces are an indication that the composite can still accommodate magnetic particles. Magnetic particles in the composite exhibit a very unique distribution pattern in the SEM images and at this stage one of the fundamental reasons is the shear induced alignment during the extrusion process. Magnetic characterization was conducted using a SQUID magnetometer to understand the magnetic characteristics of the fabricated composite. Characteristics of a permanent magnet like saturation magnetization, remanence and coercive field were derived from the hysteresis graph shown in Figure 7.4.

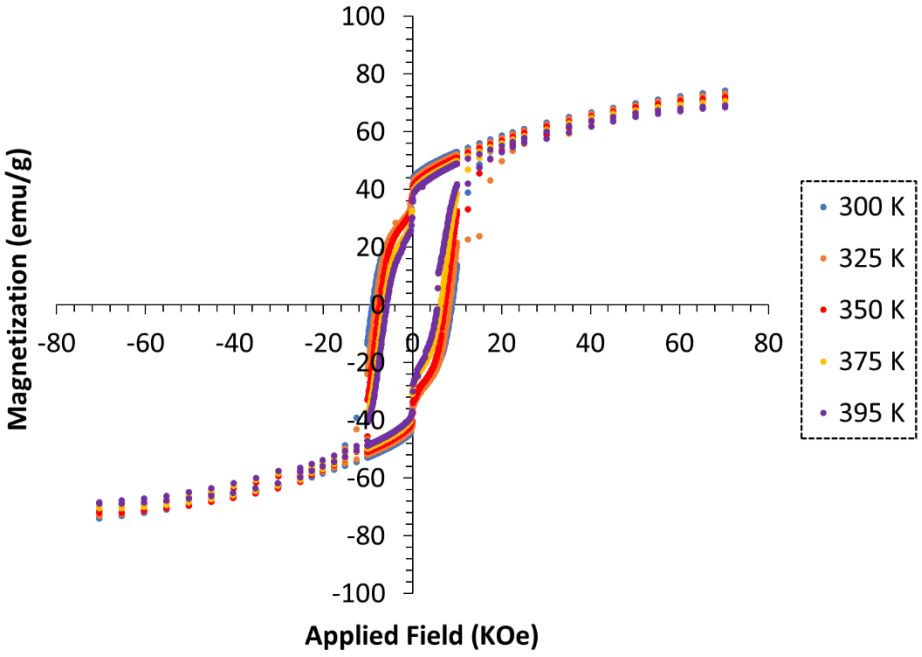

Figure 7.4: Hysteresis data for magnetization versus applied magnetic field for composites containing plate like isotropic NdFeB particles

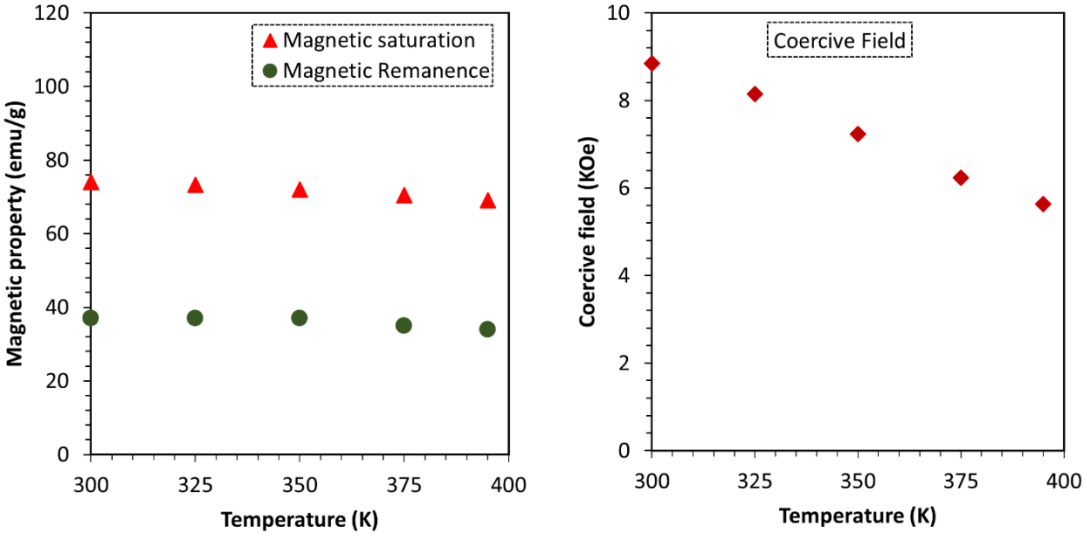

Figure 7.5: Magnetic saturation, Remanence and coercive field derived from hysteresis loops

Remanence to saturation ratio was observed to be around 0.5 indicating isotropic magnetic properties of the composite. The observed results corroborate with the observations in Chapter 6 where a reduction in magnetic properties was observed with increasing temperature.

7.3 Development of dual cure acrylate resin to print permanent magnets and magnetic composites

UV curable resin formulations require UV light for the reaction initiation step. It is only during UV irradiation, free radicals are generated which enable reaction propagation and crosslinking of the monomers. One of the challenges with magnetic particle reinforced UV curable polymers is to achieve complete cure of the deposited material on the substrate. The opaque nature of the magnetic particle reinforced UV curable resin results in solidifying only the topmost surface of the deposited layer and leaving the underlying material in its uncured state. This observation enabled to develop a formulation with the capability to cure under the influence of both UV light and heat. The dual cure reaction in the resin formulation was introduced by adding a

thermal initiator 2,2-Azobis(2-methylpropionitrile) [4]. The initiator is known as AIBN and was purchased from Thermofischer scientific. A loading fraction of 0.1 wt% was observed to be suitable for the clear PR-48 resin. The same loading was observed to be inefficient for the formulation additionally reinforced with additives and 80wt % of magnetic filler. As an initial trial attempt, 0.4wt% of AIBN was incorporated to Anisotropic MQA powder formulation containing 80 wt % of the magnetic filler. In-situ polymerization was adopted for the initial trial. The curing time was observed to be less than an hour. The cured solid was cut and grinded for initial observations. Figure 7.6 exhibits the image of the sample cured solid using AIBN initiator.

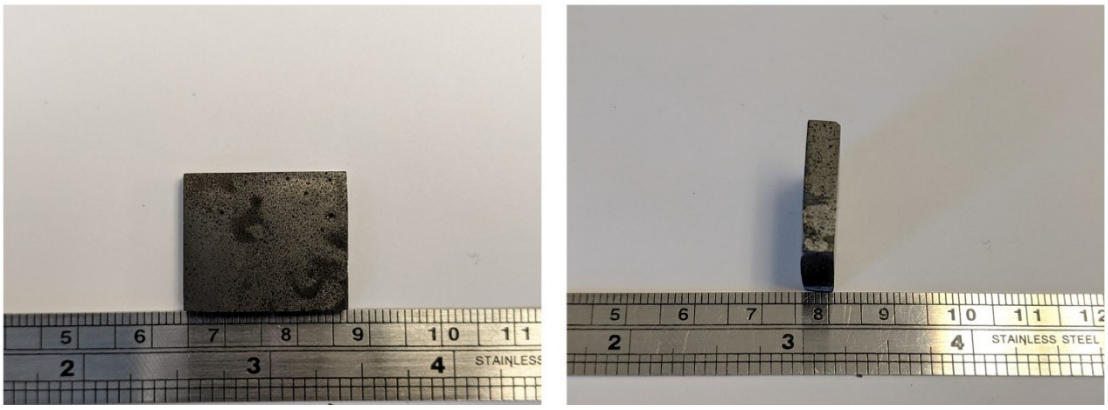

Figure 7.6: Cured permanent magnet using UV curable resin modified for thermal cure

The initially tested resin formulation through in-situ polymerization was utilized to 3D print permanent magnets using the material jetting AM process.

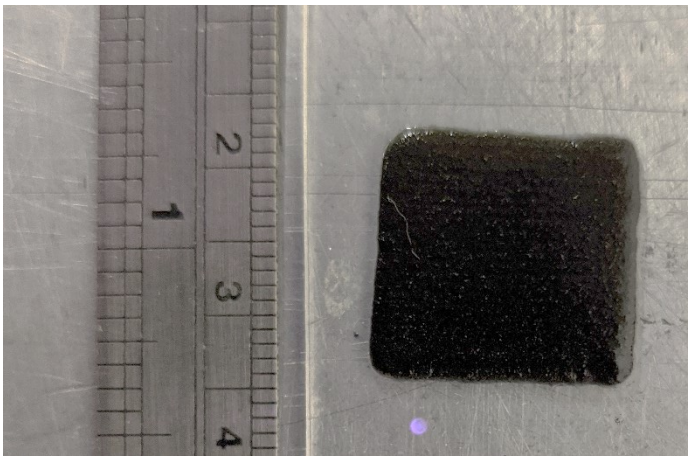

Figure 7.7: Sample image of one deposited layer using material jetting

The deposition pressure, layer thickness and speed utilized for the process were 3 kPa, 0.35 mm and 10 mm/s respectively. For subsequent material deposition, a layer thickness setting of 0.5mm was utilized. Figure 7.7 shows the image of one deposited layer on the acrylic sheet substrate. Curing of the deposited layer was accomplished using UV light adopting the manufacturing scenario B established in Chapter 4. The deposited layer was exposed to UV light for 60s. Figure 7.8 exhibits positioning the magnetic jig over the deposited layer and subsequently curing it.

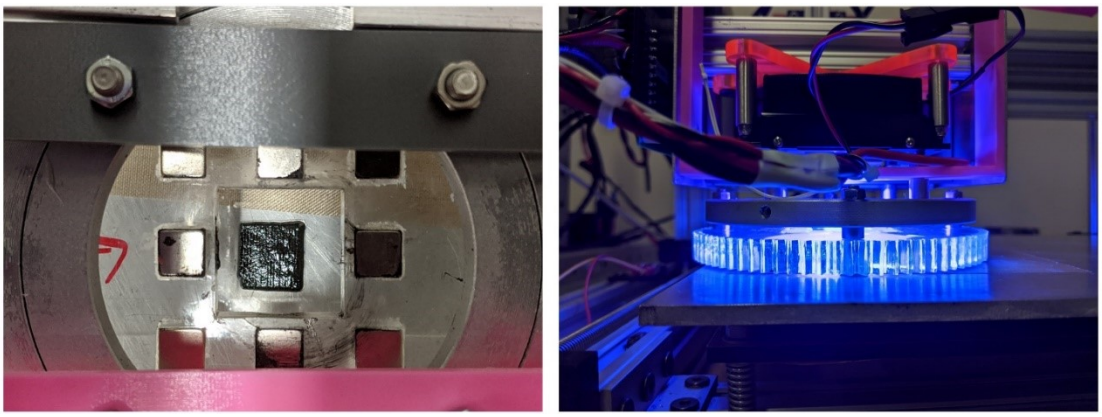

Figure 7.8: Positioning the magnetic jig and UV light above the deposited layer

Post thermal cure was accomplished by setting the furnace at 50°C. Thickness of the cured layer was measured using the Vernier caliper.

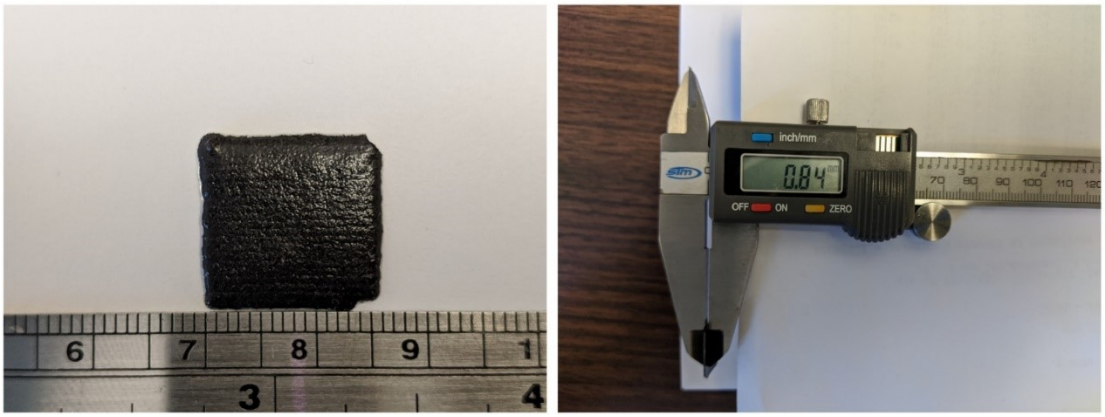

Figure 7.9: Dimensions of one cured layer using both UV and thermal curing methods

The process methodology adopted for printing a single layer was adopted to deposit subsequent layers and cure the sample using both UV and heat. Figure 7.10 shows the image of a 3D printed sample after grinding and polishing using sandpaper.

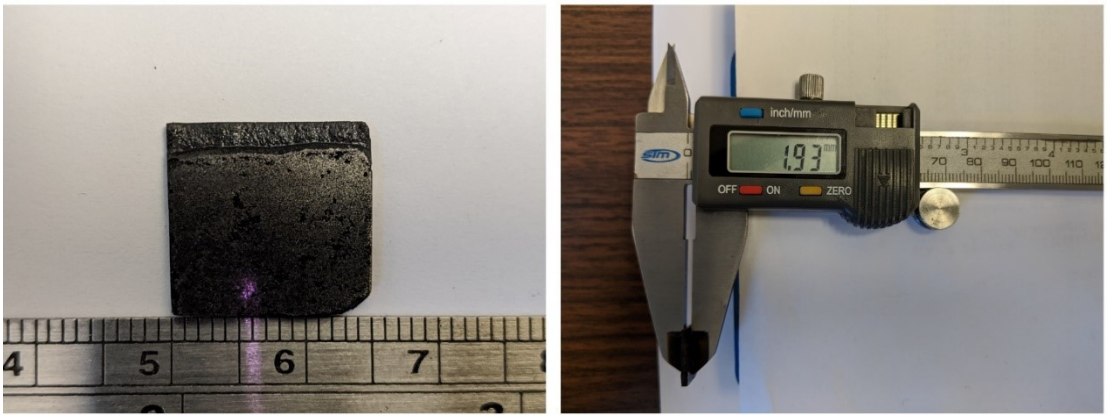

Figure 7.10: 3D printed sample after grinding and polishing

A similar methodology was adopted to print composites with strontium ferrite and neodymium iron boron fillers. Utilizing the AIBN loading of 0.4 wt% in strontium ferrite formulation resulted in specimen cracking as observed in Figure 7.11.

Figure 7.11: Specimen cracking observed at a lower magnetic filler loading

Apart from cracking, specimens when exposed to UV light exhibited uncontrollable deformations as observed in Figure 7.12.

Figure 7.12: Deformations observed with NdFeB formulation materials

Furthermore, using the same formulation with 30 wt% NdFeB filler and controlling the intensity of the incident UV light, one component was successfully printed and cured using both UV and heat cure methods.

Figure 7.13: 30 wt% NdFeB filled UV/Thermal cure resin using material jetting process

From the above mentioned results, it is significantly evident that a multitude of issues have to be addressed prior to developing a formulation for printing and curing magnetic composites using material jetting based AM process.

7.4 In-situ polymerization of magnetic composites and processing in magnetic fields

One of the fundamental steps in magnet manufacturing process is the application of an external magnetic field to align the crystallographic c-axis to enhance magnetic properties. In this section magnetic composites are developed using in-situ polymerization approach where 3D printed molds are filled with magnetic particle reinforced polymer formulations. Anisotropic MQA powder was dispersed in epoxy resin and the formulation was cured at a temperature of 80 °C. A magnetic array designed using FEMM was utilized to align the particles during the thermal curing

process. Figure 7.14 shows the image of the adopted magnetic array for aligning the particles.

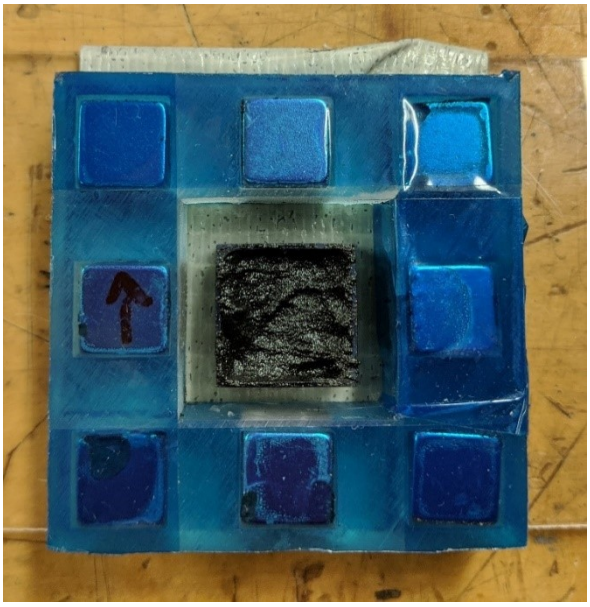

Figure 7.14: 3D printed molds filled with magnetic material formulation and cured in a magnetic field in a thermal oven

To evaluate the orientation of crystallographic c-axis, XRD was conducted on samples manufactured using the in-situ polymerization approach. From technical literature, it was understood that for neodymium iron boron ($Nd_2Fe_{14}B$) enhancement in the intensity of (006), (004) crystallographic plane relative to other peaks indicates the orientation of easy axis of magnetization in the magnetic composites [4]. Disappearance of predominant peaks normally observed for a magnetic composite with isotropic particle distribution has been reported in technical literature [5].

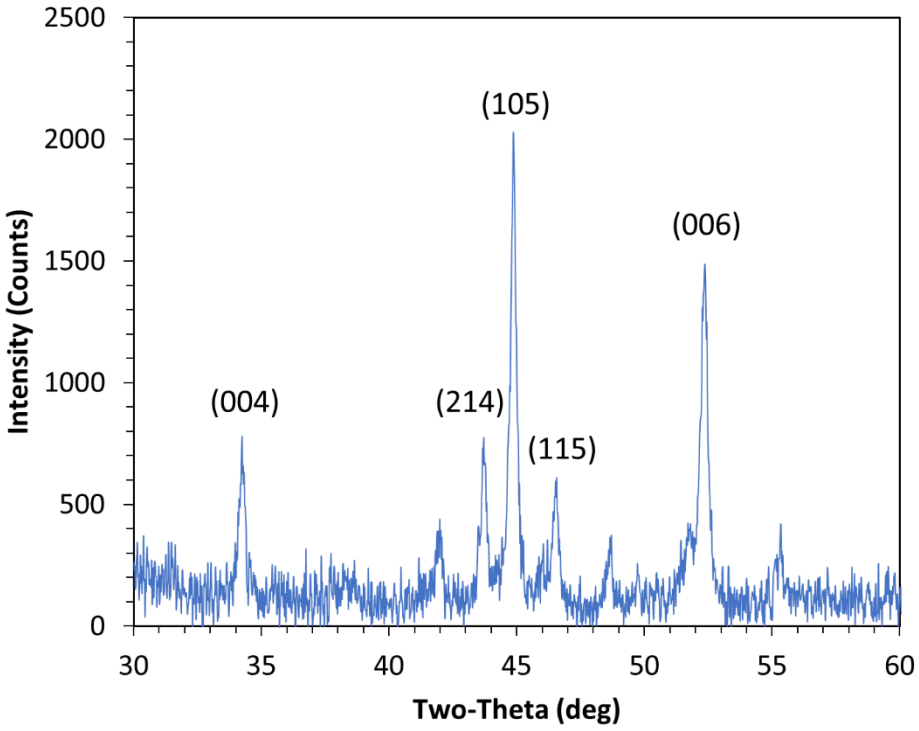

Figure 7.15: XRD peaks of field structured magnet

Results observed in Figure 7.15 are congruent to the ones reported in technical literature for textured permanent magnets [5]. Comparing figures 7.15 and 7.16, some peaks appear to have been suppressed in Figure 7.15 due to the presence of texture in the magnetic composite. Comparing the intensities to the ones reported by Narayan et.al where intensity of (006) peak was even higher compared to all other observed peaks, it suggests that further analysis and alternative characterization techniques to be adopted to validate the orientation of magnetic particles within the fabricated composites.

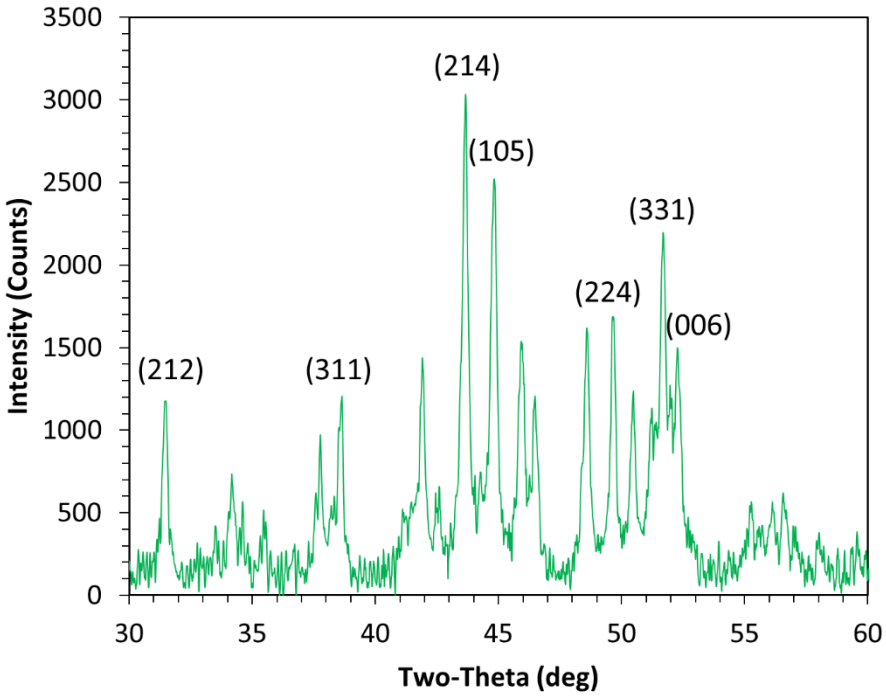

Figure 7.16: XRD peaks for isotropic permanent magnet

7.5 References

[1] L. E. Edwards, J. M. Yon, I. P. Bond, and P. H. Mellor, "Structural magnetic composites for use in electro-mechanical applications," in 20th International Conference on Composite Materials, Copenhagen, 2015, no. July, pp. 19–24.

[2] D. Fullwood, C. Haehl, and B. Lively, "Magnetically loaded filament wound composites," in SAMPE Conference Proceedings: Material and Process Innovations: Changing Our World. Long Beach, CA, May 18-22, 2008. Society for the Advancement of Material and Process Engineering. CD-ROM-5pp.

[3] T. Watanabe et al., "Photoresponsive hydrogel microstructure fabricated by two-photon initiated polymerization," Adv. Funct. Mater., vol. 12, no. 9, pp. 611–614, 2002.

[4] D. Schläfer, T. Walker, N. Mattern, W. Grünberger, and D. Hinz, "Analysis of texture distribution in NdFeB hard magnets by means of X-ray diffraction in

Bragg-Brentano geometry," Texture, Stress. Microstruct., vol. 26, pp. 71–81, 1996.

[5] N. Poudyal, C. Rong, and J. P. Liu, "Anisotropic bonded magnets fabricated via surfactant-assisted ball milling and magnetic-field processing," J. Phys. D. Appl. Phys., vol. 44, no. 33, p. 335002, 2011.

CHAPTER 8: SUMMARY, CONLUSIONS AND FUTURE WORK

In this research work, the feasibility of employing additive manufacturing (AM) as a tool to fabricate magnetically loaded polymer composites has been explored. AM processes, namely stereolithography and material jetting were utilized to understand its capabilities to print polymers reinforced with magnetic fillers. It was hypothesized that the selected AM techniques will enable manufacturing magnetic composites suitable for high performance electrical machines like flywheel energy storage systems. To validate the hypothesis, technical contributions related to material, equipment and process development have been made as a part of this research work with guidance from the technical literature.

Based on the initial hypothesis, a stereolithography based AM process utilizing a resin vat was first explored. A commercially available 3D printer (Autodesk Ember) capable of printing UV curable monomers was employed for the first phase of this research. The need for engineering magnetic particle reinforced resin formulation was realized upon observing particle settling within the resin tray of the 3D printer. Developing a formulation engineered using additives to mitigate particle settling was the first novel contribution of this research work. The additives utilized to engineer the suspensions enhanced low shear viscosity and yield strength characterized using rheometry tests. FTIR spectroscopy revealed that the degree of monomer conversion was significantly dependent on the layer thickness setting in the 3D printer. To push the limits of the 3D printer to fabricate composites with increased magnetic filler loading, an intensive design of experiment approach was adopted to study the combined effects of material formulations and 3D printing process parameters. It was observed

that the dimensional variation in the manufactured composites followed a pattern dependent on the print zones. Irrespective of the adopted materials and manufacturing process parameters, the variation patterns were observed to be the same for composite thickness and width. To determine the curing behavior of the developed material formulations, a new experimental approach was developed to evaluate the cured thickness and further determine the resin characteristic parameters like depth of penetration and critical energy of polymerization. Utilizing this fundamental understanding, resins with a magnetic filler loading of 10 wt% and 25 wt% were fabricated. Magnetic composites printed using neodymium iron boron fillers exhibited superior mechanical properties compared to strontium ferrite fillers at a filler loading of 10 wt%. Even though polymers reinforced with 25 wt% filler loading were printed, the quality of the magnetic composites were poor. Adhesion to the aluminum build head was significantly challenging and furthermore composites exhibited broken cured surfaces and layer tearing in the manufactured composite specimens. Overall, in this research work focusing on stereolithography, fabrication of magnetic composites at lower filler loadings using an open source 3D printer was successfully demonstrated. Utilizing the results obtained through this research work, it was understood that a bottom up type 3D printer is only suitable for printing polymers containing lower magnetic filler loadings. Such magnetic composites are magnetic field responsive but cannot satisfy the requirements required for high performance electrical machines.

With the motivation of developing magnetic composites with engineered microstructures, a novel material jetting based manufacturing approach was developed using fundamental scientific methods. Initially, research was focused at a systems level

to determine particle alignment setups and control systems required to develop a 3D printer. Finite element analysis was used to ascertain and understand the magnetic flux density distribution in the developed permanent magnet based particle alignment configurations. An experimental setup utilizing permanent magnet based particle alignment system was developed and utilized to evaluate the behavior of magnetic particles in UV curable resin. Optical microscopy coupled with image processing enabled quantifying the degree of particle alignment at user defined angles. Novel methodologies like magnetizing the particles prior to rotation were observed to be more efficient for orienting particles at user defined angles. Furthermore, XRD analysis enabled validating the orientation of specific crystallographic planes indicating the alignment of the easy axis of magnetization. UV curable ferromagnetic particle reinforced formulations were engineered to exhibit properties suitable for material jetting based additive manufacturing processes. Formulations exhibited additive loading dependent flow index, yield strength enhancements and time dependent viscosity recovery properties. Through this work, it was shown how to render material formulations thixotropic and engineer them to control material behavior at different processing stages. Such material behavior modifications proved their suitability for material jetting based additive manufacturing process and control of particle aggregation behavior in UV curable material formulations. Magnetic characterization of field structured composites showed enhancement in magnetic characteristics along the direction of particle structuring. Overall, a robust foundation at a system and materials level was formulated to develop composites with engineered microstructures. This novel methodology to developed composites with engineered microstructures was

demonstrated for polymers engineered with filler loadings up to 10 wt%. Such composites are magnetic field responsive but cannot generate magnetic fields required for integration into electrical machine systems.

In the final section of this research, permanent magnets were fabricated using engineered material formulations through material jetting based AM process. Material systems were developed with the motivation of developing composites that can generate magnetic fields suitable for electrical machine applications. For this purpose, high viscosity magnetic pastes were developed to suit the material jetting process. The behavior of the developed magnetic pastes was observed to exhibit transitions as a function of particle size and rheological additive loading. Rheological characterization enabled understanding that the pastes engineered using rheological additives exhibited viscoelastic behavior compared to other formulations without additives. The incorporation of a rheological additives, even though they enhanced the rheological characteristics, resulted in many processing challenges during the various processing stages. Degassing to remove entrapped bubbles was challenging as it created significant pores in the manufactured composites. The presence of entrapped air also created instabilities during the deposition process. The process parameters required modifications for depositing materials over previously deposited layers. Magnetic characterization was conducted to find the influence of formulation materials and hybrid magnetic material mixtures. Magnetic properties were observed to significantly deteriorate with increasing temperatures. Properties of developed magnetic composites were observed to meet the properties required for constructing electrical machines from such permanent magnets. Utilizing this fundamental knowledge on engineering

material and process parameters, fiber reinforced magnetic composites and composites with plate type magnetic particle were fabricated. In fiber reinforced composites, the fibers were observed to exhibit alignment as evidenced in SEM images. Furthermore, a UV curable resin was modified for heat cure using thermal initiators. Such a resin reinforced with magnetic powder also enabled fabricating permanent magnets using in-situ polymerization and a material jetting additive manufacturing process. Adopting the same methodology to print magnetic composites was challenging as material deformations were observed as a result of UV exposure. In-situ polymerization of magnetic composites in the presence of a magnetic field applied through a magnetic field enabled developing textured permanent magnets. In this research work, it was observed that the material jetting AM process enabled fabrication of permanent magnets suitable for high performance electrical machines. Overall, this research has enabled constructing a robust foundation and understanding of materials and processes for developing magnetically loaded polymer composites for a multitude of engineering applications.

Results presented in this research are key starting points for the multidisciplinary development of materials, equipment and manufacturing processes for polymer bonded magnetic solids using AM techniques. Obtaining the desired magnetic properties in composites is possible through the concurrent engineering of equipment, materials and manufacturing process. Considering these factors, the following research aspects are recommended for future work:

- Developing an experimental design to minimize the dimensional variations in 3D printed magnetic composites using stereolithography. The starting point for

this study can be tuning the factor levels that have been identified to influence the dimensional characteristics of 3D printed composites.

- The material of the build head plate can be changed to a material like an acrylic sheet, as opposed to the existing aluminum build head. This may promote improved adhesion of the cured polymer layer compared to other materials.
- In this research, the prime focus has been on enabling printability of the developed polymer formulations. Investigating the composite characteristics in terms of mechanical, electrical, and magnetic properties would enable a deeper understanding of the suitability for a multitude of engineering applications.
- Investigating the influence of UV light intensity on the rapid geometrical changes during the curing process would provide information on many undesired geometrical features and changes experienced at many stages of this research.
- Path planning for material deposition is crucial as in many cases the material remains in a liquid state prior to the curing process. In some cases, the deposition path of the nozzle was observed to distort previously deposited material layers. There is a need to restructure the deposition paths to avoid such process induced distortions.
- Investigating the mechanical strength in terms of adhesion between deposited layers is important for structures fabricated using additive manufacturing.

COMPREHENSIVE REFERENCES

- J. M. D. Coey, Magnetism and Magnetic Materials. Cambridge: Cambridge University Press, 2001.
- D. Jiles, Introduction to magnetism and magnetic materials. CRC press, 2015.
- C. Kittel, "Physical theory of ferromagnetic domains," Rev. Mod. Phys., vol. 21, no. 4, p. 541, 1949.
- J. P. Gavigan and D. Givord, "Intrinsic and extrinsic properties of rare earth-transition metal compounds and permanent magnets," J. Magn. Magn. Mater., vol. 84, no. 3, pp. 288–298, 1990.
- J. M. D. Coey, "Perspective and prospects for rare earth permanent magnets," Engineering, 2019.
- R. Skomski and D. J. Sellmyer, "Intrinsic and Extrinsic Properties of Advanced Magnetic Materials," in Handbook of Advanced Magnetic Materials, Y. Liu, D. J. Sellmyer, and D. Shindo, Eds. Boston, MA: Springer US, 2006, pp. 1–57.
- D. Brown, B.-M. Ma, and Z. Chen, "Developments in the processing and properties of NdFeb-type permanent magnets," J. Magn. Magn. Mater., vol. 248, no. 3, pp. 432–440, Aug. 2002.
- T. Ye et al., "Application of magnetic field in fabrication process of anisotropic bonded nd-fe-b magnet," J. Iron Steel Res. Int., vol. 13, pp. 279–281, 2006.
- J. Martin, E. Venturini, J. Odinek, and R. Anderson, "Anisotropic magnetism in field-structured composites," Phys. Rev. E, vol. 61, no. 3, pp. 2818–2830, Mar. 2000.
- J. E. Martin, E. L. Venturini, and D. L. Huber, "Giant magnetic susceptibility enhancement in field-structured nanocomposites," J. Magn. Magn. Mater., vol. 320, no. 18, pp. 2221–2227, Sep. 2008.
- J. Schneider and R. Knehans-Schmidt, "Bonded hybrid magnets," J. Magn. Magn. Mater., vol. 157–158, pp. 27–28, May 1996.
- B. . Ma, J. . Herchenroeder, B. Smith, M. Suda, D. . Brown, and Z. Chen, "Recent development in bonded NdFeB magnets," J. Magn. Magn. Mater., vol. 239, no. 1–3, pp. 418–423, Feb. 2002.
- X. H. Zhang, W. H. Xiong, Y. F. Li, and N. Song, "Effect of process on the

magnetic and mechanical properties of Nd-Fe-B bonded magnets," Mater. Des., vol. 30, no. 4, pp. 1386–1390, 2009.

- D. Drummer and S. Messingschlager, "Material Characterization of Strontium Ferrite Powders for Producing Sintered Magnets by Ceramic Injection Molding (MagnetPIM)," Adv. Mater. Sci. Eng., vol. 2014, pp. 1–8, 2014.
- S. V. Ketov, Y. D. Yagodkin, and V. P. Menushenkov, "Structure and magnetic properties of strontium ferrite anisotropic powder with nanocrystalline structure," J. Alloys Compd., vol. 509, no. 3, pp. 1065–1068, Jan. 2011.
- M. Krack, M. Secanell, and P. Mertiny, "Cost optimization of hybrid composite flywheel rotors for energy storage," Struct. Multidiscip. Optim., vol. 41, no. 5, pp. 779–795, 2010.
- S. K. Ha, H.-I. Yang, and D.-J. Kim, "Optimal design of a hybrid composite flywheel with a permanent magnet rotor," J. Compos. Mater., vol. 33, no. 16, pp. 1544–1575, 1999.
- D. Fullwood, C. Haehl, and B. Lively, "Magnetically loaded filament wound composites," in SAMPE Conference Proceedings: Material and Process Innovations: Changing Our World. Long Beach, CA, May 18-22, 2008. Society for the Advancement of Material and Process Engineering. CD-ROM-5pp.
- J. M. Buckley, K. Atallah, C. M. Bingham, and D. Howe, "Magnetically loaded composite for roller drives," 1998.
- P. E. Mason, K. Atallah, and D. Howe, "Hard and soft magnetic composites in high-speed flywheels," Proc. Int. Comm. Compos. Mater. Seattle, WA, USA, vol. 12, 1999.
- J. E. Martin, L. E. S. Rohwer, and J. Stupak, "Elastic magnetic composites for energy storage flywheels," Compos. Part B Eng., vol. 97, pp. 141–149, Jul. 2016.
- L. E. Edwards, J. M. Yon, I. P. Bond, and P. H. Mellor, "Structural magnetic composites for use in electro-mechanical applications," in 20th International Conference on Composite Materials, Copenhagen, 2015, no. July, pp. 19–24.
- O. Gutfleisch, M. A. Willard, E. Brück, C. H. Chen, S. G. Sankar, and J. P. Liu, "Magnetic Materials and Devices for the 21st Century: Stronger, Lighter, and

More Energy Efficient," Adv. Mater., vol. 23, no. 7, pp. 821–842, Feb. 2011.

- H. Li, T. J. Flynn, J. C. Nation, J. Kershaw, L. Scott Stephens, and C. A. Trinkle, "Photopatternable NdFeB polymer micromagnets for microfluidics and microrobotics applications," J. Micromechanics Microengineering, vol. 23, no. 6, p. 065002, Jun. 2013.
- A. Khosla and S. Kassegne, "Fabrication of NdFeB-based permanent rare-earth micromagnets by novel hybrid micromolding process," Microsyst. Technol., vol. 21, no. 11, pp. 2315–2320, Nov. 2015.
- C. Yamahata, C. Lotto, E. Al-Assaf, and M. A. M. Gijs, "A PMMA valveless micropump using electromagnetic actuation," Microfluid. Nanofluidics, vol. 1, no. 3, pp. 197–207, Jul. 2005.
- Y. Jiang, S. Masaoka, M. Uehara, T. Fujita, K. Higuchi, and K. Maenaka, "Micro-structuring of thick NdFeB films using high-power plasma etching for magnetic MEMS application," J. Micromechanics Microengineering, vol. 21, no. 4, p. 045011, Apr. 2011.
- W. Wang, Z. Yao, J. C. Chen, and J. Fang, "Composite elastic magnet films with hard magnetic feature," J. Micromechanics Microengineering, vol. 14, no. 10, pp. 1321–1327, Oct. 2004.
- N. Damean, B. A. Parviz, J. N. Lee, T. Odom, and G. M. Whitesides, "Composite ferromagnetic photoresist for the fabrication of microelectromechanical systems," J. Micromechanics Microengineering, vol. 15, no. 1, pp. 29–34, Jan. 2005.
- Z. C. Yuan, A. J. Williams, T. C. Shields, S. Blackburn, and C. B. Ponton, "The production of Sr hexaferrite thick films by screen printing," J. Magn. Magn. Mater., vol. 247, pp. 257–269, 2002.
- J. J. Romero et al., "Anisotropic polymer bonded hard-magnetic films for microelectromechanical system applications," J. Appl. Phys., vol. 99, no. 8, p. 08N303, Apr. 2006.
- J. Thévenot, H. Oliveira, O. Sandre, and S. Lecommandoux, "Magnetic responsive polymer composite materials," Chem. Soc. Rev., vol. 42, no. 17, p. 7099, 2013.

- I. Gibson, D. Rosen, and B. Stucker, Additive Manufacturing Technologies. New York, NY: Springer New York, 2015.
- P. J. Bartolo, Stereolithography: Materials, Processes and applications. Springer,London, 2011.
- X. Zhang, X. . Jiang, and C. Sun, "Micro-stereolithography of polymeric and ceramic microstructures," Sensors Actuators A Phys., vol. 77, no. 2, pp. 149–156, Oct. 1999.
- S. Baba, T. Harada, H. Shimizu, Y. Doshida, and S. Tanaka, "Colloidal processing using UV curable resin under high magnetic field for textured ceramics," J. Eur. Ceram. Soc., vol. 36, no. 11, pp. 2739–2743, 2016.
- N. Reis, C. Ainsley, and B. Derby, "Digital microfabrication of ceramic components," Am. Ceram. Soc. Bull., vol. 82, no. 9, 2003.
- J. W. Halloran et al., "Photopolymerization of powder suspensions for shaping ceramics," J. Eur. Ceram. Soc., vol. 31, no. 14, pp. 2613–2619, 2011.
- C. Sun and X. Zhang, "The influences of the material properties on ceramic micro-stereolithography," Sensors Actuators, A Phys., vol. 101, no. 3, pp. 364–370, 2002.
- T. Chartier, A. Badev, Y. Abouliatim, P. Lebaudy, and L. Lecamp, "Stereolithography process: Influence of the rheology of silica suspensions and of the medium on polymerization kinetics – Cured depth and width," J. Eur. Ceram. Soc., vol. 32, no. 8, pp. 1625–1634, Jul. 2012.
- C. Hinczewski, S. Corbel, and T. Chartier, "Ceramic suspensions suitable for stereolithography," J. Eur. Ceram. Soc., vol. 18, no. 6, pp. 583–590, Jan. 1998.
- S. P. Gentry and J. W. Halloran, "Depth and width of cured lines in photopolymerizable ceramic suspensions," J. Eur. Ceram. Soc., vol. 33, no. 10, pp. 1981–1988, 2013.
- A. Goswami, K. Ankit, N. Balashanmugam, A. M. Umarji, and G. Madras, "Optimization of rheological properties of photopolymerizable alumina suspensions for ceramic microstereolithography," Ceram. Int., vol. 40, no. 2, pp. 3655–3665, 2014.
- B. Y. Tay and M. J. Edirisinghe, "Investigation of some phenomena occurring

during continuous ink-jet printing of ceramics," J. Mater. Res., vol. 16, no. 2, pp. 373–384, 2001.

- Q. Liu and M. Orme, "High precision solder droplet printing technology and the state-of-the-art," J. Mater. Process. Technol., vol. 115, no. 3, pp. 271–283, 2001.
- D. Espalin, D. W. Muse, E. MacDonald, and R. B. Wicker, "3D Printing multifunctionality: structures with electronics," Int. J. Adv. Manuf. Technol., vol. 72, no. 5–8, pp. 963–978, 2014.
- K. Yamaguchi, "Generation of 3-dimensional microstructure by metal jet," Microsyst. Technol., vol. 9, no. 3, pp. 215–219, 2003.
- J. C. Conrad, S. R. Ferreira, J. Yoshikawa, R. F. Shepherd, B. Y. Ahn, and J. A. Lewis, "Designing colloidal suspensions for directed materials assembly," Curr. Opin. Colloid Interface Sci., vol. 16, no. 1, pp. 71–79, 2011.
- K. Sun, T. Wei, B. Y. Ahn, J. Y. Seo, S. J. Dillon, and J. A. Lewis, "3D printing of interdigitated Li-Ion microbattery architectures," Adv. Mater., vol. 25, no. 33, pp. 4539–4543, 2013.
- N. Tasnim et al., "3D bioprinting stem cell derived tissues," Cell. Mol. Bioeng., vol. 11, no. 4, pp. 219–240, 2018.
- J. Mewis and N. J. Wagner, Colloidal suspension rheology. Cambridge University Press, 2012.
- B. A. Horri, P. Ranganathan, C. Selomulya, and H. Wang, "A new empirical viscosity model for ceramic suspensions," Chem. Eng. Sci., vol. 66, no. 12, pp. 2798–2806, Jun. 2011.
- A. K. Bastola, M. Paudel, and L. Li, "Development of hybrid magnetorheological elastomers by 3D printing," Polymer (Guildf)., vol. 149, pp. 213–228, Aug. 2018.
- C. Duty et al., "What makes a material printable? A viscoelastic model for extrusion-based 3D printing of polymers," J. Manuf. Process., vol. 35, pp. 526–537, 2018.
- C. E. Duty et al., "A Viscoelastic Model for Evaluating Extrusion-Based Print Conditions," Oak Ridge National Lab.(ORNL), Oak Ridge, TN, USA, 2017.

- R. Ganguly and I. K. Puri, “Field-assisted self-assembly of superparamagnetic nanoparticles for biomedical, MEMS and BioMEMS applications,” Adv. Appl. Mech., vol. 41, pp. 293–335, 2007.
- I. Jönkkäri, M. Isakov, and S. Syrjälä, “Sedimentation stability and rheological properties of ionic liquid–based bidisperse magnetorheological fluids,” J. Intell. Mater. Syst. Struct., vol. 26, no. 16, pp. 2256–2265, Nov. 2015.
- M. T. López-López, P. Kuzhir, G. Bossis, and P. Mingalyov, “Preparation of well-dispersed magnetorheological fluids and effect of dispersion on their magnetorheological properties,” Rheol. Acta, vol. 47, no. 7, pp. 787–796, Sep. 2008.
- T. G. Mezger, “The Rheology Handbook,” Pigment Resin Technol., vol. 38, no. 5, p. prt.2009.12938eac.006, Sep. 2009.
- M. Zarek, M. Layani, I. Cooperstein, E. Sachyani, D. Cohn, and S. Magdassi, “3D Printing: 3D Printing of Shape Memory Polymers for Flexible Electronic Devices (Adv. Mater. 22/2016),” Adv. Mater., vol. 28, no. 22, pp. 4166–4166, Jun. 2016.
- I. T. Garces and C. Ayranci, “A view into additive manufactured electro-active reinforced smart composite structures,” Manuf. Lett., vol. 16, pp. 1–5, Apr. 2018.
- C. Credi, A. Fiorese, M. Tironi, R. Bernasconi, L. Magagnin, M. Levi, and S. Turri, “3D Printing of Cantilever-Type Microstructures by Stereolithography of Ferromagnetic Photopolymers,” ACS Appl. Mater. Interfaces, vol. 8, no. 39, pp. 26332–26342, Oct. 2016.
- S. J. Leigh, C. P. Purssell, J. Bowen, D. A. Hutchins, J. A. Covington, and D. R. Billson, “A miniature flow sensor fabricated by micro-stereolithography employing a magnetite/acrylic nanocomposite resin,” Sensors Actuators A Phys., vol. 168, no. 1, pp. 66–71, Jul. 2011.
- R. Domingo-Roca, J. C. Jackson, and J. F. C. Windmill, “3D-printing polymer-based permanent magnets,” Mater. Des., vol. 153, pp. 120–128, Sep. 2018.
- N. Löwa, J. Fabert, D. Gutkelch, H. Paysen, O. Kosch, and F. Wiekhorst, “Journal of Magnetism and Magnetic Materials 3D-printing of novel magnetic

composites based on magnetic nanoparticles and photopolymers," J. Magn. Magn. Mater., vol. 469, no. September 2018, pp. 456–460, 2019.

- A. Kumar, "Methods and Materials for Smart Manufacturing: Additive Manufacturing, Internet of Things, Flexible Sensors and Soft Robotics," Manuf. Lett., vol. 15, pp. 122–125, Jan. 2018.
- "Standard Test Method for Shear Thinning Index of Non-Newtonian Liquids Using a Rotational Viscometer BT - Standard Test Method for Shear Thinning Index of Non-Newtonian Liquids Using a Rotational Viscometer." 18AD.
- J. Mewis and N. J. Wagner, Colloidal Suspension Rheology. Cambridge: Cambridge University Press, 2011.
- T. G. Mezger, "The Rheology Handbook," Pigment Resin Technol., vol. 38, no. 5, p. prt.2009.12938eac.006, Sep. 2009.
- R. Berndlmaier, "Rheology additives for coatings," in Handbook of coating additives, D. J. M. John J. Florio, Ed. Marcel Dekker Inc, pp. 363–403.
- M. T. López-López, P. Kuzhir, G. Bossis, and P. Mingalyov, "Preparation of well-dispersed magnetorheological fluids and effect of dispersion on their magnetorheological properties," Rheol. Acta, vol. 47, no. 7, pp. 787–796, Sep. 2008.
- J. de Vicente, M. T. López-López, F. González-Caballero, and J. D. G. Durán, "Rheological study of the stabilization of magnetizable colloidal suspensions by addition of silica nanoparticles," J. Rheol. (N. Y. N. Y)., vol. 47, no. 5, pp. 1093–1109, Sep. 2003.
- V. S. D. Voet, T. Strating, G. H. M. Schnelting, P. Dijkstra, M. Tietema, J. Xu, A. J. J. Woortman, K. Loos, J. Jager, and R. Folkersma, "Biobased Acrylate Photocurable Resin Formulation for Stereolithography 3D Printing," ACS Omega, vol. 3, no. 2, pp. 1403–1408, Feb. 2018
- J. W. Stansbury and M. J. Idacavage, "3D printing with polymers: Challenges among expanding options and opportunities," Dent. Mater., vol. 32, no. 1, pp. 54–64, 2016.
- M. Zarek, M. Layani, I. Cooperstein, E. Sachyani, D. Cohn, and S. Magdassi, "3D Printing: 3D Printing of Shape Memory Polymers for Flexible Electronic

Devices (Adv. Mater. 22/2016)," Adv. Mater., vol. 28, no. 22, pp. 4166–4166, Jun. 2016.

- A. Mitchell, U. Lafont, M. Hołyńska, and C. Semprimoschnig, "Additive manufacturing — A review of 4D printing and future applications," Addit. Manuf., vol. 24, no. September 2017, pp. 606–626, Dec. 2018.
- H. Li, T. J. Flynn, J. C. Nation, J. Kershaw, L. Scott Stephens, and C. A. Trinkle, "Photopatternable NdFeB polymer micromagnets for microfluidics and microrobotics applications," J. Micromechanics Microengineering, vol. 23, no. 6, p. 065002, Jun. 2013.
- C. Credi et al., "3D Printing of Cantilever-Type Microstructures by Stereolithography of Ferromagnetic Photopolymers," ACS Appl. Mater. Interfaces, vol. 8, no. 39, pp. 26332–26342, Oct. 2016.
- S. J. Leigh, C. P. Purssell, J. Bowen, D. A. Hutchins, J. A. Covington, and D. R. Billson, "A miniature flow sensor fabricated by micro-stereolithography employing a magnetite/acrylic nanocomposite resin," Sensors Actuators A Phys., vol. 168, no. 1, pp. 66–71, Jul. 2011.
- N. Löwa, J. Fabert, D. Gutkelch, H. Paysen, O. Kosch, and F. Wiekhorst, "Journal of Magnetism and Magnetic Materials 3D-printing of novel magnetic composites based on magnetic nanoparticles and photopolymers," J. Magn. Magn. Mater., vol. 469, no. September 2018, pp. 456–460, 2019.
- S. Lantean et al., "3D Printing of Magnetoresponsive Polymeric Materials with Tunable Mechanical and Magnetic Properties by Digital Light Processing," Adv. Mater. Technol., vol. 4, no. 11, p. 1900505, Nov. 2019.
- J. J. Martin, B. E. Fiore, and R. M. Erb, "Designing bioinspired composite reinforcement architectures via 3D magnetic printing," Nat. Commun., vol. 6, p. 8641, 2015.
- P. F. Jacobs, Rapid prototyping & manufacturing: fundamentals of stereolithography. Society of Manufacturing Engineers, 1992.
- J. Bennett, "Measuring UV curing parameters of commercial photopolymers used in additive manufacturing," Addit. Manuf., vol. 18, pp. 203–212, 2017.
- A. Boddapati, "Modeling cure depth during photopolymerization of

multifunctional acrylates." Georgia Institute of Technology, 2010.

- X. Zhang, X. . Jiang, and C. Sun, "Micro-stereolithography of polymeric and ceramic microstructures," Sensors Actuators A Phys., vol. 77, no. 2, pp. 149–156, Oct. 1999.
- Y. Y. C. Choong, S. Maleksaeedi, H. Eng, P.-C. Su, and J. Wei, "Curing characteristics of shape memory polymers in 3D projection and laser stereolithography," Virtual Phys. Prototyp., vol. 12, no. 1, pp. 77–84, Jan. 2017.
- A. Deka and N. Dey, "Rheological studies of two component high build epoxy and polyurethane based high performance coatings," J. Coatings Technol. Res., vol. 10, no. 3, pp. 305–315, May 2013.
- B. A. Horri, P. Ranganathan, C. Selomulya, and H. Wang, "A new empirical viscosity model for ceramic suspensions," Chem. Eng. Sci., vol. 66, no. 12, pp. 2798–2806, Jun. 2011.
- E. Aznarte Garcia, A. J. Qureshi, and C. Ayranci, "A study on material-process interaction and optimization for VAT-photopolymerization processes," Rapid Prototyp. J., vol. 24, no. 9, pp. 1479–1485, Nov. 2018.
- "ISO 527-1, Plastics — Determination of tensile properties — Part 1: General principles." ISO - International Organization for Standardization, 2019.
- Henderson, G. Robin. Six Sigma Quality Improvement with Minitab, John Wiley & Sons, Incorporated, 2011. ProQuest Ebook Central, https://ebookcentral.proquest.com/lib/ualberta/detail.action?docID=819255
- Y. L. Yap, C. Wang, S. L. Sing, V. Dikshit, W. Y. Yeong, and J. Wei, "Material jetting additive manufacturing: An experimental study using designed metrological benchmarks," Precis. Eng., vol. 50, pp. 275–285, Oct. 2017.
- C. Ainsley, N. Reis, and B. Derby, "Freeform fabrication by controlled droplet deposition of powder filled melts," J. Mater. Sci., vol. 37, no. 15, pp. 3155–3161, 2002.
- T. Wang and B. Derby, "Ink-jet printing and sintering of PZT," J. Am. Ceram. Soc., vol. 88, no. 8, pp. 2053–2058, 2005.
- G. M. Hutchings, Ian M., "Inkjet Technology for Digital Fabrication," in John Wiley & Sons, 2012.

- D. Huang, F. Liao, S. Molesa, D. Redinger, and V. Subramanian, “Plastic-Compatible Low Resistance Printable Gold Nanoparticle Conductors for Flexible Electronics,” J. Electrochem. Soc., vol. 150, no. 7, p. G412, 2003.
- S. Jang, Y. Seo, J. Choi, T. Kim, J. Cho, S. Kim, and D. Kim, “Sintering of inkjet printed copper nanoparticles for flexible electronics,” Scr. Mater., vol. 62, no. 5, pp. 258–261, Mar. 2010.
- E. Saleh, P. Woolliams, B. Clarke, A. Gregory, S. Greedy, C. Smartt, R. Wildman, I. Ashcroft, R. Hague, P. Dickens, and C. Tuck, “3D inkjet-printed UV-curable inks for multi-functional electromagnetic applications,” Addit. Manuf., vol. 13, pp. 143–148, Jan. 2017.
- H. Song, J. Spencer, A. Jander, J. Nielsen, J. Stasiak, V. Kasperchik, and P. Dhagat, “Inkjet printing of magnetic materials with aligned anisotropy,” J. Appl. Phys., vol. 115, no. 17, p. 17E308, May 2014.
- D. Kokkinis, M. Schaffner, and A. R. Studart, “Multimaterial magnetically assisted 3D printing of composite materials,” Nat. Commun., vol. 6, p. 8643, 2015.
- L. Lu, E. Baynojir Joyee, and Y. Pan, “Correlation Between Microscale Magnetic Particle Distribution and Magnetic-Field-Responsive Performance of Three-Dimensional Printed Composites,” J. Micro Nano-Manufacturing, vol. 6, no. 1, p. 10904, Dec. 2017.
- R. C. Pullar, “Hexagonal ferrites: A review of the synthesis, properties and applications of hexaferrite ceramics,” Prog. Mater. Sci., vol. 57, no. 7, pp. 1191–1334, Sep. 2012.
- M. Sardela, Practical Materials Characterization. New York, NY: Springer New York, 2014.
- “Meeker, David. ‘Finite element method magnetics.’ FEMM 4 (2010): 32. http://www.femm.info/wiki/Documentation/,” vol. 4, p. 2010, 2010.
- J.-Y. Tinevez, “Directionality plugin for Fiji ImageJ.” [Online]. Available: https://imagej.net/Directionality.
- J. Schindelin, I. Arganda-Carreras, E. Frise, V. Kaynig, M. Longair, T. Pietzsch, S. Preibisch, C. Rueden, S. Saalfeld, B. Schmid, J.-Y. Tinevez, D. J. White, V.

Hartenstein, K. Eliceiri, P. Tomancak, and A. Cardona, “Fiji: an open-source platform for biological-image analysis,” Nat. Methods, vol. 9, no. 7, pp. 676–682, Jun. 2012.

- M. E. Koleva, S. Zotova, P. A. Atanasov, R. I. Tomov, and C. Ristoscu, “Sr-ferrite thin films grown on sapphire by pulsed laser deposition,” Appl. Surf. Sci., vol. 168, pp. 108–113, 2000.
- J. Martin, E. Venturini, J. Odinek, and R. Anderson, “Anisotropic magnetism in field-structured composites,” Phys. Rev. E, vol. 61, no. 3, pp. 2818–2830, Mar. 2000.
- S. Xia, E. Metwalli, M. Opel, P. A. Staniec, E. M. Herzig, and P. Müller-Buschbaum, “Printed thin magnetic films based on diblock copolymer and magnetic nanoparticles,” ACS Appl. Mater. Interfaces, vol. 10, no. 3, pp. 2982–2991, 2018.
- D. Speliotis, “Magnetic recording beyond the first 100 years,” J. Magn. Magn. Mater., vol. 193, no. 1–3, pp. 29–35, 1999.
- K. Goc et al., “Influence of magnetic field-aided filler orientation on structure and transport properties of ferrite filled composites,” J. Magn. Magn. Mater., vol. 419, pp. 345–353, Dec. 2016.
- M. Gao, M. Kuang, L. Li, M. Liu, L. Wang, and Y. Song, “Printing 1D Assembly Array of Single Particle Resolution for Magnetosensing,” Small, vol. 14, no. 19, p. 1800117, May 2018.
- R. C. Pullar, “Hexagonal ferrites: A review of the synthesis, properties and applications of hexaferrite ceramics,” Prog. Mater. Sci., vol. 57, no. 7, pp. 1191–1334, Sep. 2012.
- L. Lu, P. Guo, and Y. Pan, “Magnetic-Field-Assisted Projection Stereolithography for Three-Dimensional Printing of Smart Structures,” J. Manuf. Sci. Eng., vol. 139, no. 7, p. 071008, Mar. 2017.
- R. P. Chhabra and J. F. Richardson, Non-Newtonian flow and applied rheology: engineering applications. Butterworth-Heinemann, 2011.
- U. Eberhard et al., “Determination of the Effective Viscosity of Non-newtonian Fluids Flowing Through Porous Media,” Front. Phys., vol. 7, no. MAY, pp. 1–

9, May 2019.

- A. K. Bastola, M. Paudel, and L. Li, “Development of hybrid magnetorheological elastomers by 3D printing,” Polymer (Guildf)., vol. 149, pp. 213–228, Aug. 2018.
- T. G. Mezger, “The Rheology Handbook,” Pigment Resin Technol., vol. 38, no. 5, p. prt.2009.12938eac.006, Sep. 2009.
- H. A. Barnes, “Thixotropy—a review,” J. Nonnewton. Fluid Mech., vol. 70, no. 1–2, pp. 1–33, May 1997.
- M. T. López-López, P. Kuzhir, G. Bossis, and P. Mingalyov, “Preparation of well-dispersed magnetorheological fluids and effect of dispersion on their magnetorheological properties,” Rheol. Acta, vol. 47, no. 7, pp. 787–796, Sep. 2008.
- K. N. Al-Milaji, R. L. Hadimani, S. Gupta, V. K. Pecharsky, and H. Zhao, “Inkjet Printing of Magnetic Particles Toward Anisotropic Magnetic Properties,” Sci. Rep., vol. 9, no. 1, p. 16261, Dec. 2019.
- U. Banerjee, P. Bit, R. Ganguly, and S. Hardt, “Aggregation dynamics of particles in a microchannel due to an applied magnetic field,” Microfluid. Nanofluidics, vol. 13, no. 4, pp. 565–577, Oct. 2012.
- Ganguly and Puri, “Field-Assisted Self-Assembly of Superparamagnetic Nanoparticles for BioMEMS.,” Sciencedirect.Com, vol. 41, no. 06, pp. 293–335, 2007.
- J. Schindelin et al., “Fiji: an open-source platform for biological-image analysis,” Nat. Methods, vol. 9, no. 7, pp. 676–682, Jun. 2012.
- C. Ajinjeru et al., “Rheological survey of carbon fiber-reinforced high-temperature thermoplastics for big area additive manufacturing tooling applications,” J. Thermoplast. Compos. Mater., p. 089270571987394, Sep. 2019.
- C. Ajinjeru et al., “Rheological evaluation of high temperature polymers to identify successful extrusion parameters,” Oak Ridge National Lab.(ORNL), Oak Ridge, TN, USA, 2017.
- M. Kamkar, S. M. Nourin Sultana, S. Patangrao Pawar, A. Eshraghian, E.

Erfanian, and U. Sundararaj, “The key role of processing in tuning nonlinear viscoelastic properties and microwave absorption in CNT-based polymer nanocomposites,” Mater. Today Commun., vol. 24, no. February, p. 101010, Sep. 2020.

- A. H. A. Hoseini, M. Arjmand, U. Sundararaj, and M. Trifkovic, “Significance of interfacial interaction and agglomerates on electrical properties of polymer-carbon nanotube nanocomposites,” Mater. Des., vol. 125, pp. 126–134, 2017.
- V. Kunc, A. Lee, M. Mathews, and J. Lindahl, “Low Cost Reactive Polymers for Large Scale Additive Manufacturing,” CAMX 2018, pp. 15–18, 2018.
- A. Deka and N. Dey, “Rheological studies of two component high build epoxy and polyurethane based high performance coatings,” J. Coatings Technol. Res., vol. 10, no. 3, pp. 305–315, May 2013.
- H. Song et al., “Inkjet printing of magnetic materials with aligned anisotropy,” J. Appl. Phys., vol. 115, no. 17, p. 17E308, May 2014.
- J. Ormerod and S. Constantinides, “Bonded permanent magnets: Current status and future opportunities (invited),” J. Appl. Phys., vol. 81, no. 8, pp. 4816–4820, Apr. 1997.
- D. Brown, B.-M. Ma, and Z. Chen, “Developments in the processing and properties of NdFeb-type permanent magnets,” J. Magn. Magn. Mater., vol. 248, no. 3, pp. 432–440, Aug. 2002.
- J. Ormerod and S. Constantinides, “Bonded permanent magnets: Current status and future opportunities (invited),” J. Appl. Phys., vol. 81, no. 8, pp. 4816–4820, Apr. 1997.
- J. Xiao and J. U. Otaigbe, “Polymer-bonded magnets: Part I. Analytic thermogravimetry to determine the effect of surface modification on dispersion of Nd–Fe–B fillers,” J. Mater. Res., vol. 14, no. 7, pp. 2893–2896, Jul. 1999.
- M. Najgebauer, J. Szczygłowski, B. Ślusarek, M. Przybylski, A. Kapłon, and J. Rolek, “Magnetic Composites in Electric Motors,” in Analysis and Simulation of Electrical and Computer Systems, D. Mazur, M. Goł\kebiowski, and M. Korkosz, Eds. Cham: Springer International Publishing, 2018, pp. 15–28.
- G. Ertz, T. Hrynik, D. Lafleur, P. Mertiny, M. Secanell, and N. Wagner,

"Design of Low-Cost Fly Wheel Energy Storage Systems," SAMPE J., vol. 53, no. 6, pp. 18–26, 2017.

- L. Edwards, J. Yon, I. Bond, and P. Mellor, "STRUCTURAL MAGNETIC COMPOSITES FOR USE IN ELECTRO-MECHANICAL APPLICATIONS," in ICCM 20 20th International Conference on Composite Materials (pp. 1–8), 2015.
- J. E. Martin, L. E. S. Rohwer, and J. Stupak, "Elastic magnetic composites for energy storage flywheels," Compos. Part B Eng., vol. 97, pp. 141–149, Jul. 2016.
- J. Martin, E. Venturini, J. Odinek, and R. Anderson, "Anisotropic magnetism in field-structured composites," Phys. Rev. E, vol. 61, no. 3, pp. 2818–2830, Mar. 2000.
- C. V. Mikler et al., "Laser Additive Manufacturing of Magnetic Materials," JOM, vol. 69, no. 3, pp. 532–543, Mar. 2017.
- F. Nilsén, I. F. Ituarte, M. Salmi, J. Partanen, and S.-P. Hannula, "Effect of process parameters on non-modulated Ni-Mn-Ga alloy manufactured using powder bed fusion," Addit. Manuf., vol. 28, no. November 2018, pp. 464–474, Aug. 2019.
- Y. Yan et al., "Additive manufacturing of magnetic components for heterogeneous integration," in 2017 IEEE 67th Electronic Components and Technology Conference (ECTC), 2017, pp. 324–330.
- Y. Yan, J. Moss, K. D. T. Ngo, Y. Mei, and G.-Q. Lu, "Additive Manufacturing of Toroid Inductor for Power Electronics Applications," IEEE Trans. Ind. Appl., vol. 53, no. 6, pp. 5709–5714, Nov. 2017.
- B. G. Compton et al., "Direct-write 3D printing of NdFeB bonded magnets," Mater. Manuf. Process., vol. 0, no. 0, pp. 1–5, Aug. 2016.
- L. Li et al., "Big Area Additive Manufacturing of High Performance Bonded NdFeB Magnets," Sci. Rep., vol. 6, no. October, pp. 1–7, 2016.
- K. Gandha et al., "Additive manufacturing of anisotropic hybrid NdFeB-SmFeN nylon composite bonded magnets," J. Magn. Magn. Mater., vol. 467, no. April, pp. 8–13, 2018.

- B. Nagarajan, A. F. Eufracio Aguilera, M. Wiechmann, A. J. Qureshi, and P. Mertiny, “Characterization of magnetic particle alignment in photosensitive polymer resin: A preliminary study for additive manufacturing processes,” Addit. Manuf., vol. 22, no. May, pp. 528–536, Aug. 2018.
- E. M. Palmero et al., “Magnetic-Polymer Composites for Bonding and 3D Printing of Permanent Magnets,” IEEE Trans. Magn., vol. 55, no. 2, pp. 1–4, Feb. 2019.
- B. Khatri, K. Lappe, D. Noetzel, K. Pursche, and T. Hanemann, “A 3D-Printable Polymer-Metal Soft-Magnetic Functional Composite—Development and Characterization,” Materials (Basel)., vol. 11, no. 2, p. 189, Jan. 2018.
- K. von Petersdorff-Campen et al., “3D Printing of Functional Assemblies with Integrated Polymer-Bonded Magnets Demonstrated with a Prototype of a Rotary Blood Pump,” Appl. Sci., vol. 8, no. 8, p. 1275, Aug. 2018.
- T. G. Mezger, “The Rheology Handbook,” Pigment Resin Technol., vol. 38, no. 5, p. prt.2009.12938eac.006, Sep. 2009.
- “ASTM E3070-18, Standard Test Method for Shear Thinning Index of Non-Newtonian Liquids Using a Rotational Viscometer, ASTM International, West Conshohocken, PA, 2018,.” 18AD.
- M. Elbadawi, J. L. Rivera-Armenta, and B. A. S. Cruz, “Polymeric Additive Manufacturing: The Necessity and Utility of Rheology,” in Polymer Rheology, IntechOpen Rijeka, 2018, pp. 43–63.
- S. Burlawar, D. J. Klingenberg, T. W. Root, K. Schlafmann, and C. Tim Scott, “Effect of temperature on the rheology of concentrated fiber suspensions,” J. Rheol. (N. Y. N. Y)., vol. 63, no. 4, pp. 677–691, Jul. 2019.
- M. E. Sotomayor, A. Várez, and B. Levenfeld, “Influence of powder particle size distribution on rheological properties of 316L powder injection moulding feedstocks,” Powder Technol., vol. 200, no. 1–2, pp. 30–36, Jun. 2010.
- A. Ranellucci, “Slic3r.” [Online]. Available: https://slic3r.org/.
- C. A. Schneider, W. S. Rasband, and K. W. Eliceiri, “NIH Image to ImageJ: 25 years of image analysis,” Nat. Methods, vol. 9, no. 7, p. 671, 2012.
- M. Kamkar, E. Aliabadian, A. Shayesteh Zeraati, and U. Sundararaj,

"Application of nonlinear rheology to assess the effect of secondary nanofiller on network structure of hybrid polymer nanocomposites," Phys. Fluids, vol. 30, no. 2, p. 023102, Feb. 2018.

- K. B. Manning et al., "Self Assembly–Assisted Additive Manufacturing: Direct Ink Write 3D Printing of Epoxy–Amine Thermosets," Macromol. Mater. Eng., vol. 304, no. 3, p. 1800511, Mar. 2019.
- H. Wang, X. Liu, P. Apostolidis, and T. Scarpas, "Rheological Behavior and Its Chemical Interpretation of Crumb Rubber Modified Asphalt Containing Warm-Mix Additives," Transp. Res. Rec. J. Transp. Res. Board, vol. 2672, no. 28, pp. 337–348, Dec. 2018.
- R. Berndlmaier, "Rheology additives for coatings," in Handbook of coating additives, D. J. M. John J. Florio, Ed. Marcel Dekker Inc, pp. 363–403.
- M. Kamkar, S. Sadeghi, M. Arjmand, and U. Sundararaj, "Structural Characterization of CVD Custom-Synthesized Carbon Nanotube/Polymer Nanocomposites in Large-Amplitude Oscillatory Shear (LAOS) Mode: Effect of Dispersion Characteristics in Confined Geometries," Macromolecules, vol. 52, no. 4, pp. 1489–1504, Feb. 2019.
- E. Aliabadian, S. Sadeghi, M. Kamkar, Z. Chen, and U. Sundararaj, "Rheology of fumed silica nanoparticles/partially hydrolyzed polyacrylamide aqueous solutions under small and large amplitude oscillatory shear deformations," J. Rheol. (N. Y. N. Y)., vol. 62, no. 5, pp. 1197–1216, Sep. 2018.
- A. Rezvani Moghaddam, M. Kamkar, Z. Ranjbar, U. Sundararaj, A. Jannesari, and B. Ranjbar, "Tuning the Network Structure of Graphene/epoxy nanocomposites by Controlling Edge/Basal Localization of Functional Groups," Ind. Eng. Chem. Res., 2019.
- I. C. Nlebedim et al., "Studies on in situ magnetic alignment of bonded anisotropic Nd-Fe-B alloy powders," J. Magn. Magn. Mater., vol. 422, pp. 168–173, Jan. 2017.
- K. P. Su, Z. W. Liu, D. C. Zeng, D. X. Huo, L. W. Li, and G. Q. Zhang, "Structure and size-dependent properties of NdFeB nanoparticles and textured nano-flakes prepared from nanocrystalline ribbons," J. Phys. D. Appl. Phys.,

vol. 46, no. 24, p. 245003, Jun. 2013.

- X. F. Wang, D. Lee, and Z. L. Jiang, “Magnetic properties of hybrid polymer bonded Nd–Fe–B/ferrite magnets,” J. Appl. Phys., vol. 99, no. 8, p. 08B513, Apr. 2006.
- L. E. Edwards, J. M. Yon, I. P. Bond, and P. H. Mellor, “Structural magnetic composites for use in electro-mechanical applications,” in 20th International Conference on Composite Materials, Copenhagen, 2015, no. July, pp. 19–24.
- D. Fullwood, C. Haehl, and B. Lively, “Magnetically loaded filament wound composites,” in SAMPE Conference Proceedings: Material and Process Innovations: Changing Our World. Long Beach, CA, May 18-22, 2008. Society for the Advancement of Material and Process Engineering. CD-ROM-5pp.
- T. Watanabe et al., “Photoresponsive hydrogel microstructure fabricated by two-photon initiated polymerization,” Adv. Funct. Mater., vol. 12, no. 9, pp. 611–614, 2002.
- D. Schläfer, T. Walker, N. Mattern, W. Grünberger, and D. Hinz, “Analysis of texture distribution in NdFeB hard magnets by means of X-ray diffraction in Bragg-Brentano geometry,” Texture, Stress. Microstruct., vol. 26, pp. 71–81, 1996.
- N. Poudyal, C. Rong, and J. P. Liu, “Anisotropic bonded magnets fabricated via surfactant-assisted ball milling and magnetic-field processing,” J. Phys. D. Appl. Phys., vol. 44, no. 33, p. 335002, 2011.